Various Phenomenological Aspects of the R-parity Violating MSSM

Dissertation
zur
Erlangung des Doktorgrades (Dr. rer. nat.)
der
Mathematisch-Naturwissenschaftlichen Fakultät
der
Rheinischen Friedrich-Wilhelms-Universität Bonn

von
Dominik Köhler
aus
Köln

Bonn, August 2023

Angefertigt mit Genehmigung der Mathematisch-Naturwissenschaftlichen Fakultät der Rheinischen Friedrich-Wilhelms-Universität Bonn

1. Gutachter:	Prof. Herbert K. Dreiner, Ph.D.
2. Gutachter:	Prof. Dr. Manuel Drees
Tag der Promotion:	05.12.2023
Erscheinungsjahr:	2024

Abstract

The Standard Model (SM) faces both theoretical and experimental challenges that indicate the existence of physics beyond its current framework. Among the proposed extensions, supersymmetry (SUSY) emerges as a promising concept. The simplest extension of the SM, which incorporates SUSY, is the Minimal Supersymmetric Standard Model (MSSM). It provides a potential candidate for dark matter and offers solutions to the hierarchy problem. As part of the definition of the MSSM, imposing a discrete R-parity (R_p), to prevent proton decay, forbids every term in the Lagrangian that violates baryon or lepton number. However, imposing this symmetry is not necessary. Models that violate R-parity (RPV) exhibit a rich and diverse phenomenology different from the R_p-conserving MSSM and provide a more original mechanism for neutrino mass production.

This thesis addresses the phenomenology of the RPV-MSSM by identifying different characteristic regions within the RPV-MSSM landscape and exploring their signatures. Depending on the choice of RPV couplings, the framework may exhibit potential gaps in the coverage. We try to provide studies, which potentially close these gaps and try to give an overview of the vast RPV-MSSM landscape.

By analyzing the structures of the neutrino mass matrix, we identify minimal models for understanding neutrino masses in the B_3-conserving RPV-MSSM. These models provide valuable insights into understanding neutrino masses, in the general context of RPV scenarios that have not been analyzed.

We use several collider experiments to investigate how different types of signals can be revealed as a result of the choice and strength of RPV couplings as well as the mass of SUSY particles. We present a systematic analysis of the RPV-MSSM and its collider signatures to find a minimal number of experimental searches for comprehensive LHC coverage. The lightest neutralino with a mass of $\mathcal{O}$(GeV) and small couplings is unconstrained in the RPV-MSSM. We present three approaches for both constraining the coupling parameters and exploring the sensitivity regions of future experiments. We consider neutralino production in meson decays via $LQ\bar{D}$ operators, followed by loop-induced decays into a photon and a neutrino in `FASER`. We re-interpret experimental results, derived for heavy neutral leptons (HNL), to constrain the RPV couplings. And we study a novel proton decay involving a bino-like neutralino and the resulting decay signature.

Our approach emphasizes the potential of future experiments, including those not specifically designed for SUSY searches, to effectively probe the RPV landscape.

Acknowledgments

First of all, I would like to thank Herbi Dreiner for offering me the opportunity to be part of his research group during the last few years. I enjoyed the possibility to work in this field and to pursue the things I could do best - at least from my point of view. I am also thankful for all the non-academic discussions about bike rides, especially offering the opportunity to join him and his friends to discover the Westerwald. Not so grateful but still I appreciate his constant comments about my terrible pronunciation and my poor choice of words in the English language. Another special thanks goes to Manuel Drees, for co-reviewing my thesis. I will miss his physics insights which he provided in the Journal club, theory seminar, or any scientific discussion. Especially, I will miss the fact that he always won the quiz at the Christmas party although I tried my best to find questions which do not fall into his common knowledge. A similar thank goes to the other members of my Ph.D. committee, Florian Bernlochner, and Thomas Kesselheim.

Of course, I have not worked alone, and little of this science would have been accomplished were it not for my many collaborators who have helped; providing guidance, and being patient when I was working on the simulation code: Zeren Simon Wang, Víctor Martín Lozano, Yong Sheng Koay, Javier Montejo Berlingen, Nadja Strobbe, Martin Schürmann, and Apoorva Shah. Especially, I thank Saurabh Nangia for enduring me in all projects, providing me with (more or less) useful tasks, and keeping me busy working on his plots.

I want to acknowledge the members of the BCTP for a wonderful and inspiring time. Thank you for bringing fun into physical discussions and the lunch and coffee break. In alphabetic order: Max Berbig, Gerrit Bickendorf, Kilian Bönisch, Raphael Brinster, Annika Buchholz, Stefano Colluci, Florian Domingo, Janis Dücker, Ekta, Fabian Fischbach, Stefan Förste, Rhorry Gauld, Julian Günther, Philipp Höllmer, Joshua Kames-King, Manuel Krauss, Yannic Kruse, Abhinav Joshi, Florian Loebbert, Christoph Liyanage, Christian Maas, Sara Maggio, Rahul Mehra, Bardia Najjari Farizhendi, Christoph Nega, Hans Peter Nilles, Urmi Ninad, Julian Piribauer, Franziska Porkert, “Fake” Saurabh (Natu), Thorsten Schimmanek, Cathrin Semper, Rhitaja Sengupta, Sven Stawinski, Paarth Thakkar, Andreas Trautner, Max Wiesner, and Yong Xu.

Without the help of Christa Börsch, Lora Schindler, Petra Weiß, Andreas Wißkirchen, and Patrica Zündorf the institute would probably collapse. Thanks for your support and guidance throughout the years I spend here. Additionally, I want to thank Oliver Freyermuth for his patience in answering every stupid question concerning the cluster or `CheckMATE`.

I also want to thank Barbara Valeriani-Kaminski for fascinating me for outreach and giving me the opportunity to work with Netzwerk Teilchenwelt. During that time, I especially enjoyed working together with Philipp Bielefeldt, Maike Hansen, and Philipp König.

I am grateful to Florian Domingo and Apoorva Shah for carefully proofreading my thesis and having the patience to improve my writing with their suggestions.

Of course, I am also deeply happy that I got a lot of support from my friends. I appreciated every bike ride, tennis game, or spending time outside of the institute. Thanks for being there in my life and I am glad that I had the chance to spend with all of you. My biggest gratitude belongs to my family and my parents; for their endless support and love - not only

during my Ph.D. but also during my whole life. I also thank Katharina for her care and support in all situations in life.

The recent years of have been a wonderful experience and I am very grateful for the people I have met and the knowledge they have shared with me. I am very grateful for all people whose paths I crossed during my Ph.D.

List of Publications

[1] J. L. Feng et al.,
The Forward Physics Facility at the High-Luminosity LHC,
Published in J. Phys. G 50 (2023) 3, 030501, arXiv:2203.05090 [hep-ex].

[2] H. K. Dreiner, D. Köhler, S. Nangia, and Z. S. Wang,
Searching for a single photon from lightest neutralino decays in R-parity-violating supersymmetry at FASER,
Published in JHEP 02 (2023) 120, arXiv:2207.05100 [hep-ph].

[3] H. K. Dreiner, D. Köhler, and S. Nangia,
*A ν approach to analyzing neutrino data in the **R**-parity-violating MSSM*,
Published in Eur. Phys. J. C 83 (2023) 1, 44, arXiv:2210.07253 [hep-ph].

[4] H. K. Dreiner, Y. S. Koay, D. Köhler, V. M. Lozano, J. M. Berlingen, S. Nangia, and N. Strobbe,
The ABC of RPV: Classification of R-Parity Violating Signatures at the LHC for Small Couplings,
Published in JHEP 07 (2023) 215, arXiv:2306.07317 [hep-ph].

[5] H. K. Dreiner, D. Köhler, S. Nangia, M. Schürmann, and Z. S. Wang,
Recasting Bounds on Long-lived Heavy Neutral Leptons in Terms of a Light Supersymmetric R-parity Violating Neutralino,
Published in JHEP 08 (2023) 058, arXiv:2306.14700 [hep-ph].

The contents of this thesis are based on publications [2-5].

Contents

1 Introduction **1**
1.1 The Standard Model of Particle Physics . . . 1
1.2 Supersymmetry . . . 7
1.3 R-Parity Violation . . . 10
1.3.1 Where to find RPV Supersymmetry? . . . 12
1.3.2 Massive Neutrinos . . . 12
1.3.3 A Light Neutralino . . . 14
1.3.4 Proton Decay in the RPV-MSSM . . . 14
1.4 Outline . . . 15

2 A ν Approach to Analyzing Neutrino Data in the R-Parity-Violating MSSM **17**
2.0 Preface . . . 17
2.1 Introduction . . . 19
2.2 R-Parity Violation: Theoretical Framework . . . 20
2.3 Neutrino Masses and R-parity Violation . . . 21
2.4 Minimal Oscillation Models . . . 25
2.5 Neutrino Data . . . 28
2.6 General Features of our Results . . . 29
2.6.1 Class 1: $x^i x'^j + x'^i x^j$ . . . 30
2.6.2 Class 2: $x^i x^j + \left(x^i x'^j + x'^i x^j\right)$ . . . 34
2.6.3 Class 3: $x^i x^j + x'^i x'^j$ . . . 36
2.7 Numerical Fits . . . 37
2.8 Example Applications . . . 39
2.8.1 κ-only Models . . . 39
2.8.2 $\kappa - B$ Models . . . 40
2.8.3 Diagonal Trilinear Models I . . . 41
2.8.4 Diagonal Trilinear Models II . . . 42
2.8.5 Non-diagonal Trilinear Models . . . 43
2.8.6 Bilinear-Trilinear Models . . . 45
2.9 Conclusions . . . 46

3 The ABC of RPV: Small Couplings **47**
3.0 Preface . . . 47
3.1 Introduction . . . 49
3.2 Framework . . . 51
3.2.1 Conventions and Assumptions . . . 51
3.2.2 The RPV Landscape . . . 53
3.3 Classification of Signatures: The RPV Dictionary . . . 54
3.3.1 LLE Tables . . . 56
3.3.2 UDD Tables . . . 58
3.3.3 LQD Tables . . . 60

3.4 Sample Application of the Framework: LLE Couplings . . . 64
3.4.1 Benchmark Scenarios . . . 64
3.4.2 Results . . . 70
3.5 Conclusions and Outlook . . . 78

4 Single Photon Searches for R-parity-violating Supersymmetry at FASER 81
4.0 Preface . . . 81
4.1 Introduction . . . 83
4.2 Theoretical Framework . . . 85
4.2.1 The R-parity-violating MSSM . . . 85
4.2.2 A Very light Lightest-Neutralino . . . 85
4.2.3 Neutralino Decay . . . 87
4.3 Benchmark Scenarios . . . 88
4.4 FASER Experiment . . . 90
4.5 Simulation . . . 92
4.6 Numerical Results . . . 94
4.7 Conclusions . . . 100

5 Recasting Bounds on Long-lived Heavy Neutral Leptons in Terms of a Light Supersymmetric R-parity Violating Neutralino 101
5.0 Preface . . . 101
5.1 Introduction . . . 103
5.2 Model basics . . . 105
5.2.1 RPV-MSSM with a light bino . . . 105
5.2.2 Heavy neutral leptons . . . 106
5.2.3 The phenomenology connecting the light bino LSP and the HNL . . . 107
5.3 Experiments and recasting . . . 108
5.3.1 Direct-decay searches . . . 108
5.3.2 Displaced-vertex searches . . . 110
5.3.3 Missing-energy searches . . . 112
5.3.4 Other searches . . . 113
5.3.5 The recasting procedure . . . 113
5.4 Numerical results . . . 116
5.4.1 One-coupling scenarios . . . 116
5.4.2 Two-coupling scenarios . . . 121
5.5 Conclusions . . . 133

6 A Novel Proton Decay Signature at DUNE, JUNO and Hyper-K 135
6.0 Preface . . . 135
6.1 Introduction . . . 135
6.2 Proton Decay in R-Parity Violating MSSM . . . 136
6.2.1 Decay Width Calculation . . . 136
6.2.2 Signatures . . . 140
6.3 Proton Decay Experiments . . . 143
6.3.1 Detectors . . . 143

6.3.2 Proton Decay in Nuclei . . . 145
6.4 Simulation Procedure . . . 146
6.5 Benchmark Scenarios . . . 149
6.6 Numerical Results . . . 151
6.7 Conclusions . . . 156

7 Conclusions & Outlook **157**

A Appendix A **161**
A.1 Analytical Expressions for the MOM Solution Spaces . . . 161
A.2 A Mini-guide to MOMs . . . 163
A.3 Numerical Plots . . . 165

B Appendix B **169**
B.1 Decay Modes for Numerical Simulations . . . 169
B.2 Auxiliary Tables . . . 170
B.2.1 Production Table . . . 170
B.2.2 Flavor, Sign Configurations of Leptons . . . 173
B.3 `abc-rpv`, the RPV Python Library . . . 176
B.3.1 Introduction . . . 176
B.3.2 Assumptions and Caveats . . . 176
B.3.3 Usage . . . 176

C Appendix C **181**
C.1 Explicit neutralino production/decay widths with $LL\bar{E}$ operators . . . 181

Bibliography **183**

List of Figures **215**

List of Tables **219**

"There is nothing like looking, if you want to find something. You certainly usually find something, if you look, but it is not always quite the something you were after."

J.R.R. Tolkien, The Hobbit

1 Introduction

The aim of the introduction is to motivate supersymmetry (SUSY) as a promising form of physics beyond the Standard Model (BSM). We attempt to show where opportunities arise to discover new phenomenological consequences leading to increased recent and upcoming developments in experiments.

1.1 The Standard Model of Particle Physics

The recent progress in our experiments allows us to investigate our Universe with unprecedented precision, not only on large but also on small scales. Our fundamental knowledge about our Universe is not only strengthened by the progress in the field of cosmology but also by our understanding of elementary particles, forces, and symmetries. The modern understanding of elementary particles and their interactions was formulated in the 1960s, leading to the Standard Model of particle physics (SM). The SM has proven incredibly successful at embedding experimentally observed features within its theoretical fabric. The underlying mathematical framework of the SM is that of quantum field theory with the addition of gauge symmetry, manifesting itself through the gauge group $\mathrm{SU}(3)_C \times \mathrm{SU}(2)_L \times \mathrm{U}(1)_Y$. It embodies the fundamental particles and their interactions; it comprises the fundamental building blocks of matter - three generations of fermions (quarks and leptons), each characterized by unique quantum numbers and mass eigenstates, and the gauge bosons (photons, W and Z bosons, and gluons) that mediate interactions within the SM. A key element of the theory is the Higgs field; its non-zero vacuum expectation value breaks the gauge symmetry, which subsequently triggers the spontaneous symmetry breaking of the electroweak group to the electromagnetic subgroup:

$$SU(3)_C \times SU(2)_L \times U(1)_Y \quad \xrightarrow{\text{SSB}} \quad SU(3)_C \times U(1)_{\text{QED}}.$$

The mechanism generates the masses of the weak gauge bosons and manifests itself in the appearance of a physical scalar particle, the so-called Higgs boson. The fermion masses and mixings are also generated through spontaneous symmetry breaking. SM matter is naturally classified according to the color, weak isospin, and hypercharge, that it carries. The achievement of the SM was the elaboration of a unified description of the strong, weak, and electromagnetic forces in the language of quantum field theories. The SM achieved a coherent description of the strong, weak, and electromagnetic forces, explaining in particular short-range weak forces (spontaneously broken gauge symmetry) and the electroweak mixing. It was predicted and was incorporated into the SM by Glashow [1], Weinberg [2], and

Salam [3], and lead to the discovery of the Higgs boson, the only scalar particle predicted by the model, in 2012 [4, 5]. The Higgs particle was the last missing block of the SM framework. The successful tests of the SM quantum corrections with precision electroweak data confirm the assumed pattern of spontaneous symmetry breaking but are insufficient so far to prove the validity of the minimal Higgs mechanism embedded in the SM. The fermion mass terms are generated via gauge invariant renormalizable Yukawa couplings to the scalar Higgs field. The mass itself is, thus, directly proportional to the Yukawa coupling. After symmetry breaking one diagonalizes the mass matrices of all fields and after that one uses the freedom in the phase definition of the fields to reabsorb as many phases as possible. The remaining parameters in the Lagrangian are the physical parameters and represent the free parameters of the SM.

In the context of the SM, symmetries are not limited to internal transformations associated with particle interactions. There are also symmetries associated with the fundamental nature of spacetime itself. These spacetime symmetries are described by the Poincaré group, which is the second and more fundamental type of symmetry that appears in the SM; being the building block of the underlying quantum field theory.

While the SM is a great success, essential puzzles remain unresolved within the framework. We begin with a few observational flaws.

(i) *What is the nature of Dark Matter (DM)?*

Gravitational evidence for the existence of DM first arose in 1933[6]; from the observation of the velocity distributions of galaxies within a cluster, it became clear that the actual mass of a galaxy cluster is much larger than the sum of the masses of the luminous stars, which were thought to make up the mass of the galaxies. The observation was later confirmed by measuring rotation curves of galaxies [7, 8]. The circular velocities of stars and gas in relation to their distance from the center of the galaxy did not agree with predictions from Newtonian physics. In order to reconcile with Newtonian physics, the total mass distribution in a galaxy can only be explained by the fact that a large fraction of the galaxy's mass consists of non-luminous matter, *i.e.* Dark Matter. Further experimental evidence was provided by observations of galaxy clusters, gravitational lensing, and the cosmic microwave background (CMB) [9, 10]. Within the current cosmological Standard Model (ΛCDM), only 32% of the Universe is in the form of matter, but only one-sixth of it is baryonic. The remaining energy of the Universe is dark energy (68%) [11]. Even though the existence of DM is well-motivated by gravitational evidence at different mass scales its nature remains unknown and it does not fit within the SM structure. This makes any non-gravitational measurement of DM difficult and leads to a variety of models and corresponding detection possibilities.

(ii) *What is the origin of neutrino masses?*

The SM does not explain the origin of neutrino masses, so it must be extended; neutrino masses have first been measured in precise neutrino oscillation data [12]: the observation can be explained when the neutrinos - at least two out of three species - have a finite mass and the lepton flavors are mixed. The SM mass operator of the neutrino necessarily changes the handedness if it is to yield a non-zero value. However, right-handed neutrino fields do not enter into the SM Lagrangian and there is no way to give mass to the

neutrinos, if fermion number is to be conserved[1]. As a consequence, we find that neutrino masses are identically zero in the minimal SM.

There are several simple extensions to the SM that could generate neutrino masses without changing the local symmetry of the weak interactions. Neutrino masses can be introduced into the SM by extending it to include right-handed neutrinos, called sterile neutrinos, which do not participate in the weak interaction. A Yukawa interaction would generate a Dirac mass term for the neutrino. However, the coupling would be much smaller than the couplings of their charged lepton weak partner. A possible mechanism, which provides an explanation of why the masses are so small compared to the electroweak scale, is the seesaw mechanism. It introduces a large mass scale for the right-handed neutrinos, resulting in tiny masses for the observed left-handed neutrinos. The approach is more natural since the right-handed neutrino mass is not protected by the electroweak symmetry and, hence, can be expectedly large.

In recent years, the interest in neutrino physics has gained a lot of attention. Since the measurement of the first neutrino oscillations by `Super-Kamiokande` [13] through studying high-energy atmospheric ν_μ in 1998, many other experiments have measured flavor oscillations. Neutrino oscillations also provided an explanation for the unanswered solar neutrino problem measured at the Homestake experiment in the 1970s [14]. Experiments have now reached an era of precision measurements, the central focus of which is the determination of the angles and the CP phase of the Pontecorvo-Maki-Nakagawa-Sakata (PMNS) neutrino mixing matrix. The mass eigenstates correspond to eigenstates of the Hamiltonian describing a free neutrino, but the flavor eigenstates - eigenstates of the weak interactions - do not. The three flavor eigenstates correspond to the different reactions that produce those neutrinos. The flavor composition of the different mass eigenstates can be found in Fig. 1.1.

Since the resulting appearance and disappearance probability in oscillation experiments is a function of the difference of the squared neutrino masses, the absolute masses remain unknown. The existence of oscillations just indicates that at least two out of three mass eigenstates have non-zero values, as indicated by the two observed mass splittings. The two independent mass differences $\Delta m^2_{\text{sol}} = \Delta m^2_{21}$ and $\Delta m^2_{\text{atm}} = \Delta m^2_{31}$ measuring the solar and atmospheric neutrino oscillations are best fit when the squared neutrino mass differences are $\mathcal{O}\left(7.5 \times 10^{-5}\,\text{eV}^2\right)$ and $\mathcal{O}\left(2.5 \times 10^{-3}\,\text{eV}^2\right)$, respectively. While Δm^2_{sol} is measured to be positive, indicating that $m_1 < m_2$, the sign of Δm^2_{atm} remains unknown. This results in the possibility of two possible neutrino mass ordering schemes:

$$\begin{aligned} &\text{Normal ordering (NO):} && m_1 < m_2 \ll m_3\,, \\ &\text{Inverted ordering (IO):} && m_3 \ll m_1 < m_2\,. \end{aligned}$$

However, global fits to neutrino oscillation data over the last several years tend to favor the normal neutrino mass ordering and values of the CP phase around maximal CP

[1] One could also add a Majorana mass term with only left-handed neutrinos but this term violates the electroweak gauge symmetry of the SM.

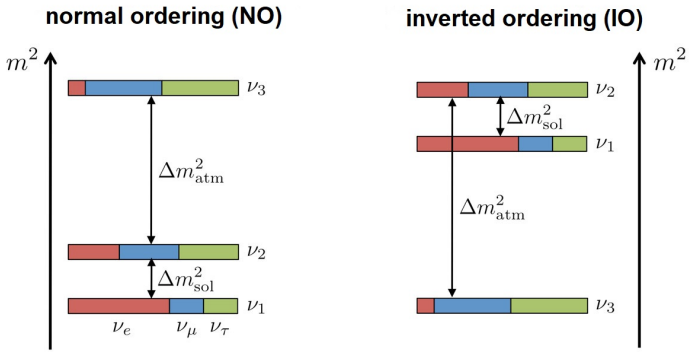

Figure 1.1: Neutrino mass eigenstate flavor composition and mass pattern in the two cases of normal (left) and inverted (right) ordering. Figure taken from [15].

violation.

(iii) *Why is there predominantly matter and only very little antimatter in the Universe observed today[16, 17]?*

According to the SM, matter and antimatter are produced in equal amounts in the early Universe. From observations, we can be almost certain that the Universe today contains no significant amounts of (baryonic) antimatter, and the baryons are the remnant of a small matter-antimatter asymmetry, approximately on the order of $\mathcal{O}(10^{-10})$. The asymmetry may be explained through baryogenesis, first proposed by Sakharov [18]. There are three necessary conditions for successful baryogenesis, these require baryon number to be violated, C and CP violation, and deviation from thermal equilibrium. In the SM, $B - L$ is accidentally conserved at the perturbative level; accidental here means that the most general renormalizable gauge-invariant (perturbative) interactions automatically preserve them. While baryon number is still violated in the SM non-perturbatively through effects such as instantons and sphalerons [19–22], these cannot account for the observed asymmetry [23–26]. In addition, P [27] and CP [28] are violated by the weak interaction and the quark Yukawa couplings [29] and the non-equilibrium condition is fulfilled due to the expansion of the Universe. As it turns out, the sources of CP violation in the SM are extremely unlikely to be sufficient to explain the observed asymmetry between matter and antimatter.

Switching now to theoretical flaws within the SM framework:

(i) *Can we achieve gauge coupling unification and embed the SM in a bigger gauge group?* Within the SM, the strong, weak, and electromagnetic interactions exist as basically unrelated and independent gauge groups. It remains a plausible scenario that all of these interactions really are arbitrary and that their origin is simply too hard for us to understand; clearly one desires a more unified theory that can combine the three interactions into one fundamental force. The SM is a formally complete theory, however, the cancellation of gauge anomalies seems rather fortuitous and calls for a justification. The idea of grand unified theories is that the observed interactions are low-energy manifestations of an underlying unified theory. In addition, a unified theory

is compelling because it can provide an explanation for charge quantization and family structure, can predict Yukawa coupling unification, and might explain the hierarchy of fermion masses. In the SM, the low-energy gauge couplings remain as seemingly arbitrary parameters[2]. This difficulty can be addressed by embedding the gauge group of the SM into a simple unified gauge group. The simplest approach involves unifying the gauge group $\mathrm{SU}(3)_C \times \mathrm{SU}(2)_L \times \mathrm{U}(1)_Y$ into the semisimple group SU(5) [30], *i.e.* the three coupling constants g_3, g_2 and g_1 are given by one coupling constant g_5[3]. One immediate consequence of the unified scheme is an explanation for the experimentally observed charge quantization. In SU(5), the electric charge is one of the generators and, thus, its eigenvalues are discrete and quantized. In such case, quarks and leptons are two sides of the same coin, related by a new grand unified gauge symmetry, then that same symmetry relates the Yukawa couplings (and hence the masses) of quarks and leptons. Quarks and leptons can be unified within a single framework, and put into corresponding irreducible representations of the gauge group. Nevertheless, Yukawa unification is not successful within the framework of the simplest unification models. The introduction of new representations of the Higgs fields generally becomes to achieve the required degrees of freedom.

One consequence of GUT models is that baryon number and lepton number are no longer symmetries at the perturbative level and the lifetime of the proton, depending on the exact model, is finite.

(ii) *What is dark energy?*

Hubble's discovery [31] that the Universe is expanding eliminated the empirical need for a static world model. Corresponding to the introduction of DM, the term "dark energy" was later introduced to explain the accelerated evolution of our Universe [32] - for a historic overview of the development of the concept of dark energy, *cf.* Ref [33]. One proposed candidate for dark energy is the cosmological constant. In recent years, we have realized that the cosmological constant can be interpreted as a measure of the energy density of the vacuum. This energy density is the sum of several seemingly unrelated contributions, each much larger than the present upper limits on the cosmological constant. This leads to the question: *why the observed vacuum energy is so small compared to the scales predicted by particle physics?* This has remained a puzzle and is called the "cosmological constant problem".

One further unsolved theoretical problem is the so-called "Hierarchy problem". The consistency of the SM is endangered by the instability of the Higgs vacuum expectation value under quantum loop corrections originating from new physics, *e.g.* unification. It is not a direct problem of the SM itself but rather it reflects the Higgs potential's sensitivity

[2] The strength of these couplings evolves with energy scale due to the renormalization group evolution (and the conformal anomaly). In turn, while coupling strengths deviate at the electroweak scale, they could potentially be equal at a higher energy scale.

[3] The attempts to embed the SM in SU(5) do not succeed since the three gauge couplings do not meet in one point. This can be cured in a multi-step unification scenario at the price of introducing new particles. In addition, SUSY close to the electroweak scale offers a way to adjust the theory so that all three coupling constants precisely match at an energy scale of approximately $\mathcal{O}\left(1 \times 10^{16}\,\mathrm{GeV}\right)$.

to the new physics energy scale under the assumption that new physics couples directly or indirectly to the Higgs boson. The need for precise fine-tuning - between the bare parameters of the high-energy model and the finite quantum corrections - to maintain the observed mass hints at the existence of a more comprehensive theory that can naturally, without excessive fine-tuning, explain the hierarchy of mass scales between the electroweak and Planck scale and whose lightest new particle resides very likely at the TeV scale. Otherwise, our Universe is oddly fine-tuned for our existence. Unlike scalars, the quantum corrections to fermion and gauge boson masses are proportional to the particle masses themselves. Corrections to the fermion masses are preserved by an approximate chiral symmetry that becomes exact when the product of the fermion mass, m_f, and the corresponding chiral field, f, approaches zero. Similarly, for gauge bosons, this is imposed because gauge symmetry is restored in the massless limit. However, there is no equivalent symmetry to protect the mass of a scalar field.

In fact, it can be seen, performing the loop corrections, that the corrections to the Higgs mass diverge quadratically with the high-energy cutoff. The Higgs mass m_H receives a correction due to the Higgs field coupling to a Dirac fermion f, whose mass m_f is proportional to its coupling λ_f with Higgs,

$$\Delta m_H^2 = -\frac{|\lambda_f|^2}{8\pi^2}\Lambda_{\mathrm{UV}}^2 + \dots , \tag{1.1}$$

where Λ_{UV}^2 is the ultraviolet momentum cutoff. We find that there are both quadratic and logarithmic divergent contributions. Notably, any renormalization procedure leaves a residual finite correction. The quadratic dependence on the energy scale is reintroduced by any new physics. One could perhaps argue that there is no contradiction, and if our theory can reproduce the data, consistent even with procedural technicalities, then other considerations might simply be philosophical. However, measuring the viability of a theory solely by the fact that it is not absolutely implausible and is consistent with the data is an extremely modest standard. We can understand naturalness as a useful guide toward new physics, and this guide has worked well in the past.

At a technical level, we can cure the quadratic divergence by a possible compensation between fermionic and scalar loops. By introducing a symmetric mapping between fermionic and bosonic representations of the Lorentz group, we end up with an equal number of fermionic and bosonic degrees of freedom. This symmetry would cure the problem by relating fermionic and bosonic masses, hence extending the chiral protection to the scalars. This approach ensures that the symmetry is not even violated at the radiative level. This field-theoretic mechanism, which prevents contributions to the Higgs mass in the UV, can be achieved by a certain symmetry, namely supersymmetry. As long as SUSY is unbroken, all particles of the same supermultiplet are degenerate in mass and, thus, cancel the instability exactly. Nevertheless, this holds only true for unbroken SUSY which has not been observed. Nevertheless, even softly-broken supersymmetric extensions of the SM [34, 35] have long been regarded as a leading class of candidates for the resolution of the hierarchy problem [36–38] without excessive fine-tuning leading to an electroweak-scale Higgs boson mass.

Among the theoretical naturalness puzzles of the SM, there is the strong CP-problem [39]. This puzzle has to do with the presence of the θ-term in the SM Lagrangian - the QCD vacuum angle. A non-vanishing θ-term generates a non-zero electric dipole moment of the

neutron, which is experimentally strong constrained [40, 41], implying the bound $|\bar{\theta}| < 10^{-10}$. Since there is *a priori* no symmetry or dynamical mechanism related to the θ-term the question arises why its value is unnaturally small if it is different from zero. A proper discussion can be found, *e.g.* in Refs. [42–44].

1.2 Supersymmetry

The following section is based on Refs. [45, 46]. Coleman and Mandula [47] proved a "no-go"-theorem that the only symmetry group of the scattering matrix that included Poincaré symmetry was the product of Poincaré symmetry and an internal symmetry group, *e.g.* a trivial tensor product of these two symmetry groups. For a possible extension, we are forced to look at a loophole of this theorem which is to consider superalgebras. Haag, Łopuszański, and Sohnius [48] showed, extending the Coleman-Mandula theorem, that SUSY is the only possible extension of the Poincaré algebra. In addition to the Poincaré algebra, we introduce complex, anticommuting spinors $Q, Q^\dagger$ which satisfy:

$$\{Q_\alpha, Q_\beta\} = 0 = \left\{Q^\dagger_\alpha Q^\dagger_\beta\right\} . \tag{1.2}$$

A supersymmetry transformation turns a bosonic state into a fermionic state, and vice versa. Thus, the spinor generates transformations with

$$Q\,|\text{boson, fermion}\rangle = |\text{fermion, boson}\rangle\ . \tag{1.3}$$

The states that transform into one another and fall into irreducible representations of the SUSY algebra form a supermultiplet. Bosons and fermions are contained in each supermultiplet. In addition, the anticommutator of the fermionic generators is proportional to the Poincaré translation generator P^μ and take the schematic form,

$$\left\{Q, Q^\dagger\right\} = P^\mu\,, \tag{1.4}$$

$$[P^\mu, Q] = \left[P^\mu, Q^\dagger\right] = 0\,. \tag{1.5}$$

The generators commute with the generators of the gauge transformation. Thus, the particles contained in a supermultiplet are in the same representation, having the same electric charge, weak isospin, and color degrees of freedom. Theories with more than one distinct copy of the SUSY generators are possible and considered in extended supersymmetry.

In order to formulate a $N = 1$ SUSY extension of the SM, each SM field must be incorporated within a supermultiplet, hence appearing together with a new, non-BSM field, which is called its superpartner. In exact SUSY, the superfields, belonging to the same multiplet, are mass degenerate and differ in spin by 1/2. The simplest extension of the SM is called the Minimal Supersymmetric Standard Model (MSSM) and contains the SM and preserves its symmetries. Its particle content is doubled by adding fermionic partners for all bosons, scalar partners for all the fermions, and an extra Higgs doublet with its corresponding fermionic partner. The interactions of superfields are described by specifying a so-called superpotential W, a polynomial in the superfields. The shape of the superpotential is specified

Superfield	spin 0	spin 1/2	gen.	$SU(3)_C$	$SU(2)_L$	$U(1)_Y$
Q	$\left(\tilde{u}_L, \tilde{d}_L\right)$	(u_L, d_L)	3	$\mathbf{3}$	$\mathbf{2}$	$\frac{1}{3}$
$\bar{U}$	$\tilde{u}_R^*$	$u_R^\dagger$	3	$\overline{\mathbf{3}}$	$\mathbf{1}$	$-\frac{4}{3}$
$\bar{D}$	$\tilde{d}_R^*$	$d_R^\dagger$	3	$\overline{\mathbf{3}}$	$\mathbf{1}$	$\frac{2}{3}$
L	$(\tilde{\nu}_L, \tilde{e}_L)$	(ν_L, e_L)	3	$\mathbf{1}$	$\mathbf{2}$	-1
$\bar{E}$	$\tilde{e}_R^*$	$e_R^\dagger$	3	$\overline{\mathbf{1}}$	$\mathbf{1}$	2
H_u	$\left(H^+, H^0\right)$	$\left(\tilde{H}^+, \tilde{H}^0\right)$	1	$\mathbf{1}$	$\mathbf{2}$	1
H_d	$\left(H^0, H^-\right)$	$\left(\tilde{H}^0, \tilde{H}^-\right)$	1	$\mathbf{1}$	$\mathbf{2}$	-1

Table 1.1: Chiral supermultiplets in the MSSM

Superfield	spin 1	spin 1/2	gen.	$SU(3)_C$	$SU(2)_L$	$U(1)_Y$
B	B	$\tilde{B}$	1	$\mathbf{1}$	$\mathbf{1}$	0
W^a	W^a	$\tilde{W}^a$	3	$\mathbf{1}$	$\mathbf{3}$	0
G^a	g^a	$\tilde{g}^a$	8	$\mathbf{8}$	$\mathbf{1}$	0

Table 1.2: Gauge supermultiplets in the MSSM

by gauge symmetries, discrete symmetries, and holomorphicity. The extra Higgs doublet is made necessary by the holomorphicity of the superpotential, which forbids simultaneous Yukawa couplings for top and bottom if only one Higgs superfield exists. In addition, the cancellation of gauge anomalies requires higgsinos, superpartners of the scalar Higgs, of opposite hypercharges. In the MSSM, quarks and leptons are parts of chiral superfields with the same SM quantum numbers, together with their superpartners squarks and sleptons, respectively. Gauge bosons and their spin-1/2 partners enter the vector superfields. We summarize the chiral supermultiplets in Table 1.1 according to their transformation properties under the SM gauge groups and the gauge superfields in Table 1.2, where the fields are gauge eigenstates. The superpotential of the MSSM is given by

$$W_{\text{MSSM}} = \mu H_u \cdot H_d + Y^e_{ij} H_d \cdot L_i \bar{E}_j + Y^d_{ij} H_d \cdot Q_i \bar{D}_j - Y^u_{ij} H_u \cdot Q_i \bar{U}_j \,,$$

where μ is the Higgsino mass parameter and Y's are 3×3 Yukawa matrices. L^i and Q^i are the $SU(2)_L$-doublet lepton and quark chiral superfields; $\bar{E}^i, \bar{U}^i, \bar{D}^i$ are $SU(2)_L$-singlet charged anti-lepton, up-type, and down-type anti-quark chiral superfields; and H_d and H_u are the Higgs chiral superfields that are responsible for the down-type and up-type masses, respectively. The gauge indices are not shown explicitly but we depict the generational ones: $i, j, k \in \{1, 2, 3\}$, and employ the summation convention. $\cdot$ denotes the $SU(2)_L$ invariant product. In order to enforce the conservation of baryon and lepton number, R-parity has been imposed in the superpotential.

The parts of the Lagrangian of the MSSM contained in superpotential W_{MSSM} are as

follows:

$$\mathscr{L}_{\text{int}} = -\frac{1}{2}\frac{\partial^2 W_{\text{MSSM}}}{\partial\phi_i\partial\phi_j}\psi_i\psi_j - \left(\frac{\partial W_{\text{MSSM}}}{\partial\phi_i}\right)^2 + \text{h.c.}\,, \tag{1.6}$$

where $\frac{\partial W_{\text{MSSM}}}{\partial\phi_k}$ is the derivative of W_{MSSM} with respect to the superfield ϕ_k and ψ_k is the fermionic component of the superfield ϕ_k. In these derivatives, one needs to first take the derivative with respect to the superfield, then the superfield is replaced by the scalar component.

Since SUSY particles have not been observed with the same masses as their SM partners, we know that there is a mass splitting between SM particles and their superpartners, if they exist. This means that, in a phenomenologically viable model, SUSY is necessarily broken. Nevertheless, this breaking may be soft, *i.e.* involves only terms that do not cause a quadratic sensitivity of the scalar masses to UV scales. This means that any dimensionless SUSY-breaking terms are not allowed. The possible soft-breaking terms of the MSSM are:

$$\begin{aligned}\mathscr{L}_{\text{soft}} &= \tilde{Q}^\dagger m_q^2\tilde{Q} + \tilde{D}^\dagger m_d^2\tilde{D} + \tilde{U}^\dagger m_u^2\tilde{U} + \tilde{L}^\dagger m_l^2\tilde{L} + \tilde{E}^\dagger m_e^2\tilde{E} + m_{H_u}^2|H_d|^2 + m_{H_d}^2|H_d|^2 \\ &+ \frac{1}{2}\left(M_1\tilde{B}\tilde{B} + M_2\tilde{W}^a\tilde{W}^a + M_3\tilde{g}^a\tilde{g}^a + \text{ h.c. }\right) \\ &+ \left(A_u^{ij}\tilde{Q}_i\cdot H_u\tilde{U}_j + A_d^{ij}\tilde{Q}_i\cdot H_d\tilde{D}_j + A_e^{ij}\tilde{L}_i\cdot H_d\tilde{E}_j + bH_d\cdot H_u + \text{ h.c. }\right),\end{aligned} \tag{1.7}$$

where $\tilde{D} = \tilde{d}_R^*, \tilde{U} = \tilde{u}_R^*, \tilde{E} = \tilde{e}_R^*$. Each $m_q^2, m_l^2, m_d^2, m_u^2, m_e^2$ is a 3×3 hermitian matrix and corresponds to quadratic parameters for the masses of the squarks, sleptons. $m_{H_u}^2$, $m_{H_d}^2$ are the squared-mass terms for the Higgs fields, while M_1, M_2, M_3 are the bino, wino, and gluino mass term. $A_u^{ij}, A_d^{ij}, A_e^{ij}, b$ define a holomorphic function of the scalar fields, with a one-to-one correspondence in the superpotential. The soft SUSY-breaking Lagrangian is essential for a successful low-energy phenomenology. The soft terms do not only cause a degeneracy in mass between the SM particles and their superpartners, but these terms are also necessary for electroweak symmetry breaking [49]. By definition, a softly broken theory is indeed still free of quadratic divergences in the corrections to scalar masses which was one of our main motivations to extend our SM. The terms are also compatible with gauge invariance.

Beyond providing a solution to the Hierarchy Problem, the MSSM has remarkable consequences for the applicability of a one-step unification at high energy. Indeed, investigating the running of the gauge couplings in the presence of SUSY superpartners at the TeV scale, it was observed that these converge almost exactly towards a common value at a scale of 10^{16} GeV. Such a scale might also suppress the proton decay rates in a unified model within the limits compatible with current bounds.

Despite its many advantages, the R_p-preserving MSSM (RPC-MSSM) here provides no new mechanism compared to the SM concerning neutrino masses. Within the RPC-MSSM seesaw-like models are possible. Nevertheless, a more original approach to address neutrino masses is to relax the lepton and baryon number conservation; neutrino masses can be incorporated by introducing new terms into the superpotential that violate lepton number conservation. The extended MSSM is often referred to as the R-parity violating MSSM or

RPV-MSSM.

1.3 R-Parity Violation

In this section, we discuss the concept of R-parity violation (RPV), which is an assumption regarding the discrete symmetry of the MSSM. R-parity, which is often referred to as matter parity, is characterized by a discrete multiplicative quantum number that takes the value $+1$ for particles and -1 for their superpartners, thus forming a $\mathbb{Z}_2$ symmetry. Although the conservation of R-parity is a standard characteristic in the MSSM, there is no compelling theoretical reason to enforce it. It only serves to forbid lepton- and baryon-number-violating terms in the renormalizable Lagrangian. We can express R-parity in terms of baryon number (B), lepton number (L), and spin (S), using the relation,

$$R_p = (-1)^{3B+L+2S} . \tag{1.8}$$

A priori, it is not clear why baryon and lepton number should be considered good quantum numbers in SUSY at energies beyond the weak scale. Even in the MSSM, the stability of the proton is not exact; if one were to regard it as an effective framework, higher-order operators can mediate proton decay [50–52]. An exact MSSM does not allow for non-renormalizable terms. However, it is clear that the MSSM itself can only be an effective theory so the existence of non-renormalizable terms satisfying R_p but violating baryon and lepton numbers would be likely, thus, hints at the need for stronger protection than R_p to avoid proton decay. In the case of no R_p, one could allow for renormalizable baryon- and lepton-number-violating interactions [45, 50, 53, 54]. To efficiently address the problem of proton decay, other types of symmetries, such as baryon-triality or proton hexality, have been proposed [55, 56]. Consequently, the possibility of RPV is a valid choice to be considered as a distinctive phenomenology.

In this work, we will explore the phenomenology of the RPV landscape that does not violate experimental bounds on the proton lifetime. By investigating the scope of RPV in the MSSM, we seek to illuminate the viability of scenarios within the known experimental limits. In addition, we will examine how RPV can lead to intriguing new signals and discuss the possibility of improving the constraints applying to the RPV-MSSM using existing experiments as well as determining sensitivity ranges for future experiments. We aim to provide new avenues for exploring striking signals being different from SM and RPC-MSSM.

First, we take a step back and introduce the superpotential of the RPV-MSSM which may be expressed in the notation of Ref. [54]:

$$W = W_{\text{MSSM}} + W_{\text{LNV}} + W_{\text{BNV}} , \tag{1.9}$$

where W_{MSSM} is the MSSM superpotential, while the terms,

$$W_{\text{LNV}} = \frac{1}{2}\lambda_{ijk} L^i L^j \bar{E}^k + \lambda'_{ijk} L^i Q^j \bar{D}^k + \kappa_i H_u L^i , \qquad W_{\text{BNV}} = \frac{1}{2}\lambda''_{ijk} \bar{U}^i \bar{D}^j \bar{D}^k , \tag{1.10}$$

violate lepton and baryon number, respectively. We employed the superfields of the MSSM,

L^i, Q^i, $\bar{E}^i, \bar{U}^i, \bar{D}^i$, H_d, and H_u as introduced in Table 1.1. Together, $W_{\text{RPV}} \equiv W_{\text{LNV}} + W_{\text{BNV}}$ are referred to as R-parity-violating terms. They include 48 (complex-valued) parameters: 3 κ bilinears mixing the charged lepton and H_d superfields, and 45 Yukawa-like couplings: 9 λs and 27 λ's which violate lepton number, and 9 λ''s which violate baryon number. One can impose the following symmetry-conditions on the parameters λ_{ijk} and λ''_{ijk} without loss of generality: $\lambda_{ijk} = -\lambda_{jik}, \lambda''_{ijk} = -\lambda''_{ikj}$. The introduction of numerous new parameters can create a nightmare when exploring the whole phenomenology. Therefore, we adopt a simplifying approach: although there is no good reason to assume that the RPV couplings are hierarchical, it is a predictive guiding principle to explore the otherwise vast parameter space. Based on the assumption, we consider just one or two RPV couplings to be dominant at a time - assuming that the others vanish.

With R_p explicitly broken, new soft SUSY-breaking terms are included, and can be expressed as follows:

$$\mathscr{L}_{\text{RPV,soft}} = m^2_{H_{di}} H_d^\dagger \tilde{L}_i + b_i H_u \tilde{L}_i + \frac{1}{2} A_{ijk} \tilde{L}_i \tilde{L}_j \tilde{E}_k + A'_{ijk} \tilde{L}_i \tilde{Q}_j \tilde{D}_k + \frac{1}{2} A''_{ijk} \tilde{U}_i \tilde{D}_j \tilde{D}_k + h.c.\,. \tag{1.11}$$

Again, only the last set of terms violate baryon number (in the squark sector), while the others violate lepton number. We emphasize that the first group of operators in the RPV superpotential, given in Eq. (1.10), and the first two groups of terms in the soft RPV Lagrangian introduce different mixtures between MSSM and SM fields. These mixtures involve neutrinos-neutralinos, charged lepton-charginos, sneutrinos-neutral Higgs, and slepton-charged Higgs interactions. While the RPC-MSSM already includes slepton, sneutrino, and squark-flavor mixing, the additional effects caused by the bilinear operators of the RPV superpotential and soft Lagrangian potentially imply new observable features for the RPV model. Therefore, when considering the full RPV-MSSM model, these new effects must be taken into account.

The terms in the RPV Lagrangian lead to a significantly changed phenomenology which we will discuss in detail in the following sections. However, we want to summarize the four main changes:

(i) The lightest supersymmetric particle (LSP) is potentially unstable and its lifetime depends on its mass and couplings. Its decay products could appear in collider searches.

(ii) In the RPC-MSSM, the LSP may have a non-vanishing relic density causing cosmologically unacceptable charged relics when the LSP is (color) charged. It follows that the LSP of the MSSM has to be electrically neutral. However, the constraint on the - now unstable - LSP can be dropped in RPV-MSSM. Thus, the lightest neutralino is not necessarily the LSP.

(iii) Baryon and lepton number can be violated as well as lepton flavor.

(iv) Single sparticle production is possible and processes with external SM particles can be mediated by sparticles, leading to interference effects.

1.3.1 Where to find RPV Supersymmetry?

Despite the fascinating aspects of phenomenological SUSY, all attempts to directly detect BSM particles by experimental means have returned negative results so far. At present, sparticles within the mass range of approximately $\mathcal{O}(1-2\,\text{TeV})$ for the colored sector and $\mathcal{O}(100-1\,000\,\text{GeV})$ for the electroweak sector have been ruled out in the MSSM [57]. Searches most commonly focus on the RPC case, where SUSY particles are produced in pairs and are expected to leave significant amounts of missing energy. RPV phenomenology can be extremely different from this picture, though, and prompts the study of new signatures in collider experiments. Detection of these signatures would provide an experimental hint for SUSY at the weak scale rejecting the RPC-MSSM[4]. The search for BSM, whether SUSY or not, particles through production and decay processes is a critical component of research programs at current and future high-energy accelerators. The work aims to predict possible signals, extract exclusion bounds, and generate candidate models that exist for particles in the mass range from sub-TeV to a few TeV in the RPV-MSSM.

To effectively distinguish between signals produced by BSM particles and SM backgrounds, it is critical to identify distinctive signatures. An important feature in the "vanilla" MSSM found in all such processes is the well-known missing transverse energy E_T^{miss}. Significant E_T^{miss} searches have been considered for the past decades as the most sensitive observable to detect the production and decay of SUSY particles at colliders. However, even in the MSSM, there are in fact scenarios with too little missing energy escaping the Large Hadron Collider (LHC) detectors. The strategy of E_T^{miss} searches can be applied to the RPV-MSSM only if the LSP is long-lived and neutral. In scenarios where this condition is not fulfilled alternative search strategies become necessary.

In this work, we consider three different approaches concerning how RPV couplings can play an important role in phenomenological searches. (i) As mentioned in the previous section, it is possible to generate neutrino masses in RPV-SUSY. (ii) If the coupling parameters and mass of the LSP are small enough, the LSP produced in a collider will decay outside the detector. In such a scenario, assuming the LSP is electrically neutral, the phenomenology of particle searches at near detectors remains the same compared to the RPC-MSSM. However, since the LSP is not stable in RPV, it will eventually decay. In some regions of the parameter space, this decay may be observed in far-forward detectors and provides a novel signature relative to the SM background. (iii) When the coupling strengths are relatively weak but the mass of the LSP is higher, the LSP decays inside nearby detectors. It is necessary to consider such decays as mediated by each of the 48 couplings in the RPV-MSSM and to determine detectable signatures.

1.3.2 Massive Neutrinos

In the RPV-MSSM, neutrino masses may result from neutrino-neutralino mixing if lepton number is violated, with an underlying seesaw mechanism [58–64]. In this case, no further BSM particles are required. Due to the violation of lepton number, the lepton doublet superfields L_i carry the same quantum numbers as the down–type H_d doublet superfield. As a result, they are not distinguishable. The neutral higgsinos and neutrinos mix due

[4] Whether SUSY is the theory behind the signal would require dedicated studies.

to the bilinear term $H_u L^i$ in the superpotential. In addition, the trilinear lepton number violating terms of the RPV-MSSM superpotential, given in Eq. (1.10), and of the soft breaking Lagrangian, given in Eq. (1.11), in particular lead to the dynamical generation of neutrino masses. Following spontaneous symmetry breaking, the neutral gauginos also mix with the neutrino, yielding:

$$\mathscr{L}_{\mathcal{M}_N} = -\frac{1}{2}\left(-i\tilde{B}, -i\tilde{W}^3, \tilde{H}_d^0, \tilde{H}_u^0, \nu_i\right)\mathcal{M}_N \begin{pmatrix} -i\tilde{B} \\ -i\tilde{W}^3 \\ \tilde{H}_d^0 \\ \tilde{H}_u^0 \\ \nu_j \end{pmatrix}. \tag{1.12}$$

$\mathcal{M}_N$ is a 7×7 mass matrix. As neutrinos are known to be extremely light, we assume that there exists a strong hierarchy between the mass scales of the neutralinos and neutrinos. Thus, we can write $\mathcal{M}_N$ as:

$$\mathcal{M}_N = \begin{pmatrix} \mathcal{M}_{\overset{\chi}{}^0} & m \\ m^T & m_\nu \end{pmatrix}, \tag{1.13}$$

where m_ν is the 3×3 mass matrix in the neutrino sector and equals 0 and $\mathcal{M}_{\overset{\chi}{}^0}$ is the 4×4 mass matrix in the neutralino sector. m denotes the 3×4 mixing matrix which arises through R-parity violation. Details of a possible diagonalization procedure can be found, for instance, in Ref. [63]. Analogously to a classic seesaw mechanism, one can end up with an approximately block-diagonal matrix,

$$\mathbf{M}_N^{\text{diag}} \approx \begin{pmatrix} \mathbf{M}_{4\times4} & 0 \\ 0 & \mathbf{M}_\nu \end{pmatrix}, \tag{1.14}$$

where $\mathcal{M}_\nu \equiv m_\nu - m\mathcal{M}_{\overset{\chi}{}^0}^{-1} m^T$. The neglected contributions to $\mathbf{M}_{4\times4}$ and $\mathbf{M}_\nu$ in the above can be estimated as $\frac{\|\mathbf{m}_{4\times3}^2\|}{\|\mathbf{M}_{4\times4}\|} \lesssim \mathcal{O}(1\,\text{eV})$, and $\frac{\|\mathbf{m}_{4\times3}^3\|}{\|\mathbf{M}_{4\times4}^2\|} \lesssim \mathcal{O}\left(10^{-6}\,\text{eV}\right)$, respectively [63]. It is important to emphasize that the rank–1 structure of $\mathcal{M}_\nu^{\text{tree}}$ leads to only one non–zero neutrino mass at tree-level. Neutrino data show that at least two neutrinos are massive. Nevertheless, it is necessary to take radiative corrections into account [58], generally leading to the emergence of a second mass eigenstate. There are two classes contributing to one-loop diagrams [61]. The first one consists of fermion–sfermion loops and depends on the RPV trilinear terms. The second, which in many cases is the dominant one, consists of sneutrino–neutralino loops and depends on the sneutrino–anti-neutrino mass splitting. Contributions to the neutrino mass matrix are generated from diagrams involving a charged lepton-slepton loop and an analogous down-type quark-squark loop. In general, the existence of a sneutrino–anti-neutrino mass splitting, which is a result of a $\Delta L = 2$ interaction, generates a one-loop contribution to the neutrino mass.

1.3.3 A Light Neutralino

As we will discuss later, certain scenarios involve a very light neutralino state and it is important to analyze how far such a setup is phenomenologically realistic. For a stable lightest neutralino which can serve as a DM candidate - as in the MSSM - chargino searches at LEP indirectly set the strongest lower limit on the mass, $m_{\tilde{\chi}_1^0} \gtrsim 46\,\text{GeV}$ [65]. However, in the RPV-MSSM, in principle, any particle can be the LSP [66, 67]. In this search, it was assumed that the soft-SUSY breaking gaugino masses SU(2) and U(1) satisfy the grand-unification mass relation $M_1 = \frac{5}{3}\tan^2\theta_W M_2 \approx 0.5 M_2$, where θ_W is the electroweak mixing angle. If we relax this assumption of gaugino mass unification and consider M_1 and M_2 as independent parameters, we gain an additional degree of freedom. No actual lower limit can be derived from the LEP search anymore. Thus, limits on electroweak charged particles make it phenomenologically impossible to consider a SUSY particle other than the bino in the sub-GeV range [68–71]. Such a light bino would necessarily emerge as the LSP.

Beyond collider experiments, limits arise from cosmology considerations: the search for dark matter places a lower limit on the mass of a stable neutralino LSP since such a particle would contribute to the relic density. The argument of Lee and Weinberg [72] then implies the bound $m_{\tilde{\chi}_1^0} \gtrsim \mathcal{O}(10)\,\text{GeV}$ [69, 73–82], or, using the argument of Cowsik and McClelland [83], $m_{\tilde{\chi}_1^0} \lesssim 0.7\,\text{eV}$ [69]. However, if the neutralino is unstable and decays via RPV coupling, then it does not intervene on cosmological scales, and these limits do not apply [68].

In contrast, an unstable high-mass neutralino with a short lifetime would be severely constrained in collider searches due to visible decays [84, 85]. Light neutralinos can also be strongly constrained by astrophysical considerations, such as the cooling of supernovas and white dwarfs [86–88]. The key point that allows us to make the limits on the mass of the neutralino void is that the neutralino is stable on collider scales but decays on astrophysical scales. This assumes that the RPV couplings are small, which we expect. Accordingly, bino-like neutralinos in the RPV-MSSM could have arbitrarily small masses [69].

1.3.4 Proton Decay in the RPV-MSSM

As we discussed in Section 1.3, the superpotential of the RPV-MSSM [34, 35, 45, 48, 89, 90] results in a framework that includes new source of baryon number violation potentially contributing to baryogenesis, with additional contributions from leptogenesis [91–94]. One drastic consequence of allowing such baryon- and lepton-number-violating operators is that they may lead to rapid proton decay [50, 95–97]. Proton decay in the RPV-MSSM has been thoroughly studied in literature; see, for instance, Refs. [98–101]. The simultaneous presence of baryon- and lepton-number-violating couplings allow for nucleons to decay into mesons and leptons via tree-level squark exchange [102, 103]; this mainly constrains *products* of RPV couplings involving the first two generation indices. The simplest possibility for proton decay is via simultaneous $L_1 Q_1 \bar{D}_i$ and $\bar{U}_1 \bar{D}_1 \bar{D}_i$ operators (with $i \in \{2, 3\}$). For this combination of operators, the proton can decay into a pion and a positron (or a neutrino). To date, there has been no observation of proton decay, and the current strongest bound on its lifetime is, $\tau(p \to \pi^0 + e^+) > 1.6 \times 10^{34}$ yrs at 90% confidence level [104]. Using this, one can estimate

the strict bound on the product of couplings,

$$\left|\lambda'_{11i}\lambda''_{11i}\right| \lesssim O\left(10^{-27}\right), \tag{1.15}$$

if the mass of the virtual squarks, mediated in the decay, is of the order $\sim O(1\text{TeV})$. More involved channels including loops, bilinear insertions, or additional electroweakinos in the diagram have also been studied [58, 105–108]. The case corresponding to a light photino has been considered in literature [58, 109]. This, and other decay modes lead to bounds on a wider set of products of RPV couplings. RPV interactions also allow for more exotic proton decay modes involving only a single RPV coupling. If the lightest neutralino is lighter than the proton, *i.e.* $m_{\tilde{\chi}_1^0} < m_p - m_{K^+}$, a direct decay $p \to K^+ + \tilde{\chi}_1^0$ becomes possible, being a one coupling scenario using only a non-zero λ''_{112}.

On the experimental side, several next-generation detectors are being planned or are even under construction, such as `DUNE` [110–113], `JUNO` [114, 115], and `Hyper-Kamiokande` [116], making the phenomenology of proton decay a central avenue to investigate BSM.

1.4 Outline

This thesis is organized as follows: in Chapter 2, we present a framework permitting neutrino mass generation in the context of the RPV-MSSM. We try to make predictions in the most general framework. As discussed earlier, the neutrino mass matrix is subject to numerous different contributions involving various RPV-MSSM parameters. We will demonstrate how our approach allows us to study the effects of neutrino oscillation data on a wide range of models in a unified and model-independent manner. In Appendix A detailed analytic expressions and further benchmarks, including CP violation, can be found.

In Chapter 3, we provide a systematic analysis of the potential final states that can occur within the RPV landscape, relying on minimal assumptions about the details of the model, particularly the mass spectrum. Our primary goal is to categorize the extensive spectrum of possibilities into a manageable and concise set of signatures in order to ensure comprehensive coverage of the model space. We conduct a detailed investigation of the current experimental coverage of these signatures. This allows us to identify potential gaps in experimental coverage if they exist. In Appendix B, we provide supplementary decay modes and tables, which might be useful for numeric simulations. In addition, we provide an introduction to a `Python` package, which might be helpful for analyzing collider signatures.

In Chapter 4, we first introduce the framework of a light neutralino being produced from mesons at the LHC. We perform a detailed simulation procedure of the radiative decay mode of the light bino at the basic setup of `FASER` at the LHC. Then we estimate the sensitivity reach in the parameter space of RPV-SUSY. Remaining in the framework, we further study the phenomenology of a light bino in various scenarios and demonstrate that it is very similar to that of a light heavy neutral lepton in Chapter 5. This allows us to find sensitivity limits and reach for the various RPV couplings including even the bilinears. A detailed calculation of neutralino production and decay width can be found in Appendix C. We continue with the proton decay mode, $p \to K^+ + \tilde{\chi}_1^0$, induced by via a single $\bar{U}\bar{D}\bar{D}$ coupling in Chapter 6. Since the bino can be massless we can compare it to the decay $p \to K^+ + \nu$, which has been

searched for. Different neutralino masses can lead to different kinematics and, thus, lead to different signatures. We shall also discuss the possibility of the neutralino further decaying inside the detector as a complementary method of proton decay detection. We finish with a conclusion in Chapter 7.

2

A ν Approach to Analyzing Neutrino Data in the R-Parity-Violating MSSM

2.0 Preface

The contents of this chapter and the supplementary material presented in Appendix A are based on the following publication:

- H. K. Dreiner, D. Köhler, and S. Nangia,
  A ν approach to analyzing neutrino data in the **R**-parity-violating MSSM,
  Published in Eur. Phys. J. C 83 (2023) 1, 44, arXiv:2210.07253 [hep-ph].

Saurabh Nangia developed the analytical framework of Minimal Oscillation Models (MOMs). The implementation of a χ^2 routine using the `MINUIT2` package, as described in Section 2.7 using the newest neutrino data in Section 2.5 was provided by the author. Further, all plots in Section 2.7, Section 2.8 and Appendix A were also made by the author. Additionally, the author implemented the analysis for the CP-violating case, which is shown in Appendix A. Finally, the author provided the different properties of the considered example scenarios by considering the numerical properties of the fit.

As previously discussed in Chapter 1, neutrino masses are the first glimpse into BSM physics. Experimental observations have revealed neutrino oscillations, implying non-zero neutrino masses. These observations indicate that neutrinos are relatively light, with direct measurements constraining their masses to be less than $m_\nu < 0.8\,\text{eV}$ [117]. Cosmological observations give more stringent upper limits of only $\sum m_{\nu_i} < 0.12\,\text{eV}$ for the sum of neutrino masses [65].The data from atmospheric and solar neutrino oscillation suggest squared-neutrino-mass differences are $\mathcal{O}\left(1 \times 10^{-3}\,\text{eV}^2\right)$ and $\mathcal{O}\left(1 \times 10^{-5}\,\text{eV}^2\right)$, respectively, implying that at least two neutrinos must be massive [118]. In principle, it is seemingly straightforward to extend the SM Lagrangian by a Dirac neutrino mass term. This requires only right-handed neutrinos and new Yukawa couplings of $\mathcal{O}\left(1 \times 10^{-12}\right)$. However, such tiny couplings appear highly unnatural and could indicate a dynamical mechanism explaining their smallness. Furthermore, right-handed neutrinos may carry an unspecified Majorana neutrino mass. Among the most discussed extensions of the SM is the see-saw mechanism which introduces right-handed neutrinos and assumes a large Majorana neutrino mass scale [119–121]. By fixing a large Majorana mass scale, it becomes possible to obtain light neutrinos with a mass $\mathcal{O}\left(0.1\,\text{eV}\right)$ even with $\mathcal{O}(1)$ Yukawa couplings.

The RPV-MSSM has been shown to be a compelling framework that naturally accommodates massive neutrinos and accounts for the observed oscillation data, as we have seen

in Section 1.3. However, the phenomenological exploration of this model is challenging due to a large number of undetermined parameters, making individual predictions difficult. To simplify the analysis, previous studies have focused on specific submodels to make progress in understanding the RPV-MSSM. Within the supersymmetric SM, there exist three $\mathbb{Z}_N$ symmetries[1], one of them being the usual and so far discussed R-parity, also referred to as matter parity. The other symmetries are a $\mathbb{Z}_3$, called baryon triality (B_3), allowing for LNV [52, 55, 122] and a $\mathbb{Z}_6$ symmetry, called proton hexality, which conserves lepton- and baryon-number. The latter symmetries forbid the presence of dangerous dimension-5 operators leading to proton decay.

In this chapter, we consider a novel and less restrictive approach for studying the parameter space of the RPV-MSSM. We focus specifically on neutrino-mass generation in the B_3-conserving case to explore the phenomenological implications of the model in the most comprehensive way possible. The primary emphasis lies in the analysis of the structure of the neutrino mass matrix, with particular attention to the case of two massive neutrinos. Under mild assumptions, we show that these contributions, up to one-loop order, can be simplified into only two types of structures. We demonstrate that there are only four essential categories of models capable of explaining neutrino data. We refer to these classes as Minimal Oscillation Models.

We address a comprehensive examination of each of the introduced MOM classes, whose individual characteristics and properties we list. Our study includes the general characteristics of each MOM class and includes numerical fits to the oscillation data. We find the implications of neutrino oscillation data across all RPV models, provided that they meet the MOM criteria. We also extend our analysis to include the CP-violating phase in the fitting procedure. Generally, the framework can be extended to also include three massive neutrinos as well as non-minimal classes of models.

In summary, this chapter presents an important contribution to the field of RPV-MSSM by providing a novel, general approach for studying neutrino masses within the (almost) completely general RPV-MSSM framework. The work explores the structure of the neutrino mass matrix and identifies minimal classes of structures.

[1] When requiring the original gauge symmetry to be anomaly-free, and demanding a viable low-energy superpotential.

2.1 Introduction

The Standard Model of particle physics (SM) is incomplete. The nature of gravity, dark matter, dark energy, the baryon asymmetry, etc. are important unresolved issues. However, the most conclusive sign of physics beyond the SM comes from the precise neutrino oscillation data. It is now established that at least two of the neutrino species are massive. One way to give neutrinos mass is to add right-handed neutrinos to the SM spectrum. Via the see-saw mechanism, one then 'naturally' obtains very light neutrinos, as required indirectly by cosmology $\left(\sum m_{\nu_i} < 0.12\,\text{eV}\right)$ [65] or, directly, for example, by the KATRIN experiment ($m_\nu < 0.8\,\text{eV}$) [117]. However, this requires the right-handed neutrinos to be very heavy.

Supersymmetry (SUSY), a well-motivated extension of the SM [34, 45], is an attractive alternative. The simplest phenomenological realization, the Minimal Supersymmetric Standard Model (MSSM), has been studied extensively. An equally well-motivated [53, 99] setting is provided by adding R-parity-violating (RPV) terms to the MSSM Lagrangian, giving the RPV-MSSM [54]. This framework leads to a starkly different phenomenology compared to the MSSM, allows for lepton- and baryon-number violation, as well as flavor violation. Most importantly for this paper: Neutrino masses arise for free, without the need for any heavy right-handed partners [58, 123].

Neutrino-mass generation in the RPV-MSSM framework has been studied extensively in the literature. Early work on the tree-level calculation can be found in Refs. [58, 59, 124, 125], and on the loop-level one in Refs. [58, 123, 126–134]. Ref. [62] gives a (nearly) complete list of one-loop contributions, presented in a basis-independent formalism. Detailed accounts of the one-loop calculation can be found in Refs. [63, 64].

There has also been a lot of work to fit the theory calculations to the neutrino data; see the above references as well as Refs. [135–145]. The main obstacle to a systematic study is the unmanageably large number of contributions to the neutrino mass matrix in the most general RPV-MSSM. Thus, all numerical studies are performed within specific submodels; for instance bilinear-only RPV models [123, 132, 146], trilinear-only RPV models [136], mixed models [135, 137, 140, 147], and constrained MSSM (cMSSM) models extended by one (or two) RPV couplings [64, 145]. For an overview of the various types of models that have been considered, see Ref. [99].

The above studies allow an interpretation of the neutrino data within a predictive framework, but are limited in their scope. In this work, we approach the problem from a different perspective. Working in the general RPV-MSSM setting, allowing for *all* terms, we analyze the possible resulting structures (textures) of the neutrino mass matrix. To this end, we first argue that the most general neutrino mass matrix in the RPV-MSSM, to a good approximation, can be written as a sum of just two types of terms. This expression is general and simple but still has far-too-many free variables to be predictive. However, appealing to minimality, we identify just four structures of the mass matrix that are relevant for the case of two massive neutrinos. We refer to these as Minimal Oscillation Models (MOMs). The advantage of this approach is its simplicity and generality. By analyzing just four cases, it allows us to study qualitative and quantitative features of all RPV models in a unified, model-independent way, as long as they satisfy the MOM criteria; we demonstrate through examples that many interesting scenarios do indeed fulfill this condition. If, in turn, new

neutrino measurements arise, then this data can be systematically analyzed in terms of the MOMs we present here, instead of in terms of the many, many different RPV-MSSM neutrino-mass models.

This paper is organized as follows. In Section 2.2, we introduce the RPV-MSSM (and our notation). In Section 2.3, we discuss neutrino masses in the R-parity-violating context. In Section 2.4, we define the MOM framework and classify the four relevant structures of the neutrino mass matrix that arise in the RPV-MSSM. In Section 2.5, we summarize the current status of the neutrino data. We then analyze the four classes of MOMs, studying their general features in Section 2.6. We solve each class by numerically fitting to the neutrino data in Section 2.7. Finally, in Section 2.8, we consider example applications to show how results from the MOM framework can be directly translated to specific neutrino-mass models in the RPV-MSSM. We conclude in Section 2.9.

2.2 R-Parity Violation: Theoretical Framework

Assuming the $N = 1$ SUSY algebra, and the MSSM particle spectrum, the most general renormalizable superpotential invariant under the SM gauge group is,

$$W = W_{\rm MSSM} + W_{\rm LNV} + W_{\rm BNV}\,, \tag{2.1}$$

with,

$$\begin{aligned} W_{\rm MSSM} &= h_e^{ij} H_d L_i \bar{E}_j + h_d^{ij} H_d Q_i \bar{D}_j + h_u^{ij} Q_i H_u \bar{U}_j \\ &\quad + \mu H_u H_d\,, \\ W_{\rm LNV} &= \frac{1}{2}\lambda^{ijk} L_i L_j \bar{E}_k + \lambda'^{ijk} L_i Q_j \bar{D}_k + \kappa^i H_u L_i\,, \\ W_{\rm BNV} &= \frac{1}{2}\lambda''^{ijk} \bar{U}_i \bar{D}_j \bar{D}_k\,. \end{aligned} \tag{2.2}$$

In the notation we employ, L (Q) and $\bar{E}$ ($\bar{U}, \bar{D}$) label the lepton (quark) SU(2)$_L$-doublet and -singlet chiral superfields, respectively, while H_u, H_d refer to the SU(2)$_L$-doublet Higgs chiral superfields. All gauge indices are suppressed while the generational ones have been retained explicitly: $i, j, k = 1, 2, 3$, with a summation implied over repeated indices. The λ's and the h's are dimensionless Yukawa couplings, while μ and the κ's are dimension-one mass parameters.

In Eq. (2.1), the $W_{\rm MSSM}$ terms conserve both lepton- (L) and baryon-number (B), the $W_{\rm LNV}$ terms violate only L, and the $W_{\rm BNV}$ terms violate only B. A disconcerting consequence of allowing unsuppressed L- and B-violating terms simultaneously is proton decay at a rate that is disallowed by experimental constraints on the proton lifetime, $\tau_p > 3.6 \times 10^{29}$ yrs [65]. The usual approach in the MSSM is to invoke R-parity [148], a $\mathbb{Z}_2$ symmetry that allows $W_{\rm MSSM}$, while disallowing the R-parity-violating terms, $W_{\rm RPV} \equiv W_{\rm LNV} + W_{\rm BNV}$. However, to stabilize the proton, R-parity is sufficient, but not necessary. For instance, forbidding either the $W_{\rm BNV}$ or the $W_{\rm LNV}$ terms alone results in a stable proton.[2] Baryon triality, B_3, is

[2] If the lightest neutralino is lighter than the proton [69], then the proton can also decay with just $W = W_{\rm MSSM} + W_{\rm BNV}$, *e.g.*, $p \to K^+ \tilde{\chi}_1^0$ [101].

such a symmetry that forbids the former and leaves the latter [122]. In fact, unlike R-parity, B_3 even forbids potentially dangerous proton-decay operators of dimension five. We note that R-parity and B_3 are the only $\mathbb{Z}_2$ or $\mathbb{Z}_3$ symmetries possible with the MSSM low-energy particle content free from gauge anomalies [51, 52]; the higher symmetries have been classified in Ref. [55].

R-parity-violating phenomenology differs strongly from the R-parity-conserving case [53, 67, 99, 149]. Collider signals are no longer dominated by missing transverse momentum, the lightest neutralino is no longer a dark matter candidate, and baryogenesis, lepton-flavor violation and neutrino masses arise naturally. We summarize the last point, central to the further discussion.

2.3 Neutrino Masses and R-parity Violation

For neutrino masses at next-to-leading order, without loss of generality, we specialize to the B_3-MSSM, and abusively call it the RPV-MSSM. Our superpotential is,

$$W_{B_3} = W_{\text{MSSM}} + W_{\text{LNV}}. \tag{2.3}$$

There is no quantum number distinguishing H_d from L_i and hence, we define the following vectors and matrix:

$$L_\alpha \equiv (H_d, L_1, L_2, L_3)\ , \tag{2.4}$$

$$\kappa^\alpha \equiv \left(\mu, \kappa^1, \kappa^2, \kappa^3\right)\ , \tag{2.5}$$

$$\lambda'^{\alpha jk} \equiv \left(h_d^{jk}, \lambda'^{1jk}, \lambda'^{2jk}, \lambda'^{3jk}\right)\ , \tag{2.6}$$

$$\lambda^{\alpha\beta k} \equiv \begin{pmatrix} 0 & h_e^{1k} & h_e^{2k} & h_e^{3k} \\ -h_e^{1k} & 0 & \lambda^{12k} & \lambda^{13k} \\ -h_e^{2k} & \lambda^{21k} & 0 & \lambda^{23k} \\ -h_e^{3k} & \lambda^{31k} & \lambda^{32k} & 0 \end{pmatrix}\ . \tag{2.7}$$

$\alpha, \beta = 0, 1, 2, 3$ label the vector and matrix components, *e.g.*, $L_0 \equiv H_d$, and $\lambda'^{0jk} \equiv h_d^{jk}$. $j, k = 1, 2, 3$ are as before. We can thus write the superpotential as,

$$\begin{aligned} W_{B_3} = &\frac{1}{2}\lambda^{\alpha\beta k} L_\alpha L_\beta \bar{E}_k + \lambda'^{\alpha jk} L_\alpha Q_j \bar{D}_k + h_u^{ij} Q_i H_u \bar{U}_j \\ &+ \kappa^\alpha H_u L_\alpha\,. \end{aligned} \tag{2.8}$$

In addition, there are the soft-breaking terms,

$$\begin{aligned} \mathcal{L}_{soft} = \text{mass terms} + &\frac{1}{2} A^{\alpha\beta k} \tilde{L}_\alpha \tilde{L}_\beta \tilde{\bar{E}}_k + A'^{\alpha jk} \tilde{L}_\alpha \tilde{Q}_j \tilde{\bar{D}}_k \\ &+ A_u^{ij} \tilde{Q}_i H_u \tilde{\bar{U}}_j + B^\alpha H_u \tilde{L}_\alpha + h.c.\,, \end{aligned} \tag{2.9}$$

where the fields appearing in the above equation are the scalar components of the corresponding chiral superfields. The definitions of the parameters with one $\left(B^\alpha, A'^{\alpha jk}\right)$, and two

$\left(A^{\alpha\beta k}\right)$ Greek indices are obvious generalizations of the MSSM soft-breaking parameters, *cf.* Eqs. (2.4)-(2.7).

After spontaneous symmetry breaking, the neutrinos, the neutral gauginos, and the higgsinos mix, leading to a 7×7 mass matrix. At tree level in the gauge eigenbasis, $\left(-i\tilde{B}; -i\tilde{W}^0; \tilde{H}_u^0; \nu_\alpha\right)$, with $\nu_\alpha \equiv \left(\tilde{H}_d^0, \nu_i\right)$, we have the overall mass matrix,

$$\mathbf{M}_N = \begin{pmatrix} \mathbf{M}_{4\times4} & \mathbf{m}_{4\times3} \\ \mathbf{m}_{3\times4}^T & \mathbf{0}_{3\times3} \end{pmatrix} , \tag{2.10}$$

with $\mathbf{M}_{4\times4}$ corresponding to the MSSM neutralino mass matrix,

$$\mathbf{M}_{4\times4} = \begin{pmatrix} M_1 & 0 & \frac{g_1 v_u}{2} & \frac{-g_1 v_d}{2} \\ 0 & M_2 & \frac{-g_2 v_u}{2} & \frac{g_2 v_d}{2} \\ \frac{g_1 v_u}{2} & \frac{-g_2 v_u}{2} & 0 & -\kappa^0 \\ \frac{-g_1 v_d}{2} & \frac{g_2 v_d}{2} & -\kappa^0 & 0 \end{pmatrix} , \tag{2.11}$$

and the sub-block $\mathbf{m}_{4\times3}$ containing the RPV terms,

$$\mathbf{m}_{4\times3} = \begin{pmatrix} \frac{-g_1 v_1}{2} & \frac{-g_1 v_2}{2} & \frac{-g_1 v_3}{2} \\ \frac{g_2 v_1}{2} & \frac{g_2 v_2}{2} & \frac{g_2 v_3}{2} \\ -\kappa^1 & -\kappa^2 & -\kappa^3 \\ 0 & 0 & 0 \end{pmatrix} . \tag{2.12}$$

$\tilde{B}$ and $\tilde{W}^0$ denote the neutral gauginos, $\tilde{H}_u^0$, $\tilde{H}_d^0$ the neutral higgsinos, and ν_i the neutrinos. M_1, M_2, and g_1, g_2 are the electroweakino soft-breaking masses and gauge couplings, respectively. $\frac{v_u}{\sqrt{2}}, \frac{v_d}{\sqrt{2}}, \frac{v_i}{\sqrt{2}}$, with $i = 1, 2, 3$, are the vacuum expectation values (vevs) of the two neutral Higgs fields and the three sneutrinos, respectively.

The mass matrix of Eq. (2.10) has been discussed abundantly in the literature. The details of the diagonalization procedure can be found, for instance, in Ref. [63]. The scales in the various blocks are expected to have a hierarchy. Given the lower mass bounds on sparticles from the LHC, one expects the lepton-number-conserving SUSY scales of $\mathbf{M}_{4\times4}$ to be at least $\sim \mathcal{O}(1\,\text{TeV})$, while the lepton-number-violating scales of $\mathbf{m}_{4\times3}$ are constrained by various stringent low-energy bounds to be much smaller [99]. For example, the cosmological limit on neutrino masses implies $v_i,\ \kappa^i \lesssim \mathcal{O}(1\,\text{MeV})$ [54]. One can then proceed à la see-saw, and end up with an approximately block-diagonal matrix,

$$\mathbf{M}_N^{\text{diag}} \approx \begin{pmatrix} \mathbf{M}_{4\times4} & 0 \\ 0 & \mathbf{M}_\nu \end{pmatrix} , \tag{2.13}$$

where,

$$\mathbf{M}_\nu^{ij} \equiv \frac{\left(M_1 g_2^2 + M_2 g_1^2\right)}{4\det\left(\mathbf{M}_{4\times4}\right)} \left(v_i\kappa^0 - v_d\kappa^i\right)\left(v_j\kappa^0 - v_d\kappa^j\right) . \tag{2.14}$$

The neglected contributions to $\mathbf{M}_{4\times4}$ and $\mathbf{M}_\nu$ in the above approximation are of order $\frac{\|\mathbf{m}^2_{4\times3}\|}{\|\mathbf{M}_{4\times4}\|} \lesssim \mathcal{O}(1\,\text{eV})$, and $\frac{\|\mathbf{m}^3_{4\times3}\|}{\|\mathbf{M}^2_{4\times4}\|} \lesssim \mathcal{O}\left(10^{-6}\,\text{eV}\right)$, respectively [63]. To this order, $\mathbf{M}_{4\times4}$ is unaffected compared to the MSSM and we identify it as the neutralino mass matrix, and the corresponding mass eigenstates as the neutralinos. The high-scale-suppressed $\mathbf{M}_\nu$ can then be identified as the effective neutrino mass matrix.

Importantly, $\mathbf{M}_\nu$ is rank one at tree level, *i.e.*, it has only one non-zero eigenvalue. However, at least two neutrinos must be massive to explain the oscillation data. This can be achieved by including one-loop corrections [58], which have been computed several times in the literature. We shall use the results of Ref. [62]. There, an almost complete list of the one-loop contributions to $\mathbf{M}_\nu$ is presented; certain contributions whose effects are expected to be negligible have been dropped.

The advantage of using the formalism of Ref. [62] is that the contributions have been written in terms of basis invariants. It is common practice in the literature to use the U(4) 'flavor' freedom to rotate L_α to a specific basis. Various useful choices have been identified – the most common being the vanishing-κ^i basis [58, 150], and the vanishing-sneutrino-vev basis [130]. The notation of Ref. [62] is invariant under this U(4) and is useful to compare results across works using different bases.

We present an adapted version of all the contributions calculated in Ref. [62] in Table 2.1. Each entry can have multiple diagrams contributing. Further, the expressions are not exact but are meant to indicate the resulting form. For brevity, we have set all the SUSY mass scales to m_{SUSY}, all gauge couplings to g, dropped some factors involving the ratio of vevs – $\tan\beta$, and taken some scalar-sector flavor matrices as diagonal. We discuss the implications of this point in more detail shortly. The δ's appearing in the table are the basis invariants. Throughout, the constraints we derive apply to them but the results can always be translated into a specific basis using the general expressions [62]. For instance, in the vanishing-sneutrino-vev basis, we have,

$$\begin{aligned} \delta^i_\kappa &= \frac{\kappa^i}{|\kappa|}\,, & \delta^i_B &= \frac{B^i}{|B|}\,, \\ \delta^{ijk}_\lambda &= \lambda^{ijk}\,, & \delta^{ijk}_{\lambda'} &= \lambda'^{ijk}\,, \end{aligned} \tag{2.15}$$

with,

$$|\kappa|^2 \equiv \sum_{\alpha=0}^{3} |\kappa^\alpha|^2, \qquad |B|^2 \equiv \sum_{\alpha=0}^{3} |B^\alpha|^2\,. \tag{2.16}$$

Motivated by the above expressions, we often loosely refer to the δ's as 'RPV couplings'.

Even though the contributions in Table 2.1 are in terms of basis invariants, they have been written in a specific basis which corresponds approximately to the charged lepton mass basis. Analogous to the neutral case, the uncolored 5×5 charged fermion mass matrix mixes the charged gaugino, charged Higgsino, and the three charged leptons. However, it also has a hierarchical structure and can be approximately block-diagonalized to obtain separate 3×3 and 2×2 mass matrices, corresponding to the charged leptons and charginos, respectively. The charged lepton matrix, subject to small neglected terms, can then be diagonalized as

usual.

With a diagonal charged lepton mass matrix, one can then diagonalize the effective neutrino mass matrix $\mathbf{M}_\nu$:

$$\mathbf{M}_\nu = U^*_{\rm PMNS}\mathbf{M}_\nu^{\rm diag}U^\dagger_{\rm PMNS}\,, \tag{2.17}$$

where $\mathbf{M}_\nu^{\rm diag}$ is the diagonalized neutrino mass matrix, and $U_{\rm PMNS}$ is the PMNS matrix that appears in the charged-current interactions of the neutrinos. It should be clear that the PMNS matrix, as defined here, is a 3×3 sub-matrix inside the larger 5×7 matrix describing the mixing between all the 5 charged fermions and 7 neutral fermions. Thus $U_{\rm PMNS}$ is not exactly unitary, here. However, these effects are suppressed by the high-energy scales and we ignore them [63].

Contribution	$16\pi^2 m_{\rm SUSY}\mathbf{M}_\nu^{ij}$
Tree-Level	$16\pi^2 m_0 m_{\rm SUSY}\delta^i_\kappa\delta^j_\kappa$
1	$\delta^{ink}_\lambda\delta^{jkn}_\lambda m_{e_n}m_{e_k} + (i\leftrightarrow j)$
2	$3\delta^{ink}_{\lambda'}\delta^{jkn}_{\lambda'} m_{d_n}m_{d_k} + (i\leftrightarrow j)$
3	$g^2\delta^i_{\rm B}\delta^j_{\rm B}m^2_{\rm SUSY}/4$
4	$3\left(\delta^i_\kappa\delta^{jkk}_{\lambda'} + \delta^j_\kappa\delta^{ikk}_{\lambda'}\right)m^2_{d_k}h^k_d$
5	$\delta^{ijk}_\lambda\delta^k_{\rm B}m_{e_k}\left(m_{e_j}h^j_e - m_{e_i}h^i_e\right)$
6	$\left(\delta^i_\kappa\delta^{jkk}_\lambda + \delta^j_\kappa\delta^{ikk}_\lambda\right)m^2_{e_k}h^k_e$
7	$\delta^i_\kappa\delta^j_\kappa m_{e_i}m_{e_j}h^i_e h^j_e + (i\leftrightarrow j)$
8	$\delta^i_\kappa\delta^j_\kappa\left[\left(m_{e_i}h^i_e\right)^2 + \left(m_{e_j}h^j_e\right)^2\right]$
9	$\delta^i_{\rm B}\delta^j_\kappa\left(m_{e_i}h^i_e\right)^2 + \delta^j_{\rm B}\delta^i_\kappa\left(m_{e_j}h^j_e\right)^2$
10	$\delta^{ijk}_\lambda\delta^k_\kappa m_{e_k}\left(m_{e_i}h^i_e - m_{e_j}h^j_e\right)$
11	$\left(\delta^i_{\rm B}\delta^j_\kappa + \delta^j_{\rm B}\delta^i_\kappa\right)h^i_e h^j_e m_{e_i}m_{e_j}$
12	$g\left(\delta^i_\kappa\delta^j_{\rm B}m^2_{e_i} + \delta^j_\kappa\delta^i_{\rm B}m^2_{e_j}\right)$
13	$g\,\delta^i_\kappa\delta^j_\kappa\left(m^2_{e_i} + m^2_{e_j}\right)$
14	$g\,m_{\rm SUSY}\left(\delta^i_\kappa\delta^{jkk}_\lambda + \delta^j_\kappa\delta^{ikk}_\lambda\right)m_{e_k}$
15	$3\,g\,m_{\rm SUSY}\left(\delta^i_\kappa\delta^{jkk}_{\lambda'} + \delta^j_\kappa\delta^{ikk}_{\lambda'}\right)m_{d_k}$
16	$g^2 m^2_{\rm SUSY}\left(\delta^i_{\rm B}\delta^j_\kappa + \delta^j_{\rm B}\delta^i_\kappa\right)/4$
17	$g\left(\delta^i_\kappa\delta^j_{\rm B}m^2_{e_j} + \delta^j_\kappa\delta^i_{\rm B}m^2_{e_i}\right)$

Table 2.1: $\mathbf{M}_\nu$ contributions as calculated in Ref. [62]. The numbered entries are due to one-loop diagrams. Summation is implied over all repeated indices other than i, j. The δ's are the RPV basis invariants. m_0 is the tree-level mass scale of Eq. (2.14), the remaining m's are the SM fermion masses, and the h's are the Yukawas.

2.4 Minimal Oscillation Models

The matrix equation to be solved is,

$$\mathbf{M}_\nu \stackrel{!}{=} \mathbf{M}_\nu^{\rm exp} = U^*_{\rm PMNS}{\rm diag}\left(m_{\nu_1}, m_{\nu_2}, m_{\nu_3}\right) U^\dagger_{\rm PMNS}\,, \tag{2.18}$$

where $\mathbf{M}_\nu$ is the one-loop effective neutrino mass matrix computed from the RPV Lagrangian and the right-hand side is to be determined through fits to the neutrino oscillation data. The difficulty of numerically analyzing the *most general* RPV neutrino-mass model should be evident from the large number of contributions in Table 2.1. The goal of this paper is to show that – despite this – due to the structure of the entries, only a small set of truly 'distinct models' is possible. These, in turn, can be systematically analyzed.

Eq. (2.18) is a set of six complex equations, or 12 real constraints. Nine of these are physical, corresponding to the three neutrino masses, the three mixing angles, and the three CP-violating phases in the PMNS matrix (see the parameterization of the PMNS matrix below). The remaining three are not physical constraints. They correspond to arbitrary phases in the PMNS matrix that can be rotated away [151].

Looking at Table 2.1, it is clear that the most general one-loop mass matrix arising in RPV models, entering Eq. (2.18) on the left-hand side, has too many parameters; the system is very much underdetermined. Just the RPV superpotential has $\left(\kappa^i, \lambda^{ijk}, \lambda'^{ijk}\right)$ $3+9+27 = 39$ free complex (or 78 real) parameters. As mentioned, the usual approach of numerical studies has been to assume specific models. For instance, bilinear-only models $\left(\lambda^{ijk} = \lambda'^{ijk} = 0\right)$ [123], or unification approaches that begin with a small number of non-zero λ's at M_X, which then generate other non-zero couplings at the low scale through renormalization-group effects [152], etc. Our aim in this work is to remain as general as possible.

In a first step, we observe that all the contributions of Table 2.1 (except entries 5 and 10 – we return to this point) can be reduced to combinations of just two types of structures:

1. $x^i x^j$

2. $x^i y^j + y^i x^j$

Here, the x^i and y^i are place-holding variables with mass-dimension $[M]^{1/2}$ that are directly proportional to the δ's of Table 2.1. For instance, when the first one-loop entry of the table is expanded out, we get,

$$\begin{aligned}\mathbf{M}_\nu^{ij} &= \frac{1}{8\pi^2 m_{\rm SUSY}}\left(\delta_\lambda^{i33}\delta_\lambda^{j33} m_\tau^2 + \delta_\lambda^{i23}\delta_\lambda^{j32} m_\tau m_\mu\right.\\ &\quad\left. + \delta_\lambda^{i32}\delta_\lambda^{j23} m_\tau m_\mu + \delta_\lambda^{i22}\delta_\lambda^{j22} m_\mu^2 + \ldots\right)\\ &= x_1^i x_1^j + \left(x_3^i x_4^j + x_4^i x_3^j\right) + x_2^i x_2^j + \ldots\,,\end{aligned} \tag{2.19}$$

with

$$x_1^i \equiv \frac{\delta_\lambda^{i33} m_\tau}{2\pi\sqrt{2\, m_{\rm SUSY}}}\,, \quad x_2^i \equiv \frac{\delta_\lambda^{i22} m_\mu}{2\pi\sqrt{2\, m_{\rm SUSY}}}\,,$$
$$x_3^i \equiv \frac{\delta_\lambda^{i23} m_\mu}{2\pi\sqrt{2 m_{\rm SUSY}}}\,, \quad x_4^i \equiv \frac{\delta_\lambda^{i32} m_\tau}{2\pi\sqrt{2 m_{\rm SUSY}}}\,. \tag{2.20}$$

We see that the first and fourth terms correspond to an $x^i x^j$ structure while the second and third terms together form an $x^i y^j + y^i x^j$ structure. The choice of the variables is non-unique. For instance, one can multiply x_3^i by a constant and divide x_4^i by the same constant without changing the total contribution. Similarly, x_1^i, x_2^i are defined only up to a sign. The important point is that the variables are chosen to be directly proportional to the δ's.

One can similarly check the other entries. So, (ignoring the two exceptions) the most general one-loop effective neutrino mass matrix in RPV models can symbolically be written as,

$$\mathbf{M}_\nu^{ij} = \sum_\alpha x^i x^j + \sum_\beta \left(x^i y^j + y^i x^j \right)\,, \tag{2.21}$$

where the sum over α (β) is such that all the contributions of the first (second) type in Table 2.1 are included. Given Eq. (2.21), the simplest neutrino mass matrix that one can construct in the RPV-MSSM is with only one set, x^i:

$$\mathbf{M}_\nu^{ij} = x^i x^j\,. \tag{2.22}$$

The rank of this matrix is one, leading to two massless neutrinos which is inconsistent with oscillation data. The next simplest case involves two sets x^i, x'^i. Consider, for instance,

$$\mathbf{M}_\nu^{ij} = x^i x^j + x'^i x'^j\,. \tag{2.23}$$

This is, in general, a rank two structure and could possibly explain neutrino data if the lightest neutrino is massless. However, it does not work if the two sets are linearly dependent. To see this, let $x'^i = k x^i$; we get,

$$\begin{aligned}\mathbf{M}_\nu^{ij} &= x^i x^j + k^2 x^i x^j = (1+k^2) x^i x^j \\ &= \tilde{x}^i \tilde{x}^j\,,\end{aligned} \tag{2.24}$$

where $\tilde{x}^i \equiv \sqrt{1+k^2}\, x^i$. The structure reduces to the rank one case. Thus, we must have two linearly independent sets.

We emphasize that the number of linearly independent x^i sets is not the same as the number of RPV-coupling sets that give rise to them. For instance, one can check that reducing the tree-level contribution and entry 7 of Table 2.1 to the form of Eq. (2.21) requires two linearly independent sets, x^i and x'^i, even if both contributions arise from just a single RPV-coupling set, δ_κ^i. The inverse is also possible: Several RPV parameters can be written in terms of just one set x^i, *cf.* Appendix A.2.

With the above in mind, all possible structures that can be written with two linearly independent sets, x^i and x'^i, are:

- Class 1: $\mathbf{M}_\nu^{ij} = x^i x'^j + x'^i x^j$
- Class 2: $\mathbf{M}_\nu^{ij} = x^i x^j + (x^i x'^j + x'^i x^j)$
- Class 3: $\mathbf{M}_\nu^{ij} = x^i x^j + x'^i x'^j$
- Class 4: $\mathbf{M}_\nu^{ij} = x^i x^j + x'^i x'^j + A\left(x^i x'^j + x'^i x^j\right)$

These four structures[3] are all rank two – the minimum required, and are the only possible solutions to the neutrino data, as long as one is interested in a minimal setup. This is a crucial observation of this paper. We analyze these structures in the following.

Let us now discuss the exceptions mentioned above – entries 5 and 10 in Table 2.1. Before proceeding, we note that the various contributions to the neutrino mass matrix in Table 2.1 have a natural hierarchy. For instance, consider a scenario with only the $\delta_\kappa^i \neq 0$, leading to four contributions: The tree-level term, and entries 7, 8 and 13. Contributions 7 and 8 are suppressed by at least two extra powers of the small lepton-Yukawas compared to the other two. Thus, to a first approximation, we can neglect them.[4] The remaining two contributions can be reduced to a Class 2 MOM structure, *cf.* Section 2.8. This is a general trend, not specific to this example; we explore several examples later.

Indeed, the exceptions 5, 10 are not too worrisome for the same reason. They are Yukawa suppressed compared to the other terms involving the same sets of couplings. Let us see this explicitly for entry 5. The RPV parameters involved are δ_B^i and δ_λ^{ijk}. Assuming other couplings vanish, this entry would be competing with entries 1 and 3. We can estimate the magnitudes of the three contributions as:

$$\begin{aligned} &\text{Entry } 1 \sim |\delta_\lambda|^2 m_\tau^2\,, \\ &\text{Entry } 3 \sim \frac{g^2 |\delta_B|^2 m_{\text{SUSY}}^2}{4\cos^2\beta}\,, \\ &\text{Entry } 5 \sim |\delta_\lambda||\delta_B| m_\tau^2 h_\tau \tan\beta\,, \end{aligned} \tag{2.25}$$

where we have assumed a common magnitude for all generations of a particular coupling and hence dropped the latin indices. Further, we have only retained the terms proportional to the dominant τ lepton Yukawas for entries 1 and 5. The $\tan\beta$ and $\cos\beta$ factors are read off from the expressions found in Ref. [62]. Substituting the known values, and taking $m_{\text{SUSY}} \sim \mathcal{O}(1\,\text{TeV})$, one can easily prove that there is no configuration of parameters for which Entry 5 becomes important relative to the other two contributions. A similar argument can be made for entry 10.

[3] The Class 4 structure follows by using Eq. (2.21) to write the most general expression involving only x^i, x'^i, or couplings that are a linear combination of the two; and then suitably redefining the variables such that all the proportionality constants appear only in A. The detailed steps are given in Appendix A.2.

[4] One should make sure that the $\tan\beta$ factors, not shown in Table 2.1, cannot undo the hierarchies. As discussed in Section 2.8, this is indeed not the case here.

Going beyond rank two, it is possible that all three neutrinos are massive, requiring a rank three structure and a third linearly independent set, x''^i. Three linearly independent sets is the most general case and hence this approach would capture all RPV-MSSM neutrino-mass models. However, the number of classes to be considered is large making them less conducive for systematic numerical studies. In this paper we focus only on the rank two case.

We should note that the MOM approach does not cover the most general rank two structure possible in an RPV model. In Table 2.1, we assume some scalar-sector mixing matrices are diagonal in the charged lepton mass basis we are working in. This includes matrices that diagonalize the charged doublet and singlet sleptons and down-type squarks, and matrices that describe the left-right sparticle mixings; that is, we assume the sparticle and particle flavors are aligned with no inter-generational mixing. The fact that all contributions can be reduced to one of just two types of structures relies on this assumption. Further, by setting all SUSY scales in Table 2.1 common, we have neglected the possibility that strong hierarchies in the scalar sector may undo some of the hierarchies that we saw above. Finally, it is possible that three linearly independent sets –x^i, x'^i, x''^i – lead to a rank two structure through specific cancellations (see Appendix A.2 for an illustration of this point). The four structures listed above with only two sets would not capture such models. Hence, we shall refer to these as Minimal Oscillation Models (MOMs). MOMs are not minimal in the sense of having the fewest number of RPV parameters. They are, rather, minimal in the sense that the mass matrix has the minimal structure demanded by the data.

In the absence of any experimental information about the scalar sector, we believe the MOM framework provides a minimal setting that is widely applicable for the interpretation of neutrino data. It is simple and predictive. After briefly reviewing the neutrino data, we analyze qualitative and quantitative features of the models in the subsequent sections.

2.5 Neutrino Data

The PMNS matrix can be parameterized [65] by the three mixing angles $(\theta_{12}, \theta_{13}, \theta_{23})$, one CP-violating Dirac phase (δ_{CP}), and two CP-violating Majorana phases (η_1, η_2):

$$U_{\rm PMNS} = \begin{pmatrix} c_{12}c_{13} & s_{12}c_{13} & s_{13}e^{-i\delta_{CP}} \\ -s_{12}c_{23} - c_{12}s_{23}s_{13}e^{i\delta_{CP}} & c_{12}c_{23} - s_{12}s_{23}s_{13}e^{i\delta_{CP}} & s_{23}c_{13} \\ s_{12}s_{23} - c_{12}c_{23}s_{13}e^{i\delta_{CP}} & -c_{12}s_{23} - s_{12}c_{23}s_{13}e^{i\delta_{CP}} & c_{23}c_{13} \end{pmatrix} \begin{pmatrix} e^{i\eta_1} & 0 & 0 \\ 0 & e^{i\eta_2} & 0 \\ 0 & 0 & 1 \end{pmatrix}, \tag{2.26}$$

where $\sin\theta_{ij}$ and $\cos\theta_{ij}$ are written as s_{ij} and c_{ij} respectively. Without loss of generality, the angles θ_{ij} can be taken to lie in the first quadrant, *i.e.*, $\theta_{ij} \in [0, \pi/2]$, and the phases $\delta_{CP}, \eta_i \in [0, 2\pi]$.

We summarize neutrino oscillation data from Ref. [118] in Table 2.2. We follow their assumption of three active oscillating neutrinos. They present the best-fit values of the combined global analysis of atmospheric, solar, reactor, and accelerator neutrinos. Here, we specifically choose their fit including the SK atmospheric data [153, 154]. The data still allows one neutrino to be massless; we work in this limit. For Normal Ordering (NO) $(m_1 < m_2 < m_3)$ this means $m_1 \approx 0$, and for Inverted Ordering (IO) $(m_3 < m_1 < m_2)$ it

means $m_3 \approx 0$. In the global neutrino fit, the Normal Ordering is preferred over the inverted ordering, however this has become less pronounced with more recent data [118, 155].

	Normal Ordering	Inverted Ordering
$\theta_{12}/^\circ$	$33.44^{+0.77}_{-0.74}$	$33.45^{+0.78}_{-0.75}$
$\theta_{23}/^\circ$	$49.2^{+0.9}_{-1.2}$	$49.3^{+0.9}_{-1.1}$
$\theta_{13}/^\circ$	$8.57^{+0.12}_{-0.12}$	$8.60^{+0.12}_{-0.12}$
$\delta_{CP}/^\circ$	197^{+27}_{-24}	282^{+26}_{-30}
$\frac{\Delta m^2_{21}}{10^{-5}\,\text{eV}}$	$7.42^{+0.21}_{-0.20}$	$7.42^{+0.21}_{-0.20}$
$\frac{\Delta m^2_{3l}}{10^{-3}\,\text{eV}}$	$+2.517^{+0.026}_{-0.028}$	$-2.498^{+0.028}_{-0.028}$

Table 2.2: Neutrino oscillation parameters from a global fit to data. The first (second) column depicts the best fit assuming NO (IO). Note that $\Delta^2_{3l} \equiv \Delta^2_{31} > 0$ for NO and $\Delta^2_{3l} \equiv \Delta^2_{32} < 0$ for IO.

We use the data as presented in Table 2.2 for our numerical fits, except we set $\delta_{CP} = 0$. Further, we also set the as-yet-undetermined Majorana phases to be zero. That is, we work in the CP-conserving scenario. We do this merely for convenience; the solution space is more symmetric. Nevertheless, to show our analysis can accommodate CP violation, we show a sample plot in Appendix A.3 for $\delta_{CP} \neq 0$.

We will also find it convenient, at times, to use the so-called tri-bi-maximal (TBM) approximation[5] for the angles instead of the values in Table 2.2 [156]:

$$\sin^2(\theta_{12}) = \frac{1}{3}\,, \quad \sin^2(\theta_{23}) = \frac{1}{2}\,, \quad \sin^2(\theta_{13}) = 0\,, \quad \delta_{CP} = 0\,. \tag{2.27}$$

Even though this scenario is ruled out by the $\sin\theta_{13}$ measurement, it gives convenient analytical expressions, provides initialization for numerical fits, and allows studying qualitative features that carry through to the experimentally viable scenarios.

2.6 General Features of our Results

In the following, we present solutions to Eq. (2.18) for each of the four classes of MOMs. As we explain below, the solution space is an infinite set. Furthermore, since the neutrino data are quite precise, we shall ignore the experimental errors in the graphical presentation of our results below; technically each line in the plot should be understood to have a finite width.

There are two subtle points applying to all MOM classes worth mentioning before we solve them. The first concerns the basis choice. Even with our basis fixed to the (approximate) charged lepton mass basis, there is remnant freedom in the U_{PMNS} matrix. This corresponds to the freedom to multiply U_{PMNS} by three arbitrary phases [151]:

$$U_{\text{PMNS}} \mapsto \text{diag}\left(e^{i\alpha_1}, e^{i\alpha_2}, e^{i\alpha_3}\right) U_{\text{PMNS}}\,. \tag{2.28}$$

[5] See Ref. [152] for relating the TBM to RPV neutrino-mass models.

Using Eq. (2.17), this corresponds to shifting $\mathbf{M}_\nu$:

$$\begin{aligned}\mathbf{M}_\nu \;\mapsto\; & \operatorname{diag}\left(e^{-i\alpha_1}, e^{-i\alpha_2}, e^{-i\alpha_3}\right) \times \mathbf{M}_\nu \times \\ & \times \operatorname{diag}\left(e^{-i\alpha_1}, e^{-i\alpha_2}, e^{-i\alpha_3}\right) . \end{aligned} \tag{2.29}$$

This, in turn, can be interpreted as shifts in the phases of the x^i, x'^i variables. For instance, if $\mathbf{M}_\nu$ has a Class 1 MOM structure, the above equation becomes:

$$\begin{aligned}\left(x^i x'^j + x'^i x^j\right) \;\mapsto\; & \sum_{a,b} e^{-i\alpha_i} \delta^{ia} \left(x^a x'^b + x'^a x^b\right) \delta^{bj} e^{-i\alpha_j} \\ = \; & \left(e^{-i\alpha_i} x^i\right)\left(e^{-i\alpha_j} x'^j\right) \\ & + \left(e^{-i\alpha_i} x'^i\right)\left(e^{-i\alpha_j} x^j\right) , \end{aligned} \tag{2.30}$$

which is equivalent to the simultaneous transformations:

$$\begin{aligned} x^i &\mapsto \tilde{x}^i \equiv \left(e^{-i\alpha_i} x^i\right) , \\ x'^i &\mapsto \tilde{x}'^i \equiv \left(e^{-i\alpha_i} x'^i\right) . \end{aligned} \tag{2.31}$$

A change of basis induces simultaneous phase rotations on the RPV couplings. This holds for all MOM classes.

The second subtlety is the issue of degrees of freedom. MOM classes 1-3 have six free (complex) parameters while the fourth has seven. One might expect the six (complex) equations in Eq. (2.18) are enough to determine the system of variables for at least the first three classes. However, for the case at hand, the experimental matrix [right-hand side of Eq. (2.18)] is rank two. Hence, its last row can be written as a linear combination of the first two rows; the sixth constraint is redundant. We, thus, have an infinite set of solutions characterized by one unconstrained variable. Correspondingly, for Class 4 MOMs, we have two unconstrained variables.

To summarize, our solution space is an infinite set parameterized by one (or two) free variables. Further, the phases of the variables are only meaningful once the basis is completely specified. Our results are presented in the basis $\alpha_1, \alpha_2, \alpha_3 = 0$ with U_{PMNS} given by Eq. (2.26).

We now study the solution spaces for MOMs in detail. The analytical expressions are presented in Appendix A.1; our emphasis here is on a qualitative discussion of the general features. We exclude a study of Class 4 models. They are straightforward to solve numerically (see Section 2.7 for the discussion on numerical fits), but the analytical expressions are rather long and awkward. Furthermore, a visual representation would require non-intuitive three-dimensional plots.

2.6.1 Class 1: $x^i x'^j + x'^i x^j$

The equations we solve are quadratic in x^i, x'^i. Thus, there are multiple distinct solution sets for each MOM class. For instance, from Eq. (A.1) in Appendix A.1, we see that Class 1 MOMs have four solution sets. However, using the symmetries of the equations, we can

relate these to each other. Let us assume we know one solution set. Taking x^1 to be our free variable and expressing the other variables as a function of it, this set has the form:

$$S_{\rm I}: \left[x^2_{\rm I}\left(x^1\right), x^3_{\rm I}\left(x^1\right), x'^1_{\rm I}\left(x^1\right), x'^2_{\rm I}\left(x^1\right), x'^3_{\rm I}\left(x^1\right)\right]. \tag{2.32}$$

The subscript I labels the solution set. More explicitly, let us choose the constraints corresponding to the elements $ij = 11, 12, 13, 22, 33$ of $\mathbf{M}^{ij}_{\nu}$ as our five independent conditions. Then, the Class 1 equations are invariant under the simultaneous transformations,

$$x^2\left(x^1\right) \mapsto -x^2\left(-x^1\right), \qquad x'^2 \mapsto -x'^2\left(-x^1\right). \tag{2.33}$$

To see this, consider the constraint corresponding to $ij = 12$; for the others, the check is trivial. We have,

$$x^1 x'^2\left(x^1\right) + x^2\left(x^1\right) x'^1\left(x^1\right). \tag{2.34}$$

Making the transformations of Eq. (2.33), we get,

$$\begin{aligned} & x^1\left[-x'^2\left(-x^1\right)\right] + \left[-x^2\left(-x^1\right)\right] x'^1\left(x^1\right), \\ =& \left[-x^1\right] x'^2\left(-x^1\right) + x^2\left(-x^1\right)\left[-x'^1\left(x^1\right)\right], \\ =& \left[-x^1\right] x'^2\left(-x^1\right) + x^2\left(-x^1\right) x'^1\left(-x^1\right), \end{aligned} \tag{2.35}$$

where, in the last line, we have used $x'^1\left(x^1\right) = -x'^1\left(-x^1\right)$ which follows straightforwardly from the $ij = 11$ constraint. Finally, replacing the dummy variable $-x^1 \mapsto x^1$, we see that we recover Eq. (2.34).

Thus, given set $S_{\rm I}$, we can obtain a new solution set:

$$S_{\rm II}: \left[x^2_{\rm II}\left(x^1\right), x^3_{\rm II}\left(x^1\right), x'^1_{\rm II}\left(x^1\right), x'^2_{\rm II}\left(x^1\right), x'^3_{\rm II}\left(x^1\right)\right], \tag{2.36}$$

with,

$$\begin{aligned} x^2_{\rm II}\left(x^1\right) &= -x^2_{\rm I}\left(-x^1\right), \\ x'^1_{\rm II}\left(x^1\right) &= x'^1_{\rm I}\left(x^1\right), \\ x'^2_{\rm II}\left(x^1\right) &= -x'^2_{\rm I}\left(-x^1\right), \\ x^{(')3}_{\rm II}\left(x^1\right) &= x^{(')3}_{\rm I}\left(x^1\right). \end{aligned} \tag{2.37}$$

The third set can be obtained by transforming the x^3, x'^3 variables instead of the x^2, x'^2 variables in an analogous manner, and the last one can be obtained by making the transformations on both sets simultaneously.

Consulting the analytical expressions in Appendix A.1, we see that, as long as $\mathbf{M}^{ii}_{\nu} \neq 0$ for any i, the solution implies that the magnitudes of the x'^i couplings are inversely proportional to the magnitude of x^1 while those of x^2, x^3 are directly proportional to it. Thus, a solution

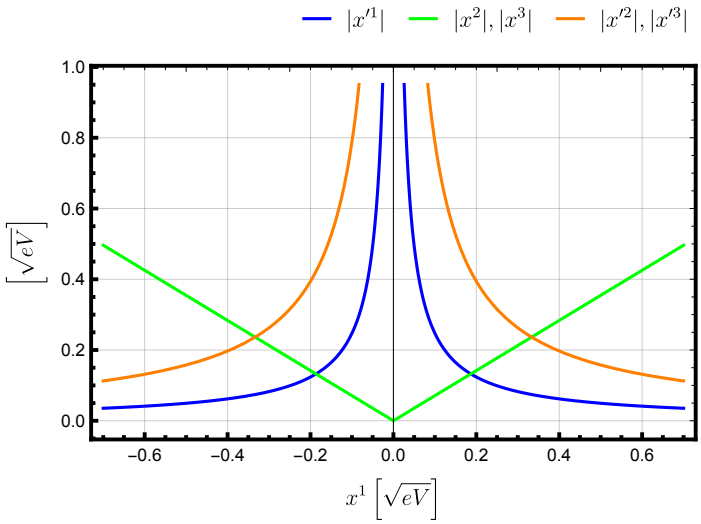

Figure 2.1: Absolute values of the couplings required to fit the IO limit of the TBM scenario in models with Class 1 structure.

point where any of the $|x'^i|$ are small comes at the price of bigger $|x^i|$, and vice-versa. Knowing which RPV coupling can be made smaller by trading for another is useful from a model-building perspective, since the low-energy bounds on RPV couplings are non-democratic, varying over orders of magnitude [157]. We draw upon this point further when we study applications to specific models.

As an illustration, we plot one solution-set for the IO limit ($m_3 \approx 0$), assuming TBM values for the angles[6] in Fig. 2.1. For visualization, we restrict ourselves to real x^1 values. The solution then constrains x'^1 to be real, while the other couplings are complex, in general. The behavior of the couplings is as described above. We observe a symmetry under $x^1 \leftrightarrow -x^1$; this is an intrinsic feature of the model structure. More generally, for a complex x^1, the magnitude of the couplings is unchanged if $|x^1|$ is unchanged. The relation between the magnitudes of $x^2(x'^2)$ and $x^3(x'^3)$ in Fig. 2.1 is a peculiarity of the numbers involved in the TBM case;[7] it is not present when using experimental data.

Another point of interest is the "total amount of RPV" a particular model requires to explain the neutrino data. As an illustration, consider how the x^i, x'^i variables relate to the RPV parameters, *i.e*, the $\delta's$ of Table 2.1:

$$x^i = A^i \delta^i \,, \qquad x'^i = A'^i \delta'^i \,, \tag{2.38}$$

where no summation is implied. In the above, δ and δ' are general symbols corresponding to any of the invariants in Table 2.1; they can both also correspond to the same invariant. One

[6] Even though we use the TBM limit for illustration in this section, all features we discuss are general.
[7] This arises due to the fact that the TBM-IO mass matrix is antisymmetric under an interchange of the second and third columns.

measure of the "total amount of RPV" we can define in the model is the sum,

$$\sigma \equiv \sum_i \left|\delta^i\right| + \sum_i \left|\delta'^i\right| \,. \tag{2.39}$$

The two terms represent the amount of RPV arising due to each individual set. Substituting Eq. (2.38),

$$\sigma = \sum_i \left(\frac{\left|x^i\right|}{\left|A^i\right|} + \frac{\left|x'^i\right|}{\left|A'^i\right|} \right) \,. \tag{2.40}$$

This will be a function of x^1. One could use the analytical expressions in Appendix A.1 to study how the RPV-amount demanded by each point varies with x^1 and find the point where it is minimal or maximal. In general, this requires that we first fix the constants A^i, A'^i, *i.e.*, we specify the model we wish to study. However, in the special case where $A^i = A\,, A'^i = A'\ \forall i$ (which holds for several contributions in Table 2.1), there is some simplification for Class 1 MOMs. Eq. (2.40), then, gives,

$$\sigma = \sum_i \left(\frac{\left|x^i\right|}{|A|} + \frac{\left|x'^i\right|}{\left|A'\right|} \right) \,. \tag{2.41}$$

Now, the structure of Class 1 MOMs allows us the freedom to choose x^i, x'^i suitably such that $A' = A$ without losing any generality. Then,

$$\sigma = \frac{1}{|A|} \sum_i \left(\left|x^i\right| + \left|x'^i\right| \right) \,. \tag{2.42}$$

Thus, with the above choice of the x^i, x'^i variables, the RPV amount is directly proportional to $\sum_i \left(\left|x^i\right| + \left|x'^i\right| \right)$ – a model-independent quantity. This allows us to find the point maximizing or minimizing the RPV amount without specifying the details of the model; determining the absolute scale, though, still requires the constant $|A|$ to be specified.

In Fig. 2.2, we plot the sum of the magnitudes of the x^i and x'^i for the IO limit of the TBM case, as well as the overall sum. We see that the latter varies from a clear minimum to an unbounded value for $|x^1| \to 0$. Thus, the neutrino data can be described by relatively small or large amounts of RPV, depending on the point one chooses. The minimum is situated precisely at the point where the individual sums of the x^i and x'^i sets are equal. The general expression for this point is lengthy. However, for the CP-conserving case – and if the conditions $\left(\mathbf{M}_\nu^{12}\right)^2 < \mathbf{M}_\nu^{11} \times \mathbf{M}_\nu^{22}$ and an analogous one with the generation index 2 replaced by 3 are satisfied – the point is given by,

$$|x^1| = \sqrt{\frac{\left|\mathbf{M}_\nu^{11}\right|}{2}} \,, \tag{2.43}$$

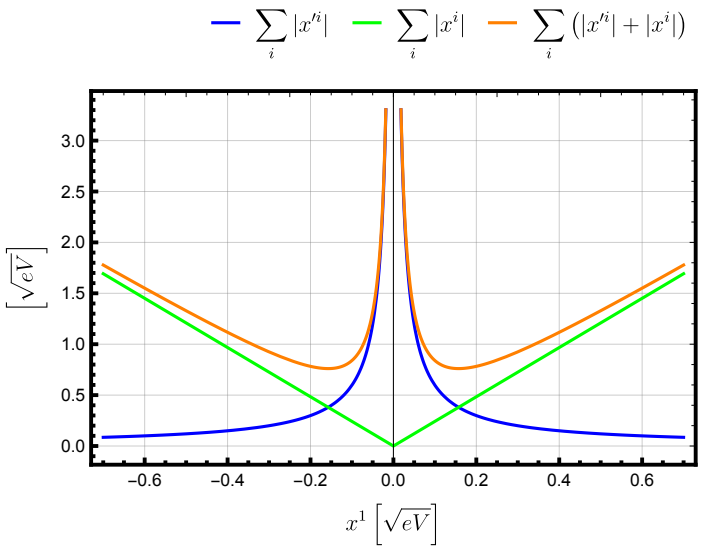

Figure 2.2: A measure of the amount of RPV required by each point in the solution space for Class 1 models. The plot corresponds to the IO limit of the TBM case.

and the magnitude of the minimum is $\sum_i \sqrt{2\left|\mathbf{M}_\nu^{ii}\right|}$. This holds for a general complex x^1. The condition we mention above is satisfied by the TBM matrix as well as the experimental data we use in our numerical fits.

2.6.2 Class 2: $x^i x^j + \left(x^i x'^j + x'^i x^j\right)$

There are four distinct solution sets related in the same way as in the previous case. Consulting Eq. (A.2) in Appendix A.1, we see that x^2, x^3 satisfy the same relations as for the Class 1 case. The behavior of the x'^i is different, however. For $|x^1| \ll \sqrt{\left|\mathbf{M}_\nu^{11}\right|}$, it is as before. However, for $|x^1| \gg \sqrt{\left|\mathbf{M}_\nu^{11}\right|}$, they grow linearly with $|x^1|$. In particular, x'^1 vanishes precisely at $x^1 = \pm\sqrt{\mathbf{M}_\nu^{11}}$ without any of the other couplings diverging. x^2, x^3 can not vanish without other couplings diverging. $|x'^2|, |x'^3|$ can also vanish but we skip the long general expressions.

We plot one of the solution sets corresponding to the TBM-IO limit for this class in Fig. 2.3, for real x^1. The symmetry under $x^1 \leftrightarrow -x^1$ is evident and again intrinsic. The relation between $x^2(x'^2)$ and $x^3(x'^3)$ is TBM-specific. We see the behavior described above. Indeed $x'^1 = 0$ at $|x^1| = \sqrt{|\mathbf{M}_\nu^{11}|}$; $|x'^2|, |x'^3|$ have their minima at $|x^1| = \sqrt{|\mathbf{M}_\nu^{11}|}$ too. This is not a general feature but holds in the CP-conserving case if, as before, $\left(\mathbf{M}_\nu^{12}\right)^2 < \mathbf{M}_\nu^{11} \times \mathbf{M}_\nu^{22}$ and the analogous condition with the index 2 replaced by 3 are satisfied. $x'^2, x'^3 = 0$ in general requires a non-zero phase for x^1.

We plot the sum of magnitudes for $|x^i|$ and $|x'^i|$ for the IO limit in Fig. 2.4. The individual sums are directly proportional to the RPV amount for each set and can be interpreted as

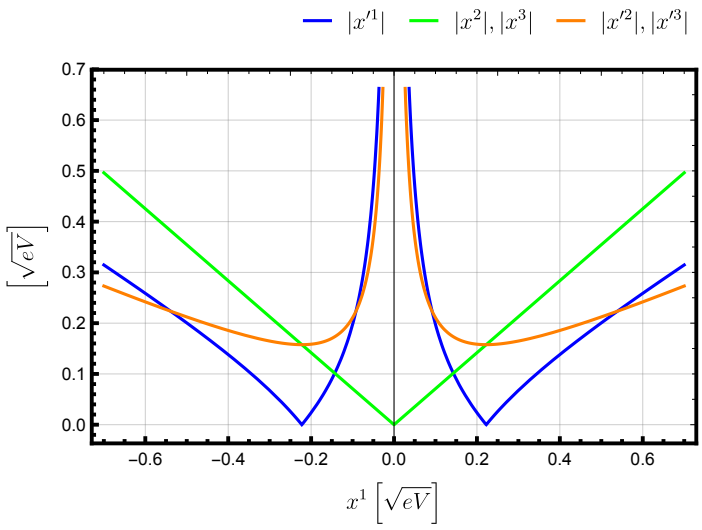

Figure 2.3: Absolute values of the couplings required to fit the IO limit of the TBM scenario in models with Class 2 structure.

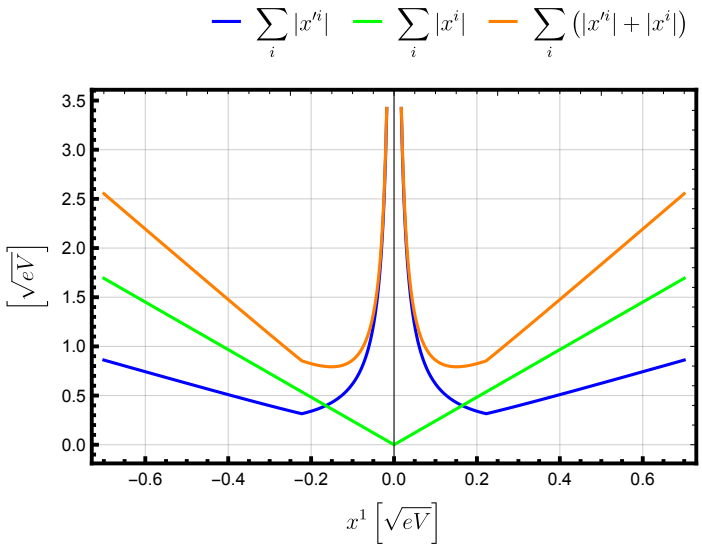

Figure 2.4: A measure of the amount of RPV required by each point in the solution space for Class 2 models. The plot corresponds to the IO limit of the TBM case.

before. However, the overall sum is no longer directly related to the total RPV amount. Unlike the case of Class 1 MOMs, we do not always have the freedom to choose $A = A'$ in Eq. (2.38) for Class 2 MOMs. We still plot the quantity; however, it should only be used for models where $A = A'$ holds.

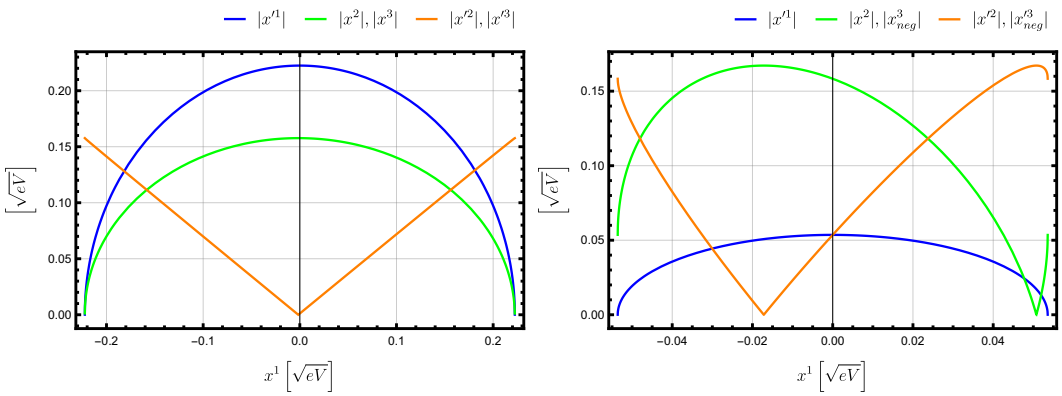

(a) Inverted Ordering (b) Normal Ordering

Figure 2.5: Absolute values of the couplings required to fit the TBM scenario in models with Class 3 structure. The notation f_{neg} means $f\left(-x^1\right)$ has been plotted instead of $f\left(x^1\right)$.

2.6.3 Class 3: $x^i x^j + x'^i x'^j$

Class 3 MOMs have eight distinct solution sets. Four can be obtained using the same arguments as before; this time the invariance is under the simultaneous transformations,

$$x^2\left(x^1\right) \mapsto -x^2\left(-x^1\right), \qquad x'^2 \mapsto x'^2\left(-x^1\right). \tag{2.44}$$

and the analogous ones for x^3 and x'^3. In addition, the whole system of equations is invariant under the simultaneous transformations,

$$x'^i \mapsto -x'^i. \tag{2.45}$$

Thus, for each of the four solution sets, we can obtain one more by changing the signs of all the x'^i couplings.

In general, the solution space is more complicated than for the other two classes. Consulting Eq. (A.3) in Appendix A.1, in the limit $|x^1| \gg \sqrt{\left|\mathbf{M}_\nu^{11}\right|}$, all the coupling magnitudes increase roughly linearly with $|x^1|$. This class is somewhat special: It allows solutions where all the couplings are simultaneously real; this occurs when $|x^1| \leq \sqrt{|\mathbf{M}_\nu^{11}|}$, with x^1 real. This also requires $\delta_{CP} = 0$, $\left(\mathbf{M}_\nu^{12}\right)^2 < \mathbf{M}_\nu^{11} \times \mathbf{M}_\nu^{22}$ and the analogous condition with the index 2 replaced by 3 to hold.

We plot one solution set for the TBM-IO and TBM-NO limits in Fig. 2.5, restricted to the above region. The symmetry of x'^1 under $x^1 \leftrightarrow -x^1$ is an intrinsic feature of the model structure. Although the TBM-IO limit numbers conspire to make it look otherwise in our plot, the other couplings do not generally possess such a symmetry – this is clear after looking at the NO limit. As before, the $x^2\left(x'^2\right)$ and $x^3\left(x'^3\right)$ relation is TBM-specific.

Within our region of interest, we see that the magnitude of x'^1 always falls as that of x^1

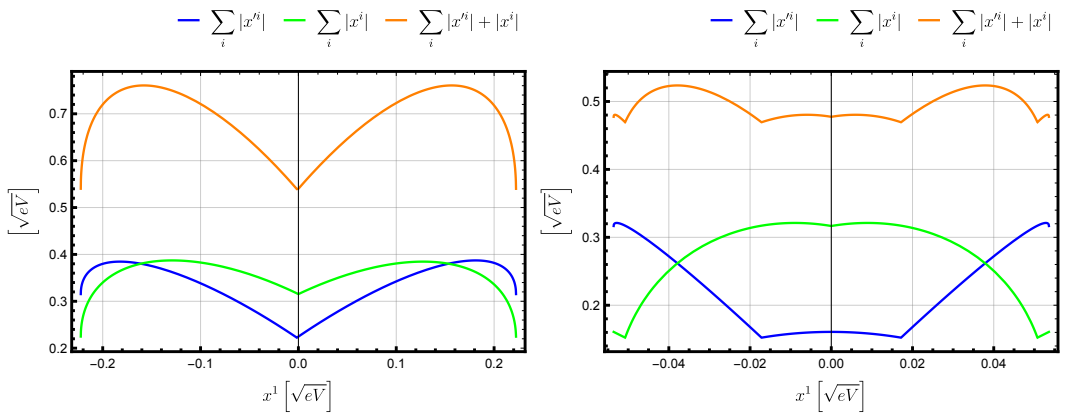

(a) Inverted Ordering (b) Normal Ordering

Figure 2.6: A measure of the amount of RPV required by each point in the solution space for Class 3 models. The plots correspond to the TBM scenario.

increases and it is zero precisely at the point $x^1 = \pm\sqrt{\mathbf{M}_\nu^{11}}$. There are no such universal trends for the other couplings. Unlike before, however, they can each be made to vanish in appropriate regions of the solution space. The $x^2\left(x^3\right)$ vanish at $x^1 = \pm\sqrt{\mathbf{M}_\nu^{11} - \frac{\mathbf{M}_\nu^{12(13)} \times \mathbf{M}_\nu^{12(13)}}{\mathbf{M}_\nu^{22(33)}}}$ while $x'^2\left(x'^3\right)$ vanish at $\pm\mathbf{M}_\nu^{12(13)}/\sqrt{\mathbf{M}_\nu^{22(33)}}$.

We study the relative RPV amount in Fig. 2.6. As for Class 2 MOMs, the overall sum may only be interpreted as the total RPV amount if $A = A'$ in Eq. (2.38). Here, the amount of RPV is dominated by the x^i for vanishing x^1, with the x'^i share growing as $|x^1|$ grows. The amount of RPV is minimal near the two $|x^1|$ extremes.

2.7 Numerical Fits

We now present the solution space for the experimental data. We numerically solve the first three MOM classes for each of the dependent parameters with x^1 as the free variable. We estimate the couplings by means of an error-weighted least-squares fit. We use the neutrino data of Table 2.2 (with $\delta_{CP} = 0$) at the 1σ level. In order to extract predictions for the couplings, we define a χ^2 function:

$$\chi^2 \equiv \frac{1}{N_{\text{obs}}} \sum_{i=1}^{3} \sum_{j=i}^{3} \left(\frac{x^{ij} - M^{ij}}{\delta^{ij}} \right)^2 , \tag{2.46}$$

where M^{ij} are the central values of the N_{obs} experimentally determined parameters of the mass matrix defined in Eq. (2.18), x^{ij} are the parameters to be determined, and δ^{ij} are the 1σ experimental uncertainties.

We initiate the fit using the TBM approximation for the x^{ij}. We minimize the χ^2 of Eq. (2.46) by using the program package MINUIT2 [158]. We consider both the NO and IO limits. We accept the minimization result as a success if the routine yields $\chi^2 < \mathcal{O}\left(10^{-5}\right)$.

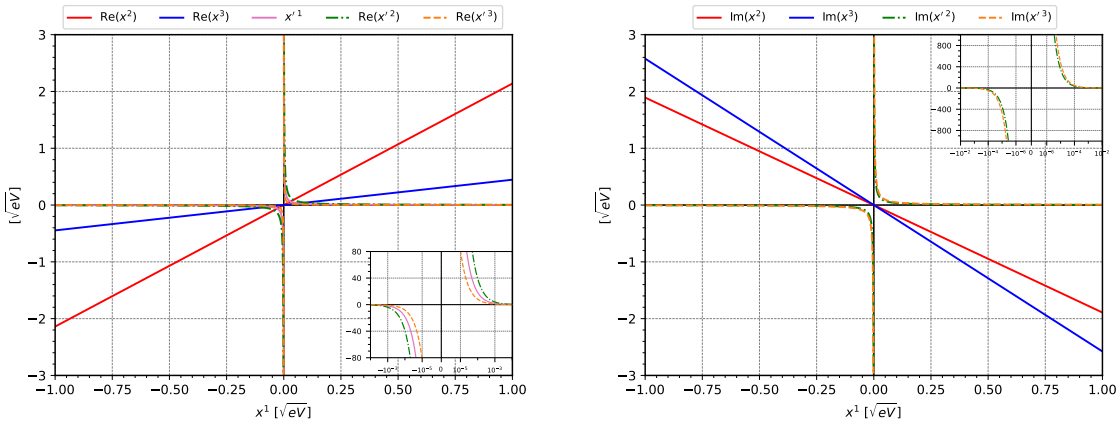

Figure 2.7: Real (left) and imaginary (right) values of the couplings required to fit the actual neutrino data for the NO limit in models with Class 1 structure.

To handle complex couplings, we fit the real and imaginary parts of each parameter separately. This extends the definition of our χ^2 function:

$$\chi^2 = \frac{1}{N_{\text{obs}}} \sum_{i=1}^{3} \sum_{j=i}^{3} \left[\left(\frac{\text{Re}\left(x^{ij}\right) - \text{Re}\left(M^{ij}\right)}{\delta^{ij}} \right)^2 + \left(\frac{\text{Im}\left(x^{ij}\right) - \text{Im}\left(M^{ij}\right)}{\delta^{ij}} \right)^2 \right], \tag{2.47}$$

where we demand that the imaginary components of the neutrino mass matrix vanish, since we are working in the CP-conserving limit.

Fig. 2.7 shows the numerical result using the neutrino data, assuming the NO limit, for Class 1 MOMs. We restrict ourselves to real x^1. This automatically implies that x'^1 has to be real. As before, we depict only one of the multiple solution sets. We see that the solution space reproduces the general features discussed in Section 2.6.1. The analogous results for the IO limit for Class 1 MOMs (Fig. A.1), as well as the plots corresponding to Class 2 MOMs (Fig. A.2), and Class 3 MOMs (Fig. A.3) can be found in Appendix A.3. A corresponding solution including a non-zero δ_{CP} can be found in Fig. A.4 with more details in Appendix A.3.

To depict the robustness of our procedure, we show, in Fig. 2.8, the variation of χ^2 by varying one of the fitted couplings – x'^1 – about the best-fit point. The other couplings are held fixed. The minimum is extremely well-defined, indicating excellent convergence.

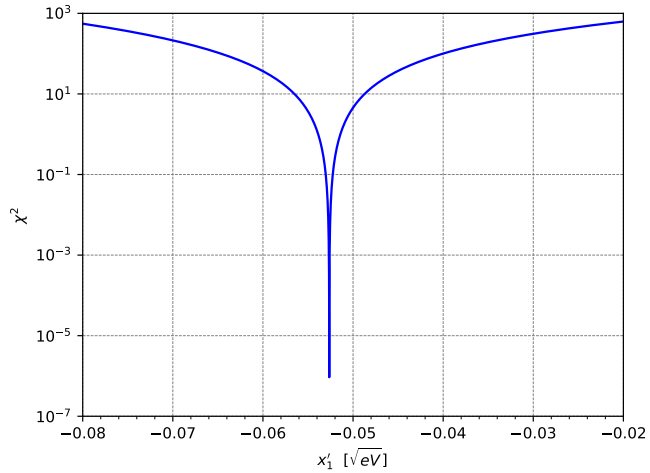

Figure 2.8: Variation of χ^2 as a function of the fitted parameter x_1' for the Class 3 NO scenario around the best-fit point as determined by MINUIT2. The other couplings are held fixed.

2.8 Example Applications

As long as a model has a MOM structure, our general results can be directly translated into model-specific numbers. We now demonstrate this by considering several examples of RPV models. The statement that only certain RPV couplings are non-vanishing in a given model is U(4)-basis dependent; our statements in this section apply to the vanishing-sneutrino-vev basis.

2.8.1 κ-only Models

In a model where the only RPV sources are the δ_κ invariants, the effective neutrino mass matrix has contributions at tree level, and of types 7, 8 and 13 in Table 2.1 at one-loop level. The expression for the mass matrix is [54, 62],

$$\begin{aligned}\mathbf{M}_\nu^{ij} = m_0 \delta_\kappa^i \delta_\kappa^j + \frac{g_2 \left[\left(m_{e_i}\right)^2 + \left(m_{e_j}\right)^2 \right]}{16\pi^2 v} \times \\ \times \left(1 + \sin^2\beta + \tan\beta \sin^2\beta\right) \delta_\kappa^i \delta_\kappa^j + \dots ,\end{aligned} \tag{2.48}$$

where $m_0 = -\frac{M_Z^2 \cos^2\beta m_{\text{SUSY}}}{m_{\text{SUSY}}^2 - M_Z^2 \sin 2\beta}$ is the tree-level mass scale of Eq. (2.14), v is the electroweak vev, g_2 is the $\text{SU}(2)_L$ gauge coupling, and the other notation is as in Table 2.1. There are three separate diagrams of type 13 that lead to the second term [62]. The ellipsis indicates all the terms of higher (fourth) order in the lepton Yukawas, due to contributions of types 7, 8. We have set all SUSY mass scales to m_{SUSY}.

Eq. (2.48) does not have a MOM structure. However, we can neglect the terms in the ellipsis to a first approximation, given their suppression by two extra powers of the small

Yukawas. Then, making the identifications,

$$x^i = \sqrt{m_0}\delta^i_\kappa\,, \quad \text{and}$$
$$x'^i = \frac{g_2\left(m_{e_i}\right)^2}{16\pi^2 v\sqrt{m_0}}\left(1+\sin^2\beta+\tan\beta\sin^2\beta\right)\delta^i_\kappa\,, \tag{2.49}$$

we see that the model reduces to a Class 2 MOM structure, and our framework can be applied. One can easily show that such a model cannot solve the neutrino pattern. The above equations imply the following relations involving the lepton masses:

$$\frac{1}{m_e^2}\frac{x'^1}{x^1} = \frac{1}{m_\mu^2}\frac{x'^2}{x^2} = \frac{1}{m_\tau^2}\frac{x'^3}{x^3}\,. \tag{2.50}$$

Consulting Eq. (A.2) in Appendix A.1, there is no point in the solution space of Class 2 models satisfying this.

2.8.2 $\kappa - B$ Models

We next consider a model also including the soft-breaking bilinear terms, *i.e.*, $\delta_\kappa, \delta_B \neq 0$ with all other RPV couplings zero (see also Ref. [123]). We have the contributions, *cf.* Table 2.1: Tree-level, and of types 3, 7, 8, 9, 11, 12, 13, 16 and 17. The complete expression is [62],

$$\mathbf{M}_\nu^{ij} = m_0\delta^i_\kappa\delta^j_\kappa + \frac{g_2^2 m_{\rm SUSY}}{64\pi^2\cos^2\beta}\delta^i_B\delta^j_B$$
$$+\frac{g_2^2 m_{\rm SUSY}}{64\pi^2\cos\beta}\left(\delta^i_\kappa\delta^j_B+\delta^i_B\delta^j_\kappa\right)+\ldots\,. \tag{2.51}$$

The ellipsis again proxies contributions of higher (second and above) order in the Yukawas. As before, the full model does not have a MOM structure but neglecting the Yukawa-suppressed terms[8], and making the identifications,

$$x^i = \sqrt{m_0}\delta^i_\kappa\,,$$
$$x'^i = \frac{g_2\sqrt{m_{\rm SUSY}}}{8\pi\cos\beta}\delta^i_B\,,$$
$$A = \frac{g_2\sqrt{m_{\rm SUSY}}}{8\pi\sqrt{m_0}}\,, \tag{2.52}$$

the model reduces to a Class 4 MOM.

As a numerical illustration, we set $m_{\rm SUSY} = 1\,\text{TeV}$, $\tan\beta = 10$, and substitute the other

[8] Some of these Yukawa-suppressed terms have $\tan\beta$ factors which may enhance them for large $\tan\beta$; however, even in this case the second and third terms in Eq. (2.51) dominate due to the $\cos\beta$ factors.

known parameters. This gives,

$$\begin{aligned} x^i &\approx \left(9.081 \times 10^3 \sqrt{\text{eV}}\right) i\delta^i_\kappa \,, \\ x'^i &= \left(2.607 \times 10^5 \sqrt{\text{eV}}\right) \delta^i_B \,, \\ A &\approx -2.857i \,. \end{aligned} \tag{2.53}$$

Numerically solving this for the TBM-IO limit – for instance, at the point with $x^1 = 0$ – yields,

$$\begin{aligned} x^2 &= -x^3 \approx 0.052 \sqrt{\text{eV}} \,, \\ x'^1 &\approx \ -0.222 \sqrt{\text{eV}} \,, \\ x'^2 &= -x'^3 \approx (-0.001 + 0.149i) \ \sqrt{\text{eV}} \,, \end{aligned} \tag{2.54}$$

or, using Eq. (2.53),

$$\begin{aligned} \kappa^1 &= 0 \,, \\ \kappa^2 &= -\kappa^3 \approx -|\kappa| \left(5.73 \times 10^{-6} i\right) \,, \\ B^1 &\approx -|B| \left(8.52 \times 10^{-7} i\right) \,, \\ B^2 &= -B^3 \approx -|B| \left(3.84 \times 10^{-9} - 5.72 \times 10^{-7} i\right) \,. \end{aligned} \tag{2.55}$$

In the above, we have made use of the forms of the δ invariants in the vanishing-sneutrino-vev basis, *cf.* Eq. (2.15). Similarly, one could also numerically solve at the point corresponding to the minimal RPV amount, and use that in order to derive a minimal bound on the couplings.

2.8.3 Diagonal Trilinear Models I

We now consider models with the trilinear sector contributing, and assume the other contributions are negligible. The effective neutrino mass matrix is zero at tree level but receives contributions at loop-level of types 1 and 2 in Table 2.1. The expression for the matrix is,

$$\begin{aligned} \mathbf{M}^{ij}_\nu = &\frac{1}{8\pi^2 m_{\text{SUSY}}} \delta^{ink}_\lambda \delta^{jkn}_\lambda m_{e_n} m_{e_k} \\ &+ \frac{3}{8\pi^2 m_{\text{SUSY}}} \delta^{ink}_{\lambda'} \delta^{jkn}_{\lambda'} m_{d_n} m_{d_k} \,, \end{aligned} \tag{2.56}$$

with a summation implied over repeated indices. The equation has too many parameters to have a MOM structure, or any predictivity in general.

In a minimal model where only the diagonal (in the last two indices) trilinear couplings

contribute, the above expression simplifies:

$$\begin{aligned}&\mathbf{M}_\nu^{ij} = \\ &\frac{1}{8\pi^2 m_{\text{SUSY}}}\left(\lambda^{i11}\lambda^{j11}m_e^2 + \lambda^{i22}\lambda^{j22}m_\mu^2 + \lambda^{i33}\lambda^{j33}m_\tau^2\right) \\ &+ \frac{3}{8\pi^2 m_{\text{SUSY}}}\left(\lambda'^{i11}\lambda'^{j11}m_d^2 + \lambda'^{i22}\lambda'^{j22}m_s^2 + \lambda'^{i33}\lambda'^{j33}m_b^2\right),\end{aligned} \tag{2.57}$$

where we have used the fact that the δ invariants can be simply replaced by the λ couplings in the vanishing-sneutrino-vev basis.

Eq. (2.57) still has too many terms for a MOM structure. We can further reduce the system, by assuming the couplings have a comparable magnitude. The terms then have a natural hierarchy due to the fermion masses. Considering only the contributions of the two heaviest particles – the b quark and the τ lepton – the largest neglected term is a factor $\frac{m_\tau^2}{m_\mu^2} \sim 300$ smaller. The model reduces to:

$$\begin{aligned}\mathbf{M}_\nu^{ij} &= \frac{1}{8\pi^2 m_{\text{SUSY}}}\lambda^{i33}\lambda^{j33}m_\tau^2 \\ &+ \frac{3}{8\pi^2 m_{\text{SUSY}}}\lambda'^{i33}\lambda'^{j33}m_b^2\,,\end{aligned} \tag{2.58}$$

which has a Class 3 MOM structure with the identifications,

$$\begin{aligned}x^i &= \sqrt{\frac{1}{8\pi^2 m_{\text{SUSY}}}}\, m_\tau \lambda^{i33}\,, \\ x'^i &= \sqrt{\frac{3}{8\pi^2 m_{\text{SUSY}}}}\, m_b \lambda'^{i33}\,.\end{aligned} \tag{2.59}$$

Due to the antisymmetry of the LLE couplings in the first two indices, $x^3 \sim \lambda^{333} = 0$. This uniquely determines the solution to the point where $x^3 = 0$ vanishes. We had discussed the location of this point earlier. Plugging in the numbers for the TBM-IO limit gives:

$$\begin{aligned}x^1 &\approx -0.2224\,\sqrt{\text{eV}}\,, \quad x^2 = x^3 \approx 0\,\sqrt{\text{eV}}\,, \\ x'^1 &\approx -0.0016\,\sqrt{\text{eV}}\,, \quad x^2 = -x^3 \approx -0.1577\,\sqrt{\text{eV}}\,.\end{aligned} \tag{2.60}$$

One can plug in the values of m_{SUSY} and the lepton masses to see what this implies for the λ couplings.

2.8.4 Diagonal Trilinear Models II

To discuss a slightly more complex application, we consider a cMSSM-like scenario, called the B_3 cMSSM in Ref. [145]. At the GUT scale, the five cMSSM parameters are appended by one (or two) RPV trilinear coupling(s). All other RPV couplings are assumed to be zero. Through the renormalization group equations (RGEs), further couplings are generated at the electroweak scale. Thus, we end up with multiple contributions to the neutrino mass

matrix. The most relevant are the bilinear terms since these contribute at tree-level; the RGE-generated trilinear couplings are suppressed and only contribute at one-loop level. The neutrino mass matrix has the structure,

$$\mathbf{M}_\nu^{ij} \sim \delta_\kappa^i \delta_\kappa^j + \delta_B^i \delta_B^j + \delta_{\lambda'}^i \delta_{\lambda'}^j + \delta_\lambda^i \delta_\lambda^j + \dots \,, \tag{2.61}$$

where we assume two non-zero GUT-scale couplings λ, λ' and only symbolically depict the type of terms contributing. The ellipsis indicates potential cross-terms. The above model again has too many terms. To a good approximation, the generated bilinear parameters are of the form,

$$\begin{aligned} \delta_\kappa^i &\approx a_1 \delta_{\lambda'}^i + b_1 \delta_\lambda^i \,, \\ \delta_B^i &\approx a_2 \delta_{\lambda'}^i + b_2 \delta_\lambda^i \,, \end{aligned} \tag{2.62}$$

where the a_i, b_i are numerical constants. Thus, the RGEs ensure that the generated couplings are approximately linearly dependent on the original δ_λ^i, $\delta_{\lambda'}^i$.[9] The model has only two linearly independent structures appearing and the MOM framework applies. Substituting Eq. (2.62) in Eq. (2.61), the matrix reduces to the form,

$$\mathbf{M}_\nu^{ij} \sim \delta_{\lambda'}^i \delta_{\lambda'}^j + \delta_\lambda^i \delta_\lambda^j + \left(\delta_{\lambda'}^i \delta_\lambda^j + \delta_{\lambda'}^i \delta_\lambda^j \right) \,, \tag{2.63}$$

which is a Class 4 MOM.

2.8.5 Non-diagonal Trilinear Models

Next, we consider the dominant contributions to arise from the non-diagonal (in the last two indices) trilinear couplings. The effective neutrino mass matrix has the form of Eq. (2.56), except now the n, k indices are not equal. Again, we exploit the natural hierarchy of the structures to reduce the model to a MOM. Performing the expansion in the vanishing-sneutrino-vev basis, we have,

$$\mathbf{M}_\nu^{ij} = \frac{3}{8\pi^2 m_{\text{SUSY}}} \left(\lambda'^{i32} \lambda'^{j23} + \lambda'^{j32} \lambda'^{i23} \right) m_b m_s + \dots \,, \tag{2.64}$$

where the ellipsis hides the other terms. For instance, assuming similar magnitudes of couplings, the next highest contribution is the one proportional to $m_\tau m_\mu$ and is smaller by a factor $\frac{3 m_b m_s}{m_\tau m_\mu} \sim 8$ compared to the first term. The factor of 3 here is due to the quark colors. Thus, we only consider the first term. This reduces the model to a MOM of Class 1 structure,

[9] The exact forms of the RGEs can be found in Ref. [145], where this approximation is also discussed.

with the identifications,

$$x^i = \sqrt{\frac{3m_b m_s}{8\pi^2 m_{\rm SUSY}}}\lambda'^{i23}\,,$$
$$x'^i = \sqrt{\frac{3m_b m_s}{8\pi^2 m_{\rm SUSY}}}\lambda'^{i32}\,. \tag{2.65}$$

We had mentioned earlier how a broader phenomenological perspective can sometimes make it relevant to know which couplings can be made smaller by trading for others. We can see an example of that here. The λ' couplings above need to satisfy certain single bounds, *cf.* Ref. [157]:

$$\begin{aligned} |\lambda'^{123}| &\leq 0.43, \qquad |\lambda'^{132}| \leq 1.04\,,\\ |\lambda'^{223}| &\leq 1.12, \qquad |\lambda'^{232}| \leq 1.04\,,\\ |\lambda'^{323}| &\leq 1.12, \qquad |\lambda'^{332}| \leq 1.04\,. \end{aligned} \tag{2.66}$$

In addition, there are also product bounds:

$$\begin{aligned} |\lambda'^{123*}\lambda'^{223}| &\leq 0.0076\,,\\ |\lambda'^{132*}\lambda'^{232}| &\leq 0.0076\,. \end{aligned} \tag{2.67}$$

In the above, we have assumed all sfermion masses to be 1 TeV, or, if stricter, we have used the perturbativity constraint. Thus, for model building, solutions with, for instance, small λ'_{123} are preferable. We recast the solution space for the two limits of Fig. 2.7, and depict it in terms of the RPV couplings using Eq. (2.65) in Fig. 2.9. The plot also depicts the regions ruled out by the above bounds as shaded grey regions.

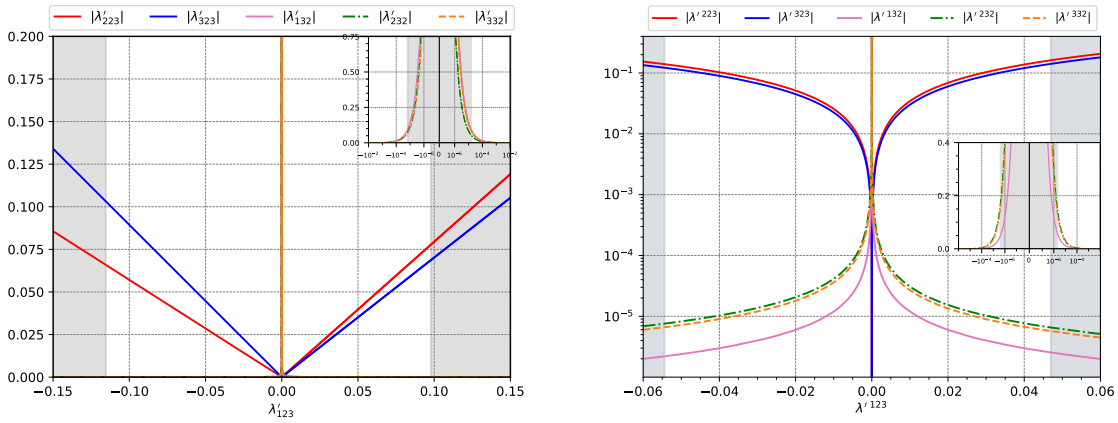

(a) Inverted Ordering

(b) Normal Ordering

Figure 2.9: The IO (left) and NO (right) solution spaces for the non-diagonal trilinear model of Section 2.8.5 including δ_{CP}. The grey regions are the ones ruled out by the bounds of Eq. (2.67). The bounds of Eq. (2.66) are beyond the scale of the plots.

2.8.6 Bilinear-Trilinear Models

The final model we consider has contributions from both the bilinear and trilinear sectors. To have predictivity, we consider a scenario where all the δ_κ bilinears and the *diagonal* trilinears contribute. The effective neutrino mass matrix is,

$$\begin{aligned}\mathbf{M}_\nu^{ij} &= m_0 \delta_\kappa^i \delta_\kappa^j + \frac{g_2 \left[\left(m_e^i\right)^2 + \left(m_e^j\right)^2\right]}{16\pi^2 v} \\ &\times \left(1 + \sin^2\beta + \tan\beta \sin^2\beta\right) \delta_\kappa^i \delta_\kappa^j \\ &+ \frac{3}{8\pi^2 m_{\text{SUSY}}} \delta_{\lambda'}^{i33} \delta_{\lambda'}^{j33} m_b^2 + \dots ,\end{aligned} \tag{2.68}$$

where, the ellipsis indicates terms that are suppressed by extra powers of the Yukawas. The above does not have a MOM structure. However, as long as $\tan\beta$ is not too large, the second term is expected to be suppressed compared to the first and third. The former is due to the extra Yukawas, while the latter follows from the fact that the bilinear invariants typically have to satisfy bounds at least a couple of orders of magnitude more stringent than the trilinear ones in order to fit the neutrino data – for instance, *cf.* the numbers in the previous applications. Ignoring the second term, the model reduces to a MOM with Class 3 structure, as can be seen by making the identifications,

$$\begin{aligned} x^i &= \sqrt{m_0}\delta_\kappa^i \,, \\ x'^i &= \sqrt{\frac{3}{8\pi^2 m_{\text{SUSY}}}} m_b \delta_\lambda'^{i33} \,. \end{aligned} \tag{2.69}$$

Once again, we show what the solution space looks like for the above model by recasting the plot corresponding to the NO limit of Fig. A.3 in Fig. 2.10.

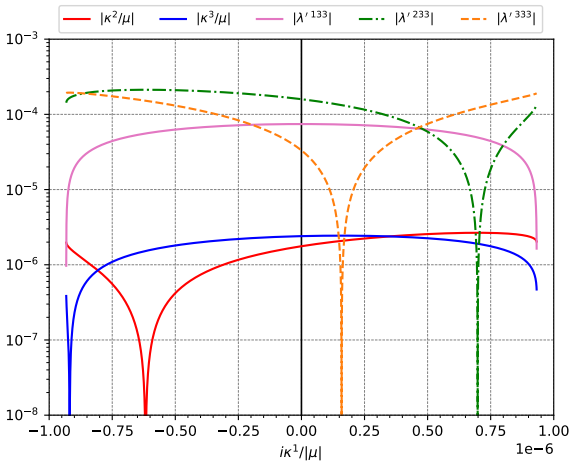

Figure 2.10: The NO limit solution space for the bilinear-trilinear mixed model of Section 2.8.6 including δ_{CP}.

2.9 Conclusions

In this paper, we have explored neutrino-mass generation in the B_3-conserving, but R-parity-violating MSSM. The main obstacle to a systematic phenomonelogical study in general RPV models is the large number of undetermined parameters. Typically, to deal with this, one specializes to specific models; this, however, restricts the applicability of the study. Here, we have taken a different route. By analyzing the structures of the neutrino mass matrix, we have identified four classes of minimal models – the Minimal Oscillation Models (MOMs) – that are consistent with the neutrino oscillation data for the case of two massive neutrinos. This allows for a model-independent study, at least for all models that satisfy the MOM criteria. Our study can be generalized to the case of three massive neutrinos.

We have analyzed each MOM class individually, and shown that it is possible to obtain solution-points consistent with the observed neutrino masses and mixings; for each class there is actually an infinite space of solutions. We have explored the general features of these solution spaces. Finally, we have presented numerical fits that can be adapted to any (MOM-like) specific RPV model without the need for re-performing the least-squares fit. As a demonstration, we have studied several examples that show the wide range of applicability of MOMs. This includes bilinear-only models, trilinear-only models (diagonal and non-diagonal), as well as mixed models.

MOMs do not solve the most general RPV case; we have described the limitations of the framework in the main text. However, given its simplicity, predictivity, and range of applicability, we believe the MOM framework is a useful way to think about neutrino masses in general RPV settings.

3

The ABC of RPV: Small Couplings

3.0 Preface

The contents of this chapter and the supplementary material presented in Appendix B are based on the following publication:

- H. K. Dreiner, Y. S. Koay, D. Köhler, V. M. Lozano, J. M. Berlingen, S. Nangia, and N. Strobbe,
  The ABC of RPV: Classification of R-Parity Violating Signatures at the LHC for Small Couplings,
  Published in JHEP 02 (2023) 120, arXiv:2306.07317 [hep-ph].

After Saurabh Nagia developed the framework to classify the topologies of the RPV-MSSM in a model-independent way the author supported the creation of benchmark scenarios involving direct LSP production. The author of this thesis implemented the numerical simulation for direct LSP production and a gluino LSP using `MadGraph5 aMC@NLO` and `CheckMATE`. All experimental analyses and corresponding plots were compiled by the author providing a detailed overview of the different LHC searches and their sensibility.

The presence of RPV processes can significantly impact search strategies and phenomenological studies at colliders, such as the LHC. Signals from sparticle production and decay in the RPV-MSSM can differ from conventional ones in the RPC-MSSM. The primary difference arises from RPV couplings which cause the decay of the LSP. Principally, searches can be categorized based on coupling strength and LSP mass[1]:

(i) If the magnitude of the RPV coupling is very small, $\lambda \lesssim \mathcal{O}(10^{-8})$, with the mass of the LSP of the order $\mathcal{O}$(TeV), an LSP produced in collisions at the LHC will decay outside the near detectors and might only be visible in far detectors. Accordingly, a lighter LSP mass would relax the limit on the RPV coupling.

(ii) With a small decay coupling, $\mathcal{O}(10^{-8}) \lesssim \lambda \lesssim \mathcal{O}(10^{-1})$, and an LSP mass of 1 TeV, the LSP will decay inside the detector, leading to a modification providing a detectable signal for RPV at colliders. This parameter region also covers a longer-lived LSP decay in the detector resulting in potential displaced vertex signatures.

[1] The order of magnitude of the couplings can be estimated by $\lambda \sim \sqrt{\frac{(\beta\gamma c\tau)}{m_{\mathrm{LSP}}}}$. The formula is derived considering two-body decay of the LSP and the results given in the following discussion follow by assuming a decay length of 1 m. A detailed estimate depends on model assumptions such as the spectrum details.

(iii) With larger magnitudes, the RPV couplings will start to compete with gauge couplings. The branching fractions of the decays are determined by the mass spectrum and the RPV couplings. This scenario will also allow for single sparticle production and for processes with external SM particles but mediated by sparticles, leading to possible interference effects.

In this chapter, we purely focus on the second scenario. It aims to answer a crucial question: *are the existing limits on supersymmetric models sufficiently robust, or could there be unexplored signatures that enable supersymmetry to be hiding at the LHC scale?* The above question was first addressed in some detail in Refs. [159, 160]. The latter argued that any "natural" SUSY framework[2] - regardless of the details of the model - can be targeted by a minimal set of searches. The resulting final states can be identified by at least one of the following components: large missing transverse momentum $\left(E_T^{\text{miss}}\right)$, high multiplicity of objects (≥ 8), or a significant number of top jets. Thus, the SUSY model can be covered by the combination of only five existing ATLAS and CMS searches and one newly proposed search [161].

To expand this, we develop a comprehensive classification of all possible RPV signatures at the LHC without making any assumptions about the particle-spectrum details. By investigating all scenarios, we identify six different experimental signatures for the $LL\bar{E}$-case, six for the $LQ\bar{D}$-case, and five for the $\bar{U}\bar{D}\bar{D}$-case, thereby noting what searches would provide comprehensive coverage of the RPV-MSSM landscape. The results show that, while all of the identified signatures have been covered to some extent by previous LHC searches, certain aspects have not yet been tested at the required sensitivity.

To determine the sensitivity of existing searches, we consider the case of a dominant $LL\bar{E}$ operator and consider several benchmark scenarios - involving the full range of LSP types - to determine the lower mass-bounds by using `CheckMATE`. Two primary production mechanisms are examined: direct production of the LSP and production via cascade decay. The re-analysis finds strong exclusion limits for all $LL\bar{E}$ operators - in all LSP combinations - showing that LHC searches provide a comprehensive coverage for these couplings. Notably, the results show that the obtained limits for the masses in RPV-MSSM scenarios involving LLE operators are comparable to or even exceed those obtained in RPC-MSSM.

In summary, in this chapter, we develop a systematic classification of all possible RPV signatures at the LHC, providing a comprehensive overview of the RPV-MSSM landscape. While the previous searches have covered a substantial fraction of these signatures, further exploration is crucial to investigate the direct production of all LSP types and RPV couplings, especially in the $LQ\bar{D}$ and $\bar{U}\bar{D}\bar{D}$ regions. With the possibility for future extensions, as developing benchmarks for dominant $LQ\bar{D}$ and $\bar{U}\bar{D}\bar{D}$ operators or considering a different regime for the magnitude of the RPV couplings, this study serves as a basis for both - a review of the current status of RPV searches, as well as a basis for future investigation of RPV-SUSY at the LHC.

[2] Natural in this context means the presence of light higgsinos $m_{\tilde{H}} \lesssim 400\,\text{GeV}$, and light stops $m_{\tilde{t}} \lesssim 1\,\text{TeV}$.

3.1 Introduction

Supersymmetry (SUSY) [89, 90, 162, 163] is a well-motivated extension of the Standard Model (SM). It uniquely extends the SM algebra [47, 48], addresses the 'naturalness problem' of the Higgs boson [36, 164], and has many further appealing features, as reviewed in Refs. [34, 45, 165]. Extensive experimental effort has been devoted in its search, particularly at the Large Hadron Collider (LHC) by the ATLAS and CMS Collaborations. However, no evidence for SUSY has been found so far with lower mass bounds reaching $\mathcal{O}(1-2)$ TeV for the colored sector [57, 166–188], and $\mathcal{O}(100-1000)$ GeV for the electroweak sector [57, 84, 178, 180, 181, 189–203], with some dependence on the model details.

As we prepare for more data through Run 3 at the LHC, and especially in the high-luminosity era, it is an excellent opportunity to assess the current status of supersymmetric searches and gain insight into how we should proceed. An interesting question is: *are the above bounds robust, or are there gaps/loopholes that could still allow LHC-scale SUSY to be hiding?* Typically, ATLAS and CMS derive these limits within the framework of various simplified models or a limited number of complete models such as the Constrained Minimal Supersymmetric Standard Model (CMSSM); it is not clear whether these results can be used to conclude that low-scale SUSY has been definitively excluded.

The above question was first addressed in Ref. [159], and – after LHC Run 1 – in Ref. [160], in more detail. In the latter, it was argued that any 'natural' SUSY model[3] with kinematically accessible gluinos – independent of model details – results in final states containing at least one of the following ingredients: large missing transverse momentum $\left(E_{\mathrm{T}}^{\mathrm{miss}}\right)$, high multiplicity of objects (≥ 8), or a significant number of top quarks. Using this, the authors showed that combining just five existing ATLAS and CMS searches, and one newly proposed search [161] excludes almost any 'natural' SUSY model containing gluinos lighter than 1 TeV. Of course, using current data and a similar strategy should yield a higher mass bound. Nevertheless, the demonstration that a minimal set of searches can target almost any SUSY setup, independent of details concerning the model, mass spectrum, UV-completion, etc., is noteworthy. Such an approach is desirable, especially since it informs us about potential gaps that may exist in our SUSY coverage. For instance, the search proposed by Ref. [161] represented a real gap that has since been filled by ATLAS and CMS in Refs. [204, 205].

In this work, we wish to consider the same question but with two important differences. First, beyond assuming the MSSM particle content, we remain completely blind to the particle-spectrum details. In particular, we do not require that the gluinos are kinematically accessible. With the LHC transitioning from an era of energy upgrades to one of increasing luminosity, we should seriously entertain the possibility that the colored sector may be heavy, while a focus on rarer production channels may yield fruit. We also do not make any 'naturalness' requirements in the sense of Ref. [160].

Second, our focus will be on the R-parity Violating MSSM (RPV-MSSM). The most general, renormalizable superpotential with the MSSM particle content includes lepton- and baryon-number violating operators, together referred to as RPV terms [45, 50, 53, 99]. These are usually set to zero by imposing a discrete $\mathbb{Z}_2$-symmetry called R-parity as they can lead to proton decay [101, 148] at rates in excess of the strict experimental bound [65].

[3] The 'naturalness' criterion in Ref. [160] requires the Higgsinos and stops to be light.

However, the proton-decay problem can be averted without removing all RPV terms [51, 52, 206]; in general, there is no theoretical or phenomenological reason to consider the MSSM without RPV terms [53]. On the other hand, as we demonstrate in Section 3.2, the different configurations of couplings and types of the lightest SUSY particle (LSP) in the RPV-MSSM lead to a bewildering number of possible signatures. In particular, with the requirements on gluino and higgsino masses absent, a large number of these signatures do not possess any of the characteristics listed in Ref. [160]. In comparison, the 'vanilla' MSSM is less interesting as it tends to retain its characteristic significant E_T^{miss} signal, irrespective of spectrum details.[4] This makes a systematic treatment and classification particularly crucial in the case of the RPV-MSSM.

To summarize, we study the coverage of the most general RPV-MSSM setup at the LHC, without making any assumptions about the particle-spectrum details. We seek a minimal set of searches that would provide complete coverage; this will allow us to identify any potential gaps in our current searches. We will restrict ourselves to the case of small RPV couplings in this work, leaving the large-coupling case for a dedicated study in the future. Thus, the production of sparticles is unchanged from the MSSM case and we only need to consider pair-production channels. The final state signatures will be altered, however, due to the RPV couplings affecting decays.

The paper is organized as follows. In Section 3.2, we set notation and state the assumptions of our framework. Further, we explicitly describe the vast phenomenology of the RPV-MSSM, in order to demonstrate our point about the need for a systematic method of classification. In Section 3.3, we provide such a systematic classification by grouping signatures in a meaningful way, according to the coupling and nature of the LSP. Our approach allows us to identify a minimal set of searches that would provide complete RPV-MSSM coverage at the LHC, and discuss the current status of such a program. Then, in Section 3.4, we demonstrate applications of our framework – as a first study – for the case of a dominant $LL\bar{E}$ RPV-operator. We consider several benchmark scenarios with such lepton-number violating operators, involving the full range of LSP types, and derive exclusion limits. Our results demonstrate that, irrespective of model details, the minimal set of searches proposed in this work can be used to derive strong limits. Finally, we conclude and discuss the implications and limitations of our work, and provide an outlook in Section 3.5. Additionally, we provide a set of appendices containing supplementary details about our simulation procedure (Appendix B.1), information that can be used to optimize future searches (Appendix B.2), and an introduction to `abc-rpv` (Appendix B.3), an accompanying RPV Python library[5] that can be used to generate all the signature tables in this paper.

[4] We note that the E_T^{miss} signature can be diluted even in the case of the MSSM through scenarios with a compressed spectrum or a 'Hidden Valley'; see, for instance, Refs. [160, 207] for details. Despite the varied phenomenology offered by these models, we believe that it is more efficient to thoroughly explore the minimal setup provided by the RPV-MSSM before adding further complexities.

[5] Available at: `https://github.com/kys-sheng/abc-rpv.git`

3.2 Framework

3.2.1 Conventions and Assumptions

With the MSSM particle content and the $N = 1$ supersymmetry algebra, the most general $\mathrm{SU}(3)_C \times \mathrm{SU}(2)_L \times \mathrm{U}(1)_Y$-invariant, renormalizable superpotential is,

$$W = W_{\mathrm{MSSM}} + W_{\mathrm{LNV}} + W_{\mathrm{BNV}}\,, \tag{3.1}$$

where W_{MSSM} is the usual MSSM superpotential – see, for instance, Ref. [54] – while,

$$W_{\mathrm{LNV}} = \frac{1}{2}\lambda^{ijk} L_i L_j \bar{E}_k + \lambda'^{ijk} L_i Q_j \bar{D}_k + \kappa^i H_u L_i\,, \qquad W_{\mathrm{BNV}} = \frac{1}{2}\lambda''^{ijk} \bar{U}_i \bar{D}_j \bar{D}_k\,, \tag{3.2}$$

violate lepton- and baryon-number, respectively. Together, $W_{\mathrm{RPV}} \equiv W_{\mathrm{LNV}} + W_{\mathrm{BNV}}$, are called the RPV superpotential terms. In our notation, L ($\bar{E}$) and Q ($\bar{U}$, $\bar{D}$) are the MSSM lepton- and quark-doublet (-singlet) chiral superfields, respectively, while H_u labels the (up-type) $\mathrm{SU}(2)_L$-doublet Higgs chiral superfield. We do not write gauge indices explicitly but retain the generational ones: $i, j, k \in \{1, 2, 3\}$ with a summation implied over repeated indices. The λ's and the κ's are the trilinear and bilinear couplings, respectively.

We shall employ the particle content of the MSSM and the superpotential of Eq. (3.1) as the basis for this study. As mentioned in the Introduction, some terms in the superpotential can lead to rapid proton decay. In general, this requires combinations of certain $LQ\bar{D}$ and $\bar{U}\bar{D}\bar{D}$ operators.[6] As long as these combinations are kept small, the proton's lifetime remains consistent with the bounds. Indeed, there are symmetries that can achieve this – see, for instance, Refs. [51, 52, 206]. In this study, we will not bother with the details of how this is done; our focus will be on classifying all possible collider signatures coming from the various couplings. We will, however, ignore the bilinear couplings. These are severely constrained by neutrino mass data [54] and are expected to be relevant for colliders only in limited contexts [99, 208]. Furthermore, at a fixed energy scale they can be rotated away [58, 150].

The optimal search strategy for RPV-MSSM scenarios at colliders depends on the magnitude of the RPV couplings. We will restrict ourselves to the case where these couplings are small enough such that the production of sparticles and their cascade decays down to the LSP remain unchanged from the MSSM case, but large enough so that the LSP decays promptly in the detector (we also require the cascade decays of the other sparticles to be prompt). While the exact magnitudes depend on the spectrum details, we can estimate it to roughly mean the range,

$$\sqrt{\frac{(\beta\gamma)\, 10^{-12}\,\mathrm{GeV}}{m_{\mathrm{LSP}}}} \lesssim \lambda \ll g\,, \tag{3.3}$$

where λ is the relevant RPV coupling, g is a gauge coupling, m_{LSP} is the mass of some LSP that has a two body-decay via the RPV coupling, and β and γ are its velocity and Lorentz factor, respectively. The left condition is derived from the requirement that the LSP has a decay length of about 1 cm in the lab frame.[7] For an LSP mass of 1 TeV, Eq. (3.3) implies

[6] One exception is if the lightest neutralino is lighter than the proton in which case the decay can occur via $\bar{U}\bar{D}\bar{D}$ operators alone [101].

[7] We have considered a two-body decay here. For comparison, a similar estimate for an LSP with mass

the range $\mathcal{O}\left(10^{-7}\right) \lesssim \lambda \ll \mathcal{O}\left(10^{-1}\right)$. Considering λ values smaller or larger than the above range leads to unique features that require separate studies. The former can lead to new kinds of signals such as displaced vertices or long-lived particles, and both topics have received some attention in recent times [209–220]. The latter also leads to interesting features; in particular, single production of sparticles [149, 221–224], and RPV effects in cascade chains can lead to phenomenological changes requiring a dedicated study that we shall pursue in the future, as a continuation of this work.

One assumption, related to the above point, that we will need to make in this work is that the LSP is not too light, *i.e.*, $m_{\text{LSP}} > \mathcal{O}\,(200\,\text{GeV})$. While current mass bounds on most SUSY particles place them well above this limit, a bino-like neutralino is still allowed to be massless [69, 86]. Requiring the above condition ensures that the decay of the LSP can be prompt without requiring the RPV couplings to be too large. Further, it allows the LSP to decay into all SM fermions (except for, perhaps, the top quark).[8] Dedicated LHC studies for a very light neutralino can be found in, for instance, Refs. [225–227].

Table 3.1: Summary of notation for labeling the RPV-MSSM particle content used in this work. For the particles not mentioned in the table, we use standard notation.

Symbol	**Particles**
ℓ	e/μ
L	ℓ/τ
j_l	$u/d/c/s$ jets
j_3	t/b jets
j	j_l/j_3 jets
V	$W/Z/h$
$\tilde{\ell}(\tilde{\nu})$	$\tilde{e}_L(\tilde{\nu}_e)/\tilde{\mu}_L(\tilde{\nu}_\mu)$
$\tilde{e}$	$\tilde{e}_R/\tilde{\mu}_R$
$\tilde{q}$	$\tilde{u}_L/\tilde{d}_L/\tilde{c}_L/\tilde{s}_L$
$\tilde{u}$	$\tilde{u}_R/\tilde{c}_R$
$\tilde{d}$	$\tilde{d}_R/\tilde{s}_R$
$\tilde{q}_3$	$\tilde{t}_L/\tilde{b}_L$
$\tilde{t}$	$\tilde{t}_R$
$\tilde{b}$	$\tilde{b}_R$
$\tilde{B}$	Bino
$\tilde{W}$	Winos (charged/neutral)
$\tilde{H}$	Higgsinos (charged/neutral)

Finally, before concluding this subsection, we introduce our notation for labeling the particle content in Table 3.1. We will find the groupings we define useful in presenting our

500 GeV undergoing a three-body decay via a virtual sfermion of mass 1 TeV (this is how a neutralino decays, for instance) gives the range $\mathcal{O}\left(10^{-5}\right) \lesssim \lambda \ll \mathcal{O}\left(10^{-1}\right)$. We note that, in some cases, four-body decays are also possible, *e.g.*, a slepton LSP decaying via λ'' couplings.

[8] Note that, throughout this work, we will neglect all SM Yukawas, except for that of the top quark.

results later. For simplicity, we will also assume all SUSY particles belonging to a particular grouping are mass degenerate – *i.e.*, we treat mass splittings between components of the same doublet (for instance, $\tilde{H}^{\pm}$ and $\tilde{H}^{0}$), as well as between first and second generation sparticles as negligible. The former assumption holds true to a very good approximation [45]. The latter is not essential for our framework but allows us to be concise; generalization is straightforward.

3.2.2 The RPV Landscape

The presence of even small RPV couplings can drastically change collider phenomenology compared to the MSSM. In the latter case, SUSY particles are pair-produced at colliders and undergo gauge-cascade decays into the LSP – typically the neutralino[9] – which then escapes the detector unobserved, giving the characteristic E_T^{miss} signature. The presence of RPV couplings changes this simple picture in two main ways. First, the LSP is no longer constrained to be the neutralino but can be any SUSY particle [66, 67]. Second, the RPV couplings make the LSP unstable; the E_T^{miss} signature is now replaced (diluted, or even completely absent) by the objects arising in this decay, which are determined by the dominant RPV coupling. The total number of possible signatures for the RPV-MSSM at a hadron collider can be summarized as (adapted from Ref. [67], see also Ref. [229]):

$$\text{RPV signature} = \begin{pmatrix} \tilde{g}\tilde{g} \\ \tilde{g}\tilde{q}, \tilde{g}\tilde{u}\ldots \\ \tilde{q}\tilde{q}, \tilde{q}_3\tilde{q}_3, \tilde{q}\tilde{u}\ldots \\ \tilde{\ell}\tilde{\ell}, \tilde{\tau}_L\tilde{\tau}_L, \tilde{\ell}\tilde{\nu}\ldots \\ \tilde{H}\tilde{H} \\ \tilde{W}\tilde{W} \\ \tilde{B}\tilde{B} \end{pmatrix}_{\substack{\text{Production} \\ \text{Channels}}} \otimes \begin{pmatrix} \tilde{B} \\ \tilde{H} \\ \tilde{W} \\ \tilde{\ell}(\tilde{\nu}) \\ \tilde{\tau}_L(\tilde{\nu}_\tau) \\ \tilde{e} \\ \tilde{\tau}_R \\ \tilde{q} \\ \tilde{u} \\ \tilde{d} \\ \tilde{q}_3 \\ \tilde{t} \\ \tilde{b} \\ \tilde{g} \end{pmatrix}_{\substack{\text{Possible} \\ \text{LSPs}}} \otimes \begin{pmatrix} L_1L_2\bar{E}_1 \\ \ldots \\ L_1Q_1\bar{D}_1 \\ \ldots \\ \bar{U}_3\bar{D}_2\bar{D}_3 \end{pmatrix}_{\substack{\text{LSP} \\ \text{Decay}}} \tag{3.4}$$

There are 45 different RPV trilinear couplings to consider above. Further, the final state will depend on the details of the cascade decays which, in turn, are determined by the mass orderings in the SUSY spectrum: the total number of possibilities is immense! The first systematic analysis of these signatures was performed in Ref. [149], for the particular case of a neutralino LSP. A more general classification, allowing for all possible LSPs, has been presented in Ref. [229] (see also Ref. [230]). However, the study assumes that the lightest colored particle is kinematically accessible at the collider. In this work, we extend this by also

[9] The nature of the LSP in the MSSM follows from the strict constraints on charged or colored stable particles [99, 228].

including the possibility that the colored sector lies beyond LHC energies. More importantly, the emphasis in Ref. [229] was on finding signatures arising most frequently from Eq. (3.4), when one considers the space of all possible mass orderings of the SUSY spectrum. Our approach here is different: we wish to create a minimal set of signatures that provides complete coverage for the space of RPV-MSSM models, irrespective of how frequently an individual signature may arise. Furthermore, we will concretely tie this to the LHC search program, discussing the current experimental coverage and identifying possible gaps; this aspect is absent in Ref. [229]. Ref. [67] has studied it for the case of the RPV-CMSSM, but a more general model-independent treatment is missing in the literature.

3.3 Classification of Signatures: The RPV Dictionary

We now describe our approach for classifying the most general RPV-MSSM signatures. Since we assume the RPV couplings are small, sparticles are pair-produced at the LHC via gauge interactions, as in the MSSM. The production channels that we consider are listed in Eq. (3.4) on the left; the mass spectrum determines which of these are kinematically accessible. The produced sparticles – if not the LSP – will then cascade-decay via gauge interactions until the LSP is reached with the details of the cascade also depending on the model (*i.e.*, the spectrum). The LSP, once produced, decays promptly via the relevant RPV coupling.

In our model-independent approach, we target the last step above: the LSP decay. The essential features of the signatures can be characterized by specifying the nature of the LSP and the RPV coupling, independent of any spectrum-specific details such as the exact chain leading to the LSP production, the mass hierarchies, etc. This is obviously true when the LSP couples directly to the relevant RPV decay operator, leading to a two-body decay. However, it is also true more generally. To illustrate this point, we consider a scenario with a $\tilde{q}$ LSP (first or second generation squark doublet, *cf.* Table 3.1), with λ''_{312} the only non-zero RPV coupling. In this case, there is no direct two-body decay available for $\tilde{q}$. Instead, it must decay via a virtual $\tilde{t}$ or $\tilde{d}$; some of the paths it can take are depicted in Fig. 3.1. Without specifying the model spectrum, it is impossible to state which path will be favored. However, note that in each case we end up with the final state $t + 3j_l + X$.[10] This is a general feature, independent of the path it actually takes. Thus, any model with a $\tilde{q}$ LSP and a dominant λ''_{312} operator has a characteristic $t + 3j_l$ signature, irrespective of any other spectrum details. We can target all such scenarios with a single search – this observation is the most crucial aspect of this work.

Using the above approach, we can compile the characteristic signatures arising from each LSP and dominant RPV coupling combination, in order to arrive at a minimal set of searches that would provide complete coverage for the RPV-MSSM, in a model-independent way. We present this set in the form of tables below. We will also compare it to what has been covered by the vast program of BSM searches by the `ATLAS` and `CMS` collaborations. Although only a small subset of these searches provides an explicit interpretation in terms of RPV-SUSY models, the wide range of final states considered covers the majority of signatures expected from RPV decays. Thus, appropriately reinterpreted, they could be used to restrict the RPV

[10] There is one subtlety here: the $\tilde{H}$ path in Fig. 3.1 leads to a b-jet instead of t if it proceeds via $\tilde{H}^{\pm}$. However, since we assume $\tilde{H}^{\pm}$ and $\tilde{H}^{0}$ are mass-degenerate, the corresponding path via $\tilde{H}^{0}$ is always equally likely.

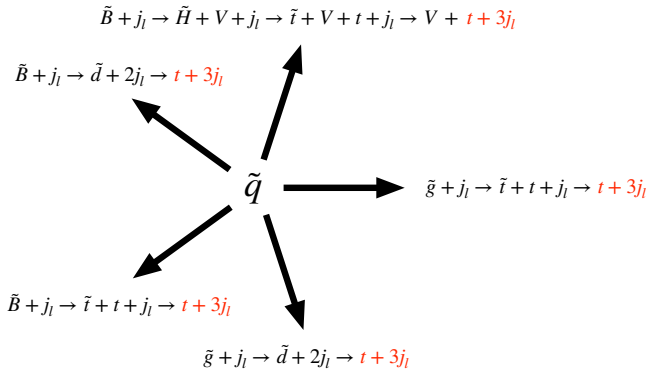

Figure 3.1: Some possible paths a $\tilde{q}$ LSP can take while decaying through λ''_{312}. Since $\tilde{q}$ is the LSP here, all the intermediate sparticles are virtual. See Table 3.1 for the notation employed.

parameter space.

In order to facilitate a systematic exploration of the RPV-MSSM landscape with our approach, we have developed an RPV Python library called `abc-rpv`. This library provides a powerful toolkit containing a range of features for analyzing the characteristic signatures arising from various RPV scenarios. The main functionalities include identifying signatures and decay chains for any LSP and RPV coupling combination, as well as going in the other direction: identifying potential RPV scenarios leading to a user-given final state. Using this library, one can reproduce all signature tables in this paper – for instance, (Tables 3.2-3.11) shown below, as well as Table B.1 in Appendix B.2. The information in Fig. 3.1 (possible decay chains for a given LSP) can also be generated easily up to a fixed number of vertices. An introduction to the `abc-rpv` library, including a quick user manual is provided in Appendix B.3.

We note that one downside of our approach is that only final state objects arising in the LSP decay are targeted, and all objects arising in the cascade decays are neglected. In specific models – for instance, one with squark pair-production and a neutralino LSP – one could certainly optimize by targeting the additional jets arising in the cascade decays of the parent squarks, thus improving the search sensitivity. However, in order to analyze the status of complete coverage while being model-independent, our approach is necessary. For completeness, we compile a list of additional objects that can arise in cascade decays for various production channels in Table B.1 in Appendix B.2. That table may be used to optimize the searches compiled below for particular scenarios when the model details are known. Further, it can help understand the loss in sensitivity for searches that veto additional

Table 3.2: Characteristic signatures arising from LSP decays for $L_iL_j\bar{E}_k$ operators. The first column depicts the LSPs. The second and third columns represent the signatures from *pair-production* of LSPs for the cases where the indices $i,j,k \in \{1,2\}$, and where the indices $i,k \in \{1,2\}$ and $j=3$, respectively. For cases involving degenerate LSPs, *e.g.*, $\tilde{\ell}\,(\tilde{\nu})$, all pair combinations are considered. Further, only the relevant signatures are retained and we have introduced color-coding to improve the readability of the table; the details are in the main text.

LSP	**LLE**	**LL$_3$E**
$\tilde{\ell}\,(\tilde{\nu})$	$3\ell + E_T^{\rm miss}/4\ell$	$2\ell + \tau + E_T^{\rm miss}/2\ell + 2\tau$
$\tilde{e}$	$2\ell + E_T^{\rm miss}$	$2\ell + E_T^{\rm miss}/\ell + \tau + E_T^{\rm miss}$
$\tilde{\tau}_L\,(\tilde{\nu}_\tau)$	$4\ell + 2\tau + E_T^{\rm miss}/4\ell + \tau + E_T^{\rm miss}$	$3\ell + E_T^{\rm miss}/4\ell$
$\tilde{\tau}_R$	$4\ell + 2\tau + E_T^{\rm miss}$	$4\ell + 2\tau + E_T^{\rm miss}/3\ell + 3\tau + E_T^{\rm miss}$
$\tilde{g}$	$4\ell + 4j + E_T^{\rm miss}$	$4\ell + 4j + E_T^{\rm miss}/3\ell + \tau + 4j + E_T^{\rm miss}$
$\tilde{q},\ \tilde{u},\ \tilde{d}$	$4\ell + 2j_l + E_T^{\rm miss}$	$4\ell + 2j_l + E_T^{\rm miss}/3\ell + \tau + 2j_l + E_T^{\rm miss}$
$\tilde{t}_L(\tilde{b}_L)$	$4\ell + 2j_3 + E_T^{\rm miss}$	$4\ell + 2j_3 + E_T^{\rm miss}/3\ell + \tau + 2j_3 + E_T^{\rm miss}$
$\tilde{t}_R$	$4\ell + 2t + E_T^{\rm miss}$	$4\ell + 2t + E_T^{\rm miss}/3\ell + \tau + 2t + E_T^{\rm miss}$
$\tilde{b}_R$	$4\ell + 2b + E_T^{\rm miss}$	$4\ell + 2b + E_T^{\rm miss}/3\ell + \tau + 2b + E_T^{\rm miss}$
$\tilde{B},\ \tilde{W},\ \tilde{H}$	$4\ell + E_T^{\rm miss}$	$4\ell + E_T^{\rm miss}/3\ell + \tau + E_T^{\rm miss}$

objects to help with background suppression.

3.3.1 LLE Tables

We depict the signatures corresponding to the decay of a pair of LSPs for the $LL\bar{E}$ operators of Eq. (3.2) in Tables 3.2 and 3.3. The tables have been written assuming that LSPs are gauge eigenstates, and the pair decays via the same coupling. However, if one is interested in scenarios where the mass eigenstates have significant mixing, or where several dominant RPV couplings contribute, the results can be generalized by considering linear combinations of the table entries.

The tables show the LSP in the first column. The second and third columns depict the resulting signature depending on the generation structure of the $LL\bar{E}$ operator responsible for decay; we employ the compact notation of Table 3.1. Note that, to be concise, we assume all RPV operators within a given category are non-zero, *e.g.*, both $L_1L_2\bar{E}_1$ and $L_1L_2\bar{E}_2$ are non-zero for the category $LL\bar{E}$. Otherwise, more objects may arise, *e.g.*, with a $\tilde{\mu}_R$ LSP and a non-zero $L_1L_2\bar{E}_1$ operator, the smuon would first need to transition into $\tilde{\ell}(\tilde{\nu})$ or $\tilde{e}_R$ leading to two extra muons; the extension is straightforward. In some cases, there is more than one signature possible. If two signatures are equally likely, we have listed the one that contains more electrons or muons, since we expect it to be more readily observable. In cases where a signature with fewer e/μ can have a higher cross-section, we have retained both separated by a '/'. For instance, in the case of a $\tilde{\ell}(\tilde{\nu})$ LSP (we assume mass degeneracy of SU(2)$_L$-doublets, *cf.* Table 3.1) decaying via λ_{121}, the $\tilde{\ell}$ decays into one charged lepton and one neutrino, while

Table 3.3: Same as Table 3.2 but for $L_iL_j\bar{E}_k$ operators with $i,j \in \{1,2\}$ and $k=3$ (second column), and $j,k=3$ and $i \in \{1,2\}$ (third column).

LSP	**LLE$_3$**	**LL$_3$E$_3$**
$\tilde{\ell}\,(\tilde{\nu})$	$\ell + 2\tau + E_T^{\text{miss}}/2\ell + 2\tau$	$3\tau + E_T^{\text{miss}}/4\tau$
$\tilde{e}$	$4\ell + 2\tau + E_T^{\text{miss}}$	$4\ell + 2\tau + E_T^{\text{miss}}/3\ell + 3\tau + E_T^{\text{miss}}$
$\tilde{\tau}_L\,(\tilde{\nu}_\tau)$	$2\ell + 4\tau + E_T^{\text{miss}}/2\ell + 3\tau + E_T^{\text{miss}}$	$2\ell + 2\tau/\ell + 2\tau + E_T^{\text{miss}}$
$\tilde{\tau}_R$	$2\ell + E_T^{\text{miss}}$	$2\ell + E_T^{\text{miss}}/\ell + \tau + E_T^{\text{miss}}$
$\tilde{g}$	$2\ell + 2\tau + 4j + E_T^{\text{miss}}$	$2\ell + 2\tau + 4j + E_T^{\text{miss}}/\ell + 3\tau + 4j + E_T^{\text{miss}}$
$\tilde{q},\ \tilde{u},\ \tilde{d}$	$2\ell + 2\tau + 2j_l + E_T^{\text{miss}}$	$2\ell + 2\tau + 2j_l + E_T^{\text{miss}}/\ell + 3\tau + 2j_l + E_T^{\text{miss}}$
$\tilde{t}_L(\tilde{b}_L),$	$2\ell + 2\tau + 2j_3 + E_T^{\text{miss}}$	$2\ell + 2\tau + 2j_3 + E_T^{\text{miss}}/\ell + 3\tau + 2j_3 + E_T^{\text{miss}}$
$\tilde{t}_R$	$2\ell + 2\tau + 2t + E_T^{\text{miss}}$	$2\ell + 2\tau + 2t + E_T^{\text{miss}}/\ell + 3\tau + 2t + E_T^{\text{miss}}$
$\tilde{b}_R$	$2\ell + 2\tau + 2b + E_T^{\text{miss}}$	$2\ell + 2\tau + 2b + E_T^{\text{miss}}/\ell + 3\tau + 2b + E_T^{\text{miss}}$
$\tilde{B},\ \tilde{W},\ \tilde{H}$	$2\ell + 2\tau + E_T^{\text{miss}}$	$2\ell + 2\tau + E_T^{\text{miss}}/\ell + 3\tau + E_T^{\text{miss}}$

the $\tilde{\nu}$ decays into two charged leptons. Thus, the possible signatures from pair production are: 4ℓ, $3\ell + E_T^{\text{miss}}$, $2\ell + E_T^{\text{miss}}$. In the table, we retain the first and second signatures: the former because it has the highest number of charged leptons, and the latter because it has the highest cross-section. $2\ell + E_T^{\text{miss}}$ is not retained since it has both a lower cross-section compared to the $3\ell + E_T^{\text{miss}}$ signature, as well as fewer leptons and, hence, will never be the most relevant final state for searches.

From the tables, we see that the $LL\bar{E}$ case can be completely covered through the following six searches:

1. $2L + E_T^{\text{miss}}$
2. $3L + E_T^{\text{miss}}$
3. $4L$
4. $4L + (0-4)j + E_T^{\text{miss}}$
5. $5L + E_T^{\text{miss}}$
6. $6L + E_T^{\text{miss}}$

To improve the readability of the table, we have introduced a color scheme based on the number of charged leptons in the search region: red (two), blue (three), yellow (four without missing energy), green (four with missing energy), purple (five), and gray (six).

Thus, indeed – in spite of the large number of possibilities that RPV offers – it is possible to organize experimental searches into a small, workable set. The identification of these minimal signatures and the corresponding experimental coverage is one of the main results of this paper. We stress that this is more than just a convenient notational scheme. As will be shown, all signatures that we will classify in our tables – except for one – are experimentally covered

by ATLAS and CMS in one form or another, although in some cases strong improvements in sensitivity are required to reach the electroweak production cross-sections. In Section 3.4, we will further apply these to see how the same small set of searches provides exclusion limits across a broad class of RPV models.

One point to note is that, in the above, we have only classified the total number of leptons in each search. However, often it may be useful to know the flavor/sign combinations of these leptons. While we do not employ them in our numerical studies, we provide tables in Appendix B.2 that explicitly show these configurations. These may be useful in developing more sensitive search regions, in case one wishes to target specific scenarios.

We now discuss the experimental coverage of the above signatures. The six final states identified include multiple leptons, may include additional jets, and may come with or without E_T^{miss}. Searches for R-parity Conserving SUSY (RPC-SUSY) typically have good coverage for signatures with E_T^{miss} or with at least three leptons (or two with the same charge), with several of these searches providing some interpretations in RPV-SUSY models as well. Other searches sensitive to the $LL\bar{E}$ case include analyses targeting heavy leptons or additional Higgs bosons. LHC searches relevant for the $LL\bar{E}$ coupling broadly span the final states of (1.) $2\ell + E_T^{\text{miss}}$ [180–182, 193, 198, 199, 203, 231, 232], (2.) $3\ell + E_T^{\text{miss}}$ [180, 182, 190, 195, 233, 234], (3.) 4ℓ [195, 235–239], and (4., 5., 6.) $\geq 4\ell + E_T^{\text{miss}}$ [182, 195, 234, 240]. Searches with four leptons are typically inclusive and include events with more than four leptons, therefore covering also the $5L$ and $6L$ categories.

3.3.2 UDD Tables

Next, we show analogous results for the $\bar{U}\bar{D}\bar{D}$ case in Tables 3.4 and 3.5. The comments from before apply here too. These scenarios can be completely covered through the following five searches:

1. $4j$
2. $2j_l + 4j$
3. $2j_l + 6j$
4. $1L + 2j_l + 4j + E_T^{\text{miss}}$
5. $2L + 2j_l + 4j$

The color scheme is based on the number of jets and charged leptons: red (four jets), blue (six jets, no leptons), yellow (eight jets), green (six jets, one lepton), and purple (six jets, two leptons).

One interesting point worth noting is that we write j_3 and not t in Table 3.5 for the non-colored LSPs (j_3 indicates that the jet could be t/b, *cf.* Table 3.1). This is to account for the possibility that kinematic suppression may lead to the decay into a b (via a virtual chargino) to be preferred over the decay into a t (via a neutralino). Generally, in all tables to follow, we will take this consideration into account for all the non-colored LSPs.

Three of the five $U\bar{D}\bar{D}$ final states listed above contain only jets and correspond to the largest fraction of the possible LSP decays. However, up to two of the jets listed could be top

Table 3.4: Characteristic signatures arising from LSP decays for $\bar{U}_i\bar{D}_j\bar{D}_k$ operators. The first column depicts the LSPs. The second and third columns represent the signatures from *pair-production* of LSPs for the cases where the indices $i, j, k \in \{1, 2\}$, and where the indices $i, k \in \{1, 2\}$ and $j = 3$, respectively. For cases involving degenerate LSPs, *e.g.*, $\tilde{\ell}\,(\tilde{\nu})$, all pair combinations are considered. Further, only the relevant signatures are retained and we have introduced color-coding to improve the readability of the table; the details are in the main text.

LSP	**UDD**	**UD$_3$D**
$\tilde{\ell}\,(\tilde{\nu})$	$2\ell + 6j_l/\ell + 6j_l + E_T^{\text{miss}}$	$2\ell + 2b + 4j_l/\ell + 2b + 4j_l + E_T^{\text{miss}}$
$\tilde{e}$	$2\ell + 6j_l$	$2\ell + 2b + 4j_l$
$\tilde{\tau}_L\,(\tilde{\nu}_\tau)$	$2\tau + 6j_l/\tau + 6j_l + E_T^{\text{miss}}$	$2\tau + 2b + 4j_l/\tau + 2b + 4j_l + E_T^{\text{miss}}$
$\tilde{\tau}_R$	$2\tau + 6j_l$	$2\tau + 2b + 4j_l$
$\tilde{g}$	$6j_l$	$2b + 4j_l$
$\tilde{q}$	$8j_l$	$2b + 6j_l$
$\tilde{u}$	$4j_l$	$2b + 2j_l$
$\tilde{d}$	$4j_l$	$2b + 2j_l$
$\tilde{t}_L(\tilde{b}_L)$	$6j_l + 2j_3$	$2b + 4j_l + 2j_3$
$\tilde{t}_R$	$2t + 6j_l$	$2t + 2b + 4j_l$
$\tilde{b}_R$	$2b + 6j_l$	$4j_l$
$\tilde{B},\ \tilde{W},\ \tilde{H}$	$6j_l$	$2b + 4j_l$

quarks in certain configurations. This would result in additional final state jets or leptons which can be used as experimental handles to improve sensitivity. The last two signatures listed arise from slepton LSPs and always include leptons and/or E_T^{miss} in the final state. `ATLAS` and `CMS` have covered the signatures of (1.) 4 jets [241–243], (2.) 6 jets [244, 245], (3.) 8 jets [205, 239, 246–248], (4.) 1 lepton plus at least 6 jets [184, 204, 205, 249, 250], and (5.) 2 leptons plus 6 jets [182, 250, 251].

Some of these searches explicitly require a minimum number of b-tagged jets, whereas others are more inclusive. The searches considering leptons typically only consider electrons or muons, which reduces the sensitivity to scenarios featuring tau leptons. The searches for signatures (1.), (2.), and (3.) reduce the potentially overwhelming multijet background by requiring the presence of two same-mass resonances in each event. Even so, while some final states are nominally covered, the large difference in production cross-sections leads to exclusion limits being available for some production modes (*e.g.*, $\tilde{g} \to 3j_l$) but still requiring orders of magnitude of improvement to reach others (*e.g.*, $\tilde{H} \to 3j_l$).

Table 3.5: Same as Table 3.4 but for $\bar{U}_i\bar{D}_j\bar{D}_k$ operators with $j,k \in \{1,2\}$ and $i = 3$ (second column), and $i,j = 3$ and $k \in \{1,2\}$ (third column).

LSP	$\mathbf{U_3DD}$	$\mathbf{U_3D_3D}$
$\tilde{\ell}\,(\tilde{\nu})$	$2\ell + 4j_l + 2j_3/\ell + 4j_l + 2j_3 + E_T^{\text{miss}}$	$2\ell + 2b + 2j_l + 2j_3/\ell + 2b + 2j_l + 2j_3 + E_T^{\text{miss}}$
$\tilde{e}$	$2\ell + 4j_l + 2j_3$	$2\ell + 2b + 2j_l + 2j_3$
$\tilde{\tau}_L\,(\tilde{\nu}_\tau)$	$2\tau + 4j_l + 2j_3/\tau + 4j_l + 2j_3 + E_T^{\text{miss}}$	$2\tau + 2b + 2j_l + 2j_3/\tau + 2b + 2j_l + 2j_3 + E_T^{\text{miss}}$
$\tilde{\tau}_R$	$2\tau + 4j_l + 2j_3$	$2\tau + 2b + 2j_l + 2j_3$
$\tilde{g}$	$2t + 4j_l$	$2t + 2b + 2j_l$
$\tilde{q}$	$2t + 6j_l$	$2t + 2b + 4j_l$
$\tilde{u}$	$2t + 6j_l$	$2t + 2b + 4j_l$
$\tilde{d}$	$2t + 2j_l$	$2t + 2b$
$\tilde{t}_L(\tilde{b}_L)$	$4j_l + 4j_3$	$2b + 2j_l + 4j_3$
$\tilde{t}_R$	$4j_l$	$2b + 2j_l$
$\tilde{b}_R$	$2t + 2b + 4j_l$	$2t + 2j_l$
$\tilde{B}$, $\tilde{W}$, $\tilde{H}$	$4j_l + 2j_3$	$2b + 2j_l + 2j_3$

3.3.3 LQD Tables

Lastly, we show the results for the $LQ\bar{D}$ case in Tables 3.6-3.11. The comments from before apply here. Analyzing the tables, we see that the $LQ\bar{D}$ scenarios can be completely covered through the following six searches:

1. $4j$
2. $2b + 2j + E_T^{\text{miss}}$
3. $1L + (2-6)j + E_T^{\text{miss}}$
4. $2L + (2-6)j + (E_T^{\text{miss}})$
5. $3L + 4j + E_T^{\text{miss}}$
6. $4L + 4j$

The color scheme is based on the number of charged leptons and jets: red (no charged leptons, four jets, without missing energy), blue (no charged leptons, four jets, with missing energy), yellow (one charged lepton), green (two charged leptons), purple (three charged leptons), and gray (four charged leptons).

As can be seen from the tables, $LQ\bar{D}$ operators result in a wide range of possible final states, typically including at least one lepton and several jets. Therefore, searches targeting a wide range of BSM models beyond RPV-SUSY can be sensitive, *e.g.*, searches for RPC-SUSY, leptoquarks, etc. It is important to consider whether one of the generation indices of the $L_iQ_j\bar{D}_k$ operator is 3 since this changes the experimental signature significantly. For example, searches explicitly requiring b-tagged jets typically are the most sensitive for $j,k = 3$. An

operator with $i = 3$ requires searches exploiting final states with τ leptons. The relevant existing searches for the $LQ\bar{D}$ coupling cover the final states of (1.) 4 jets [241–243], (2.) ≥ 4 jets (including b-tags) plus E_T^{miss} [186, 187], (3.) 1ℓ plus 2 jets [252, 253] or 1ℓ plus 6 jets [179, 188, 204, 205, 249, 250], (4.) 2ℓ-same-sign plus 2 jets [254], or 2ℓ-same-sign plus 6 jets [176, 182], or 2ℓ-opposite-sign plus 2 or more jets [170, 175, 181, 185, 250, 255–258], (5.) 3ℓ plus 4 jets [182, 195, 259], and (6.) 4ℓ plus 4 jets [195, 240].

It is important to note that for signatures 1. ($4j$) and 2. ($2b + 2j + E_T^{\text{miss}}$), the relevant searches target strong production cross-sections. As seen from Tables 3.7 to 3.11, these signatures arise from the decays $\tilde{\ell} \to jj$ and $\tilde{\chi}_1^0 \to \nu jb$ respectively. While the latter is experimentally less sensitive than the competing $\tilde{\chi}_1^0 \to \ell jt$ decay, phase-space effects due to the top-quark mass can lead to a strong suppression of channels involving t. In both cases, the existing analyses target strong production, via $\tilde{q} \to jj$ and $\tilde{g} \to bj\tilde{\chi}_1^0$, respectively,[11] and have no sensitivity to low masses and electroweak cross sections. We do note the special case of $\tilde{\chi}_1^0 \to \nu bb$, leading to the $4b$+E_T^{miss} final state which has already been explored for Higgsino production [260, 261]. However, crucially, the searches require an intermediate Higgs resonance which is not present in the RPV case.

Table 3.6: Characteristic signatures arising from LSP decays for $L_iQ_j\bar{D}_k$ operators. The first column depicts the LSPs. The second and third columns represent the signatures from *pair-production* of LSPs for the cases where the indices $i, j, k \in \{1, 2\}$, and where the indices $i, j \in \{1, 2\}$ and $k = 3$, respectively. For cases involving degenerate LSPs, *e.g.*, $\tilde{\ell}\,(\tilde{\nu})$, all pair combinations are considered. Further, only the relevant signatures are retained and we have introduced color-coding to improve the readability of the table; the details are in the main text.

LSP	**LQD**	**LQD$_3$**
$\tilde{\ell}\,(\tilde{\nu})$	$4j_l$	$2b + 2j_l$
$\tilde{e}$	$4\ell + 4j_l / 3\ell + 4j_l + E_T^{\text{miss}}$	$4\ell + 2b + 2j_l / 3\ell + 2b + 2j_l + E_T^{\text{miss}}$
$\tilde{\tau}_L\,(\tilde{\nu}_\tau)$	$2\ell + 2\tau + 4j_l / \ell + 2\tau + 4j_l + E_T^{\text{miss}}$ / $2\ell + \tau + 4j_l + E_T^{\text{miss}} / \ell + \tau + 4j_l + E_T^{\text{miss}}$	$2\ell + 2\tau + 2b + 2j_l / \ell + 2\tau + 2b + 2j_l + E_T^{\text{miss}}$ / $2\ell + \tau + 2b + 2j_l + E_T^{\text{miss}} / \ell + \tau + 2b + 2j_l + E_T^{\text{miss}}$
$\tilde{\tau}_R$	$2\ell + 2\tau + 4j_l / \ell + 2\tau + 4j_l + E_T^{\text{miss}}$	$2\ell + 2\tau + 2b + 2j_l / \ell + 2\tau + 2b + 2j_l + E_T^{\text{miss}}$
$\tilde{g}$	$2\ell + 4j_l / \ell + 4j_l + E_T^{\text{miss}}$	$2\ell + 2b + 2j_l / \ell + 2b + 2j_l + E_T^{\text{miss}}$
$\tilde{q}$	$2\ell + 2j_l$	$2\ell + 2b$
$\tilde{u}$	$2\ell + 6j_l / \ell + 6j_l + E_T^{\text{miss}}$	$2\ell + 2b + 4j_l / \ell + 2b + 4j_l + E_T^{\text{miss}}$
$\tilde{d}$	$2\ell + 2j_l / \ell + 2j_l + E_T^{\text{miss}}$	$2\ell + 2b + 4j_l / \ell + 2b + 4j_l + E_T^{\text{miss}}$
$\tilde{t}_L(\tilde{b}_L)$	$2\ell + 4j_l + 2j_3 / \ell + 4j_l + 2j_3 + E_T^{\text{miss}}$	$2\ell + 2b + 2j_l + 2j_3 / \ell + 2b + 2j_l + 2j_3 + E_T^{\text{miss}}$
$\tilde{t}_R$	$2\ell + 2t + 4j_l / \ell + 2t + 4j_l + E_T^{\text{miss}}$	$2\ell + 2t + 2b + 2j_l / \ell + 2t + 2b + 2j_l + E_T^{\text{miss}}$
$\tilde{b}_R$	$2\ell + 2b + 4j_l / \ell + 2b + 4j_l + E_T^{\text{miss}}$	$2\ell + 2j_l / \ell + 2j_l + E_T^{\text{miss}}$
$\tilde{B}$, $\tilde{W}$, $\tilde{H}$	$2\ell + 4j_l / \ell + 4j_l + E_T^{\text{miss}}$	$2\ell + 2b + 2j_l / \ell + 2b + 2j_l + E_T^{\text{miss}}$

[11] The scenario with an almost massless neutralino matches the $LQ\bar{D}$ signature of $\tilde{g} \to bj\nu$.

Table 3.7: Same as Table 3.6 but for $L_iQ_j\bar{D}_k$ operators with $i,k \in \{1,2\}$ and $j=3$.

LSP	$\mathbf{LQ_3D}$
$\tilde{\ell}\,(\tilde{\nu})$	$2j_l + 2j_3$
$\tilde{e}$	$4\ell + 2t + 2j_l / 3\ell + t + b + 2j_l + E_T^{\text{miss}} / 2\ell + 2b + 2j_l + E_T^{\text{miss}}$
$\tilde{\tau}_L\,(\tilde{\nu}_\tau)$	$2\ell + 2\tau + 2t + 2j_l / \ell + 2\tau + t + b + 2j_l + E_T^{\text{miss}} / 2\tau + 2b + 2j_l + E_T^{\text{miss}} / 2\ell + \tau + 2t + 2j_l + E_T^{\text{miss}} / \ell + \tau + t + b + 2j_l + E_T^{\text{miss}} / \tau + 2b + 2j_l + E_T^{\text{miss}}$
$\tilde{\tau}_R$	$2\ell + 2\tau + 2t + 2j_l / \ell + 2\tau + t + b + 2j_l + E_T^{\text{miss}} / 2\tau + 2b + 2j_l + E_T^{\text{miss}}$
$\tilde{g}$	$2\ell + 2t + 2j_l / \ell + t + b + 2j_l + E_T^{\text{miss}}$
$\tilde{q}$	$2\ell + 2t + 4j_l / \ell + t + b + 4j_l + E_T^{\text{miss}}$
$\tilde{u}$	$2\ell + 2t + 4j_l / \ell + t + b + 4j_l + E_T^{\text{miss}}$
$\tilde{d}$	$2\ell + 2t / \ell + t + b + E_T^{\text{miss}}$
$\tilde{t}_L(\tilde{b}_L)$	$2\ell + 2j_l$
$\tilde{t}_R$	$2\ell + 4t + 2j_l / \ell + 3t + b + 2j_l + E_T^{\text{miss}}$
$\tilde{b}_R$	$2\ell + 2t + 2b + 2j_l / \ell + t + 3b + 2j_l + E_T^{\text{miss}}$
$\tilde{B},\ \tilde{W},\ \tilde{H}$	$2\ell + 2j_l + 2j_3 / \ell + 2j_l + 2j_3 + E_T^{\text{miss}} / 2b + 2j_l + E_T^{\text{miss}}$

Table 3.8: Same as Table 3.6 but for $L_iQ_j\bar{D}_k$ operators with $j,k=3$ and $i \in \{1,2\}$.

LSP	$\mathbf{LQ_3D_3}$
$\tilde{\ell}\,(\tilde{\nu})$	$2b + 2j_3$
$\tilde{e}$	$4\ell + 2t + 2b / 3\ell + t + 3b + E_T^{\text{miss}} / 2\ell + 4b + E_T^{\text{miss}}$
$\tilde{\tau}_L\,(\tilde{\nu}_\tau)$	$2\ell + 2\tau + 2t + 2b / \ell + 2\tau + t + 3b + E_T^{\text{miss}} / 2\tau + 4b + E_T^{\text{miss}} / 2\ell + \tau + 2t + 2b + E_T^{\text{miss}} / \ell + \tau + t + 3b + E_T^{\text{miss}} / \tau + 4b + E_T^{\text{miss}}$
$\tilde{\tau}_R$	$2\ell + 2\tau + 2t + 2b / \ell + 2\tau + t + 3b + E_T^{\text{miss}} / 2\tau + 4b + E_T^{\text{miss}}$
$\tilde{g}$	$2\ell + 2t + 2b / \ell + t + 3b + E_T^{\text{miss}}$
$\tilde{q}$	$2\ell + 2t + 2b + 2j_l / \ell + t + 3b + 2j_l + E_T^{\text{miss}}$
$\tilde{u}$	$2\ell + 2t + 2b + 2j_l / \ell + t + 3b + 2j_l + E_T^{\text{miss}}$
$\tilde{d}$	$2\ell + 2t + 2b + 2j_l / \ell + t + 3b + 2j_l + E_T^{\text{miss}}$
$\tilde{t}_L(\tilde{b}_L)$	$2\ell + 2b$
$\tilde{t}_R$	$2\ell + 4t + 2b / \ell + 3t + 3b + E_T^{\text{miss}}$
$\tilde{b}_R$	$2\ell + 2t / \ell + t + b + E_T^{\text{miss}}$
$\tilde{B},\ \tilde{W},\ \tilde{H}$	$2\ell + 2b + 2j_3 / \ell + 2b + 2j_3 + E_T^{\text{miss}} / 4b + E_T^{\text{miss}}$

Table 3.9: Same as Table 3.6 but for $L_iQ_j\bar{D}_k$ operators with $j,k \in \{1,2\}$ and $i = 3$ (second column), and $i,k = 3$ and $j \in \{1,2\}$ (third column).

LSP	$\mathbf{L_3QD}$	$\mathbf{L_3QD_3}$
$\tilde{\ell}\,(\tilde{\nu})$	$2\ell+2\tau+4j_l/2\ell+\tau+4j_l+E_T^{\text{miss}}/$ $\ell+2\tau+4j_l+E_T^{\text{miss}}/\ell+\tau+4j_l+E_T^{\text{miss}}$	$2\ell+2\tau+2b+2j_l/2\ell+\tau+2b+2j_l+E_T^{\text{miss}}/$ $\ell+2\tau+2b+2j_l+E_T^{\text{miss}}/\ell+\tau+2b+2j_l+E_T^{\text{miss}}$
$\tilde{e}$	$2\ell+2\tau+4j_l/2\ell+\tau+4j_l+E_T^{\text{miss}}$	$2\ell+2\tau+2b+2j_l/2\ell+\tau+2b+2j_l+E_T^{\text{miss}}$
$\tilde{\tau}_L\,(\tilde{\nu}_\tau)$	$4j_l$	$2b+2j_l$
$\tilde{\tau}_R$	$4\tau+4j_l/3\tau+4j_l+E_T^{\text{miss}}$	$4\tau+2b+2j_l/3\tau+2b+2j_l+E_T^{\text{miss}}$
$\tilde{g}$	$2\tau+4j_l/\tau+4j_l+E_T^{\text{miss}}$	$2\tau+2b+2j_l/\tau+2b+2j_l+E_T^{\text{miss}}$
$\tilde{q}$	$2\tau+2j_l$	$2\tau+2b$
$\tilde{u}$	$2\tau+6j_l/\tau+6j_l+E_T^{\text{miss}}$	$2\tau+2b+4j_l/\tau+2b+4j_l+E_T^{\text{miss}}$
$\tilde{d}$	$2\tau+2j_l/\tau+2j_l+E_T^{\text{miss}}$	$2\tau+2b+4j_l/\tau+2b+4j_l+E_T^{\text{miss}}$
$\tilde{t}_L(\tilde{b}_L)$	$2\tau+4j_l+2j_3/\tau+4j_l+2j_3+E_T^{\text{miss}}$	$2\tau+2b+2j_l+2j_3/\tau+2b+2j_l+2j_3+E_T^{\text{miss}}$
$\tilde{t}_R$	$2\tau+2t+4j_l/\tau+2t+4j_l+E_T^{\text{miss}}$	$2\tau+2t+2b+2j_l/\tau+2t+2b+2j_l+E_T^{\text{miss}}$
$\tilde{b}_R$	$2\tau+2b+4j_l/\tau+2b+4j_l+E_T^{\text{miss}}$	$2\tau+2j_l/\tau+2j_l+E_T^{\text{miss}}$
$\tilde{B},\ \tilde{W},\ \tilde{H}$	$2\tau+4j_l/\tau+4j_l+E_T^{\text{miss}}$	$2\tau+2b+2j_l/\tau+2b+2j_l+E_T^{\text{miss}}$

Table 3.10: Same as Table 3.6 but for $L_iQ_j\bar{D}_k$ operators with $i,j = 3$ and $k \in \{1,2\}$.

LSP	$\mathbf{L_3Q_3D}$
$\tilde{\ell}\,(\tilde{\nu})$	$2\ell+2\tau+2t+2j_l/2\ell+\tau+t+b+2j_l+E_T^{\text{miss}}/2\ell+2b+2j_l+E_T^{\text{miss}}/\ell+2\tau+2t+2j_l+E_T^{\text{miss}}/$ $\ell+\tau+t+b+2j_l+E_T^{\text{miss}}/\ell+2b+2j_l+E_T^{\text{miss}}$
$\tilde{e}$	$2\ell+2\tau+2t+2j_l/2\ell+\tau+t+b+2j_l+E_T^{\text{miss}}/2\ell+2b+2j_l+E_T^{\text{miss}}$
$\tilde{\tau}_L\,(\tilde{\nu}_\tau)$	$2j_l+2j_3$
$\tilde{\tau}_R$	$4\tau+2t+2j_l/3\tau+t+b+2j_l+E_T^{\text{miss}}/2\tau+2b+2j_l+E_T^{\text{miss}}$
$\tilde{g}$	$2\tau+2t+2j_l/\tau+t+b+2j_l+E_T^{\text{miss}}$
$\tilde{q}$	$2\tau+2t+4j_l/\tau+t+b+4j_l+E_T^{\text{miss}}$
$\tilde{u}$	$2\tau+2t+4j_l/\tau+t+b+4j_l+E_T^{\text{miss}}$
$\tilde{d}$	$2\tau+2t/\tau+t+b+E_T^{\text{miss}}$
$\tilde{t}_L(\tilde{b}_L)$	$2\tau+2j_l$
$\tilde{t}_R$	$2\tau+4t+2j_l/\tau+3t+b+2j_l+E_T^{\text{miss}}$
$\tilde{b}_R$	$2\tau+2t+2b+2j_l/\tau+t+3b+2j_l+E_T^{\text{miss}}$
$\tilde{B},\ \tilde{W},\ \tilde{H}$	$2\tau+2j_l+2j_3/\tau+2j_l+2j_3+E_T^{\text{miss}}/2b+2j_l+E_T^{\text{miss}}$

Table 3.11: Same as Table 3.6 but for $L_iQ_j\bar{D}_k$ operators with $i,j,k=3$.

LSP	$\mathbf{L_3Q_3D_3}$
$\tilde{\ell}\,(\tilde{\nu})$	$2\ell+2\tau+2t+2b/2\ell+\tau+t+3b+E_T^{\text{miss}}/2\ell+4b+E_T^{\text{miss}}/\ell+2\tau+2t+2b+E_T^{\text{miss}}/\ell+\tau+t+3b+E_T^{\text{miss}}/\ell+4b+E_T^{\text{miss}}$
$\tilde{e}$	$2\ell+2\tau+2t+2b/2\ell+\tau+t+3b+E_T^{\text{miss}}/2\ell+4b+E_T^{\text{miss}}$
$\tilde{\tau}_L\,(\tilde{\nu}_\tau)$	$2b+2j_3$
$\tilde{\tau}_R$	$4\tau+2t+2b/3\tau+t+3b+E_T^{\text{miss}}/2\tau+4b+E_T^{\text{miss}}$
$\tilde{g}$	$2\tau+2t+2b/\tau+t+3b+E_T^{\text{miss}}$
$\tilde{q}$	$2\tau+2t+2b+2j_l/\tau+t+3b+2j_l+E_T^{\text{miss}}$
$\tilde{u}$	$2\tau+2t+2b+2j_l/\tau+t+3b+2j_l+E_T^{\text{miss}}$
$\tilde{d}$	$2\tau+2t+2b+2j_l/\tau+t+3b+2j_l+E_T^{\text{miss}}$
$\tilde{t}_L(\tilde{b}_L)$	$2\tau+2b$
$\tilde{t}_R$	$2\tau+4t+2b/\tau+3t+3b+E_T^{\text{miss}}$
$\tilde{b}_R$	$2\tau+2t/\tau+t+b+E_T^{\text{miss}}$
$\tilde{B},\ \tilde{W},\ \tilde{H}$	$2\tau+2b+2j_3/\tau+2b+2j_3+E_T^{\text{miss}}/4b+E_T^{\text{miss}}$

3.4 Sample Application of the Framework: LLE Couplings

3.4.1 Benchmark Scenarios

We now demonstrate the practical application of our framework by using it to calculate mass bounds on SUSY particles in a wide range of RPV scenarios. Throughout this section, for simplicity, we assume that the only non-zero RPV coupling corresponds to a single $LL\bar{E}$ operator, although – as mentioned – generalization to several non-zero RPV couplings is possible by combining the different rows of our signature tables. Further, we assume all mass eigenstates are aligned with the gauge eigenstates, except for the neutral Higgsinos which are assumed to be maximally mixed.

As discussed in Section 3.3, the signatures in our 'RPV Dictionary' have significant coverage through existing `ATLAS` and `CMS` searches, even if only indirectly. We can, therefore, reinterpret these searches in the context of RPV scenarios to set limits on the latter. In the $LL\bar{E}$ scenario, these can be comparable to or even more constraining than the MSSM limits.

In order to calculate the mass limits, we have simulated SUSY processes at leading order using the program `MadGraph5_aMC@NLO` [262] linked to `PYTHIA 8.2` [263]. We have employed the `UFO RPV-MSSM` model file available at Ref. [264]. The decays are computed under the narrow-width approximation. The branching ratios for two-body decays are computed by `MadGraph5_aMC@NLO`, while for higher-multiplicity decays – to save computational time – we set them by hand; the details of how we do this are given in Appendix B.1. The width is always set by hand to a small arbitrary value (smaller than the experimental resolution) such that the decay of the LSP remains prompt; under the narrow-width approximation, the results are independent of the number. `PYTHIA 8.2` then produces the final decayed and showered event samples. These are passed through `CheckMATE 2` [265–269] which uses

a database of several existing ATLAS and CMS analyses in order to determine whether the RPV-MSSM parameter point used to generate the event sample can be excluded or not.[12] Detector effects have been accounted for through the DELPHES 3 [271] detector simulation module linked with CheckMATE 2.

We now describe the various benchmark scenarios we study. These have been designed to cover what, we believe, should be all relevant possibilities for the $LL\bar{E}$ case, subject to our minimal assumptions.

Gluino LSP: The first set of scenarios we consider is with a gluino LSP. It is sufficient to consider only direct gluino-pair production since the cross-section is higher than any channel where the gluino LSP is produced in cascade decays (see discussion in Appendix B.2). Thus, in our simulation, we consider the rest of the spectrum to be decoupled; this gives us the most conservative, model-independent exclusion limits. However, we assume that, despite this decoupling, the gluino LSP still decays promptly; see Appendix B.1 for details on the specific decay modes chosen in the simulation. In the first three scenarios, we consider λ_{121} to be the only non-zero RPV operator. The characteristic signature for the gluino decay is $2\ell + 2j + E_T^{\text{miss}}$, *cf.* Table 3.2. Here j can be a light, top, or bottom jet depending on the nature of the virtual squark involved in the decay; the three scenarios target the possible dependence of the coverage on this choice. Next, to study how the results are affected if the RPV operator leads to more muons or taus instead of electrons, we consider three more scenarios corresponding to $\lambda_{122}, \lambda_{311}$, and λ_{313}, respectively, being the sole non-zero RPV couplings. The details of all gluino benchmarks have been summarized in Table 3.12.

Table 3.12: Details of our benchmarks: the first two columns depict the LSP and the production mode considered, respectively; the RPV coupling assumed to be non-zero is shown in the third column; the fourth column represents the possible decays of the LSP (these are split into two columns for better readability); the last column shows the notation we use for labeling the scenario.

LSP	**Production**	**Coupling**		LSP Decay	**Label**
$\tilde{g}$	Direct	λ_{121}	$2e + 2j_l + \nu_\mu$	$e + \mu + 2j_l + \nu_e$	$\mathrm{D}_{\tilde{g}}^{e\mu e}$
	Direct	λ_{121}	$2e + 2b + \nu_\mu$	$e + \mu + 2b + \nu_e$	$\mathrm{D}_{\tilde{g}}^{e\mu e-b}$
	Direct	λ_{121}	$2e + 2t + \nu_\mu$	$e + \mu + 2t + \nu_e$	$\mathrm{D}_{\tilde{g}}^{e\mu e-t}$
	Direct	λ_{122}	$2\mu + 2j_l + \nu_e$	$e + \mu + 2j_l + \nu_\mu$	$\mathrm{D}_{\tilde{g}}^{e\mu\mu}$
	Direct	λ_{311}	$2e + 2j_l + \nu_\tau$	$e + \tau + 2j_l + \nu_e$	$\mathrm{D}_{\tilde{g}}^{\tau ee}$
	Direct	λ_{313}	$2\tau + 2j_l + \nu_e$	$e + \tau + 2j_l + \nu_\tau$	$\mathrm{D}_{\tilde{g}}^{\tau e\tau}$

Squark LSPs: Similar to above, for squark LSP scenarios, we first consider only direct pair production with the other sparticles decoupled. Thus, we have selected two scenarios each

[12] We note that we limit ourselves to the analyses already implemented in CheckMATE 2 as of December 2022; the list of implemented analyses can be found at Ref. [270]. Some analyses explicitly targeting $LL\bar{E}$ models such as the most relevant SRs from Ref. [240] are not implemented. Despite this, we observe excellent coverage.

for the light-flavor squarks ($\tilde{q}$, $\tilde{u}$, $\tilde{d}$), and the heavy-flavor ones ($\tilde{q}_3$, $\tilde{t}$, $\tilde{b}$), corresponding to the couplings λ_{121} and λ_{313}.[13] All squarks within a particular scenario are considered mass-degenerate for simplicity.

For the squarks, cascade decays involving gluino production channels (pair as well as associated) can also be relevant since these can have a higher cross-section than the direct production channels, *cf.* the discussion in Appendix B.2. Thus, we include four more scenarios – covering the two couplings for each of the two squark groups – where the gluino and squarks are both kinematically accessible, while the rest of the spectrum is decoupled (again, in a way that the squarks still decay promptly according to branching ratios described in Appendix B.1). The corresponding results are presented as two-dimensional plots in the gluino mass vs. squark mass plane. The details of all the squark benchmarks have been summarized in Table 3.13.

Table 3.13: As in Table 3.12 but for the squark LSP benchmarks.

LSP	Production	Coupling		LSP Decay	Label
$\tilde{q}/\tilde{u}/\tilde{d}$	Direct $\tilde{g}$	λ_{121}	$2e + j_l + \nu_\mu$	$e + \mu + j_l + \nu_e$	$\mathrm{D}_{\tilde{q}}^{e\mu e}$ $\mathrm{I}_{\tilde{g}\to\tilde{q}}^{e\mu e}$
	Direct $\tilde{g}$	λ_{313}	$2\tau + j_l + \nu_e$	$e + \tau + j_l + \nu_\tau$	$\mathrm{D}_{\tilde{q}}^{\tau e\tau}$ $\mathrm{I}_{\tilde{g}\to\tilde{q}}^{\tau e\tau}$
$\tilde{q}_3/\tilde{t}/\tilde{b}$	Direct $\tilde{g}$	λ_{121}	$2e + j_3 + \nu_\mu$	$e + \mu + j_3 + \nu_e$	$\mathrm{D}_{\tilde{q}_3}^{e\mu e}$ $\mathrm{I}_{\tilde{g}\to\tilde{q}_3}^{e\mu e}$
	Direct $\tilde{g}$	λ_{313}	$2\tau + j_3 + \nu_e$	$e + \tau + j_3 + \nu_\tau$	$\mathrm{D}_{\tilde{q}_3}^{\tau e\tau}$ $\mathrm{I}_{\tilde{g}\to\tilde{q}_3}^{\tau e\tau}$

Electroweakino LSPs: For the electroweakinos, we study three sets of scenarios corresponding to the winos ($\tilde{W}$), the Higgsinos ($\tilde{H}$), or the bino ($\tilde{B}$) being the LSP(s), respectively.

For the winos and the higgsinos, as before, we look at scenarios focusing on the direct modes, as well as the relevant indirect modes mentioned in Appendix B.2. For winos, the latter includes production of gluinos, light-flavor squarks, or heavy-flavor squarks. However, the latter two scenarios have similar features, so we only focus on the light-flavor squarks. For the higgsinos, we include only production of gluinos and the heavy-flavor squarks since their coupling to the light-flavor squarks is suppressed.

For the bino, direct production is not relevant due to the small cross-section, and thus we only study indirect modes. This time, we need to consider the possibility of each of the other

[13] These couplings correspond to the two extreme cases: maximum and minimum number of light leptons in the final state. For the remaining scenarios we will only consider these cases; the results for the other coupling configurations can be interpolated from the gluino LSP results.

SUSY particles being the parent: this includes the colored sector, the winos, the Higgsinos, and the sleptons.

As before, apart from the LSP(s) and the relevant parent sparticle(s), all other SUSY fields are considered decoupled, in a way that the LSP decay remains prompt. We study scenarios corresponding to both λ_{121} and λ_{313}. The details for all benchmarks corresponding to electroweakino LSPs have been summarized in Table 3.14.

Slepton LSPs: Finally, we have the slepton LSP scenarios. For each case – light-flavor sleptons ($\tilde{\ell}/\tilde{\nu}/\tilde{e}$), and heavy-flavor sleptons ($\tilde{\tau}_L/\tilde{\nu}_\tau/\tilde{\tau}_R$) – we study direct and indirect production, once again for the couplings λ_{121} and λ_{313}. The relevant indirect modes include every sparticle except the Bino, *cf.* discussion in Appendix B.2. We only study scenarios with $\tilde{g}$ or $\tilde{W}$ parents; results for other colored sparticles or electroweakinos can be interpolated.

Unlike sparticles considered so far, sleptons can couple directly to the $LL\bar{E}$ operators, depending on the flavor configuration. This can significantly affect the decay modes for a given slepton. To study this effect, we also include scenarios with non-zero λ_{122} and λ_{311} for both slepton classes. The details of the slepton benchmarks are summarized in Table 3.15.

Table 3.14: As in Table 3.12 but for the electroweakino LSP benchmarks.

LSP	Production	Coupling		LSP Decay	Label
$\tilde{W}$	Direct	λ_{121}	$2e+\nu_\mu/2e+\mu$	$e+\mu+\nu_e/e+\nu_e+\nu_\mu$	$\mathrm{D}^{e\mu e}_{\tilde{W}}$
	$\tilde{g}$				$\mathrm{I}^{e\mu e}_{\tilde{g}\to\tilde{W}}$
	$\tilde{q}/\tilde{u}/\tilde{d}$				$\mathrm{I}^{e\mu e}_{\tilde{q}\to\tilde{W}}$
	Direct	λ_{313}	$2\tau+\nu_e/e+2\tau$	$e+\tau+\nu_\tau/\tau+\nu_e+\nu_\tau$	$\mathrm{D}^{\tau e\tau}_{\tilde{W}}$
	$\tilde{g}$				$\mathrm{I}^{\tau e\tau}_{\tilde{g}\to\tilde{W}}$
	$\tilde{q}/\tilde{u}/\tilde{d}$				$\mathrm{I}^{\tau e\tau}_{\tilde{q}\to\tilde{W}}$
$\tilde{H}$	Direct	λ_{121}	$2e+V+\nu_\mu$	$e+\mu+V+\nu_e$	$\mathrm{D}^{e\mu e}_{\tilde{H}}$
	$\tilde{g}$				$\mathrm{I}^{e\mu e}_{\tilde{g}\to\tilde{H}}$
	$\tilde{q}_3/\tilde{t}/\tilde{b}$				$\mathrm{I}^{e\mu e}_{\tilde{q}_3\to\tilde{H}}$
	Direct	λ_{313}	$2\tau+V+\nu_e$	$e+\tau+V+\nu_\tau$	$\mathrm{D}^{\tau e\tau}_{\tilde{H}}$
	$\tilde{g}$				$\mathrm{I}^{\tau e\tau}_{\tilde{g}\to\tilde{H}}$
	$\tilde{q}_3/\tilde{t}/\tilde{b}$				$\mathrm{I}^{\tau e\tau}_{\tilde{q}_3\to\tilde{H}}$
$\tilde{B}$	$\tilde{g}$	λ_{121}	$2e+\nu_\mu$	$e+\mu+\nu_e$	$\mathrm{I}^{e\mu e}_{\tilde{g}\to\tilde{B}}$
	$\tilde{q}/\tilde{u}/\tilde{d}$				$\mathrm{I}^{e\mu e}_{\tilde{q}\to\tilde{B}}$
	$\tilde{q}_3/\tilde{t}/\tilde{b}$				$\mathrm{I}^{e\mu e}_{\tilde{q}_3\to\tilde{B}}$
	$\tilde{\ell}/\tilde{\nu}/\tilde{e}$				$\mathrm{I}^{e\mu e}_{\tilde{\ell}\to\tilde{B}}$
	$\tilde{\tau}_L/\tilde{\nu}_\tau/\tilde{\tau}_R$				$\mathrm{I}^{e\mu e}_{\tilde{\tau}\to\tilde{B}}$
	$\tilde{W}$				$\mathrm{I}^{e\mu e}_{\tilde{W}\to\tilde{B}}$
	$\tilde{H}$				$\mathrm{I}^{e\mu e}_{\tilde{H}\to\tilde{B}}$
	$\tilde{g}$	λ_{313}	$2\tau+\nu_e$	$e+\tau+\nu_\tau$	$\mathrm{I}^{\tau e\tau}_{\tilde{g}\to\tilde{B}}$
	$\tilde{q}/\tilde{u}/\tilde{d}$				$\mathrm{I}^{\tau e\tau}_{\tilde{q}\to\tilde{B}}$
	$\tilde{q}_3/\tilde{t}/\tilde{b}$				$\mathrm{I}^{\tau e\tau}_{\tilde{q}_3\to\tilde{B}}$
	$\tilde{\ell}/\tilde{\nu}/\tilde{e}$				$\mathrm{I}^{\tau e\tau}_{\tilde{\ell}\to\tilde{B}}$
	$\tilde{\tau}_L/\tilde{\nu}_\tau/\tilde{\tau}_R$				$\mathrm{I}^{\tau e\tau}_{\tilde{\tau}\to\tilde{B}}$
	$\tilde{W}$				$\mathrm{I}^{\tau e\tau}_{\tilde{W}\to\tilde{B}}$
	$\tilde{H}$				$\mathrm{I}^{\tau e\tau}_{\tilde{H}\to\tilde{B}}$

Table 3.15: As in Table 3.12 but for the slepton LSP benchmarks. For brevity, we skip showing decay modes explicitly (indicated by $*$) for some sleptons that do not couple directly to the relevant RPV operator (*e.g.*, $\tilde{\mu}_R$ LSP with λ_{121}). However, the details of how we include these modes in our simulations can be found in Appendix B.1.

LSP	**Production**	**Coupling**		LSP Decay	**Label**
$\tilde{\ell}/\tilde{\nu}/\tilde{e}$	Direct				$\mathrm{D}^{e\mu e}_{\tilde{\ell}}$
	$\tilde{g}$	λ_{121}	$2e/e+\mu$	$e+\nu_e/e+\nu_\mu$	$\mathrm{I}^{e\mu e}_{\tilde{g}\to\tilde{\ell}}$
	$\tilde{W}$		$\mu+\nu_e$	$*$	$\mathrm{I}^{e\mu e}_{\tilde{W}\to\tilde{\ell}}$
	Direct				$\mathrm{D}^{\tau e\tau}_{\tilde{\ell}}$
	$\tilde{g}$	λ_{313}	$2\tau/\tau+\nu_\tau$	$*$	$\mathrm{I}^{\tau e\tau}_{\tilde{g}\to\tilde{\ell}}$
	$\tilde{W}$				$\mathrm{I}^{\tau e\tau}_{\tilde{W}\to\tilde{\ell}}$
	Direct	λ_{122}	$2\mu/e+\mu/e+\nu_\mu$	$\mu+\nu_e/\mu+\nu_\mu/*$	$\mathrm{D}^{e\mu\mu}_{\tilde{\ell}}$
	Direct	λ_{311}	$e+\tau/e+\nu_\tau$	$\tau+\nu_e/*$	$\mathrm{D}^{\tau ee}_{\tilde{\ell}}$
$\tilde{\tau}_L/\tilde{\nu}_\tau/\tilde{\tau}_R$	Direct				$\mathrm{D}^{e\mu e}_{\tilde{\tau}}$
	$\tilde{g}$	λ_{121}	$2e+\tau+\nu_\mu$	$2e+\nu_\mu+\nu_\tau$	$\mathrm{I}^{e\mu e}_{\tilde{g}\to\tilde{\tau}}$
	$\tilde{W}$		$e+\mu+\tau+\nu_e$	$e+\mu+\nu_e+\nu_\tau$	$\mathrm{I}^{e\mu e}_{\tilde{W}\to\tilde{\tau}}$
	Direct				$\mathrm{D}^{\tau e\tau}_{\tilde{\tau}}$
	$\tilde{g}$	λ_{313}	$e+\tau/e+\nu_\tau$	$\tau+\nu_e$	$\mathrm{I}^{\tau e\tau}_{\tilde{g}\to\tilde{\tau}}$
	$\tilde{W}$				$\mathrm{I}^{\tau e\tau}_{\tilde{W}\to\tilde{\tau}}$
	Direct	λ_{122}	$2\mu+\tau+\nu_e/e+\mu+\tau+\nu_\mu$	$2\mu+\nu_e+\nu_\tau/e+\mu+\nu_\mu+\nu_\tau$	$\mathrm{D}^{e\mu\mu}_{\tilde{\tau}}$
	Direct	λ_{311}	$2e/e+\nu_e$	$2e+\tau+\nu_\tau/e+2\tau+\nu_e$	$\mathrm{D}^{\tau ee}_{\tilde{\tau}}$

3.4.2 Results

Before presenting the numerical results of our simulations, we stress one important detail: even though our benchmarks correspond to simple scenarios where all sparticles other than the LSP (and NLSP) are decoupled, we expect our results to be more general. Since the characteristic signature from the LSP decay – which provides the exclusion, as we show below – is independent of the spectrum details, the sensitivity should only be slightly modified for scenarios with arbitrary sparticle mass spectra, as long as the objects in the characteristic topology do not become too soft.

We now discuss our results. All relevant details for the `ATLAS` and `CMS` searches implemented in `CheckMATE 2` that show sensitivity to our scenarios have been summarized in Table 3.16 for reference. This list is merely meant to illustrate the searches with the strongest sensitivity and is not exhaustive. When there are multiple overlapping searches offering comparable sensitivity, we have omitted some of them.

Table 3.16: Summary of the most sensitive searches in our numerical simulations. The first column lists existing `ATLAS` and `CMS` searches providing sensitivity and our shorthand notation for each; the second column summarizes the relevant cuts; and the last column refers to the scenario labels presented in Tables 3.12-3.15. We have color-coded the labels according to the final state topologies of Section 3.3: $3L + E_T^{\rm miss}$, $4L + (0-4)j + E_T^{\rm miss}$, and $5L + E_T^{\rm miss}$. The same searches also constrain the $\mathrm{I}_{\tilde{x}\to\tilde{p}}$ scenarios (not shown here).

Reference and search region	Representative cuts	Most sensitive for
`CMS-ewk-4`ℓ [196] SR **G05**	$\geq 4\ell$, $0b$, $E_T^{\rm miss}$	$D^{e\mu e}_{\tilde{g}}$, $D^{e\mu\mu}_{\tilde{g}}$, $D^{e\mu e}_{\tilde{q},\tilde{W},\tilde{H}}$, $D^{\tau ee}_{\tilde{\ell}}$, $D^{e\mu e}_{\tilde{\tau}}$, $D^{e\mu\mu}_{\tilde{\tau}}$
`ATLAS-gluino-SS/3`ℓ [176] SR **Rpv2L**	$\geq 2\ell$, $\geq 6j$	$D^{e\mu e}_{\tilde{g}}$, $D^{e\mu\mu}_{\tilde{g}}$, $D^{e\mu e-b}_{\tilde{g}}$, $D^{e\mu e-t}_{\tilde{g}}$, $D^{\tau ee}_{\tilde{g}}$, $D^{e\mu e}_{\tilde{q}_3}$
`ATLAS-RPV-1`ℓ`/SS` [204] SR **SS-6j100-0b**	$\geq 2\ell$, $\geq 6j$, $0b$	$D^{\tau ee}_{\tilde{g}}$, $D^{\tau e\tau}_{\tilde{g}}$, $D^{\tau e\tau}_{\tilde{q}}$
`ATLAS-gluino-SS/3`ℓ`-1b` [272] SR **Rpc3L1bH**	$\geq 3\ell$, $\geq 4j$, $\geq 1b$, $E_T^{\rm miss}$	$D^{e\mu e}_{\tilde{q}_3}$, $D^{\tau e\tau}_{\tilde{q}_3}$
`CMS-ewk-2`$\tau 2\ell$ [196] SR **K03**	2ℓ, 2τ, $E_T^{\rm miss}$	$D^{\tau e\tau}_{\tilde{W}}$, $D^{\tau e\tau}_{\tilde{H}}$
`CMS-ewk-3`ℓ [196] SR **A44**	3ℓ, $E_T^{\rm miss}$	$D^{e\mu e}_{\tilde{\ell}}$, $D^{e\mu\mu}_{\tilde{\ell}}$, $D^{\tau ee}_{\tilde{\tau}}$
`CMS-ewk-1`$\tau 3\ell$ [196] SR **I04**	3ℓ, 1τ, $E_T^{\rm miss}$	$D^{\tau e\tau}_{\tilde{\ell}}$
`CMS-ewk-2`$\tau 1\ell$ [196] SR **F12**	1ℓ, 2τ, $E_T^{\rm miss}$	$D^{\tau e\tau}_{\tilde{\tau}}$

Direct Production

Fig. 3.2 shows a summary of the mass limits corresponding to 95% confidence level for the direct-production scenarios, *i.e.*, all the $\mathrm{D}_{\tilde{p}}$ scenarios from Tables 3.12-3.15, where $\tilde{p}$ stands for the relevant LSP. The rest of the spectrum is assumed to be decoupled in these benchmarks, while the LSP decays remain prompt. We see that the exclusion limits are comparable to the current mass bounds corresponding to the regular MSSM (see, for instance, Ref. [57]). We now discuss the results in more detail in the following paragraphs.

The $\tilde{g}$-LSP scenarios can be ruled out up to about $m_{\tilde{g}} \sim 2.1 - 2.4\,\mathrm{TeV}$, with the weaker limits corresponding to cases where the λ_{ijk} coupling involves third-generation indices. The strongest limit is achieved for scenarios involving couplings to light leptons and decay via off-shell top squarks. The signature from pair production for the gluino benchmarks is $4L + 4j + E_T^{\rm miss}$. In general, the strongest sensitivity comes, as expected, from multilepton

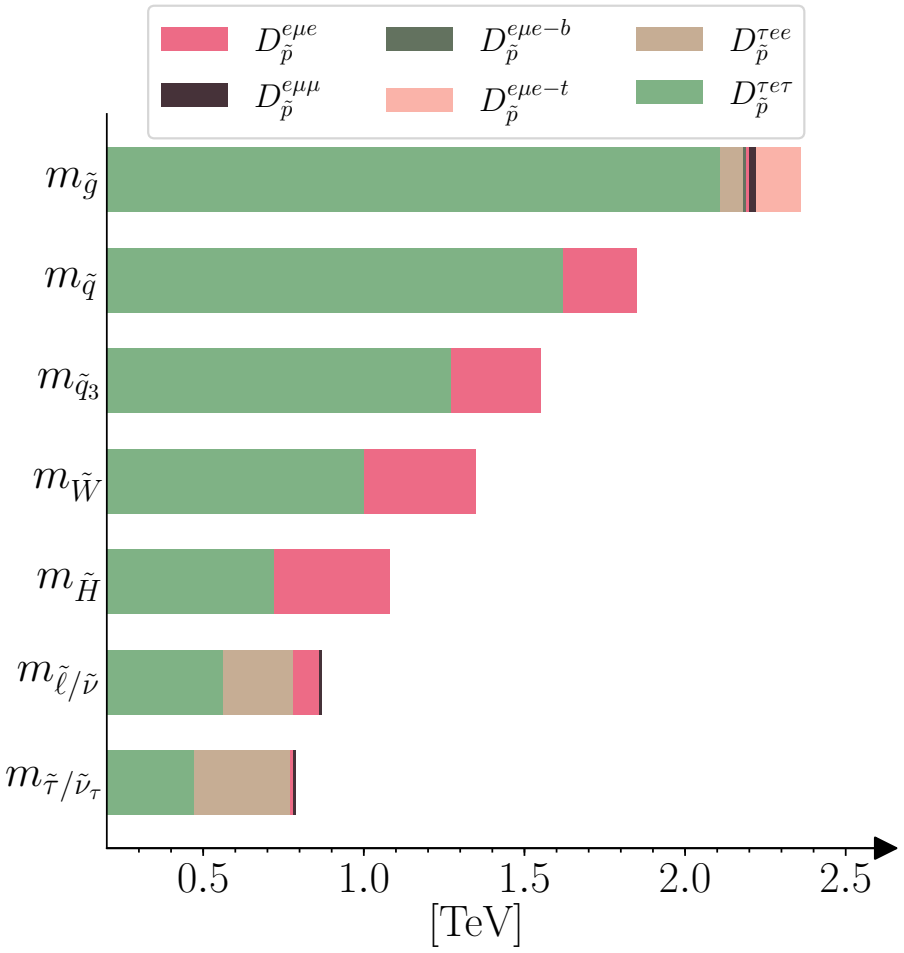

Figure 3.2: 95% confidence-level mass-exclusion limits for various LSPs corresponding to direct pair production. In each scenario, all sparticles other than the LSP(s) ($\tilde{p}$) are assumed to be decoupled, while the LSP decays are still prompt.

searches, especially `CMS-ewk-4`ℓ and `ATLAS-gluino-SS/3`ℓ.[14] In scenarios with heavy-flavor squarks, $\mathrm{D}_{\tilde{g}}^{e\mu e-b}$ and $\mathrm{D}_{\tilde{g}}^{e\mu e-t}$, `CMS-ewk-4`$\ell$ shows a weaker sensitivity due to the veto of b-jets. Finally, for couplings that involve τ leptons, $\mathrm{D}_{\tilde{g}}^{\tau ee}$ and $\mathrm{D}_{\tilde{g}}^{\tau e\tau}$, the most relevant analyses are `ATLAS-gluino-SS/3`ℓ and `ATLAS-RPV-1`ℓ`/SS`. Both searches offer sensitivity despite the fact that they focus only on light leptons. This is due to the fraction of gluino decays into electrons (*cf.* Table 3.12), and the leptonic decay of taus. The hadronic decays of taus are reconstructed as additional jets which satisfy the jet multiplicity requirement of both searches. None of the searches are optimized for our signal but they still provide great sensitivity.

For the squarks and the electroweakinos, the final states are similar to the gluino case, albeit with fewer jets: $4L + (0-2)j + E_T^{\mathrm{miss}}$. The most stringent limits for the $\mathrm{D}_{\tilde{p}}^{e\mu e}$ scenarios are provided by `CMS-ewk-4`ℓ: $m_{\tilde{q}} \gtrsim 1.85\,\mathrm{TeV}$, $m_{\tilde{W}} \gtrsim 1.35\,\mathrm{TeV}$, $m_{\tilde{H}} \gtrsim 1.1\,\mathrm{TeV}$. The reduced jet multiplicity limits the sensitivity of `ATLAS-gluino-SS/3`ℓ and `ATLAS-RPV-1`ℓ`/SS`. The $\mathrm{D}_{\tilde{W}}^{\tau e\tau}$

[14] See Table 3.16 for the notation we employ for searches.

and $\mathrm{D}_{\tilde{H}}^{\tau e\tau}$ scenarios are now instead covered by `CMS-ewk-2`τ`2`ℓ, a search explicitly targeting two hadronic taus, leading to the limits, $m_{\tilde{W}} \gtrsim 1\,\text{TeV}$ and $m_{\tilde{H}} \gtrsim 720\,\text{GeV}$. However, similar to the gluino case, `ATLAS-RPV-1`ℓ`/SS` is the most sensitive for $\mathrm{D}_{\tilde{q}}^{\tau e\tau}$ and rules out this scenario up to $m_{\tilde{q}} \approx 1.6\,\text{TeV}$.

The production of stops and sbottoms is special due to the presence of additional b jets, which are vetoed by `CMS-ewk-4`ℓ and `ATLAS-RPV-1`ℓ`/SS`. Thus, the best limits in this case come from `ATLAS-gluino-SS/3`ℓ`-1b` and `ATLAS-gluino-SS/3`ℓ for $\mathrm{D}_{\tilde{q}_3}^{e\mu e}$ ($m_{\tilde{q}_3} \gtrsim 1.55\,\text{TeV}$) and $\mathrm{D}_{\tilde{q}_3}^{\tau e\tau}$ ($m_{\tilde{q}_3} \gtrsim 1.3\,\text{TeV}$).

Finally, we have the slepton-LSP scenarios. For $\tilde{\ell}/\tilde{\nu}/\tilde{e}$, the exclusion limits lie in the broad range $m_{\tilde{\ell}} \sim 560 - 860\,\text{GeV}$. The most constraining search for scenarios $D_{\tilde{\ell}}^{e\mu e}$ and $D_{\tilde{\ell}}^{e\mu\mu}$ turns out to be `CMS-ewk-3`ℓ. This search matches the $3L + E_T^{\text{miss}}$ topology from $\tilde{\ell}\tilde{\nu}$ production, as listed in Table 3.2. For scenarios $D_{\tilde{\ell}}^{\tau ee}$ and $D_{\tilde{\ell}}^{\tau e\tau}$, the most relevant searches are `CMS-ewk-4`ℓ and `CMS-ewk-1`τ`3`ℓ, respectively. The latter needs at least three light leptons and at least one hadronic tau.

In the case of $\tilde{\tau}_L/\tilde{\nu}_\tau/\tilde{\tau}_R$, a large gap in sensitivity is observed between scenarios $D_{\tilde{\tau}}^{e\mu e}$, $D_{\tilde{\tau}}^{e\mu\mu}$, and $D_{\tilde{\tau}}^{\tau ee}$ which are excluded up to $m_{\tilde{\tau}} \sim 780 - 790\,\text{GeV}$; and the $D_{\tilde{\tau}}^{\tau e\tau}$ scenario with a reach of just $m_{\tilde{\tau}} \gtrsim 470\,\text{GeV}$. The former are covered by `CMS-ewk-4`ℓ and `CMS-ewk-3`ℓ, while the latter is targeted by `CMS-ewk-2`τ`1`ℓ. The topologies targeted by all the above search regions match those in Tables 3.2-3.3.

Cascade Decays

We next look at the results for the indirect-production/cascade-decay scenarios, *i.e.*, all the $\mathrm{I}_{\tilde{x}\to\tilde{p}}$ benchmarks from Tables 3.12-3.15, where $\tilde{p}$ is the LSP and $\tilde{x}$ denotes the directly produced parent particle decaying into the LSP. Cascade decays are especially important for scenarios with a bino LSP, where direct production is irrelevant. For all other LSP types, the limits from direct LSP production (corresponding to $D_{\tilde{p}}$) are also taken into account.

In general, exclusion limits are mostly independent of the LSP mass (with a few exceptions) as the signal regions have high acceptance and the limit is driven by the production cross-section. A loss in sensitivity is observed in regions with small mass splittings only for models where the most sensitive signal region requires additional jets. In the bino scenarios, a loss in sensitivity is also observed for low LSP masses as its decay products carry energies that are too low to survive the search region cuts. This effect is not observed for other scenarios as the direct production of LSP becomes dominant for lower masses.

Squark LSPs: In Fig. 3.3, we show the exclusion limits for $\tilde{q}/\tilde{u}/\tilde{d}$-LSPs (Fig. 3.3(a)) and $\tilde{q}_3/\tilde{t}/\tilde{b}$-LSPs (Fig. 3.3(b)) for a non-decoupled gluino. The relevant production processes are gluino-gluino, squark-squark, and associated gluino-squark production, followed by the decay of the gluino into the squark LSP(s) and a jet, and finally the LSP decay via the RPV operator into $2L + j + E_T^{\text{miss}}$.[15] The phase-space region $m_{\tilde{g}} < m_{\tilde{q}}$ ($m_{\tilde{g}} < m_{\tilde{q}_3} + m_t$) is kinematically disallowed[16] in the light-flavor (heavy-flavor) scenario, where we have neglected

[15] See Appendix B.1 for a detailed discussion on the specific decay modes we pick for each simulation.

[16] Technically, for the heavy-flavor scenario, the region $m_{\tilde{q}_3} \leq m_{\tilde{g}} < m_{\tilde{q}_3} + m_t$ lets the gluino decay into a sbottom (ignoring the b-quark mass), and is allowed. However, for simplicity, we will ignore this here.

the masses of all SM fermions except the top quark. These regions are depicted in gray in the plot.

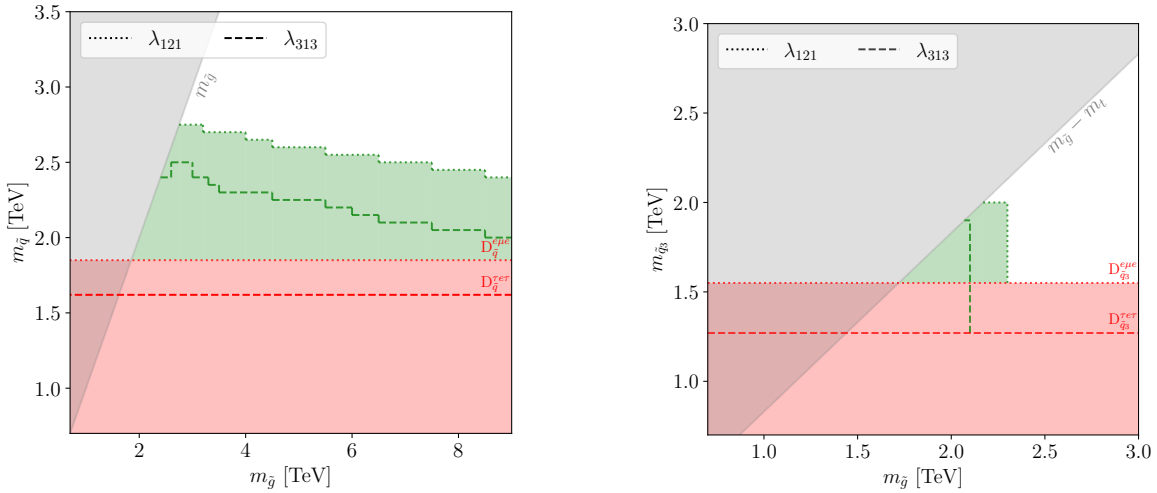

(a) $\tilde{q}/\tilde{u}/\tilde{d}$-LSPs with non-decoupled $\tilde{g}$.

(b) $\tilde{q}_3/\tilde{t}/\tilde{b}$-LSPs with non-decoupled $\tilde{g}$.

Figure 3.3: Exclusion regions (in green) corresponding to 95% confidence level for the $I_{\tilde{g}\to\tilde{q}}$ (left) and $I_{\tilde{g}\to\tilde{q}_3}$ (right) scenarios. The bounds of Fig. 3.2 from direct squark production also apply to the scenario and are shown in red. The gray region is kinematically disallowed in the scenario. The dotted (dashed) contours correspond to coupling λ_{121} (λ_{313}).

From Fig. 3.3(a), we see that $I_{\tilde{g}\to\tilde{q}}$ can be excluded roughly up to the kinematic limit as long as we are below the threshold for $\tilde{g}\tilde{g}$ production, *cf.* Fig. 3.2. However, even above this threshold, we can exclude large regions of the parameter space that lie beyond the bounds from direct squark-pair production with a decoupled gluino. For instance, we see that even with $m_{\tilde{g}} \sim 8\,\text{TeV}$, we get higher exclusion in the squark mass compared to the limit coming from $D_{\tilde{q}}$ (shown in red in the figure). This is due to two reasons. First, the associated-production channel (involving a single gluino) can stay kinematically accessible for longer. More importantly, a non-decoupled gluino significantly boosts direct squark-pair production cross-sections through its t-channel contributions [273]. For very high masses, the gluino is essentially decoupled and the limits start converging, *i.e.*, the scenarios reduce to the $D_{\tilde{q}}$ cases.

For Fig. 3.3(b), the exclusion limits behave differently. For both couplings, roughly all kinematically viable regions can be excluded up to the corresponding $m_{\tilde{g}}$ limits of Fig. 3.2. However, the limits reduce sharply to the $D_{\tilde{q}_3}$ bounds beyond this. For third-generation squarks, associated production as well as the boost in squark-squark cross-sections due to non-decoupled gluinos are suppressed by the small parton distribution functions (PDFs) for the heavy quarks inside the proton. Thus, as soon as gluino-pair production becomes kinematically inaccessible, the scenarios reduce to the $D_{\tilde{q}_3}$ cases.

Electroweakino LSPs: We next show the results for wino-LSP production with a non-decoupled gluino in Fig. 3.4(a) and non-decoupled light-flavor squarks in Fig. 3.4(b).

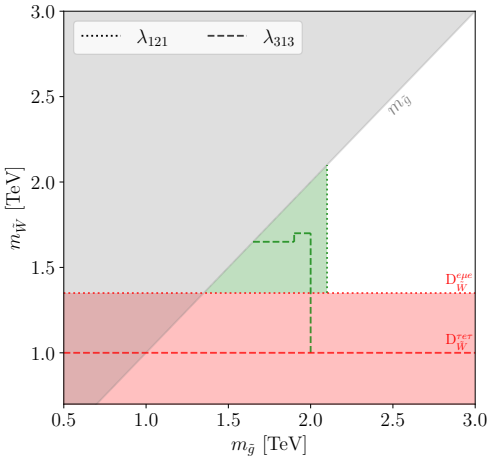

(a) $\tilde{W}$ LSP with non-decoupled $\tilde{g}$.

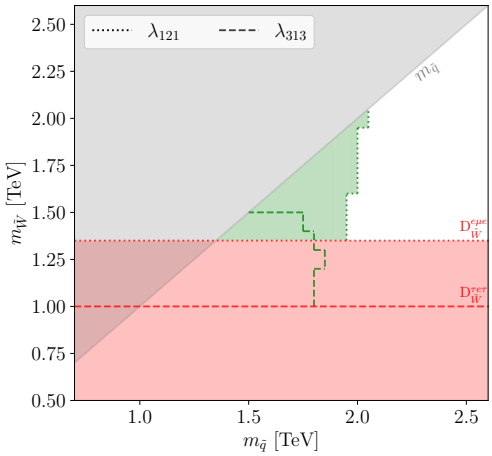

(b) $\tilde{W}$ LSP with non-decoupled $\tilde{q}/\tilde{u}/\tilde{d}$.

Figure 3.4: As in Fig. 3.3 but for the $I_{\tilde{g}\to\tilde{W}}$ (left) and $I_{\tilde{q}\to\tilde{W}}$ (right) scenarios.

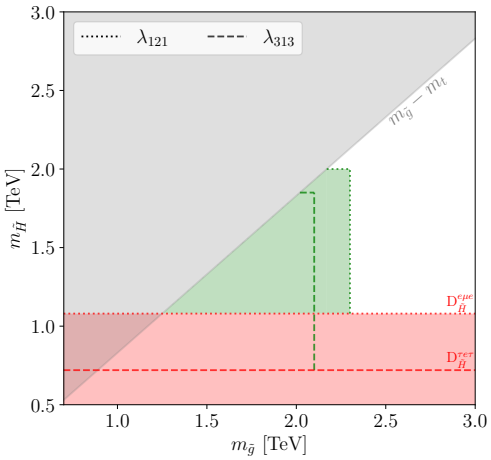

(a) $\tilde{H}$ LSP with non-decoupled $\tilde{g}$.

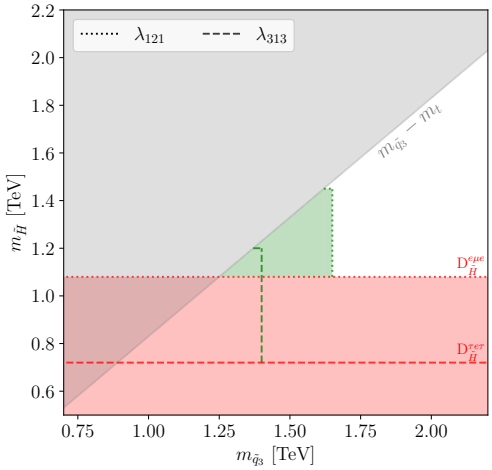

(b) $\tilde{H}$ LSP with non-decoupled $\tilde{q}_3/\tilde{t}/\tilde{b}$.

Figure 3.5: As in Fig. 3.3 but for the $I_{\tilde{g}\to\tilde{H}}$ (left) and $I_{\tilde{q}_3\to\tilde{H}}$ (right) scenarios.

For the gluino case, we see features similar to Fig. 3.3(b). For both couplings, all phase-space regions almost up to the gluino-pair production threshold can be ruled out. Beyond this, the results from $D_{\tilde{W}}$ apply. One interesting feature is the flattening of the exclusion contour for λ_{313} at $m_{\tilde{W}} \sim 1.7\,\text{TeV}$ for gluino masses, $m_{\tilde{g}} \sim 1.7 - 2\,\text{TeV}$. This reduction in sensitivity occurs because the cuts in `ATLAS-RPV-1ℓ/SS` place a high demand on the transverse momentum of the six required jets, $p_{\text{T}} > 100\,\text{GeV}$. If the wino and gluino are too close in mass, the jets produced in the gauge decay of the latter may not pass these requirements.

Fig. 3.4(b) is more interesting. We again see that the parameter space roughly up to the squark-production thresholds can be ruled out and we observe the flattening effect mentioned

above. However, we also see a new effect. The exclusion limit slightly weakens as we move lower in wino mass. This is clearly seen for the λ_{121} case but the reduction in sensitivity occurs for both couplings throughout the phase space. This is because squark-pair production can also occur via t-channel wino exchange which can interfere negatively with the QCD contribution [274]; this interference term is bigger for lighter winos.

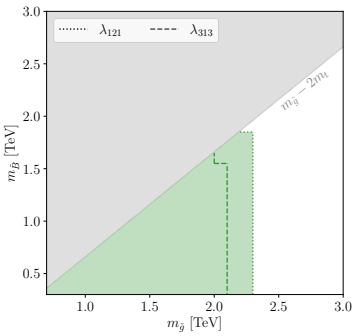

(a) $\tilde{B}$ LSP with non-decoupled $\tilde{g}$.

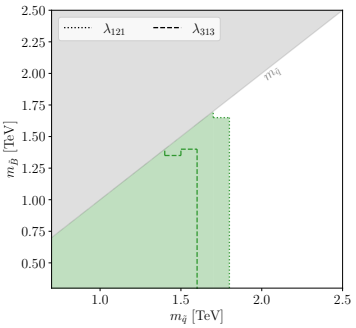

(b) $\tilde{B}$ LSP with non-decoupled $\tilde{q}/\tilde{u}/\tilde{d}$.

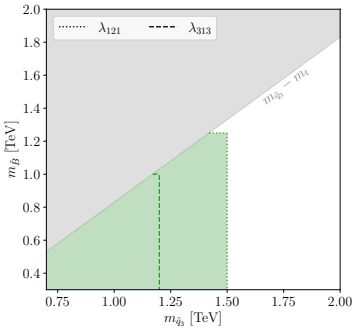

(c) $\tilde{B}$ LSP with non-decoupled $\tilde{q}_3/\tilde{t}/\tilde{b}$.

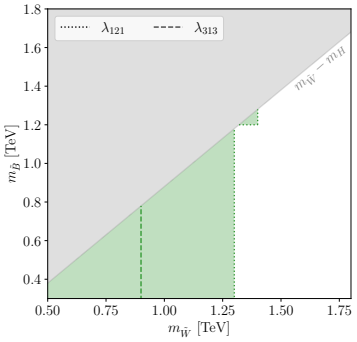

(d) $\tilde{B}$ LSP with non-decoupled $\tilde{W}$.

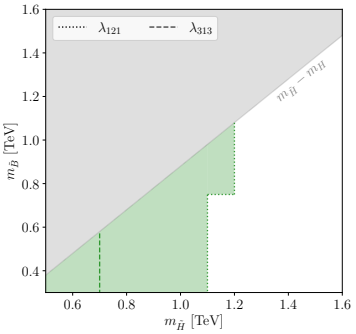

(e) $\tilde{B}$ LSP with non-decoupled $\tilde{H}$.

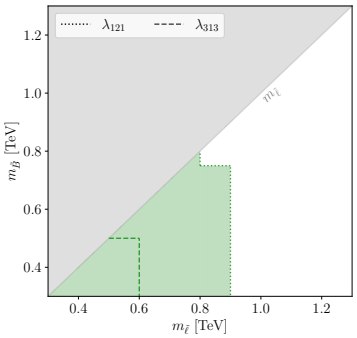

(f) $\tilde{B}$ LSP with non-decoupled $\tilde{\ell}/\tilde{\nu}/\tilde{e}$.

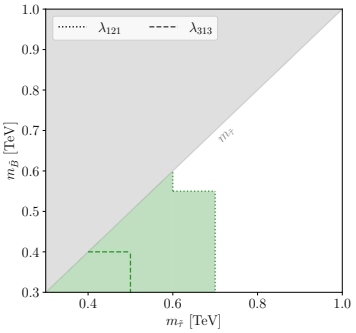

(g) $\tilde{B}$ LSP with non-decoupled $\tilde{\tau}_L/\tilde{\nu}_\tau/\tilde{\tau}_R$.

Figure 3.6: As in Fig. 3.3 but for the $I_{\tilde{\chi}^* \tilde{B}}$ scenarios.

Next, we show the Higgsino-LSP results for non-decoupled gluinos and non-decoupled third-generation squarks in Fig. 3.5(a) and Fig. 3.5(b), respectively. The exclusion limits

show features similar to the earlier cases and are straightforward to interpret. Beyond the pair-production thresholds for the parents, the benchmarks reduce to the respective $D_{\tilde{H}}$ scenarios.

The bino-LSP results are depicted in Fig. 3.6: these correspond to scenarios with gluinos (Fig. 3.6(a)), light-flavor squarks (Fig. 3.6(b)), heavy-flavor squarks (Fig. 3.6(c)), winos (Fig. 3.6(d)), Higgsinos (Fig. 3.6(e)), light-flavor sleptons (Fig. 3.6(f)), and third-generation sleptons (Fig. 3.6(g)). Generally, the exclusion limits cover almost the whole phase-space region up to the kinematic thresholds for the pair-production of the parents. However, there are a couple of features worth mentioning. First, we see the flattening effect, that we had described for Fig. 3.4, in scenarios $I^{\tau e\tau}_{\tilde{x}\to\tilde{B}}$ with $\tilde{x} = \tilde{q}, \tilde{\ell}, \tilde{\tau}$. The other interesting effect is the slight increase in sensitivity as the $\tilde{B}$ mass increases from very low masses to higher values. This effect can be most clearly seen in Fig. 3.6(e) but is a general feature in the other $\tilde{B}$ plots too. This happens due to the reason mentioned at the beginning of this subsection: for very low bino masses, the decay products are not energetic enough to pass the cuts of the analyses. We did not encounter it in the case of the other LSPs since the mass scales there were higher.

Slepton LSPs: Finally, we show the slepton-LSP results in Fig. 3.7. The exclusion limits can extend significantly in the cascade decay due to the much higher production cross-sections of other parent particles compared to direct slepton production.

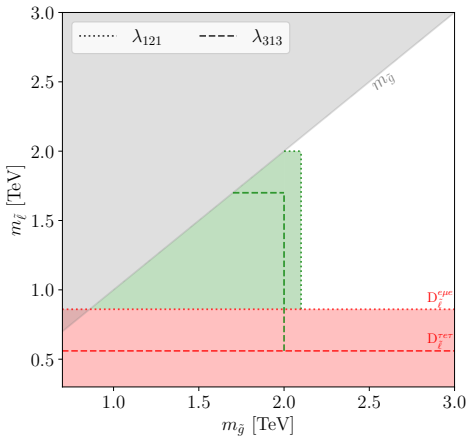

(a) $\tilde{\ell}/\tilde{\nu}/\tilde{e}$ LSPs with non-decoupled $\tilde{g}$.

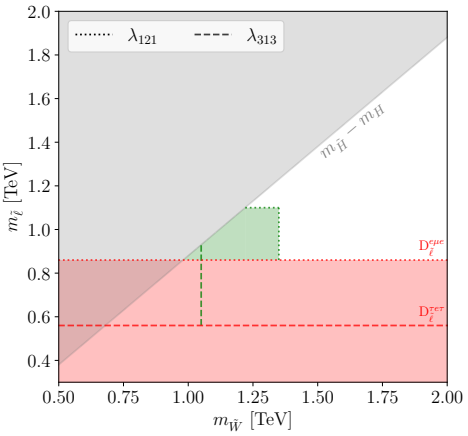

(b) $\tilde{\ell}/\tilde{\nu}/\tilde{e}$ LSPs with non-decoupled $\tilde{W}$.

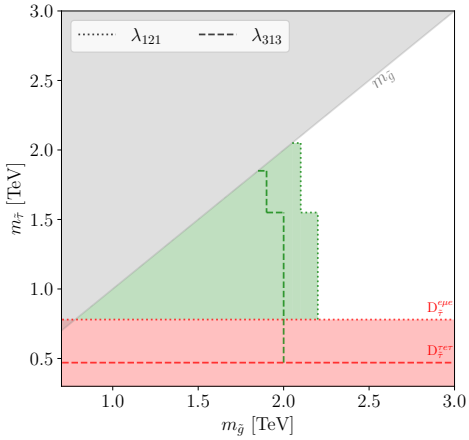

(c) $\tilde{\tau}_L/\tilde{\nu}_\tau/\tilde{\tau}_R$ LSPs with non-decoupled $\tilde{g}$.

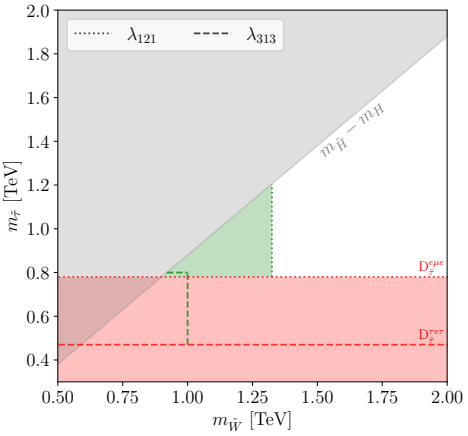

(d) $\tilde{\tau}_L/\tilde{\nu}_\tau/\tilde{\tau}_R$ LSPs with non-decoupled $\tilde{W}$.

Figure 3.7: As in Fig. 3.3 but for the $I_{\tilde{x}\to\tilde{\ell}/\tilde{\tau}}$ scenarios.

LSP summary: To summarize, we collect, in Fig. 3.8, the minimum excluded mass for each sparticle, $\tilde{p}$, undergoing a cascade decay (*i.e.*, the minimum limits obtained for each of the $\mathrm{I}_{\tilde{p}\to\tilde{x}}$ scenarios with $\tilde{x}$ the various LSPs), and compare it to the limit obtained from direct production of the sparticle when it is the LSP (*i.e.*, the corresponding $\mathrm{D}_{\tilde{p}}$ scenarios). It is interesting to note that, although cascade decays generally lead to final states with more visible objects, the sensitivity can be both degraded or improved. The reduction in E_T^{miss} and the distribution of energy across more decay products can reduce the sensitivity. For example, the decay to a slepton or bino LSP yields in most cases the worst limits given that intermediate particles in the decay chain can become soft for compressed spectra, *e.g.*, $\tilde{g} \to 2j + \ell + \tilde{\ell}(\to \ell\nu)$. However, changes in the decay modes due to the varying nature of the LSP can also lead to a higher number of leptons or third-generation quarks which leads to an improvement in the limits. It is worth highlighting that the degradation is around 20% at maximum, and the exclusion limits remain for all sparticles under all variations of LSP hypotheses, LSP masses, and coupling choice.

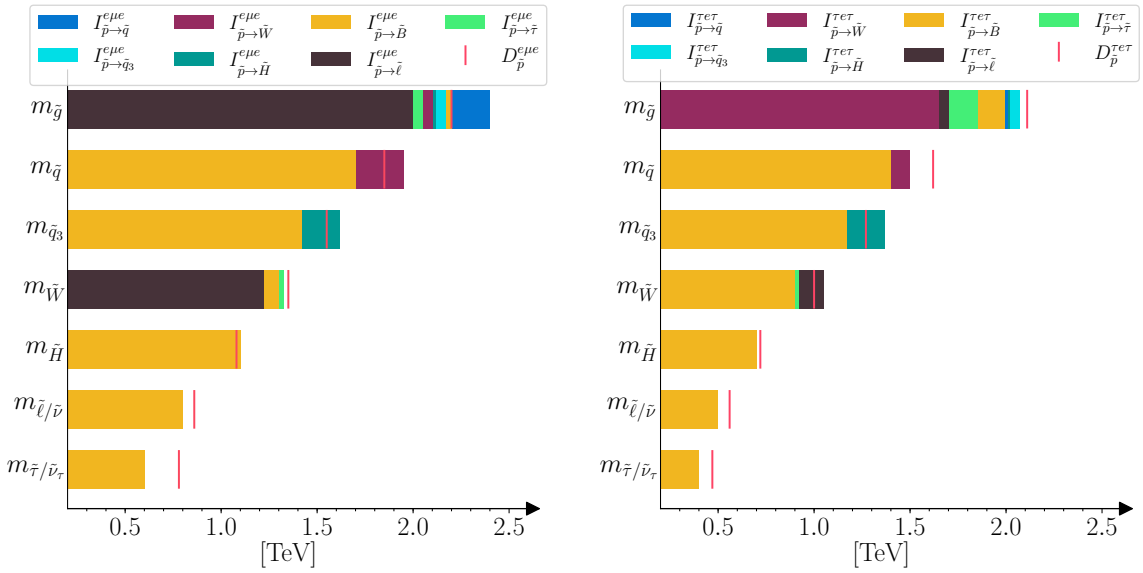

(a) λ_{121}. (b) λ_{313}.

Figure 3.8: Summary of minimum mass bounds on sparticle $\tilde{p}$ across the various $I_{\tilde{p}\to\tilde{x}}$ benchmarks considered, where $\tilde{x}$ corresponds to the LSPs. The vertical red line represents the direct production mass bound when $\tilde{p}$ is the LSP, *i.e.*, the limit corresponding to $D_{\tilde{p}}$.

3.5 Conclusions and Outlook

In this paper, we have systematically analyzed the RPV-MSSM and classified the possible signatures at the LHC with the goal of compiling a minimal set of experimental searches that provides complete coverage. Our study provides, for the first time, a completely general and model-independent treatment of the phenomenology, for the case of small RPV couplings. We briefly summarize the central results of the paper:

- As demonstrated, the phenomenological space for the most general RPV-MSSM setup is vast and complicated. Nevertheless, we have shown that just 17 final state topologies (six for $LL\bar{E}$, five for $\bar{U}\bar{D}\bar{D}$, and six for $LQ\bar{D}$) are sufficient to provide complete coverage for the RPV-MSSM at the LHC; we call this the 'RPV Dictionary'. Our signature tables can be generated by using the accompanying `abc-rpv` Python library, described in Appendix B.3.

- Using the 'RPV Dictionary', we have analyzed the current coverage of the RPV-MSSM at the LHC. In general, we find that even though most RPV scenarios have not been searched for directly, the vast landscape of searches implemented by `ATLAS` and `CMS` provides full coverage of the possible RPV-MSSM signatures.

- However, we do point out the need for strong experimental improvements in some of the final states in order to achieve sensitivity to electroweak production cross-sections. Some examples are found for $LQ\bar{D}$ and $U\bar{D}\bar{D}$ decays, such as $\tilde{\ell} \to jj$, $\tilde{\chi}^0_1 \to jb\nu$, and $\tilde{\chi}^0_1 \to jjj$.

- As an application of our framework, and in order to demonstrate the second point above, we have performed numerical simulations specifically for the case of a dominant $LL\bar{E}$ operator (single non-zero coupling at a time), in order to quantitively assess the coverage. We have derived mass bounds on SUSY particles within several RPV benchmark models corresponding to all relevant LSPs. We find that strong exclusion limits comparable to, or even better than, the RPC-MSSM are obtained, and these are robust across the wide range of models. Apart from clarifying the current status of several of these scenarios for which there are no explicit exclusion limits in the literature, our numerical examples demonstrate that our approach of using just a few characteristic topologies to cover the most general RPV-MSSM setting is not merely a reductionist fantasy, but can indeed offer a viable, model-independent search strategy. We have left the detailed analyses of the $LQ\bar{D}$ and $\bar{U}\bar{D}\bar{D}$ cases for future work.

We stress that there are a couple of limitations of our framework. As mentioned in the main body, we require that all decays in the cascade chain are prompt, including that of the LSP. Furthermore, we require that the final state decay products of the LSP are not too soft to be detected. This assumption is crucial and restricts us to scenarios with $m_{\text{LSP}} > \mathcal{O}(200\,\text{GeV})$. Further, while we require the RPV coupling to be large enough to cause the LSP to decay promptly, it cannot be too large, as that would modify the pattern of the cascade decays. Similarly, adding exotic particles to the MSSM spectrum that can modify the sparticle decay chains also affects our analysis. In such cases, our classification may not apply anymore. The most important restriction is that our approach – in prioritizing model independence – compromises on search sensitivity for certain scenarios. For example, if the colored sector is always kinematically accessible at the LHC, stricter bounds can be obtained by including the cascade decay products in the search signature, whereas, in our approach, we only target decay products from the LSP. The former approach is usually adopted by `ATLAS` and `CMS` in their searches for specific RPV-SUSY scenarios.

On the other hand, we believe our unbiased approach is highly relevant, given that no supersymmetry has yet been discovered at the LHC, and with the HL-LHC era just around the corner. Nevertheless, we have compiled auxiliary tables in Appendix B.2 that can help in designing optimized search strategies in exchange for some model-independence.

As a continuation of this work, we shall pursue a detailed numerical treatment of the $LQ\bar{D}$ and $\bar{U}\bar{D}\bar{D}$ scenarios analogous to the $LL\bar{E}$ case considered in this paper. In those cases, present coverage is less comprehensive and it is important to identify potential gaps. Furthermore, we would like to extend the present work to a systematic study of the large RPV coupling case, affecting both production and decay.

4

Single Photon Searches for R-parity-violating Supersymmetry at FASER

4.0 Preface

The contents of this chapter and the supplementary material presented in Appendix C are based on the following publication:

- H. K. Dreiner, D. Köhler, S. Nangia, and Z. S. Wang,
  Searching for a single photon from lightest neutralino decays in R-parity-violating supersymmetry at FASER,
  Published in JHEP 07 (2023) 215, arXiv:2207.05100 [hep-ph].

The author of this thesis derived all numerical results, including the simulations of signal events in FASER(2) using FORESEE [275]. Further, all benchmark plots presented in this chapter were provided by the author. Finally, the interpretation of the results was performed by the author together with Saurabh Nangia, with insights from Zeren Simon Wang.

Recently, there has been an increased interest in neutral long-lived particles (LLPs), which arise in various models of dark matter or baryogenesis. LLPs have gained attention due to the variety of models and different implications for signals, leading to several experimental proposals with improved sensitivities. Remarkably, the LHC detectors ATLAS and CMS have relevant sensitivity for LLPs, although they were originally not designed for this purpose [276–278]. Nevertheless, there are still significant gaps in coverage of the LLP models at the LHC. LLPs can generally have long lifetimes compared to SM particles at the electroweak scale. When produced in experiments like the LHC, these LLPs can decay far from the interaction point of the primary proton-proton collision propagating over finite distances on the order of tens of meters before decaying back into SM particles. Dedicated efforts are underway or planned for fixed-target experiments, B-factories, and beam-dump experiments to search for these LLPs. Extensive studies have been conducted using various search techniques, including missing energy, peak searches, and displaced vertex (DV) searches.

In the upcoming years, the LHC is expected to be upgraded and will provide up to $\mathcal{L} = 3\,000\,\text{fb}^{-1}$ of integrated luminosity [279]. In this context, there are a number of new proposals for searches for LLPs, all to exploit the large luminosity of the LHC, *e.g.* FASER [280, 281], FACET [282], MATHUSLA [283–285], CODEX-b [286], ANUBIS [287], and MoEDAL-MAPP [288]. These detectors are positioned at different locations relative to the interaction points (IPs) of ATLAS, CMS, LHC-b, or ALICE and use LHC events for their studies.

This chapter focuses on scenarios in which a bino-like lightest neutralino in the RPV framework decays into a photon and a neutrino. The decay occurs at loop level. Although

this mode might be loop-suppressed, it can become relevant for very light neutralinos and might even be the only kinematically allowed channel depending on the nature of dominant RPV couplings and the neutralino mass. This particular decay signature has not yet received much attention in the literature. However, it allows us to determine sensitivity reaches on the production and decay coupling of the neutralino. In RPV-SUSY, it is possible for the lightest neutralino to have a mass below the GeV scale or even be massless, without violating existing experimental limits. However, it must be unstable. In this chapter, we consider the lightest neutralino as the LSP, which can be produced through the decay of light mesons. Due to the smallness of RPV couplings, imposed by the current constraints, the bino-like neutralino is expected to have a long lifetime in the sub-GeV mass range. Furthermore, when produced from meson decays at the LHC, it exhibits a high boost in the forward direction. Thus, the proper decay length of the light neutralino can be estimated to be $c\tau \sim \mathcal{O}(1 - 100)\,\mathrm{m}$. We aim to evaluate the sensitivity range of the already operating far-detector experiment, `FASER`, and its planned successor, `FASER2`. These detectors are designed to detect forward-boosted LLPs produced by the proton-proton collisions at the `ATLAS` IP, set 480 m away.

We establish six benchmark studies, including one single coupling scenario, to cover all relevant possibilities for a radiatively decaying neutralino at `FASER`. We use `FORESEE` [275] to determine the neutralino energy spectrum and production rate at the LHC, by specifying the decay branching ratios. We perform Monte Carlo simulations to estimate the probability for the light neutralino to decay within the detector volume.

Our analysis shows that the experimental setups of both `FASER` and `FASER2` are platforms that provide good coverage for detecting the characteristic single-photon signature arising from the decay of the neutralino within their respective decay volumes. Remarkably, our study shows that both `FASER` and `FASER2` provide sensitivity to large regions of parameter space that lie orders of magnitude beyond current limits.

Noteworthy, the physical potential of these experiments has not been explored extensively in the literature. The goal of the present chapter is to evaluate the sensitivity of these proposals to LLPs in the context of a class of RPV-SUSY and to compare them with previous experiments. The regime considered involves long lifetimes and small couplings, expanding the coverage of the RPV landscape. In summary, we conclude that different experiments can complement each other in the parameter space of the models considered here. Future work could investigate this model for these other detectors mentioned and make comparisons.

4.1 Introduction

The discovery of a Higgs boson [4, 5] at the Large Hadron Collider (LHC) at CERN, Switzerland, has completed the spectrum of the Standard Model (SM) of particle physics. Despite the huge successes, the SM provides an incomplete description of the Universe. For instance, the observed neutrino oscillations [118, 289, 290] require massive neutrinos, in disagreement with the SM. The fine-tuning problem of the Higgs boson – or hierarchy problem [36, 164] – is only resolved beyond the SM (BSM), *e.g.*, by supersymmetry (SUSY) [34, 45]. Furthermore, dark matter and dark energy, as well as baryogenesis in the early Universe are all unexplained within the SM.

Searches for BSM physics have been performed since even prior to the Higgs-boson discovery, on various experimental and observational fronts. These probes include colliders, beam-dump experiments, nuclear- and electron-recoil experiments, and astrophysical observations.

Here, we focus on collider probes for BSM-physics searches. In particular, we study high-energy proton-proton collisions at the LHC, currently aiming to reach a center-of-mass energy of 14 TeV in the near future. The two largest experiments at the LHC – `ATLAS` [291] and `CMS` [292] – have hitherto mainly searched for events with large missing energy and/or high p_T objects (jets, leptons, etc.), emphasizing signatures expected to stem from heavy new fields.

Among various signatures, high-energy photons plus missing energy is one interesting example as it is clean with modest SM background, and is predicted in well-motivated theoretical models. One classic example is Gauge-mediated Supersymmetry Breaking (GMSB) models [293]. Given a light and stable gravitino as the lightest supersymmetric particle (LSP), the lightest Minimal Supersymmetric Standard Model (MSSM) superpartner is actually the next-to-lightest supersymmetric particle (NLSP). If the NLSP is neutral, it can be either a neutralino, or a sneutrino. The lightest neutralino can be bino, wino, Higgsino, or a mixture, and can decay to a photon and a non-observable gravitino, either promptly or with a long lifetime; see, *e.g.*, Refs. [294–297] for some LHC phenomenology studies. This signature has been searched for at the Tevatron – at `CDF` and `D0` [298, 299] – and at the LHC – at `ATLAS` [300] and `CMS` [301].

One additional theory benchmark is a class of models with universal extra dimensions [302]. If the new dimensions are only accessible to gravity, the lightest Kaluza-Klein particle (LKP) can decay to a photon and a gravity excitation. Both the lightest neutralino (assuming R-parity conservation) and the LKP should be pair-produced, and thus lead to the signature of two highly energetic photons plus missing energy at the LHC.

Here, we consider R-parity-violating (RPV) supersymmetry in its minimal form – the RPV Minimal Supersymmetric Standard Model (RPV-MSSM) [54] – with a bino-like lightest neutralino as the LSP (see Refs. [53, 99, 303] for reviews). The RPV-MSSM is as well-motivated as the R-parity-conserving (RPC) MSSM. It not only solves the hierarchy problem, but also provides a natural solution to the neutrino masses [58, 122, 123, 130, 145], as well as a much richer collider phenomenology than the RPC-MSSM. In addition, it can explain various experimental anomalies observed in recent years, such as the B-anomalies [304–309], muon $g-2$ [307–309], and the ANITA anomaly [308, 310].

As we discuss in more detail in Section 4.2 below, in the RPV-MSSM, it is possible to have a light neutralino of mass below 10 GeV, or even massless. Once produced, the neutralino

decays via non-vanishing RPV couplings into SM particles. Since these couplings are required by various (low-energy) experiments to be small [99, 157, 311], light LSP neutralinos with mass below the GeV scale are expected to be long-lived; after production at a collider, they travel a macroscopic distance before decaying to SM particles.

Long-lived particles (LLPs) have in recent years received increased attention [209, 210, 284, 312–314]. LLPs are predicted in a wide range of BSM models such as split SUSY, RPV-SUSY, a class of portal-physics models [axion-like particles (ALPs), heavy neutral leptons, a dark Higgs scalar, dark photons], and models of neutral naturalness – which are often related to the non-vanishing neutrino masses or dark matter. In particular, a series of dedicated far-detector programs have been proposed to be operated in the vicinity of LHC interaction points (IPs), mainly aiming to look for LLPs with a proper decay length $c\tau \sim (1 - 100)\,\mathrm{m}$, or even larger. Some examples currently under discussion include `FASER` [280, 281], `FACET` [282], `MATHUSLA` [283–285], `CODEX-b` [286], `ANUBIS` [287], and `MoEDAL-MAPP` [288].

`FASER` has been approved and installed at the LHC TI12 tunnel. It consists of a small cylindrical decay volume of $\sim 0.05\,\mathrm{m}^3$. It is expected to achieve excellent constraining power for a number of theoretical benchmark models such as ALPs [315], dark photons [280], and inelastic dark matter [316]. It is now under operation with the ongoing LHC Run 3. For the high-luminosity LHC (HL-LHC) period, a larger version of `FASER`, known as `FASER2` [281], is also planned to be installed and running, potentially at the same location or at a collective facility – the Forward Physics Facility (FPF) [317] – hosting various experiments, all in the very forward region of the LHC, including `FORMOSA` [318] and `FLArE` [319]. These potential future experiments are all intended to look for various BSM signatures.

Here, we focus on long-lived light neutralinos. They have been studied extensively for various present and future experiments including `SHiP` [225, 320], `ATLAS` [225], far detectors at the LHC [226, 321–323], `Belle II` [324], `Super-Kamiokande` [325], and future lepton colliders [326, 327]. These works mostly consider the signature of a neutralino decay into a charged lepton plus a meson, induced by $LQ\bar{D}$ operators [328], while the production can result from decays of either mesons, τ leptons, or Z-boson.

In this work, we propose a novel signature associated with very light lightest-neutralino $\left(\tilde{\chi}_1^0\right)$ decays: A single photon plus missing energy. Such a signature can appear as a result of the radiative decay associated with neutrinos,

$$\tilde{\chi}_1^0 \to \nu_i + \gamma \text{ or } \bar{\nu}_i + \gamma\,, \tag{4.1}$$

arising at the loop level via the RPV couplings λ'_{ijj} of the $LQ\bar{D}$ operators or λ_{ijj} of the $LL\bar{E}$ operators. This decay can dominate in certain mass ranges and for certain choices of RPV couplings.[1] We consider the lightest neutralino to be produced from rare decays of mesons such as pions and B-mesons copiously created at the LHC, and study the probing potential of `FASER` and `FASER2` to these scenarios, for the signature of a single, displaced photon. As discussed in Section 4.5, the background is expected to be negligible.

The paper is organized as follows. We briefly introduce the RPV-MSSM, as well as the light neutralino scenario in the next section. In Section 4.3 we present a list of representative

[1] We note that light long-lived particles (LLPs) decaying to a light neutrino and a photon may explain the `MiniBooNE` anomaly [329, 330], but given the recent negative results by `MicroBooNE` [331], and possible SM explanations for the anomaly [332, 333], we do not consider it any further here.

benchmark scenarios, which we investigate in this paper. In Section 4.4 we discuss the experimental setup at FASER and FASER2, and in Section 4.5 we detail our simulation procedure for estimating the sensitivity reach. The results are then presented with a discussion in Section 4.6. We conclude the paper with a summary and an outlook in Section 4.7.

4.2 Theoretical Framework

Here, we discuss the underlying supersymmetric model, as well as details of the light neutralino scenario.

4.2.1 The R-parity-violating MSSM

Given the $(N = 1)$ supersymmetry algebra, and the MSSM particle content, the most general $\mathrm{SU}(3)_C \times \mathrm{SU}(2)_L \times \mathrm{U}(1)_Y$-invariant, renormalizable superpotential can be written as,

$$W = W_{\mathrm{MSSM}} + W_{\mathrm{LNV}} + W_{\mathrm{BNV}}\,, \tag{4.2}$$

where W_{MSSM} is the usual MSSM superpotential – see, for instance, Ref. [54] – while the terms,

$$W_{\mathrm{LNV}} = \frac{1}{2}\lambda^{ijk} L_i L_j \bar{E}_k + \lambda'^{ijk} L_i Q_j \bar{D}_k + \kappa^i H_u L_i\,, \qquad W_{\mathrm{BNV}} = \frac{1}{2}\lambda''^{ijk} \bar{U}_i \bar{D}_j \bar{D}_k\,, \tag{4.3}$$

violate lepton- and baryon-number, respectively. In the above, L (Q), and $\bar{E}$ $(\bar{U}, \bar{D})$ are the MSSM lepton (quark) $\mathrm{SU}(2)_L$-doublet and $\mathrm{SU}(2)_L$-singlet chiral superfields, respectively, while H_u, H_d label the $\mathrm{SU}(2)_L$-doublet Higgs chiral superfields. We do not show gauge indices explicitly but write the generational ones: $i, j, k = 1, 2, 3$ with a summation implied over repeated indices. The λ's are dimensionless coupling parameters, the κ's are dimension-one mass parameters.

The combined lepton- and baryon-violation contained in the above terms may cause the proton to decay too quickly [101, 334]. Thus, in the MSSM, all operators in $W_{\mathrm{LNV}} + W_{\mathrm{BNV}}$ are set to zero by invoking a $\mathbb{Z}_2$ symmetry called R-parity [148]. This allows W_{MSSM} while disallowing $W_{\mathrm{RPV}} \equiv W_{\mathrm{LNV}} + W_{\mathrm{BNV}}$. However, the proton can be protected without completely forbidding W_{RPV}. For instance, forbidding W_{BNV}, while keeping W_{LNV}, results in a stable proton. Baryon triality – B_3 – is a $\mathbb{Z}_3$-symmetry that achieves exactly this [52, 55, 122, 206].

Importantly, RPV phenomenology can be starkly different compared to the RPC case [53, 67, 99, 149, 208]. The LSP is no longer guaranteed to be stable leading to vastly different final state signatures. The collider phenomenology of RPV models is rich and complex [67, 149], and it is crucial that our SUSY search strategies cover all possibilities. We now discuss in some detail one interesting realization of RPV-SUSY: A very light neutralino.

4.2.2 A Very light Lightest-Neutralino

In principle, any supersymmetric particle can be the LSP in RPV models [66, 67, 335]. Here, we restrict ourselves to the case of a neutralino. Potentially important mass bounds

come from colliders, dark matter (cosmology), and astrophysics. For collider searches of a stable neutralino, the strongest bound comes from LEP, $m_{\tilde{\chi}_1^0} \gtrsim 46\,\text{GeV}$ [334]. This is based on chargino searches, and assumes the grand-unified mass relation is satisfied between the electroweak supersymmetry breaking gaugino masses, $M_1 = \frac{5}{3}\tan^2\theta_W M_2 \approx 0.5 M_2$, with θ_W the electroweak mixing angle. However, once the relation is dropped, the mass of the lightest neutralino is experimentally unconstrained [69]. Such a scenario typically requires the lightest neutralino to be dominantly bino-like [68, 69].

A stable lightest neutralino is further constrained by dark matter limits. The Lee-Weinberg bound gives $m_{\tilde{\chi}_1^0} \gtrsim \mathcal{O}(10)\,\text{GeV}$ [69, 72–74, 82, 86, 336–338]. However, in RPV models where the LSP is unstable, this bound does not apply [69].

Then, from our discussion above, if the RPV couplings are small – which is what one expects – the neutralino can be stable on collider scales while unstable on cosmological scales, thus evading all existing constraints. Such a neutralino is allowed to be very light and, in principle, even massless [69, 334]. It is also consistent with astrophysical constraints, such as the cooling of supernoavae and white dwarfs, if the sfermions are heavy enough [86–88].

We next consider the phenomenology of RPV-SUSY scenarios with such light neutralinos as the LSP. If the neutralino is massive enough, and/or the RPV couplings are sizeable, such that the proper decay length of the neutralino is $c\tau \lesssim \mathcal{O}(1)\,\text{m}$, various RPV searches performed at ATLAS and CMS – including those for displaced vertices – apply; see, *e.g.*, Refs. [220, 339]. These searches rely on detecting the decay products of the neutralino, which can contain jets and leptons, depending on the dominant RPV couplings. On the other hand, for very light neutralinos, and/or if the RPV couplings are very small, the neutralino LSP is stable on macroscopic scales. Then, the signature is invisible to colliders, just as in the RPC case. Thus, as long as heavier SUSY particles are produced at the LHC, that then cascade-decay down to the neutralino LSP, the RPC searches for large missing transverse momentum apply even to the RPV case.

However, in light of to-date unsuccessful supersymmetry searches, one possibility is that the heavier SUSY spectrum may be inaccessible at the LHC. Very light neutralinos, $m_{\tilde{\chi}_1^0} \lesssim \mathcal{O}(4.5)\,\text{GeV}$, can still be produced in abundance in such a scenario in RPV models through the rare decays of mesons via an $LQ\bar{D}$ operator [68, 70, 225]. These neutralinos would be highly boosted in the forward direction of the momentum of the decaying meson. None of the above search strategies applies in such a case, and the scenario represents a realistic possibility of low-scale SUSY manifesting in a way that would have escaped our searches so far. With the long-lived particle programs at the LHC picking up pace, there is the possibility of filling this gap. If the highly boosted, light neutralino decays with a proper decay length, $c\tau \sim \mathcal{O}(1-100)\,\text{m}$, it may be visible in dedicated far-detector experiments such as FASER. Before we discuss the decay modes of such light neutralinos, we provide, for completeness, the unpolarized decay width of pseudoscalar mesons into a light neutralino and a lepton via an $LQ\bar{D}$ operator, reproduced from Ref. [225],

$$\Gamma\left(M_{ab} \to \tilde{\chi}_1^0 + l_i\right) = \frac{\lambda^{\frac{1}{2}}\left(m_{M_{ab}}^2, m_{\tilde{\chi}_1^0}^2, m_{l_i}^2\right)}{64\pi m_{M_{ab}}^3} \left|G_{iab}^{S,f}\right|^2 \left(f_{M_{ab}}^S\right)^2 \left(m_{M_{ab}}^2 - m_{\tilde{\chi}_1^0}^2 - m_{l_i}^2\right) , \quad (4.4)$$

where l_i denotes a charged lepton $\ell_i^{\pm}$ or a neutrino ν_i, depending on whether M_{ab} is charged or neutral, and $\lambda^{\frac{1}{2}}$ is the Källén function $\lambda^{\frac{1}{2}}(x,y,z) \equiv \sqrt{x^2+y^2+z^2-2xy-2xz-2yz}$. The coupling constants $G^{S,f}_{iab}$ and the meson decay constant $f^S_{M_{ab}}$ are defined as in Ref. [225]. In particular, the $LQ\bar{D}$ coupling λ' is proportional to $G^{S,f}_{iab}$. In the above, the charge-conjugated mode is implied.

4.2.3 Neutralino Decay

The dominant decay mode of the neutralino is dictated by the relative sizes of the RPV couplings, as well as the neutralino mass [328]. For $m_{\tilde{\chi}_1^0} \lesssim \mathcal{O}(4.5)\,\text{GeV}$, the neutralino can decay into a meson and a lepton via an $LQ\bar{D}$ operator, if kinematically allowed. Similarly, it can decay as $\tilde{\chi}_1^0 \to \ell^+\ell'^-\nu + \text{c.c.}$ via the $LL\bar{E}$ operators. For operators $L_iQ_j\bar{D}_j$ or $L_iL_j\bar{E}_j$, there is also the possibility for the loop-induced decays,

$$\tilde{\chi}_1^0 \to (\gamma + \nu_i\,, \gamma + \bar{\nu}_i)\ , \tag{4.5}$$

which has essentially no kinematic threshold. We show example Feynman diagrams in Fig. 4.1. The fermions/sfermions in the loop have generation index j. The decay rate is given by [58, 328, 340, 341]:

$$\begin{aligned}\Gamma(\tilde{\chi}_1^0 \to \gamma + \nu_i) &= \frac{\lambda^2\alpha^2 m^3_{\tilde{\chi}_1^0}}{512\pi^3\cos^2\theta_W}\left[\sum_f \frac{e_f N_c m_f\,(4e_f+1)}{m^2_{\tilde{f}}}\left(1+\log\frac{m_f^2}{m^2_{\tilde{f}}}\right)\right]^2 \\ &= \Gamma\left(\tilde{\chi}_1^0 \to \gamma + \bar{\nu}_i\right)\ .\end{aligned} \tag{4.6}$$

In the above expression, λ is the relevant $L_iQ_j\bar{D}_j$ or $L_iL_j\bar{E}_j$ coupling, α is the (QED) fine-structure constant, while θ_W is the electroweak mixing angle. e_f, N_c and $m_f(m_{\tilde{f}})$ are the electric charge in units of e, color factor (3 for $LQ\bar{D}$, 1 for $LL\bar{E}$), and the mass, respectively, of the fermion (sfermion) inside the loop. We note that the above simple formula for the width neglects any mixings in the scalar sector. While this effect – depending on the supersymmetric parameters – may become significant, it introduces several undetermined SUSY-parameters in the expression. At the level of precision of our study, we find it convenient to work with this simplified approximation. The two decay widths in Eq. (4.6) are equal as a result of the Majorana nature of the neutralino. The logarithmic function in Eq. (4.6), $\log\frac{m_f^2}{m^2_{\tilde{f}}}$, changes only by about a factor of two if we vary $m_{\tilde{f}}$ between 1 TeV and 100 TeV. Therefore, in our numerical simulations, we will fix $m_{\tilde{f}}$ at 1 TeV for the log term, so that we can use $\lambda/m^2_{\tilde{f}}$ as a single combined parameter, without separating λ and $m_{\tilde{f}}$.

Despite the loop-suppression, the radiative mode, Eq. (4.5), can be relevant for very light neutralinos. The partial width is proportional to $\left(m^3_{\tilde{\chi}_1^0} m_f^2\right)/m^4_{\tilde{f}}$, compared to $m^5_{\tilde{\chi}_1^0}/m^4_{\tilde{f}}$ for the tree-level three-body decay into fermions [58, 149, 340], and can thus be important for small masses. Depending on the generation indices of the dominant RPV coupling(s) and the neutralino mass, it might even be the only kinematically allowed mode. In this paper we focus on the scenario where the neutralino dominantly decays as in Eq. (4.5), as this channel

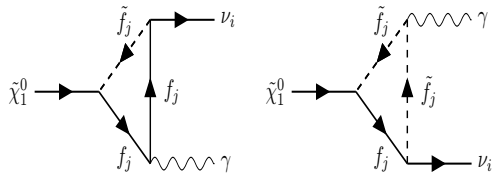

Figure 4.1: Feynman diagrams for the radiative neutralino decay.

has not been considered before in the context of long-lived light neutralino searches. We now present some benchmark scenarios for phenomenological studies.

4.3 Benchmark Scenarios

In order to study the phenomenology of a very light neutralino decaying only via the radiative mode, Eq. (4.5), we present some representative benchmark scenarios which we believe cover all relevant possibilities, and which we investigate in detail in the next section. We list the corresponding parameters in Table 4.1. In each case, we assume the listed couplings are the only non-negligible RPV couplings. The neutralino is produced through the rare decay of the meson M via the coupling $\lambda^{\rm P}_{ijk}$: $M \to \tilde{\chi}_1^0 + \ell\,(\nu)$ [68, 70, 71, 225], and then decays in one of the ways discussed in the previous section via the coupling $\lambda^{\rm D}_{ijj}$.[2] In the table, we also list the current best bounds on the couplings $\lambda^{\rm P}_{ijk}$ and $\lambda^{\rm D}_{ijj}$.

For benchmark **B1**, the neutralino is produced via the most abundant mesons at the LHC – pions – in association with muons (neutrinos). This occurs via the coupling $\lambda^{\rm P}_{ijk} = \lambda'_{211}$. The charged production mode ($\pi^\pm \to \tilde{\chi}_1^0 + \mu^\pm$) is only possible if the mass of the neutralino satisfies the bound,

$$m_{\tilde{\chi}_1^0} < m_{\pi^\pm} - m_{\mu^\pm} \approx 35\,\text{MeV}\,. \tag{4.7}$$

For neutralinos heavier than the above threshold, only the neutral production mode ($\pi^0 \to \tilde{\chi}_1^0 + \nu_\mu$) contributes; however, this mode is suppressed owing to the short lifetime of the neutral pion which translates into a low decay branching fraction into neutralinos. For the benchmark, we choose $m_{\tilde{\chi}_1^0} = 30\,\text{MeV}$; the lightness of the neutralino means that the radiative mode is the only kinematically allowed decay. In principle, with the coupling $\lambda^{\rm P}_{ijk} = \lambda'_{111}$ instead, a heavier neutralino can be produced in charged pion decays: $\pi^\pm \to \tilde{\chi}_1^0 + e^\pm$, but the severe bound, [157]

$$\lambda'_{111} \lesssim 0.001 \left(\frac{m_{\tilde{d}_R}}{1\,\text{TeV}}\right)^2\,, \tag{4.8}$$

implies this mode can not be probed at the experiments we consider here.

For the decay coupling, we choose $\lambda^{\rm D}_{ijj} = \lambda'_{333}$. The decay width, Eq. (4.6), is roughly proportional to m_f^2. Thus, the heavier the fermion in the loop, the shorter the lifetime of the

[2] We note that, in this work, we are neglecting the effects of the suppressed three-body decay that can proceed at one-loop level via an off-shell Z, e.g., $\tilde{\chi}_1^0 \to 3\nu$. We thank Florian Domingo for a discussion on this topic.

Scenario	$m_{\tilde{\chi}_1^0}$	Production $\left(\lambda^{\mathrm{P}}_{ijk}\right)$	Decay $\left(\lambda^{\mathrm{D}}_{ijj}\right)$	Current Constraints
B1	30 MeV	$\lambda'_{211}\left(M=\pi^{\pm},\pi^0\right)$	λ'_{333}	$\lambda'_{211}<0.59\left(\frac{m_{\tilde{d}_R}}{1\,\mathrm{TeV}}\right),\ \lambda'_{333}<1.04$
B2	75 MeV	$\lambda'_{212}\left(M=K^{\pm},K^0_{L/S}\right)$	λ'_{333}	$\lambda'_{212}<0.59\left(\frac{m_{\tilde{s}_R}}{1\,\mathrm{TeV}}\right),\ \lambda'_{333}<1.04$
B3	200 MeV	$\lambda'_{112}\left(M=K^{\pm},K^0_{L/S}\right)$	λ_{322}	$\lambda'_{112}<0.21\left(\frac{m_{\tilde{s}_R}}{1\,\mathrm{TeV}}\right),\ \lambda_{322}<0.7\left(\frac{m_{\tilde{\mu}_R}}{1\,\mathrm{TeV}}\right)$
B4	300 MeV	$\lambda'_{221}\left(M=D^{\pm},K^0_{L/S}\right)$	λ_{233}	$\lambda'_{221}<1.12,\ \lambda_{233}<0.7\left(\frac{m_{\tilde{\tau}_R}}{1\,\mathrm{TeV}}\right)$
B5	500 MeV	$\lambda'_{222}\left(M=D_S^{\pm}\right)$	λ'_{222}	$\lambda'_{222}<1.12$
B6	1 GeV	$\lambda'_{313}\left(M=B^{\pm},B^0\right)$	λ'_{333}	$\lambda'_{313}<1.12,\ \lambda'_{333}<1.04$

Table 4.1: Benchmark scenarios considered in this paper. The neutralino is produced through the rare decay of the meson M via the coupling $\lambda^{\mathrm{P}}_{ijk}$: $M\to\tilde{\chi}_1^0+\ell\,(\nu)$. The neutralino decay is as in Eq. (4.5) via the coupling $\lambda^{\mathrm{D}}_{ijj}$. The photon energy in the neutralino rest frame is $E_\gamma=m_{\tilde{\chi}_1^0}/2$, but can range from $\mathcal{O}\,(0.1)$ to $\mathcal{O}\,(1)$ TeV at FASER. In the furthest-to-the-right column, we list the current best bounds on the couplings, see for example, Ref. [157].

neutralino. For the very light neutralino in **B1**, we require a heavy fermion in the loop to get testable scenarios at FASER; we expect maximum sensitivity to couplings λ'_{i33} or λ_{i33}.

For the benchmarks **B2** and **B3**, we choose the parameters such that the neutralinos are produced in kaon decays. This time, unlike the pion case, both the charged and neutral modes have comparable contributions. For **B2**, the neutralino decays only radiatively, as in Eq. (4.5). For **B3**, the decay coupling $\lambda^{\mathrm{D}}=\lambda_{322}$ also allows for tree-level leptonic decays:

$$\tilde{\chi}_1^0\to\left(\nu_\tau\mu^{\pm}\mu^{\mp},\,\tau^{\pm}\mu^{\mp}\nu_\mu\right)+\text{c.c.}\,. \tag{4.9}$$

However, these are kinematically blocked for $m_{\tilde{\chi}_1^0}\lesssim 2m_\mu$. Thus, we have chosen $m_{\tilde{\chi}_1^0}=200$ MeV. Later, when we present numerical results, we go beyond the strict parameters in the benchmark scenarios and consider plots in the RPV coupling vs. neutralino mass plane. One then has to account for the fact that additional decay modes can open. Note that in **B3**, we now select a decay coupling that is not third generation in the last two indices, since the neutralino is now heavy enough to avoid a too-small decay width, even for lighter fermions in the loop.

We have chosen benchmark **B4** such that a single coupling leads to production of the neutralinos from both kaons and $D^{\pm}$. Since kaons are more abundant at the LHC than D-mesons, the former production mode contributes more to the neutralino flux. For the selected mass of 300 MeV, there are no other relevant decay modes of the neutralino than the radiative one. But for the coupling vs. mass plot, the neutralino can decay into kaons above the relevant thresholds. The neutralino *production* through kaons is, of course, blocked for these heavier masses. In addition, for this scenario and the ones below, there can also be three-body decays into two mesons and a lepton, mediated via the $LQ\bar{D}$ operators; these can become relevant in the very high mass regime, $m_{\tilde{\chi}_1^0}\gtrsim\mathcal{O}\,(1.5)$ GeV. These are neglected for simplicity in the present work as their impact for sub-GeV neutralinos – which are the focus of our study – is minor. We will also neglect any Cabibbo-Kobayashi-Maskawa-mixing effects for similar reasons. More details on these effects can be found in Ref. [328].

Benchmark **B5** is a special case: It requires only a single non-zero RPV coupling (λ'_{222}) for both production (via $D_S^{\pm}$ mesons) and decay. This is absent in the tree-level neutralino decay case [225], except for an extremely small mass-window of around 4 MeV. For the given mass, $m_{\tilde{\chi}_1^0} = 500\,\text{MeV}$, the neutralino decays only radiatively. But at higher masses, it may decay into η, η', or ϕ.

Finally, we have chosen benchmark **B6** such that the neutralinos are produced via B-meson decays, thereby allowing the neutralino to be relatively heavy, leading to more energetic photons. The neutralino is produced in association with a $\tau^{\pm}$ (ν_τ) via the charged (neutral) mode; the two modes have comparable contributions. For $m_{\tilde{\chi}_1^0} > m_{B^{\pm}} - m_{\tau^{\pm}}$, only the neutral mode is kinematically allowed. The radiative mode is the only relevant decay channel.

We note in passing the interesting observation that the radiative decay of a neutralino gives us a method of producing significant ν_τ fluxes. These are suppressed in the SM. With FASERν [342, 343] under operation, this may give us an interesting opportunity to detect the neutralino by looking for ν_τ events. However, we leave an investigation in this direction for the future.

Before closing the section, we provide a plot in Fig. 4.2, showing the decay branching ratios of the lightest neutralino into our signature, $\gamma + \overset{(-)}{\nu}$, as a function of the neutralino mass, for all the considered benchmark scenarios.

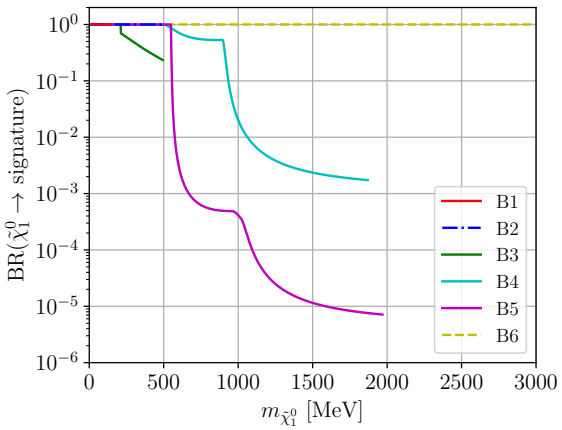

Figure 4.2: Branching ratios of the lightest neutralino into the single-photon signature, with varying neutralino mass.

4.4 FASER Experiment

The FASER experiment [280, 281] is a cylindrical detector that has recently been installed inside the TI12 tunnel, 480 m from the ATLAS IP along the beam collision axis line of sight. The detector is composed of tracking stations, scintillators, and a calorimeter. The cylinder axis is along the extended beam collision axis. Its decay volume has a radius of 10 cm and a length of 1.5 m. It is currently running during Run 3 of the LHC and is expected to collect data from proton-proton collisions of around $150\,\text{fb}^{-1}$ integrated luminosity. At the front

end of FASER, an additional emulsion detector known as FASERν [342, 343] has been installed, which is aimed at detecting high-energy neutrinos produced at the ATLAS IP. In this work, we do not study the potential of FASERν.

A follow-up experiment – FASER2 [281] – is currently slated to be operated during the HL-LHC period. If it is to be installed at the same position as FASER, it will be at a distance of 480 m from the ATLAS IP. Otherwise, it could be one of the experiments to be hosted at the FPF [317], 620 m from the ATLAS IP, also along the beam axis. We expect the difference between 480 m and 620 m distance to the IP to lead to only relatively minor changes in the sensitivity reach, as discussed in Ref. [317]. For this study, we work with the geometrical setup of a radius of 1 m and a length of 5 m for the FASER2 decay fiducial volume, and consider it 480 m away from the IP. By the end of Run 5 at the LHC, FASER2 should have collected about $3\,\text{ab}^{-1}$ integrated luminosity of collision data. Similarly, an emulsion detector has been proposed to be installed at the front face of FASER2, known as FASERν2. We will assume the detector components of FASER2 and hence detection principles and efficiencies are similar to those of FASER, except for the different geometrical acceptances.

In Ref. [315], the authors studied axion-like particles (ALPs) at FASER, where the ALPs decay to *a pair* of photons. They estimated that the calorimeter spatial resolution should be sufficiently good for resolving the two photons with an efficiency of about 50%, and the background should be negligible for diphoton events. Here, our signature includes only *one* photon. To provide a discussion on the expected background level, we follow the arguments given in Ref. [344]. At FASER, the single photons are detected as high-energy deposits in the electromagnetic calorimeter. Other objects may also cause such deposits, *e.g.*, neutrinos interacting deep inside the calorimeter via charged-current interactions. In order to differentiate the photon signal, a pre-shower station has been installed right before the calorimeter [345] which first converts the photon, thereby identifying it. Moreover, during Run 3 of the LHC program, the FASER detector is planned to be upgraded with a high-precision preshower detector. This would allow to distinguish two very closely spaced highly energetic photons [346]. Furthermore, neutrinos and muons coming from the IP can penetrate the 100 m of rock in front of FASER and reach the detector with energies in the TeV scale. These neutrinos could interact with the detector resulting in energetic particles including individual photons. However, these energetic photons are accompanied by tens of charged particles, allowing to veto such events easily with the tracker stations. The muons could radiate high-energy photons as well, mainly via Bremsstrahlung, but the veto stations positioned right in front of the FASER decay volume [345] should enable the rejection of muon-associated events.[3] Finally, neutral pions produced in hadronic showers initiated by muons in the absorber-rock material could also constitute a background for our signal if the two photons produced in their decays cannot be spatially resolved or only one of them is observed.[4] In such a case, requiring an energy threshold for the signal may help since the photons from our signal are expected to be more energetic; see Ref. [344] for more details on the point of using energy thresholds. A detailed estimate, however, requires a full simulation of hadronic interactions inside the rock. In this work, we will assume zero background for

[3] One possible background that we neglect here could come from off-axis muons that can penetrate FASER without passing through the veto stations; estimating such a background would require a detailed simulation. We thank Max Fieg for bringing up this point.

[4] We thank Michael Albrow for bringing this to our attention.

our signal.

Since the search proposed here with the single-photon signature does not require the usage of the tracker, in principle the tracker volume could be considered as effectively part of the fiducial volume. Taking this into account would allow to enlarge the length of the fiducial volume of FASER and FASER2 by roughly 1 m [345] and 5 m [317], respectively, enhancing the sensitivity reach to some extent. In this work, we only comment on this possibility and choose to stay with the standard benchmark geometries, as given explicitly above.

There are several other past and ongoing experiments that should have sensitivity to a radiatively decaying light neutralino. These include beam-dump experiments such as LSND [347], E613 [348], MiniBooNE [349], E137 [350], and NA64 [351–353], as well as B-factory experiments such as BaBar [354] and Belle II [355, 356]. Typically, each of these experiments is optimized to primarily produce only a certain type of meson, at rates which could be higher than the LHC. Correspondingly, they can probe a subset of the RPV models we have presented here in a somewhat cleaner environment. The LHC has the advantage of producing all types of mesons at significant rates, thus providing a scenario-independent probe. However, given a signal, it could be difficult to disentangle the underlying model(s). Further, given the different center-of-mass energies (and hence the spectra of the produced neutralinos), and the detector layouts, the phase-space region probed by these other experiments may complement that probed by FASER. However, detailed simulations are required to make more precise statements; this is beyond the scope of the present work.

Further, limits coming from searches for heavy neutral leptons can also be relevant for us. We will include these in our plots in Section 4.6.

Finally, we note that our signature could also be probed by FACET – a proposed new subsystem of the CMS experiment. In this study, however, we only focus on FASER and FASER2.

4.5 Simulation

We now proceed to describe the simulation procedure for estimating the number of signal events in the two experiments. We use the package FORESEE [275] to obtain the neutralino spectrum in the far-forward region, relevant for FASER and FASER2. As mentioned, the dominant sources of the neutralinos are the rare decays of mesons produced at the ATLAS IP:

$$M \to \tilde{\chi}_1^0 + \ell\,(\nu)\ . \tag{4.10}$$

Direct pair-production of neutralinos, in comparison, is expected to be several orders of magnitude lower [70, 225, 321], and is hence neglected here. We include all possible production modes for the different benchmark scenarios, summing over all meson contributions, to estimate the total number of produced neutralinos over the runtime of the experiment. However, it is necessary but not sufficient for the mother meson to decay into a neutralino: The meson itself may be long-lived, *e.g.*, charged pions and kaons. Thus, we require the meson to decay before hitting any absorber material or leaving the beam pipe; otherwise, the meson could be stopped and the neutralino is no longer boosted in the direction of FASER. Keeping this in mind, we use FORESEE to determine the neutralino production rate and spectrum from the meson spectrum by specifying the decay branching ratios corresponding

Detector	$\mathcal{L}$	$\sqrt{s}$	**L**	**Δ**	**R**
FASER	$150\,\mathrm{fb}^{-1}$	14 TeV	480 m	1.5 m	10 cm
FASER2	$3\,000\,\mathrm{fb}^{-1}$	14 TeV	480 m	5 m	1 m

Table 4.2: Integrated luminosities and geometries of the detectors used in the simulations. Here, $\mathcal{L}$, $\sqrt{s}$, **L**, **Δ**, and **R** label, respectively, the integrated luminosity, the collider center-of-mass energy, the distance from the IP, the detector length, and the detector radius.

to Eq. (4.10). The generated spectrum is two-dimensional, in terms of angle and momentum.

We also use FORESEE to compute the probability for the neutralino to decay inside the detector volume. See Table 4.2 for the values corresponding to the detector position and geometry we employ in our simulation for FASER and FASER2. We take into account the full neutralino lifetime, $\tau_{\tilde{\chi}_1^0}$, as well as its kinematics. The former is computed using all possible decay channels of the neutralino (including the decay into pseudoscalar and vector mesons) as a function of its mass and the non-vanishing RPV couplings, *cf.* the discussion in Section 4.3. However, in the numerical results presented in the next section, we have chosen an explicit signal for detecting the neutralino decay. Although all neutralino decays inside the detector are technically visible, we estimate the signal strength based on the specific radiative mode alone. This is done to avoid the consideration of background events; the decay into a neutrino and a photon gives a clean and unique signature.

Given the neutralino spectra, we estimate the number of decays that occur inside the detector defined by its position and geometry. For the analysis, the simulation takes into account the distance L between the ATLAS IP and the FASER detector, and the acceptance rate $P[\tilde{\chi}_1^0]$ in terms of the neutralino's three-momentum, its position of production (accounting for the mesons' lifetimes), as well as the lifetime of the neutralino itself. In our simulation, we do not make any momentum cuts. By further specifying the branching ratio into the radiative mode, the simulation counts the number of signal events passing the selection criteria. Thus, we can finally estimate the number of single-photon neutralino decay observations,

$$N_{\tilde{\chi}_1^0}^{\mathrm{obs}} = P[\tilde{\chi}_1^0] \cdot \mathrm{BR}\left[\tilde{\chi}_1^0 \to (\gamma + \nu_i\,, \gamma + \bar{\nu}_i)\right] \cdot \sum_{\mathrm{mesons}} N_{\tilde{\chi}_1^0}^{\mathrm{prod}}\,. \tag{4.11}$$

We stress again that we assume zero background, *cf.* the discussion in Section 4.4. Further, we assume a detector efficiency of 100%.

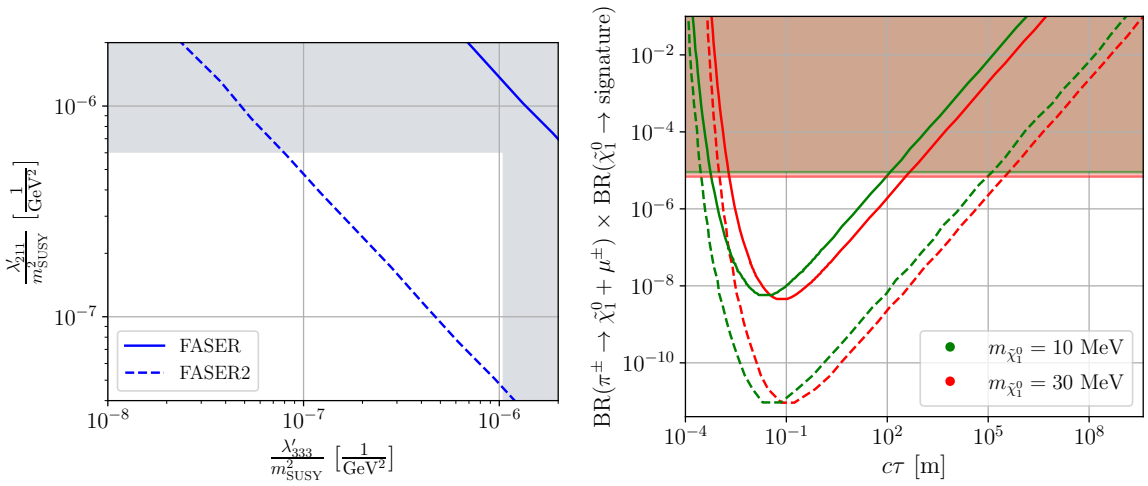

Figure 4.3: Sensitivity reach for `FASER` (solid lines) and `FASER2` (dashed lines) for the benchmark scenario **B1**, *cf.* Table 4.1. The left plot shows the sensitivity reach in the production coupling ($\frac{\lambda'_{211}}{m^2_{\text{SUSY}}}$) vs. decay coupling ($\frac{\lambda'_{333}}{m^2_{\text{SUSY}}}$) plane, for a neutralino mass of 30 MeV. The gray areas are excluded by the low-energy bounds, also given in Table 4.1. The right plot shows the sensitivity reach in BR($\pi^\pm \to \tilde{\chi}^0_1 + \mu^\pm$)×BR($\tilde{\chi}^0_1 \to$ signature) as a function of the neutralino decay length, $c\tau$, for $m_{\tilde{\chi}^0_1} = 10$ and 30 MeV. The shaded regions correspond to existing constraints from HNL searches.

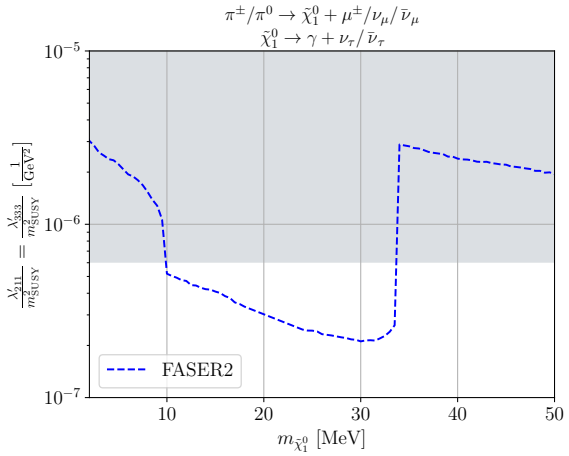

Figure 4.4: Sensitivity reach in the neutralino mass-coupling plane for `FASER2` for the same physics scenario as in **B1** but with variable neutralino mass. The production ($\frac{\lambda'_{211}}{m^2_{\text{SUSY}}}$) and decay ($\frac{\lambda'_{333}}{m^2_{\text{SUSY}}}$) couplings have been set equal. The gray areas are excluded by the low-energy bounds.

4.6 Numerical Results

We now present our numerical results. For the sensitivity limits, we require the observation of 3 radiative decays of the lightest neutralino in the detector for an integrated luminosity at the LHC of 150 fb^{-1} for `FASER`, and 3 000 fb^{-1} for `FASER2`. This corresponds to a potential 95 % confidence-level exclusion limit under the assumption of vanishing background.

We first show, in Fig. 4.3, results for the benchmark scenario **B1** of Table 4.1. On the left, we plot the sensitivity in the $\lambda^{\rm P}/m^2_{\rm SUSY} = \lambda'_{211}/m^2_{\rm SUSY}$ versus $\lambda^{\rm D}/m^2_{\rm SUSY} = \lambda'_{333}/m^2_{\rm SUSY}$ plane for a fixed neutralino mass of 30 MeV. In gray we include the low-energy bounds given in Table 4.1, for fixed sfermion masses of 1 TeV (the same choice is taken for the other model-dependent plots in this section). We see that FASER has no new sensitivity for this scenario beyond the low-energy bounds, whereas FASER2 can extend the reach by more than an order of magnitude in $\lambda^{\rm P}/m^2_{\rm SUSY}$ or $\lambda^{\rm D}/m^2_{\rm SUSY}$ in units of GeV^{-2}. The right plot in Fig. 4.3 is model-independent, in that it is valid for any new, neutral long-lived particle (LLP) produced in charged pion decays, which decays with a signature at FASER or FASER2, here specifically with a mass of 10 or 30 MeV. The maximum sensitivity (the minima of the curves) depends on the location of the detector, and also on the momentum distribution of the produced pions and, correspondingly, of the pions' decay product neutralinos [322]. That is why the minimum of the curve shifts to slightly smaller LLP lifetimes for lighter LLP masses, which are more boosted. We see that FASER (FASER2) can probe the product of the decay branching fractions of the charged pion into an LLP and a muon and the LLP into the signature, down to a few times 10^{-9} $\left(10^{-12}\right)$. We note that existing searches for heavy neutral leptons (HNLs), N, which mix with active neutrinos and are produced from pion decays, may be recast into bounds on the right plot. The leading bounds for HNLs of mass 10 MeV and 30 MeV in $\pi^\pm \to \mu^\pm + N$ decays stem from two peak searches: Ref. [357], and Ref. [358], respectively. The former shows a bound of 10^{-5} on BR$(\pi^\pm \to \mu^\pm + N)$ for mass 10 MeV. Ref. [358] presents 90% confidence-level exclusion limits in the mixing-squared vs. mass plane; we convert these into limits on BR$(\pi^\pm \to \mu^\pm + N)$ [359], obtaining a bound of 6.9×10^{-6} for mass 30 MeV. These two bounds are model-independent and are plotted as shaded areas in the right plot of Fig. 4.3, using BR$(\tilde{\chi}^0_1 \to \text{signature}) = 1$. One easily observes that FASER and FASER2 are sensitive to large parts of the parameter space beyond these existing bounds.

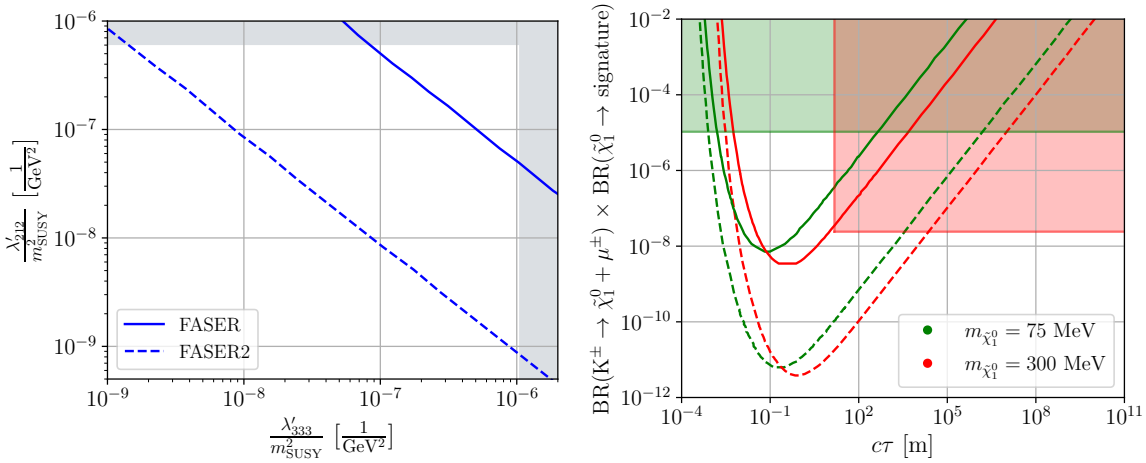

Figure 4.5: As in Fig. 4.3 but for the benchmark scenario **B2** with $m_{\tilde{\chi}^0_1} = 75$ MeV, *cf.* Table 4.1. The right plot shows the sensitivity reach in BR$(K^\pm \to \tilde{\chi}^0_1 + \mu^\pm)\times$BR$(\tilde{\chi}^0_1 \to$ signature$)$ as a function of the neutralino decay length, $c\tau$, for $m_{\tilde{\chi}^0_1} = 75$ and 300 MeV.

Fig. 4.4 shows the sensitivity reach of FASER2 for the benchmark scenario **B1** of Table 4.1, but allowing the neutralino mass to vary and fixing $\lambda^P = \lambda^D$. The gray band, as before, indicates the low-energy constraints on the couplings. Since FASER does not provide any new sensitivity reach beyond these low-energy bounds, we do not depict it in the plot. We see a maximum sensitivity is reached for neutralino masses between 10 and 35 MeV. In general, the sensitivity reach in the couplings improves; for instance, as we increase the neutralino mass up to 30 MeV, and again in the region beyond 35 MeV. Heavier neutralinos translate into shorter lifetimes, and hence more decays of the neutralino within the volume of FASER2, *cf.* Eq. (4.6). There is, however, a sharp drop in sensitivity near the neutralino mass, $m_{\tilde{\chi}_1^0} \sim 34$ MeV. This is the threshold for the decay of charged pions to neutralinos accompanied by a muon. The branching fraction of the neutral pion mode, $\pi^0 \to \tilde{\chi}_1^0 + \nu_\mu$, is suppressed by the short lifetime.

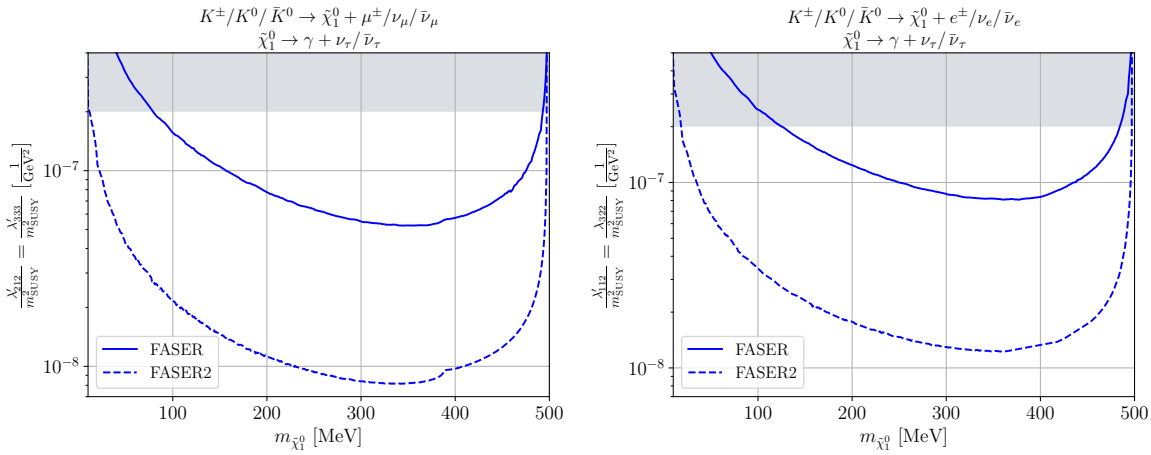

Figure 4.6: As in Fig. 4.4 but for the benchmark scenarios **B2** (left) and **B3** (right). The sensitivity reach corresponds to FASER (solid line) and FASER2 (dashed line).

In Figs. 4.5 and 4.6 (left), we display the sensitivity plots for benchmark scenario **B2**. The left plot of Fig. 4.5 shows that now both FASER and FASER2 have significant new reach in the couplings, $\lambda^{\rm P}$ and $\lambda^{\rm D}$, for $m_{\tilde{\chi}_1^0} = 75$ MeV. The right plot in Fig. 4.5 looks similar to the right plot of Fig. 4.3, but it is now a plot of the branching ratio product $\text{BR}(K^\pm \to \tilde{\chi}_1^0 + \mu^\pm) \times \text{BR}(\tilde{\chi}_1^0 \to \text{signature})$ versus the neutralino decay length, $c\tau$, and we have considered heavier LLP masses: 75 and 300 MeV. Similar to **B1**, we overlap these results with existing bounds from searches for HNLs from kaon two-body decays, $K^\pm \to \mu^\pm + N$. Refs. [360, 361] give the strongest current limits for HNL masses of 75 MeV and 300 MeV. Ref. [360] is a peak search and bounds the HNL mixing-squared with the muon neutrino at 1.3×10^{-5} for HNL mass of 75 MeV. Ref. [361] searches for invisible particles and places a limit of 10^{-8} on the mixing-squared. We convert these limits into bounds on $\text{BR}(K^\pm \to \mu^\pm + N)$ and obtain 10^{-5} and 2.4×10^{-8}, respectively. We depict these bounds in the right plot of Fig. 4.5, using $\text{BR}(\tilde{\chi}_1^0 \to \text{signature}) = 1$. In particular, since Ref. [361] is a missing-energy search, the limits are valid only for proper decay length larger than 15 m, as explicitly mentioned in the abstract of the paper. We find that FASER and FASER2 can probe the

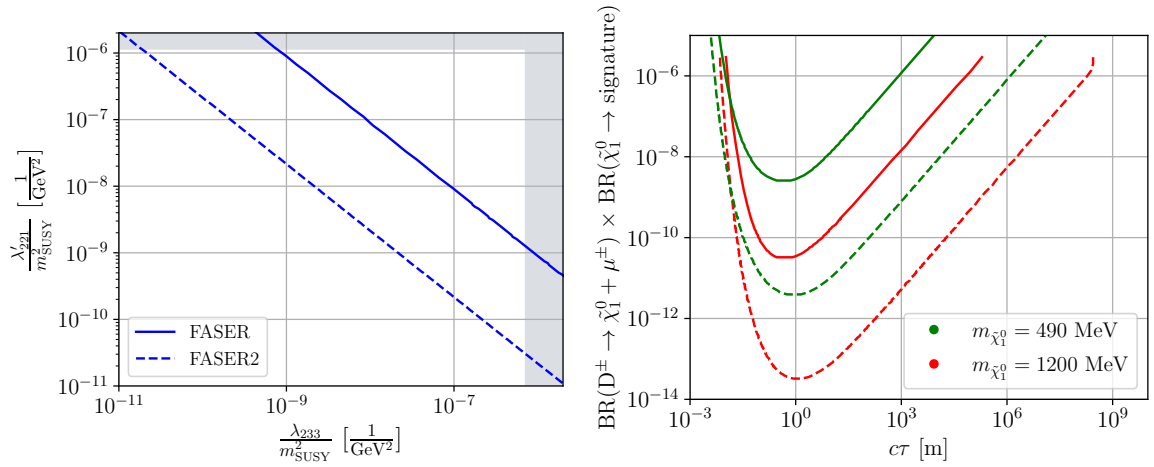

Figure 4.7: As in Fig. 4.3 but for the benchmark scenario **B4** with $m_{\tilde{\chi}_1^0} = 300\,\text{MeV}$, *cf.* Table 4.1. The right plot shows the sensitivity reach in $\text{BR}(D^\pm \to \tilde{\chi}_1^0 + \mu^\pm) \times \text{BR}(\tilde{\chi}_1^0 \to \text{signature})$ as a function of the neutralino decay length, $c\tau$, for $m_{\tilde{\chi}_1^0} = 490$ and $1\,200\,\text{MeV}$.

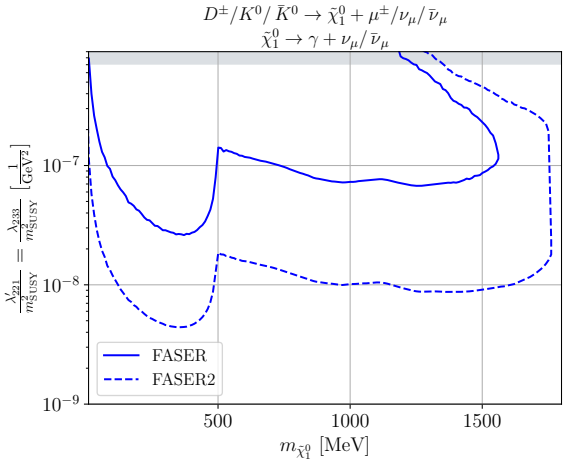

Figure 4.8: As in Fig. 4.4 but for the benchmark scenario in **B4** while varying the neutralino mass. The sensitivity reach corresponds to `FASER` (solid line) and `FASER2` (dashed line).

BR-product down to values significantly lower than these current limits.

In the neutralino mass-couping plane plot of Fig. 4.6 (left), we observe that the sensitivity at `FASER2` is reduced for lower masses compared to that in benchmark scenario **B1**, but, unlike the pion case, is robust over the entire higher-mass regime, right up to the kaon mass. This is because even though the charged decay production mode is kinematically forbidden beyond $m_{\tilde{\chi}_1^0} = m_{K^\pm} - m_{\mu^\pm} \approx 390\,\text{MeV}$ – leading to the small bump in the plot at that point – the neutral decay mode has a comparable branching fraction.

The two plots of $\lambda^{\text{P}}/m^2_{\text{SUSY}}$ vs. $\lambda^{\text{D}} m^2_{\text{SUSY}}$ and branching ratio product vs. $c\tau$ for **B3** with neutralino mass of 200 MeV, are very similar to Fig. 4.5 for **B2** and are hence not

shown explicitly here. In Fig. 4.6 (right), we present the sensitivity plot for scenario **B3** for $\lambda'_{112} = \lambda^{\mathrm{P}} = \lambda^{\mathrm{D}} = \lambda_{322}$, as a function of the neutralino mass. We note that for $m_{\tilde{\chi}_1^0} \gtrsim 2m_\mu$, the decay mode $\tilde{\chi}_1^0 \to \mu^\pm \mu^\mp \nu_\tau + \text{c.c.}$ opens up, leading to additional visible events. These are not included in Fig. 4.6 (right).

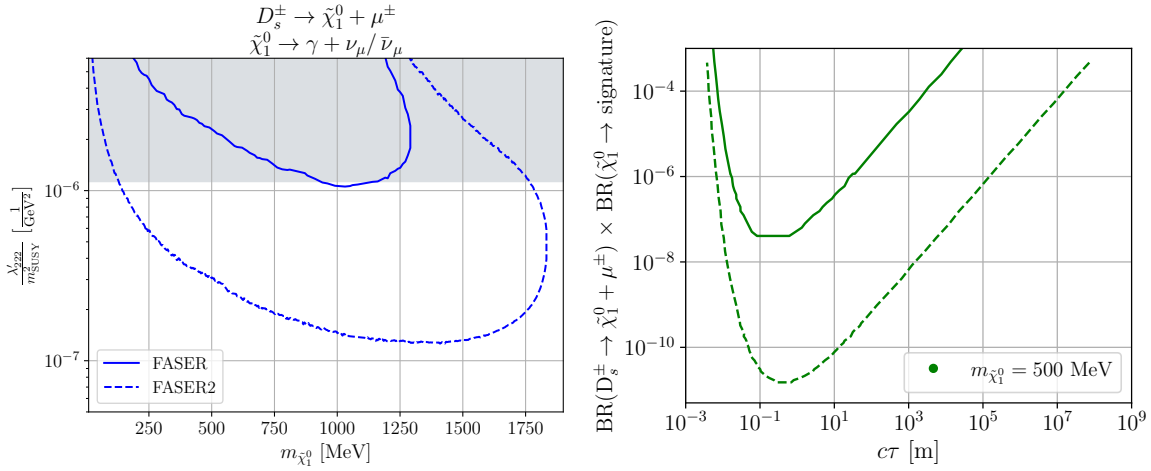

Figure 4.9: The left plot is as in Fig. 4.4 but for the single coupling benchmark scenario in **B5** while varying the neutralino mass. The right plot shows the sensitivity reach in $\mathrm{BR}(D_S^\pm \to \tilde{\chi}_1^0 + \mu^\pm) \times \mathrm{BR}(\tilde{\chi}_1^0 \to \text{signature})$ as a function of the neutralino decay length, $c\tau$, for $m_{\tilde{\chi}_1^0} = 500\,\mathrm{MeV}$. The sensitivity reaches correspond to `FASER` (solid line) and `FASER2` (dashed line).

In Figs. 4.7 and 4.8, we show the corresponding plots for the benchmark involving both D and K mesons – scenario **B4**. One interesting feature in the mass-coupling plane is the kink in the sensitivity curve near the kaon mass, $m_{K^0} \sim 497\,\mathrm{MeV}$. This is because for $m_{\tilde{\chi}_1^0} \gtrsim m_{K^0}$, the kaon production mode, $K^0/\bar{K}^0 \to \tilde{\chi}_1^0 + \nu_\mu/\bar{\nu}_\mu$ switches off. Since kaons are more abundant than D mesons at the LHC, this leads to reduced senstivity beyond this threshold. For larger masses, the neutralino has decay modes into K^0 and K^{*0} plus neutrino opening up at the respective mass thresholds; as before, we only count the photon events as signal. There is an additional interesting feature for this scenario: The sensitivity curve starts to 'turn back' in the large coupling, large mass region indicating a drop in sensitivity. This happens as the lifetime of the neutralino becomes too short, decaying well before reaching `FASER` or `FASER2`; this effect is made more acute by the additional decay modes that open up. To our knowledge, there are no existing searches for HNLs in $D^\pm \to \mu^\pm + N$ decays; therefore, we do not place any existing bounds in the right plot of Fig. 4.7.

Fig. 4.9 shows the sensitivity reach for scenario **B5**, where only one RPV coupling is switched on (thus, there is no coupling-coupling plane plot). The left plot shows the sensitivity reach of `FASER` and `FASER2` in the mass-coupling plane. Once again, for the plots, we do not consider the additional decay modes into η, η' or ϕ plus neutrino that open up at the respective mass thresholds, for our signature. The large mass, large coupling regime has reduced sensitivity for the same reason stated above. The right plot then contains the sensitivities of `FASER` and `FASER2` to the decay branching fraction product as a function of $c\tau$ for $m_{\tilde{\chi}_1^0} = 500\,\mathrm{MeV}$. For this plot, as in **B4**, there is no existing limit that can be obtained from an HNL search in

$D_s^\pm \to \mu^\pm + N$ decays.

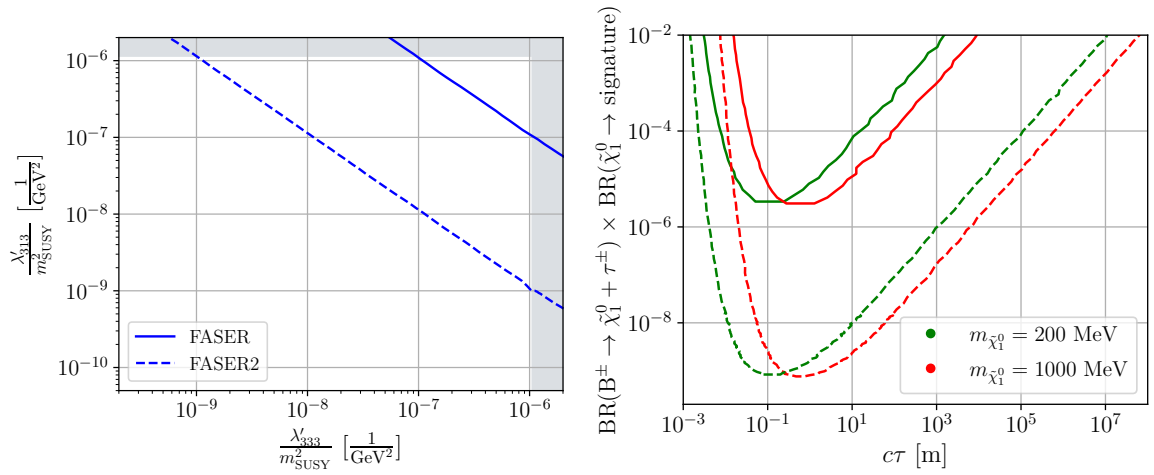

Figure 4.10: As in Fig. 4.3 but for the benchmark scenario **B6** with $m_{\tilde{\chi}_1^0} = 1\,\text{GeV}$, *cf.* Table 4.1. The right plot shows the sensitivity reach in BR($B^\pm \to \tilde{\chi}_1^0 + \tau^\pm$)×BR($\tilde{\chi}_1^0 \to$ signature) as a function of the neutralino decay length, $c\tau$, for $m_{\tilde{\chi}_1^0} = 200$ and $1\,000\,\text{MeV}$.

Finally, Figs. 4.10 and 4.11 contain the sensitivity plots for benchmark scenario **B6**, involving B mesons. We observe in the right plot of Fig. 4.10, that the reaches in the branching ratio product are weaker than those in the previous scenarios, because the production rates of the B mesons are orders-of-magnitude smaller than those of the lighter mesons at the LHC. As in the previous two benchmark scenarios, we do not find an existing search for HNLs in $B^\pm \to \tau^\pm + N$ decays that could be recast into bounds relevant to us, in the BR-product vs. $c\tau$ plane. In Fig. 4.11, as before, we see that the sensitivity in the mass-coupling plane is robust across the kinematically allowed mass range since the neutral mode is available even when the charged mode is switched off for $m_{\tilde{\chi}_1^0} \geq m_{K^\pm} - m_{\tau^\pm}$. This time the drop in sensitivity in the large mass, large coupling region is milder compared to the previous two cases as there are no additional decay modes contributing.

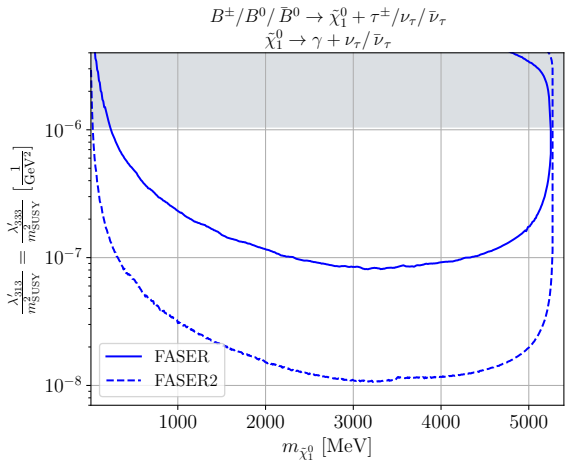

Figure 4.11: As in Fig. 4.4 but for the benchmark scenario in **B6** while varying the neutralino mass. The sensitivity reach corresponds to `FASER` (solid line) and `FASER2` (dashed line).

4.7 Conclusions

We have estimated the sensitivity reach of `FASER` and `FASER2` at the LHC, for a sub-GeV bino-like lightest neutralino decaying to a photon in the context of R-parity-violating supersymmetry. With R-parity broken, the lightest neutralino can be lighter than the GeV scale, or even massless, without violating observational and experimental bounds, as long as it decays. Assuming the lightest neutralino is the lightest supersymmetric particle (LSP), it can be produced from rare meson decays, and can decay to a photon and a neutrino, via certain RPV couplings.

In the sub-GeV mass range, since the RPV couplings are required to be small by existing constraints, the bino-like neutralino is expected to have a long lifetime. Once produced from mesons' decays at the LHC, it is highly boosted in the very forward direction. Therefore, we have chosen to focus on the experimental setups of `FASER` and `FASER2` for observing the single-photon signature resulting inside the detector decay volumes.

We have considered several theoretical benchmark scenarios and performed Monte Carlo simulations in order to determine the projected sensitivity reaches at `FASER` and `FASER2`. Our study has found that these experiments are sensitive to parameter space beyond the current bounds by orders of magnitude.

5

Recasting Bounds on Long-lived Heavy Neutral Leptons in Terms of a Light Supersymmetric R-parity Violating Neutralino

5.0 Preface

The contents of this chapter and the supplementary material presented in Appendix C are based on the following publication:

- H. K. Dreiner, D. Köhler, S. Nangia, M. Schürmann, and Z. S. Wang,
  Recasting Bounds on Long-lived Heavy Neutral Leptons in Terms of a Light Supersymmetric R-parity Violating Neutralino,
  Published in JHEP 08 (2023) 058, arXiv:2306.14700 [hep-ph].

The idea to recast the heavy neutral lepton (HNL) sensitivity limits in terms of the RPV-MSSM was independently thought of by Herbi Dreiner (in the context of BEBC) after stimulating discussions with Subir Sarkar and Giacomo Marocco; Saurabh Nangia after an insightful comment raised by the anonymous referee of the publication presented in Chapter 4 of this thesis and the author after calculating the bounds on the RPV-MSSM coming from the invisible widths of the mesons in a different context. The author numerically integrated the result of the neutralino decay width via $LL\bar{E}$ operators, performed by Martin Schürmann. Further, all the numerical framework and simulation provided in this chapter, including the data corresponding to `FASER(2)`, `BaBar`, `MoEDAL-MAPP(2)`, and the invisible widths, were developed by the author. Finally, all benchmark plots of RPV scenarios to which HNL searches would be sensitive were provided by the author.

In Chapter 3, we explored the diverse landscape of the RPV-MSSM which can be divided into three distinct regimes. There, our focus was on a specific scenario where the LSP decays immediately within the detector, providing crucial signatures for analysis. By considering different LSPs and couplings, we have determined the current coverage of such scenarios. In this chapter now, our focus shifts: we consider the case where the size of the couplings and mass of the LSP is so small that it decays outside of nearby detectors, necessitating detection in far-forward detectors instead.

Previously, in Chapter 4, we explored an example of an LLP within the RPV framework; we studied the longevity of the neutralino and its decay in a distant detector, searching for a unique signature. Now, we extend this approach to achieve near-comprehensive coverage of the RPV model space.

HNLs, also called sterile neutrinos N, are singlets under the SM gauge group. The term "sterile neutrino" comes from their exclusive interaction with SM fields through a Higgs Yukawa coupling to the lepton doublet. The neutral nature of N allows the introduction of a Majorana mass term consistent with SM gauge invariance. After breaking the electroweak symmetry, the SM Higgs field acquires a nonzero vacuum expectation value v, contributing to the mass terms for both active and sterile neutrinos. The mass eigenstates in the active-plus-sterile sector are mixtures of ν and N, characterized by small mixing angles and large splitting between mass scales of the sterile and active neutrinos. In collider phenomenology, only the masses of the HNL(s) and the values of the mixing angles $|U_\alpha|$ can be measured. Therefore, from a phenomenological point of view, a simplified approach is sufficient, where only one sterile neutrino has to be described and only four parameters are needed: the sterile neutrino mass M_N and its mixtures with all three active neutrinos $|U_\alpha|$.

In recent years GeV-scale HNLs have attracted considerable attention. Remarkably, the experimental search strategy can be applied for neutralinos in the same mass range. By recasting the experimental sensitivity for HNLs, we can derive the potential sensitivity for RPV couplings from decaying neutralinos. As we have seen in the previous chapter, it is possible for light neutralinos to be produced in proton-proton collisions. Several experiments can cover the parameter space of different trilinear couplings, including `T2K` and `BEBC`. These experiments have already accumulated a wealth of data and provide a unique opportunity to further constrain the RPV parameter space. Evaluating each scenario allows us to derive new limits on couplings that are up to three to four orders of magnitude above current constraints. In this study, we additionally find several benchmark scenarios to determine the sensitivity of future experiments such as `FASER`, `DUNE`, and `MoEDAL-MAPP`.

Furthermore, it is worth noticing that the presence of bilinear couplings leads to mixing between the light bino and the three light neutrinos. Consequently, experimental searches that constrain the mixing between HNLs and neutrinos also impose constraints on these bilinear couplings. We find that the HNL searches from `PIENU`, `NA62`, and `T2K` have sensitivity to regions beyond the current limits at low neutralino masses below 500 MeV.

To summarize, this chapter presents a simple reinterpretation of recent HNL searches in the context of RPV. Many experiments often present their results only for a limited number of simple models due to the complexity and time-consuming nature of running full simulations. Therefore, reinterpretation approaches, such as the one we take here, can be valuable tools; our work demonstrates the benefits and convenience of such methods by applying them to re-evaluate the constraints on HNLs. We place new constraints on the lightest neutralinos in the RPV-SUSY models. This, in turn, should encourage further research using these reinterpretation methods.

5.1 Introduction

With the discovery of a Standard-Model (SM)-like Higgs boson at the LHC in 2012 [4, 5], the SM is complete. Yet many questions beyond the Standard Model (BSM) remain. One avenue of exploration which has received considerable attention is new light, feebly interacting particles [70, 210, 362–369]. Such exotic states are predicted in many BSM theories and are often long-lived. Theoretical candidates for such long-lived particles (LLPs) range from heavy neutral leptons (HNLs), axion-like particles, dark scalars, and dark photons, to electroweakinos in variations of supersymmetric models, inelastic dark matter (DM), and many more. See, *e.g.*, Refs. [209, 210, 284, 370] for reviews on LLPs. They are usually motivated as explanations of either the non-vanishing active neutrino masses or of dark matter and could have a spin of $0, \frac{1}{2}, 1, \ldots$, and a mass usually ranging from the sub-MeV scale up to the multi-TeV scale.

As an example, the HNLs (labeled as N in this work) are proposed hypothetical spin-half fermions that are SM-singlets which mix with the light active neutrinos. For certain mass values, they can explain simultaneously the neutrino masses, the observed dark matter, as well as the baryon asymmetry of the Universe [371]. They can give light neutrinos Dirac masses via the Yukawa term LHN in the Lagrangian with L and H being the lepton and Higgs doublets. This implies unnaturally small Yukawa couplings given the tiny neutrino masses [118, 289, 372]. One can also write down a Majorana mass term in the Lagrangian, leading to light Majorana neutrinos via the seesaw mechanisms [119, 373–376]. While the vanilla type-I seesaw mechanism demands the mixing parameters should be small for the tiny active neutrino masses, larger values of mixing are legitimately conceived in other variations such as the linear seesaw model [377–379] and inverse seesaw model [380, 381]. Therefore, in phenomenological studies, the HNL mass and the mixing angles with the SM neutrinos are often assumed to be independent parameters.

Via mixing with the active neutrinos, the HNLs can participate in both charged-current and neutral-current interactions, coupled to both gauge bosons directly and the Higgs boson indirectly. They can thus be produced from decays of these bosons or from mesons, or through direct production at colliders. The HNL can decay leptonically or semi-leptonically, leading to a variety of signatures at the different experimental facilities. In particular, GeV-scale HNLs have received substantial attention in recent years, for they could originate from rare decays of mesons, which are copiously produced, *e.g.*, at beam-dump experiments, B-factories, and high-energy hadron colliders. Given the strict experimental upper bounds on the mixing of the HNLs and the active neutrinos, the more recent focus has been on small mixing angles, for which the GeV-scale HNLs are usually long-lived. Searches for these long-lived HNLs have been performed via many different signatures, including searches for missing energy, peak searches, as well as searches for displaced vertices (DV). See, *e.g.*, Refs. [382, 383] for summaries of these searches. Moreover, one could use the uncertainty on the measurements of the invisible decay width of mesons to put upper bounds on the long-lived HNLs, which contribute to the invisible decay width.

Besides the HNLs, supersymmetric electroweakinos, including charginos and neutralinos, are often considered as LLP candidates. See for instance Refs. [384, 385]. In particular, a specific type of light neutralino in the GeV mass scale is still allowed by all observational and experimental constraints [68, 69, 71, 86, 88, 152, 386–391]; they are necessarily bino-like [68,

69] and have to decay to avoid overclosing the Universe [73, 82, 392]. One possibility is to consider R-parity-violating supersymmetry (RPV-SUSY) (see Refs. [53, 99, 303] for reviews), where the light binos decay via small but non-vanishing RPV couplings (see Ref. [328] for a detailed study of light bino decays). The minimal version is known as the R-parity-violating Minimal Supersymmetric Standard Model (RPV-MSSM) [54]. The RPV-MSSM solves the SM hierarchy problem as in the MSSM, and also predicts a very rich phenomenology at colliders [67, 149, 208, 393]. *A priori* it is unknown if R-parity is conserved or broken, SUSY models with R-parity conservation or violation are equally legitimate, *e.g.*, see Refs. [52, 55]. Moreover, the RPV-MSSM can explain several experimental anomalies reported in recent years including the B-meson anomalies [304–307, 309], the ANITA anomaly [308, 310], as well as the anomalous magnetic moment of the muon [306, 307, 309]. If R-parity is broken, one can write down operators which violate baryon- or lepton-number. Allowing all these operators to be non-vanishing would lead to a too fast proton decay rate, in conflict with the current experimental measurements [65, 101], unless all their couplings are extremely small. Therefore, we assume the discrete anomaly-free baryon triality symmetry B_3 [122, 145, 394], so that baryon-number is conserved. In this work, we restrict ourselves to the lepton-number-violating terms only. Further, the light bino is the lightest supersymmetric particle (LSP) in our study and decays only into SM particles via RPV couplings.

Via the lepton-number-violating RPV operators, the light bino decays lead to very similar final states as the NHL decays. Moreover, the corresponding RPV couplings are all bounded to be small by various low-energy observables and collider searches [99, 157, 311, 395, 396]. The GeV-scale binos are hence expected to be long-lived, too, resulting in signatures such as missing energy and displaced vertices at various experiments. These similarities raise the question: is it possible to recast the extensive exclusion bounds on the HNLs in the literature into corresponding bounds on the light binos in the RPV-SUSY? In this work, we answer this question positively, by compiling a list of bounds on long-lived HNLs obtained in searches for all types of signatures mentioned above and recasting them into exclusion limits on the RPV-SUSY couplings as functions of the light bino mass for a selected list of benchmark scenarios.[1] We focus on exclusion bounds acquired in past experiments, as well as predicted search sensitivities for experiments that are ongoing or under construction. For future (and not yet approved) experiments, we consider only `MoEDAL-MAPP2` [397, 398] and `FASER2` [281] with 300 and 3000 fb^{-1} integrated luminosity, respectively, as they would be the successors of some ongoing experiments at the LHC, while the other future concepts such as `MATHUSLA` [283–285], and `ANUBIS` [287] are independent ones and are hence not studied here. We do not consider the approved experiment `Hyper-Kamiokande` [399, 400] for there is no available HNL-search sensitivity prediction that can be used with our recasting methods.

In the following section, we give the model basics of light binos in the RPV-SUSY and of the HNLs that mix with active neutrinos. The considered experiments are introduced in Sec 5.3, along with an explanation of our recasting procedure. We then present our numerical results for some representative benchmark scenarios in Sec. 5.4. Finally, in Sec. 5.5 we conclude the paper with a summary.

[1] Recently during the completion of this work, Ref. [383] appeared on arXiv; it employed similar strategies to recast the bounds on the HNLs in the minimal scenarios into those on the HNLs in effective field theories.

5.2 Model basics

5.2.1 RPV-MSSM with a light bino

In the R-parity-violating MSSM, the usual MSSM superpotential is extended by the following terms [54, 58]:

$$W_{\text{RPV}} = \kappa_i L_i H_u + \frac{1}{2}\lambda_{ijk} L_i L_j \bar{E}_k + \lambda'_{ijk} L_i Q_j \bar{D}_k + \frac{1}{2}\lambda''_{ijk} \bar{U}_i \bar{D}_j \bar{D}_k \,, \tag{5.1}$$

where L_i, $\bar{E}_i$, Q_i, $\bar{U}_i$, and $\bar{D}_i$ are chiral superfields with generation indices $i, j, k \in \{1, 2, 3\}$ and H_u is one of the MSSM Higgs superfields. The λ_{ijk}, λ'_{ijk} (and λ''_{ijk}) are dimensionless Yukawa couplings, which imply lepton- (baryon-) number violating interactions and κ_i are dimensionful bilinear couplings violating lepton number. The Lagrangian in superfield-component form, as well as a complete list of RPV Feynman rules can be found, *e.g.*, in Appendix L of Ref. [401].

The RPV-MSSM allows for an unstable light long-lived neutralino, which we focus on here. A very light neutralino is necessarily dominantly bino-like [68] and a light bino currently avoids all experimental and astrophysical constraints even if it is massless [86, 152, 386]. In the following, we provide a concise overview of the production and decay of the lightest neutralino via $LL\bar{E}$ or $LQ\bar{D}$ operators. Moreover, for simplicity, we consider the lightest neutralino to be the LSP in this work. Note that we use the two-component fermion notation reviewed in Ref. [401].

Neutralino production and decay via $LL\bar{E}$ operators

For non-zero $LL\bar{E}$ couplings, neutralinos can be produced through charged lepton decays and can decay to lighter leptons. We provide the explicit general forms of the total decay widths for both the charged lepton and neutralino decays, employing the matrix element and necessary phase space integration in Appendix C.1. For all the relevant processes, we assume that all sfermions appear at the energy scale of the decaying particle as mass degenerate, *i.e.*, $m_{\tilde{f}} \simeq m_{\text{SUSY}} \gg m_{\tilde{\chi}_1^0}, m_{\ell^\pm}$. Further, the R-parity conserving neutralino gauge coupling is g' ($U(1)_Y$), since the neutralino is bino-like. As a result, we can write out the coefficients appearing in the matrix elements as, (*cf.* Appendix C.1)

$$c_{ijk} \simeq -\frac{\frac{1}{\sqrt{2}}\lambda_{ijk} g'}{m^2_{\text{SUSY}}} \qquad \text{and} \qquad k_{ijk} \simeq \frac{\sqrt{2}\lambda_{ijk} g'}{m^2_{\text{SUSY}}} \,. \tag{5.2}$$

Using Eq. (C.1), the relevant production widths can then be expressed as

$$\Gamma(\ell_k^\pm \to \tilde{\chi}_1^0 + \nu_i + \ell_j^\pm) = \Gamma_{LL\bar{E}}(\ell_k^\pm; \tilde{\chi}_1^0, \nu_i, \ell_j^\pm)[k_{ijk}, c_{ijk}, c_{ijk}] \,, \tag{5.3}$$

$$\Gamma(\ell_k^\pm \to \tilde{\chi}_1^0 + \bar{\nu}_i + \ell_j^\pm) = \Gamma_{LL\bar{E}}(\ell_k^\pm; \tilde{\chi}_1^0, \bar{\nu}_i, \ell_j^\pm)[c_{ikj}, k_{ikj}, c_{ikj}] \,. \tag{5.4}$$

Similarly, the total widths of the subsequent neutralino decays $\tilde{\chi}_1^0 \to \overset{(-)}{\nu}_i + \ell_j^- + \ell_k^+$ can be written as

$$\Gamma(\tilde{\chi}_1^0 \to \nu_i + \ell_j^- + \ell_k^+) = \Gamma_{LL\bar{E}}(\tilde{\chi}_1^0; \nu_i, \ell_j^-, \ell_k^+)[c_{ijk}, c_{ijk}, k_{ijk}]\,, \tag{5.5}$$
$$\Gamma(\tilde{\chi}_1^0 \to \bar{\nu}_i + \ell_j^- + \ell_k^+) = \Gamma_{LL\bar{E}}(\tilde{\chi}_1^0; \bar{\nu}_i, \ell_j^-, \ell_k^+)[c_{ikj}, k_{ikj}, c_{ikj}]\,. \tag{5.6}$$

Neutralino production and decay via $LQ\bar{D}$ operators

Via the $LQ\bar{D}$-operators mesons can decay into a bino accompanied by a lepton l_i. Subsequently, the bino decays via the same or another $LQ\bar{D}$-operator to a lepton and two quarks, where the latter again hadronize into a meson (for a light enough bino). We consider charged mesons M_{ab}^+ with quark flavor content $(u_a\,\bar{d}_b)$ as well as neutral mesons M_{ab}^0 composed of $(d_a\,\bar{d}_b)$ and their charge conjugated equivalents. Neutral mesons composed of $(u_a\bar{u}_b)$ only contribute to higher multiplicity processes as $M \to \tilde{\chi}^0 + l_i + M'$, where M' denotes a lighter meson and l_i a charged lepton. We do *not* consider them here, since these are phase space suppressed by two to three orders of magnitude [225]. Both the bino production and decay width are therefore given by Ref. [225]:

$$\Gamma(M_{ab} \to \tilde{\chi}_1^0 + l_i) = \frac{\lambda^{\frac{1}{2}}(m_{M_{ab}}^2, m_{\tilde{\chi}_1^0}^2, m_{l_i}^2)}{64\pi m_{M_{ab}}^3} |G_{iab}^{S,f}|^2 (f_{M_{ab}}^S)^2 \left(m_{M_{ab}}^2 - m_{\tilde{\chi}_1^0}^2 - m_{l_i}^2\right)\,, \tag{5.7}$$

$$\Gamma(\tilde{\chi}_1^0 \to M_{ab} + l_i) = \frac{\lambda^{\frac{1}{2}}(m_{\tilde{\chi}_1^0}^2, m_{M_{ab}}^2, m_{l_i}^2)}{128\pi m_{\tilde{\chi}_1^0}^3} |G_{iab}^{S,f}|^2 (f_{M_{ab}}^S)^2 \left(m_{\tilde{\chi}_1^0}^2 + m_{l_i}^2 - m_{M_{ab}}^2\right)\,, \tag{5.8}$$

where $\lambda^{\frac{1}{2}}(x,y,z) = \sqrt{x^2+y^2+z^2-2xy-2xz-2yz}$ is the square root of the Källén function and $l_i = \ell_i^\pm$ or ν_i depending on the charge of M_{ab}. The coefficients $|G_{iab}^{S,f}|^2$ include the trilinear RPV couplings and are defined in Ref. [225], together with the meson scalar decay constants $f_{M_{ab}}^S$.

Furthermore, the $L_iL_j\bar{E}_j$ and $L_iQ_j\bar{D}_j$ operators additionally open the decay mode $\tilde{\chi}_1^0 \to (\gamma + \nu_i, \gamma + \bar{\nu}_i)$ at the one-loop level, *cf.* Ref. [227], but this signature is not considered in the present paper since to our knowledge the corresponding HNL-decay has to-date not been searched for.

Besides the displaced-vertex signature related to the decay channels computed above, it is possible that the lightest neutralino is so long-lived that it does not decay inside the considered detector and appears as missing energy.

5.2.2 Heavy neutral leptons

Heavy neutral leptons are a common feature of many SM extensions attempting to give an underlying explanation of the observed neutrino sector. The simplest HNL model one can implement is

$$\mathcal{L} \supset i\hat{N}_\alpha^\dagger \bar{\sigma}^\mu \partial_\mu \hat{N}^\alpha - \left[(Y_\nu)_\alpha^i \left(\Phi^0 \hat{\nu}_i \hat{N}^\alpha - \Phi^+ \ell_i \hat{N}^\alpha\right) + \frac{1}{2} M_\beta^\alpha \hat{N}_\alpha \hat{N}^\beta + \text{h.c.}\right]\,, \tag{5.9}$$

where $i = 1, 2, 3$, Φ^+ and Φ^0 are the components of the SM $SU(2)_L$ Higgs doublet, and ℓ_i are the charged lepton mass eigenstates. Fields with a hat, $\hat{\nu}$ and $\hat{N}$, are the states before mass-diagonalizing the neutral lepton sector. $(Y_\nu)^i_\alpha$ are dimensionless Yukawa couplings and $M^\alpha_\beta = \mathrm{diag}(M_{\hat{N}_1}, ...)$ is a diagonal mass matrix. The index $\alpha = 1, 2, 3, \ldots$ labels the (arbitrary many) HNLs in the theory. During electroweak symmetry breaking, the Higgs obtains a vacuum expectation value (vev) $v/\sqrt{2}$ with $v = 246$ GeV, which gives rise to mixing of the HNLs $\hat{N}_\alpha$ with active neutrinos $\hat{\nu}_i$, described by the mass matrix $M_{\nu N}$:

$$M_{\nu N} = \begin{pmatrix} \mathbb{0}_{3\times 3} & M_D \\ M_D^T & M \end{pmatrix} . \tag{5.10}$$

Here, the off-diagonal entries are given by $(M_D)^i_\alpha = (Y_\nu)^i_\alpha v/\sqrt{2}$. The mass matrix can be perturbatively Takagi-block-diagonalized by introducing a unitary matrix U [401]. For simplicity, we assume there is only one kinematically relevant HNL in our study. In this case, the gauge eigenstate $\hat{\nu}_i$ receives first-order contributions from the mass eigenstate N, proportional to the following mixing matrix entry:

$$U_i \equiv U_4^i \equiv (Y_\nu^*)^i_1 \frac{v}{\sqrt{2}M} . \tag{5.11}$$

The interaction Lagrangian with the neutrino mass eigenstates ν_i and N is then given by:

$$\mathscr{L} \supset -\frac{g}{\sqrt{2}} U_4^i W_\mu^- \ell_i^\dagger \bar{\sigma}^\mu N - \frac{g}{2c_W} U_4^i Z_\mu \nu_i^\dagger \bar{\sigma}^\mu N + \text{h.c.} , \tag{5.12}$$

where g is the $SU(2)_L$ gauge coupling and $c_W = \cos\theta_W$ is the cosine of the weak mixing angle.

5.2.3 The phenomenology connecting the light bino LSP and the HNL

The phenomenologies of the RPV-MSSM with a light bino $\tilde{\chi}_1^0$ and the SM extensions with one relevant HNL turn out to be very similar. This is not surprising, as the HNL and the bino have the same gauge quantum numbers after electroweak symmetry breaking. Currently existing bounds in the HNL parameter space spanned by (m_N, U_4^i) can thus be translated into bounds in the light-bino-RPV parameter space $(m_{\tilde{\chi}_1^0}, \lambda/m^2_{\mathrm{SUSY}})$, where λ labels here any appropriate $LL\bar{E}$ or $LQ\bar{D}$ coupling.

An additional analogy between the theories can be constructed by considering the bilinear RPV couplings κ_i [402], see Eq. (5.1). After integrating out the heavy higgsinos in the neutral fermion sector of the RPV-MSSM, one obtains a tree-level mixing of neutrinos with the bino, which is of the form

$$\mathscr{L} \supset \frac{g'}{2} \left(v_i - \frac{v_d \kappa_i}{\kappa^0} \right) \hat{\nu}_i \tilde{\chi}_1^0 + \text{h.c.} , \tag{5.13}$$

where v_i and v_d are the vevs of the sneutrinos and the MSSM Higgs H_d, respectively. κ^0 is the Higgsino mass parameter and g' the $U(1)_Y$ gauge coupling. This mixing can be interpreted as the off-diagonal entries in the neutral lepton mass matrix given in Eq. (5.10), such that the elements of the matrix U, *cf.* Eqs. (5.11) and (5.12), can be mapped to the

neutralino-neutrino mixing considered here:

$$U_4^i = \frac{g'}{2m_{\tilde{\chi}_1^0}} \left(v_i - \frac{v_d \kappa_i}{\kappa^0} \right) . \tag{5.14}$$

For phenomenological computations, the Lagrangian given in Eq. (5.12) can be used, which would correspond to the trivial replacement

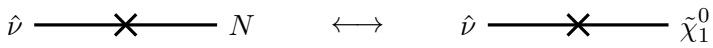

(5.15)

where the inserted crosses denote the mixing. Thus, current HNL exclusion limits can be directly translated into bounds on the mixing strength in Eq. (5.13).

5.3 Experiments and recasting

In this section, we present the details of existing HNL searches and classify them according to their search strategy. We consider experiments employing the signatures: (i) direct decays, (ii) displaced vertices, and (iii) missing energy. For the direct-decay searches, we further partition our analysis into: (i.a) peak searches and (i.b) branching ratio searches. The displaced-vertices searches are also split further into: (ii.a) beam-dump searches and (ii.b) collider searches. Missing-energy searches allow us to derive new and stronger constraints on single RPV couplings. In addition, we present selected benchmark scenarios for which we will obtain single-coupling and coupling-product bounds within the RPV-MSSM framework. We provide an overview of the experiments, discussed in this section, in Table 5.1.

5.3.1 Direct-decay searches

One of the main ways to produce light HNLs is via the decay of light mesons such as pions and kaons. In direct searches, a beam of charged mesons is brought to a stop inside a scintillator where the mesons decay at rest, or the beam mesons are tagged and their positions, momenta, and timing information are measured by a silicon pixel spectrometer.

The energy spectrum of the visible secondary particle, *i.e.*, a muon or an electron, arising from these meson decays is measured. The signal shape of the energy spectrum can be compared with Monte-Carlo simulations for different HNL mass hypotheses. Finding no extra peaks in the secondary energy spectrum or rejecting each mass hypothesis allows us to exclude the relevant HNL parameters.

Peak searches

In peak searches, the energy spectrum of the secondary particle is scanned for additional peaks hinting at HNLs.

- At the Swiss Institute for Nuclear Research (`SIN`), a pion beam was used to put bounds on the mixing $|U_\mu|^2$ in the HNL mass range of 1-16 MeV [357].

Search Strategy	Ref.	Experiment	Status	HNL Mixing	HNL Mass region
Peak	[403]	PIENU	curr.	$\lvert U_e\rvert$	65-153 MeV
	[404]	PIONEER	proj.	$\lvert U_\mu\rvert$	15.7-33.8 MeV
	[404]	PIONEER	proj.	$\lvert U_e\rvert$	65-135 MeV
	[357]	SIN	curr.	$\lvert U_\mu\rvert$	1-16 MeV
	[405]	NA62	curr.	$\lvert U_\mu\rvert$	144-462 MeV
	[361]	NA62	curr.	$\lvert U_e\rvert$	200-384 MeV
	[406]	KEK	curr.	$\lvert U_\mu\rvert$	160-230 MeV
	[407]	KEK	curr.	$\lvert U_\mu\rvert$	70-300 MeV
Branching Ratio	[403]	PIENU	curr.	$\lvert U_e\rvert$	0-65 MeV
	[404]	PIONEER	proj.	$\lvert U_e\rvert$	0-65 MeV
Beam-dump	[408]	DUNE	proj.	$\lvert U_e\rvert$, $\lvert U_\mu\rvert$, $\lvert U_\tau\rvert$	0-1 968.34 MeV
	[409]	T2K	curr.	$\lvert U_e\rvert$, $\lvert U_\mu\rvert$	10-490 MeV
	[410, 411]	CHARM	curr.	$\lvert U_e\rvert$, $\lvert U_\mu\rvert$	300-1 869.65 MeV
	[412]	CHARM	curr.	$\lvert U_\tau\rvert$	290-1 600 MeV
	[413]	NuTeV	curr.	$\lvert U_\mu\rvert$	259-2 000 MeV
	[414]	MicroBooNE	curr.	$\lvert U_\mu\rvert$	20-200 MeV
	[415]	BEBC	curr.	$\lvert U_e\rvert$, $\lvert U_\mu\rvert$	500-1 750 MeV
	[416]	BEBC	curr.	$\lvert U_\tau\rvert$	100-1 650 MeV
	[417]	SK	curr.	$\lvert U_e\rvert$, $\lvert U_\mu\rvert$	150-400 MeV
Collider	[418]	FASER	proj.	$\lvert U_e\rvert$, $\lvert U_\mu\rvert$, $\lvert U_\tau\rvert$	0-6 274.9 MeV
	[419]	MoEDAL-MAPP1	proj.	$\lvert U_e\rvert$	0-6 274.9 MeV
	[420]	BaBar	curr.	$\lvert U_\tau\rvert$	100-1 360 MeV
Missing Energy	[421]	NA62	curr.	BR($\pi^0 \to$ inv.)	0-134.97 MeV
	[422]	BaBar	curr.	BR($B^0 \to$ inv.)	0-5 279.65 MeV

Table 5.1: Summary of experiments reviewed in Sec. 5.3, sorted by search strategy. We list the relevant references, the status of derived bounds (current or projected), the relevant HNL mixing, and the experimentally accessible HNL mass range.

- A search for massive neutrinos at the PIENU experiment [403] has been made in the decay of pions into positrons. No evidence was found for additional peaks in the positron energy spectrum. Thus, upper limits at 90% confidence level (CL) on $|U_e|^2$ were derived in the HNL mass region 60-135 MeV. In another analysis of the PIENU experiment [358], heavy neutrinos were searched for in pion decays into muons. The energy spectrum did not show any additional peaks other than the expected peak for a light neutrino. Thus, the analysis derived a bound on $|U_\mu|^2$ for the HNL mass range of 15.7-33.8 MeV.

- The PIONEER [404] experiment is a next-generation rare pion decay experiment. The experiment will perform the same search strategy as the PIENU experiment with higher statistics and significantly suppressed background. A peak search in the positron spectrum will allow probing $|U_e|^2$ in the HNL mass region 65-135 MeV. Further, a search for an additional peak within the muon energy spectrum will allow us to test $|U_\mu|^2$ for $15.7\,\text{MeV} < m_N < 33.8\,\text{MeV}$.

- KEK [406] derived an upper bound on $|U_\mu|^2$ for a massive HNL in the mass range of 160-230 MeV. A similar search at KEK [407] led to an upper bound on $|U_\mu|^2$ in the HNL mass range of 70-300 MeV.

- Using a kaon beam, the NA62 collaboration placed bounds on $|U_e|^2$ for an HNL with a mass of 144-462 MeV [405]. The analysis approach is different from PIENU. In this case, a peak-search procedure measures the $K^+ \to e^+ N$ decay rate with respect to the $K^+ \to e^+ \nu$ rate for an assumed HNL mass m_N. The HNL mass is varied over the mentioned mass range. The benefit of this approach is the cancellations of residual detector inefficiencies, as well as trigger inefficiencies, and random veto losses. A similar analysis [361] has been performed to measure $|U_\mu|^2$ within the HNL mass range of 200-384 MeV. Note that both bounds of NA62 are derived with the assumption that the lifetime of the neutral particle exceeds 50 ns.

- The BaBar experiment [420] at SLAC has performed a search for the rare decay $\tau^- \to \pi^-\pi^-\pi^+ + N$ in the mass region of $100 < m_N < 1\,360$ MeV. The observed kinematic phase space distribution of the hadronic system allows BaBar to place a stringent bound on $|U_\tau|^2$. However, the search is based on three-prong tau events. Technically, this allows us to derive a single coupling bound on λ'_{311}. However, the four-body production mode of the light neutralino would need proper phase-space consideration. Therefore, we do not include a reinterpretation of this search in our work and shall discuss it elsewhere.

Branching-ratio searches

It is possible to measure branching ratios of different pion decay modes. The ratio

$$R_{e/\mu} = \frac{\Gamma\left(\pi^+ \to e^+ + \nu(\gamma)\right)}{\Gamma\left(\pi^+ \to \mu^+ + \nu(\gamma)\right)}, \tag{5.16}$$

can be used to derive limits on the mixing $|U_e|^2$ in the region $m_N < 65$ MeV. This has been performed by PIENU [423] and is planned for PIONEER [404].

5.3.2 Displaced-vertex searches

Beam-dump and collider experiments can produce HNLs via the same processes that produce light neutrinos. A proton beam hitting a fixed target typically produces a large number of pions and kaons, and also heavier mesons. If kinematically allowed, the decay of the primary mesons can produce HNLs, which will propagate freely since they are long-lived and interact only feebly. The HNLs produced at beam-dump experiments are typically boosted in the forward direction, which further increases their decay length in the lab frame. Hence, only a fraction of the produced HNLs decay at the location of the detector. To reduce possible background events, the experiments usually have a system of veto detectors equipped for both charged and neutral particles. The search strategy relies on the visibility of the HNL decay products inside the detector; we will discuss these later.

In the following, we present displaced-vertex searches at beam-dump and collider experiments separately.

Beam-dump search

- At DUNE [110], HNLs can be produced via pion-, kaon-, and D-meson-decays. Ref. [408] predicts constraints on HNLs by searching for their decay products inside the DUNE Near Detector. It is assumed that only the three-neutrino final state is not detectable. The search strategy allows to measure all three mixings $|U_e|^2, |U_\mu|^2$ and $|U_\tau|^2$ for an HNL mass range up to the mass of the D_s-meson. Note that in the analysis, a single mixing element is assumed to dominate over the other two at a time.

- The T2K experiment [409] follows the same approach but uses a kaon beam. Thus, they derive bounds on both $|U_e|^2$ and $|U_\mu|^2$ for $10\,\text{MeV} < m_N < 490\,\text{MeV}$.

- Heavy neutral leptons in the CHARM beam-dump experiment are produced from D and D_s-meson decays.[2] The former allows to set bounds on $|U_e|^2, |U_\mu|^2$ for an HNL mass of 300-1 869.65 MeV [410, 411], and the latter allows to probe $|U_\tau|^2$ for $290\,\text{MeV} < m_N < 1\,600\,\text{MeV}$ [412].

- A search for HNLs has been performed at the NuTeV experiment [413] at Fermilab. The data were examined for HNLs decaying into muonic final states to derive bounds on the mixing $|U_\mu|^2$ of HNLs in the 0.25-2.0 GeV mass range. See also Ref. [70] which directly considers the NuTeV data in terms of a light neutralino.

- An analysis of current data from the MicroBooNE experiment [414] can constrain the parameters of HNLs, that mix predominantly with muon-flavored neutrinos, for HNL masses between 20-200 MeV.

- The BEBC experiment derived limits on the HNL-light neutrino mixing parameters from a search for decays of heavy neutrinos in a proton beam-dump experiment [415]. It derived bounds on $|U_e|^2, |U_\mu|^2$ for an HNL mass between 0.5 GeV and 1.75 GeV. A re-analysis [416, 424] has demonstrated that the BEBC detector was also able to place bounds on the $|U_\tau|^2$ mixing for HNL masses higher than the kaon mass. This re-analysis has taken into account several production and decay channels of HNLs.

- For Super-Kamiokande (SK), the largest contribution to HNL production is through the decay of mesons produced in the atmosphere via cosmic rays. A secondary contribution to the flux comes from the HNL production in neutral-current scattering of atmospheric neutrinos passing through the Earth. The total number of HNL decays inside the detector within a given time window results in an upper bound on the HNL mixing. This approach is different from the displaced-decay search limits from beam dumps and allows one to derive bounds on $|U_e|^2$ and $|U_\mu|^2$ in the minimal HNL scenarios for masses between 150-400 MeV [417].

[2] In this work, we use "D-mesons" ("B-mesons") to label the $D^\pm$ mesons ($\overset{(-)}{B}{}^0$ and $B^\pm$ mesons), while D_s and B_c mesons are separately discussed. We do not take into account $\overset{(-)}{D}{}^0$ or $\overset{(-)}{B}_s$ mesons.

Collider searches

HNLs can be also searched for in (semi-)leptonic decays of mesons produced at the LHC via a similar mechanism as in beam-dump experiments. At colliders, particle collisions produce an abundance of mesons, such as pions, kaons, D-mesons, and B-mesons, which can further decay into HNLs. Far detectors at the LHC are sensitive to decaying, light LLPs with a decay length comparable with their distance to the interaction point, *e.g.*, of $\mathcal{O}(1) - \mathcal{O}(100)$ m. HNLs decaying inside the detector can be identified by their decay products, except for the invisible three-neutrino final state. To ensure a low background environment, the experiments are proposed to be set far away from the primary proton-proton collision points and require shielding between the interaction points and the detectors.

Some of the new detectors at the LHC are already approved and currently running: `FASER` [280] and `MoEDAL-MAPP1` [397]. We include these running HNL searches in order to reinterpret their projected sensitivity. Their follow-up programs, `FASER2` [281] and `MoEDAL-MAPP2` [398], have been proposed for operation during the high-luminosity LHC phase, with an expected final integrated luminosity $3\,\text{ab}^{-1}$ and $300\,\text{fb}^{-1}$ respectively, and are taken into account in our numerical analysis, as well.

`FASER(2)` [418][3] is intended to detect long-lived particles decaying inside the detector volume. A sensitivity estimate, taking the detector geometry into account, leads to a specific reach in $|U_e|^2, |U_\mu|^2$, and $|U_\tau|^2$ for an HNL with a mass up to the mass of the B_c-meson. Similarly, `MoEDAL-MAPP1(2)` [419, 425] can probe the mixing $|U_e|^2$ for HNL being produced in decays of D- and B-mesons for the same mass range as `FASER(2)`.

In addition, other experimental proposals for LLP far detectors include `MATHUSLA` [283–285], `ANUBIS` [287], `CODEX-b` [286], and `FACET` [282]. None of these proposed detectors has been officially approved. We therefore do *not* include them in our reinterpretation strategy. We still want to emphasize the prospect of these experiments in the search for light long-lived particles. Sensitivity estimates, worked out in detail on the minimal HNL scenarios in Ref. [419], would also provide possible discovery potential for the discussed light neutralino scenarios, as worked out for example in Refs. [226, 227, 322, 323]. These potential future experiments all intend to look for various BSM signatures which include neutralino decays induced by all of the LH_u, $LL\bar{E}$, and $LQ\bar{D}$ operators.

5.3.3 Missing-energy searches

The `NA62` search [421] allows us to derive bounds on the branching ratio of pions decaying into an invisible final state. This is achieved by the reconstruction of the charged particles in the process $K^+ \to \pi^+\pi^0$. The analysis relies on the tracking of the charged K^+ and π^+ and can probe π^0 decay to any invisible final state. `NA62` reported a 90% CL upper limit on $\text{BR}(\pi^0 \to \text{inv.}) < 4.4 \times 10^{-9}$. The search can be recast to derive bounds on RPV couplings which also contribute to the invisible decays of the pion. It turns out that the obtained limits are weaker than the currently existing bounds [67, 157] and are, therefore, omitted.

[3] In principle, Ref. [281] employs the most updated geometrical setup of `FASER(2)`, but the results shown therein for the HNLs do not separate the contributions from D- and B-mesons. Therefore, we have chosen to reinterpret the results given in Ref. [418] for the HNLs from the heavy mesons' decays, which are only slightly different from those given in Ref. [281].

The BaBar experiment has also searched for rare decays $B_0 \to \text{inv.}$ [422]. The search relies on the identification of the other neutral B-meson, as the 'tag side', and thus, can measure a purely invisible decay width of the B-meson. The upper limit at the 90% CL yields $\text{BR}(B_0 \to \text{inv.}) < 2.4 \times 10^{-5}$. We can recast this search into bounds on the production coupling of a light long-lived neutralino.

We could not find existing searches for invisible decays of the other uncharged mesons, *i.e.*, K_S, K_L, and B_s. To derive limits on the decay of these mesons into a neutralino we consider the uncertainty of the total decay width of the mesons. We assume all visible decay modes to be measured within the decay width. The resulting uncertainty can be extended to account for additional invisible decays and potential errors in measurements. Thus, we use the uncertainty to establish an upper limit on the branching ratio into invisible final states, if kinematically allowed. These could contain neutrinos, HNLs, or neutralinos. Assuming the latter saturates the width uncertainty, we derive bounds on the $LQ\bar{D}$ couplings. The measured uncertainties can be found in Ref. [65].

We could not find bounds from direct searches for massive HNLs in the leptonic decays $\mu^- \to e^- + \nu + N$ and $\tau^- \to e^-/\mu^- + \nu + N$. There are only searches for the muons and the τ leptons to decay to a lighter charged lepton plus active neutrinos or a photon [426]. Thus, the existing limits on the branching ratio cannot be generalized for a massive HNL owing to kinematic assumptions. In this case, we again rely on the uncertainty of the decay widths. This allows us to derive bounds on the $LL\bar{E}$ couplings. Again, the uncertainties of the decay width are taken from Ref. [65].

5.3.4 Other searches

For the bilinear coupling scenarios, we use the most relevant and up-to-date constraints on the HNLs existing in the literature, which are summarized in Ref. [383]. Therefore, we supplement the results from the previously discussed experiments with data from TRIUMF [427], PSI [357], Borexino [428, 429], and atmospheric neutrinos scattering in the Earth [430].

5.3.5 The recasting procedure

The procedures for recasting the HNL bounds into limits on RPV scenarios depend on the RPV couplings that are switched on, and the search strategy of the experiments; they fall into one of the following three categories:

- The most straightforward case is for scenarios involving bilinear RPV couplings. As discussed in Sec. 5.2, these couplings lead to mixing between the neutralino and the neutrinos, *cf.* Eq. (5.13). Thus, we directly translate HNL exclusion limits in the mixing vs. mass plane into bounds in the RPV coupling vs. neutralino mass plane, using Eq. (5.14).

- In RPV scenarios involving $LQ\bar{D}$ or $LL\bar{E}$ operators, and a (detector-level) stable neutralino produced in the decay of a meson or lepton, missing-energy searches and peak searches can provide sensitivity. We use the HNL exclusion limits (typically in

the mixing vs. mass plane) in order to determine the bounds on the decay width of the relevant meson/lepton into an HNL (see, for instance, Refs. [359, 431]). Since replacing the HNL with a light bino of the same mass does not change the experimental signature and the kinematics, we can simply equate the above with the corresponding decay width of the same meson/lepton into a bino in the RPV model, using the expressions given in Sec. 5.2; this gives us the bound on the relevant RPV coupling in terms of the bino mass.

- For RPV scenarios involving $LQ\bar{D}$ or $LL\bar{E}$ operators where the neutralino is produced in meson/lepton decays, and is *unstable* at the detector scales, displaced-vertex searches (beam dump or collider) can apply. In this case, we use the long-lifetime approximation to calculate the number of decay events reconstructed in the detector, following the arguments outlined in Ref. [425] (see also Ref. [383]); we review the procedure briefly now. Consider a beam-dump or collider experiment that searches for HNLs via displaced vertices. Let the HNL, N, be produced in the decay of a parent particle P (for instance, a pion).[4] Then, the number of detected events for a final state, Y, produced in the decay of N can be estimated as,

$$N_{\text{events}}^{\text{HNL}} = N_P \times \text{BR}(P \to N + X) \times \text{BR}(N \to Y) \times \epsilon \,, \tag{5.17}$$

where N_P is the number of P produced at the experiment, X are any additional objects produced in P's decay that are not of interest to us, and the BRs are the corresponding branching ratios. ϵ is a factor accounting for the detector acceptance and efficiency. This factor is linearly proportional to the probability for the HNL to decay inside the detector (P[decay]). It also depends on experiment-specific information such as the detector type and its geometry. In the limit of a long-lived HNL, such that the boosted decay length is much larger than the distance ΔL from the interaction point of the experiment to the first edge of the detector along the direction of travel of the HNL, to a good approximation we have [425],

$$P[\text{decay}] \approx \frac{\Delta L \times \Gamma_N}{\beta_N \gamma_N} \,, \tag{5.18}$$

where Γ_N, β_N, and γ_N represent the total decay width, the relativistic velocity, and the Lorentz boost factor of the HNL, respectively. Inserting this in Eq. (5.17), we obtain,

$$N_{\text{events}}^{\text{HNL}} = A \times \frac{\text{BR}(P \to N + X) \times \Gamma(N \to Y)}{\beta_N \gamma_N} \,, \tag{5.19}$$

where all the quantities depending on the HNL model details are written explicitly, and the remaining experiment-specific factors of Eq. (5.19) have been absorbed into the proportionality factor A. Now, assume that there is also an RPV scenario in which the light bino, $\tilde{\chi}_1^0$, is produced in P decays, and has a decay mode into Y. Analogously,

[4] We are assuming that the direct production of the HNL (or bino) is suppressed compared to indirect production via decays of mesons and leptons, which is typically the case.

we can write,

$$N_{\text{events}}^{\text{RPV}} = A \times \frac{\text{BR}(P \to \tilde{\chi}_1^0 + X') \times \Gamma(\tilde{\chi}_1^0 \to Y)}{\beta_{\tilde{\chi}_1^0}\gamma_{\tilde{\chi}_1^0}}\,, \tag{5.20}$$

where the HNL is now replaced by the bino. Here, since both the light bino and the HNL are produced in the same meson's decay at the identical experiment, the proportionality factor A can be legitimately assumed to be essentially the same. Thus, combining the two equations, we obtain a simple scaling relation between the two models:

$$\frac{N_{\text{events}}^{\text{RPV}}}{N_{\text{events}}^{\text{HNL}}} = \frac{\text{BR}(P \to \tilde{\chi}_1^0 + X') \times \Gamma(\tilde{\chi}_1^0 \to Y) \times \beta_N\gamma_N}{\text{BR}(P \to N + X) \times \Gamma(N \to Y) \times \beta_{\tilde{\chi}_1^0}\gamma_{\tilde{\chi}_1^0}}\,. \tag{5.21}$$

For an HNL and a light bino with the same mass, we can further simplify the above expression in the limit where the HNL and the bino carry the same energy in the lab frame. In this case, the $\beta\gamma$ factors cancel out, and we have,

$$\frac{N_{\text{events}}^{\text{RPV}}}{N_{\text{events}}^{\text{HNL}}} = \frac{\text{BR}(P \to \tilde{\chi}_1^0 + X') \times \Gamma(\tilde{\chi}_1^0 \to Y)}{\text{BR}(P \to N + X) \times \Gamma(N \to Y)}\,, \tag{5.22}$$

which is completely free from any experiment-specific factors. This will be the master expression we use for recasting DV searches. We note that, technically, having different X and X' induces different kinematics for the HNL and the bino. For instance, the two final states could have different masses, or even contain differing number of objects, thus affecting the energy carried by the bino relative to the HNL. However, typically, the experiments we consider produce the parent particles (or their decay products) with significant boosts, in which case the above formula is only modified mildly. On the other hand, we stress that the HNL and the bino must be produced in the decay of the same (or similar) parents, and must decay into the same final state since these can significantly alter the detector acceptances and efficiencies.[5]

To use Eq. (5.22), assume that a given DV search for HNLs concludes without discovery, and obtains bounds on the HNL model parameters corresponding to a certain signal-event number, $[N_{\text{events}}^{\text{HNL}}]_{\text{bound}}$. Since the signal (and kinematics) in the RPV model is the same, this bound also applies to the light binos: $[N_{\text{events}}^{\text{RPV}}]_{\text{bound}} = [N_{\text{events}}^{\text{HNL}}]_{\text{bound}}$. Plugging this into Eq. (5.22), we arrive at,

$$[\text{BR}(P \to \tilde{\chi}_1^0 + X') \times \Gamma(\tilde{\chi}_1^0 \to Y)]_{\text{bound}} = [\text{BR}(P \to N + X) \times \Gamma(N \to Y)]_{\text{bound}}\,. \tag{5.23}$$

The right-hand side of the above equation can be evaluated by using the bounds on the HNL mass and mixings as input (see, for instance, Refs. [431, 432] for explicit expressions for all relevant decay widths in terms of these parameters), while the expressions for the RPV counterparts appear in Sec. 5.2 and depend on the RPV

[5] Actually, the final states into which the HNL and bino decay need not be identical, *e.g.*, the invisible objects contained in both do not need to match; the crucial part is that the detection efficiencies at the considered experiment must be the same.

couplings, sfermion masses, as well as the neutralino mass.

5.4 Numerical results

In order to present our results, we consider benchmark scenarios with one or two non-vanishing RPV couplings. Additional non-zero RPV couplings could allow for further neutralino decay channels to open up; these would modify the relevant branching ratios and neutralino decay length, and hence, the presented sensitivity limits.

5.4.1 One-coupling scenarios

We first consider scenarios where only one non-zero RPV operator contributes to the relevant physical process at a time. For each of the RPV couplings in Eq. (5.1) (except the λ''_{ijk}'s), we list the relevant HNL searches providing constraints in Table 5.2. We now discuss the sensitivity limits for each category of RPV coupling in detail.

Bilinear scenarios

The bilinear couplings (κ^i and the sneutrino vacuum expectation values) induce a mixing between the light bino and the three light neutrinos, *cf.* Eq. (5.13). Thus, all HNL searches constraining the mixing between the HNL and the neutrinos directly imply constraints on these couplings. The exclusion limits are shown in Fig. 5.1. These have been read off from Ref. [383]. The bilinear couplings also generate mass terms for the neutrinos – see, for instance, Refs. [54, 58, 59, 124, 125] – leading to the constraint $v_i,\ \kappa^i \lesssim \mathcal{O}\,(1\,\text{MeV})$ [54]; this is depicted as a gray horizontal line in the plot.[6] We find that the reinterpreted bounds from the HNL searches corresponding to the light-flavor neutrinos (e and μ) have sensitivity to regions beyond the current limits at low neutralino masses below 500 MeV. In this region, the most constraining limits come from `PIENU` [358, 403, 423], `NA62` [361, 405], and `T2K` [409, 433]. Beyond this mass, and for the tau case – where charged kaon and pion decay into HNLs are kinematically forbidden – existing limits are weaker.

$LQ\bar{D}$ scenarios

For the remaining one-coupling scenarios, all existing limits on the RPV couplings are taken from Ref. [67]. The $L_iQ_1\bar{D}_1$-operators couple to pions. With $i = 1$, the decay $\pi^\pm \to e^\pm + \tilde{\chi}_1^0$ is allowed, for masses $m_{\tilde{\chi}_1^0} \leq m_{\pi^\pm} - m_e$.[7] This process has been searched for in the context of HNLs, and the most stringent existing limits are provided by `PIENU` [403]. Additionally, the approved `PIONEER` [404] experiment is projected to have sensitivity beyond these limits. We show the resulting contours in Fig. 5.2(a). The sharp drop in sensitivity at $m_{\tilde{\chi}_1^0} \approx 65\,\text{MeV}$ occurs because branching ratio measurements provide bounds below this mass, and peak

[6] We note that the existing limit comes from the cosmological bound on the neutrino masses, and is thus scenario-dependent [65]. Further, there is also dependence on undetermined supersymmetric parameters.

[7] In the small region of phase space, $m_{\pi^0} + m_{\nu_e} < m_{\tilde{\chi}_1^0} < m_\pi^\pm - m_e$, $\lambda'_{111} \neq 0$ allows for the neutralino to decay into a neutrino and a pion; displaced-vertex searches can constrain this process. However, we have ignored this in Table 5.2 (also analogously for the kaon).

Coupling	Direct Decays	E_T^{miss}	DV	Label
κ^i	ν-mixing [383]	ν-mixing [383]	ν-mixing [383]	$\boldsymbol{\kappa}$
λ'_{a11}	$\pi^\pm \to e_a^\pm + \tilde{\chi}_1^0$ [358, 403, 404, 423]	$\pi^0 \to$ invis. [421]	×	$\boldsymbol{\lambda'_\pi}$
λ'_{311}	$(\times)\, \tau^\pm \to \{\pi^\pm/\rho^\pm\} + \tilde{\chi}_1^0$	$\pi^0 \to$ invis. [421]	$\tau^\pm \to \pi^\pm + \tilde{\chi}_1^0; \tilde{\chi}_1^0 \to \nu_\tau + \{\pi^0/\rho^0/\eta/\eta'/\omega\}$ [408, 418, 419, 425]	
λ'_{a12}	$K^\pm \to e_a^\pm + \tilde{\chi}_1^0$ [361, 405–407]	$K_L^0 \to$ invis. [65]	×	$\boldsymbol{\lambda'_K}$
λ'_{312}	$(\times)\, \tau^\pm \to K^\pm + \tilde{\chi}_1^0$	$K_L^0 \to$ invis. [65]	×	
λ'_{i13}	$(\times)\, B^\pm \to e_i^\pm + \tilde{\chi}_1^0$	$B^0 \to$ invis. [422]	×	$\boldsymbol{\lambda'_{B1}}$
λ'_{i21}	$(\times)\, D^\pm \to e_i^\pm + \tilde{\chi}_1^0$	$K_L^0 \to$ invis. [65]	×	$\boldsymbol{\lambda'_{D/K}}$
λ'_{i22}	$(\times)\, D_s^\pm \to e_i^\pm + \tilde{\chi}_1^0$	×	$D_s^\pm \to e_i^\pm + \tilde{\chi}_1^0; \tilde{\chi}_1^0 \to \nu_e + \{\phi/\eta/\eta'\}$ [408, 418, 419, 425]	$\boldsymbol{\lambda'_{D_s}}$
λ'_{i23}	$(\times)\, B_c^\pm \to e_i^\pm + \tilde{\chi}_1^0$	$B_s^0 \to$ invis. [65]	×	$\boldsymbol{\lambda'_{B_c/B_s}}$
λ'_{i31}	×	$B^0 \to$ invis. [422]	×	$\boldsymbol{\lambda'_{B2}}$
λ'_{i32}	×	$B_s^0 \to$ invis. [65]	×	$\boldsymbol{\lambda'_{B_s}}$
λ'_{i33}	×	×	×	–
λ_{12a}	×	$\mu^\pm \to e^\pm +$ invis. [65]	×	$\boldsymbol{\lambda_\mu}$
$\lambda_{123}; \lambda_{13i}; \lambda_{232}; \lambda_{233}$	×	$\tau^\pm \to \{e^\pm/\mu^\pm\} +$ invis. [65]	×	$\boldsymbol{\lambda_\tau}$
λ_{231}	×	$\{\tau^\pm/\mu^\pm\} \to e^\pm +$ invis. [65]	×	$\boldsymbol{\lambda_{\tau/\mu}}$

Table 5.2: Details of the searches providing constraints when only one non-zero RPV operator contributes at a time. We list all the bilinear, $LQ\bar{D}$, and $LL\bar{E}$ operators in the first column (by coupling). The second to fourth columns contain the physical processes that provide constraints and the references to the relevant existing HNL searches targeting them. The fifth column indicates our labeling scheme for the scenarios. × denotes the absence of a constraining process, while $(\times)$ labels that, in principle, the listed process may provide constraints but we could not find a relevant existing HNL search. In the table, $a \in \{1, 2\}$ and $i \in \{1, 2, 3\}$.

searches above this threshold, *cf.* discussion in Sec. 5.3. Similarly, for $i = 2$, the pion can decay into a muon instead of an electron, in the mass range, $m_{\tilde{\chi}_1^0} \leq m_{\pi^\pm} - m_\mu$. This time, the sensitivity range, shown in Fig. 5.2(b), comes from `SIN` [357] in addition to `PIENU` [358] and `PIONEER`. Finally, with $i = 3$, the decays, $\tau^\pm \to \pi^\pm(\rho^\pm) + \tilde{\chi}_1^0$, can occur if kinematically allowed. While we could not find a direct search for such a process involving an HNL, $\lambda'_{311} \neq 0$ additionally allows the neutralino to decay into a tau neutrino and one of $\pi^0/\rho^0/\eta/\eta'/\omega$. Thus, displaced-vertex searches at `DUNE` [408], `FASER(2)` [418] and `MoEDAL-MAPP2` [419, 425] can show sensitivity.[8] We present the corresponding combined projected sensitivity reach in Fig. 5.2(c). In all the plots, we also show the best existing constraints on the RPV couplings for different sfermion masses. For λ'_{111}, this comes from neutrinoless double beta decay searches [311, 434], and is rather stringent compared to the other two couplings. Nevertheless,

[8] See also Ref. [324] for a proposed search at Belle II [355, 356] for a light bino with non-vanishing RPV couplings λ'_{311} or λ'_{312}.

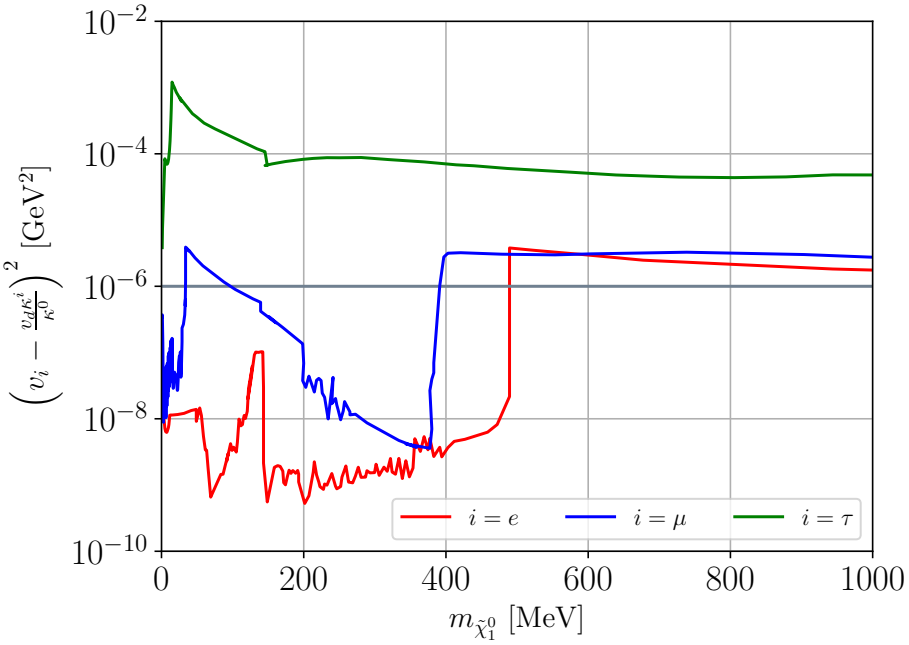

Figure 5.1: Exclusion limits on bilinear RPV couplings as a function of the light bino mass, reinterpreted from existing HNL searches. The current limit on the bilinear couplings is shown as a horizontal gray line.

we see that the reinterpreted bounds easily outperform these existing constraints in the major part of the phase space region. We also note that in all of the above scenarios, the RPV couplings contribute to the invisible decay width of the pion, via the decay into a neutrino and the bino, given the long lifetime of the latter. However, the limits obtained this way are not competitive compared with the above ones.

Next, we consider the kaon scenarios, involving couplings of the type λ'_{i12}. For $i \in \{1, 2\}$, as for the pion case above, the decay mode into an electron or a muon along with the bino opens up for the kaon, below the relevant kinematic thresholds. The most constraining current limits come from KEK [406, 407] and NA62 [361, 405], and are depicted in Fig. 5.3(a) (electron case), and Fig. 5.3(b) (muon case). The degradation at $m_{\tilde{\chi}_1^0} \sim 200\,\text{MeV}$ in Fig. 5.3(b) occurs because the KEK-limit only applies up to this mass; beyond it the NA62 limit applies. Once again, both $L_i Q_1 \bar{D}_2$ also contribute to the invisible decays of the kaon but the resulting limits are weaker than those shown. However, for λ'_{312} – where we could not find an existing HNL direct search for the charged decay, $\tau^\pm \to K^\pm + \tilde{\chi}_1^0$ (see Footnote 8), the invisible width of K_L^0 can indeed be used to derive limits. Since there is no direct bound on this width, we use the uncertainty on the total measured width of K_L^0 [65] to estimate the upper bound, $\text{BR}(K_L^0 \to \text{invis.}) < 4.1 \times 10^{-3}$. This, then, can be used to constrain λ'_{312} since it induces the decay of K_L^0 into a neutrino and a bino. Analogously, the invisible width also provides limits on couplings of the type λ'_{i21}. Here also, we could not find existing direct searches for the relevant charged decay of D into a lepton and an HNL. All these constraints are displayed in Fig. 5.3(c). Once again, we can see that the reinterpreted bounds exclude regions of phase

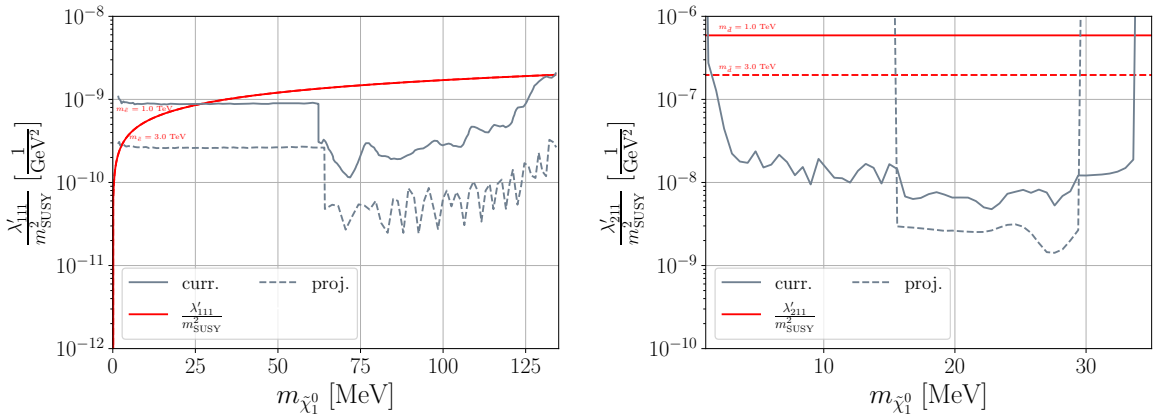

(a) λ'_{111}. (b) λ'_{211}.

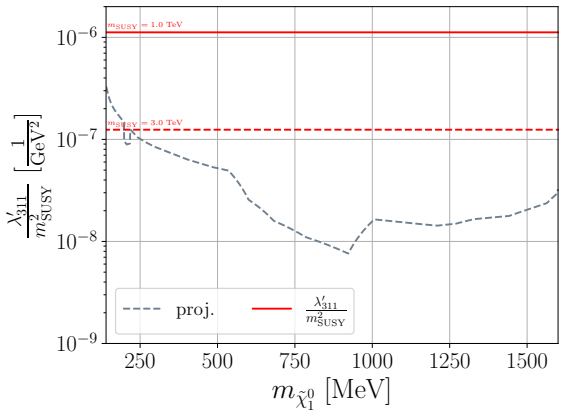

(c) λ'_{311}.

Figure 5.2: Sensitivity limits on the $\boldsymbol{\lambda'_\pi}$ one-coupling scenarios of Table 5.2 as a function of the light bino mass, reinterpreted from existing HNL searches. Current (projected) limits obtained from the reinterpretation are shown as solid (dashed) gray lines. The existing limits on the RPV couplings are also shown in red, with the solid and dashed lines corresponding to varying assumptions of unknown SUSY mass scales.

space orders of magnitude beyond those ruled out by the existing constraints on the RPV operators (also shown in the plots).

Similarly, for couplings of the type λ'_{i13} and λ'_{i31}, we can use the invisible width of B^0. Here, direct measurements at `BaBar` [422] provide the stringent constraint, $\mathrm{BR}(B^0 \to \text{invis.}) < 2.4 \times 10^{-5}$. The resulting bounds are shown in Fig. 5.4.

For the couplings λ'_{a22}, with $a \in \{1, 2\}$, we use potential future displaced-vertex searches from `DUNE` [408], `FASER2` [418], and `MoEDAL-MAPP2` [419, 425] since we could not find a direct search for the decay of $D_s^\pm$ into an HNL. In these scenarios, the neutralino decays via the RPV operator into a neutrino and one of $\phi/\eta/\eta'$. This implies the mass range, $548\,\mathrm{MeV} \lesssim m_{\tilde{\chi}_1^0} < m_{D_s} - m_{e_a}$. Thus, the corresponding scenario with $\lambda'_{322} \neq 0$ involving a tau lepton is not possible. We show the resulting sensitivity limits in Fig. 5.5.

For the remaining $LQ\bar{D}$ operators, there are either no relevant processes providing con-

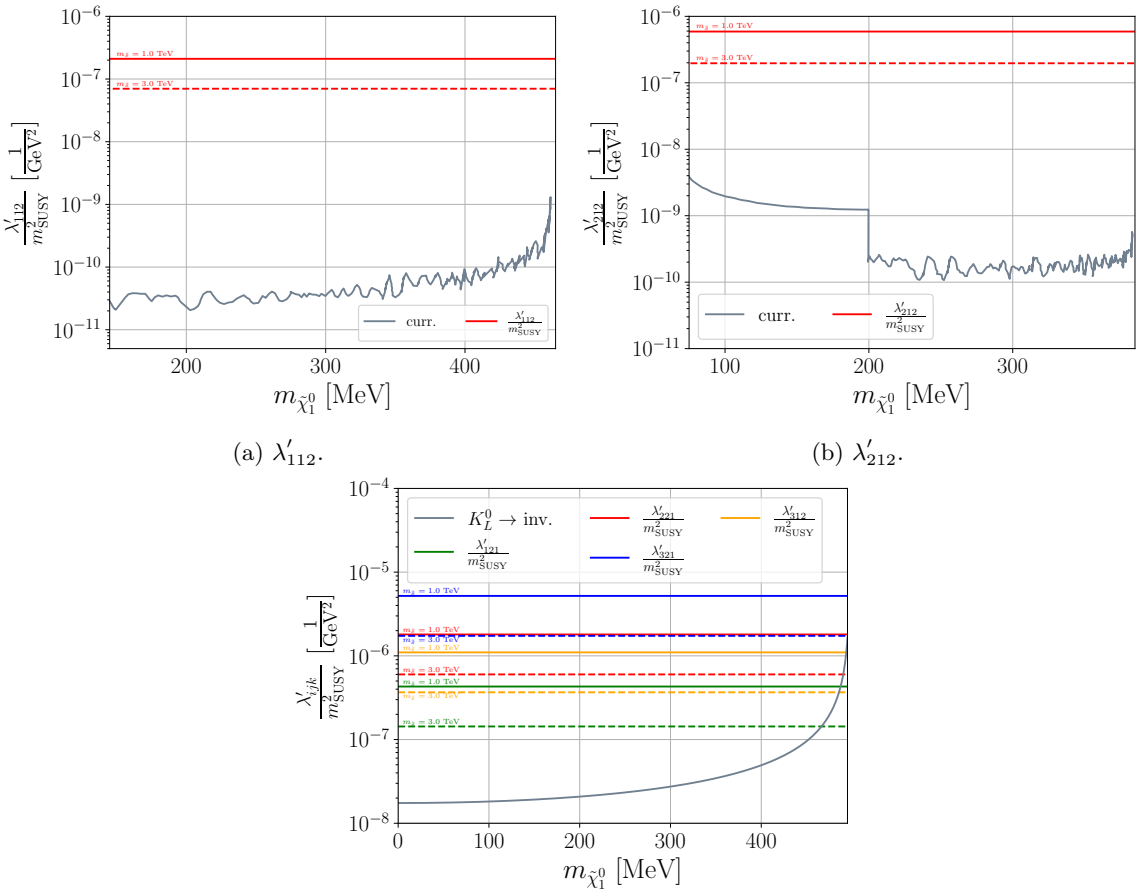

(a) λ'_{112}. (b) λ'_{212}.

(c) λ'_{312} and λ'_{i21}.

Figure 5.3: As in Fig. 5.2 but for the $\boldsymbol{\lambda'_K}$ and $\boldsymbol{\lambda'_{D/K}}$ benchmarks of Table 5.2. The existing limits on the RPV couplings are shown in red, yellow, green, and blue.

straints through meson or lepton decays ($\lambda'_{322}, \lambda'_{i33}$), or the obtained limits are not competitive with the existing bounds ($\lambda'_{i23}, \lambda'_{i32}$).

$\boldsymbol{LL\bar{E}}$ scenarios

For the $\boldsymbol{\lambda_\mu}, \boldsymbol{\lambda_\tau}$ and $\boldsymbol{\lambda_{\tau/\mu}}$ scenarios of Table 5.2, the corresponding operators contribute to the leptonic decays of the muon and the tau. Since we could not find direct measurements for the process $\mu^\pm \to e^\pm +$ invis. (and analogously for $\tau \to e$ and $\tau \to \mu$), where the invisible final state may be massive, we use the uncertainty on the muon decay width [65] to obtain an estimated bound, $\mathrm{BR}(\mu^\pm \to e^\pm + \text{invis.}) < 1.0 \times 10^{-6}$. This leads to constraints on the $\boldsymbol{\lambda_\mu}$ and $\boldsymbol{\lambda_{\tau/\mu}}$ scenarios, as shown in Fig. 5.6. The analogous procedure with τ leads to limits weaker than the existing constraints and are hence not presented here.

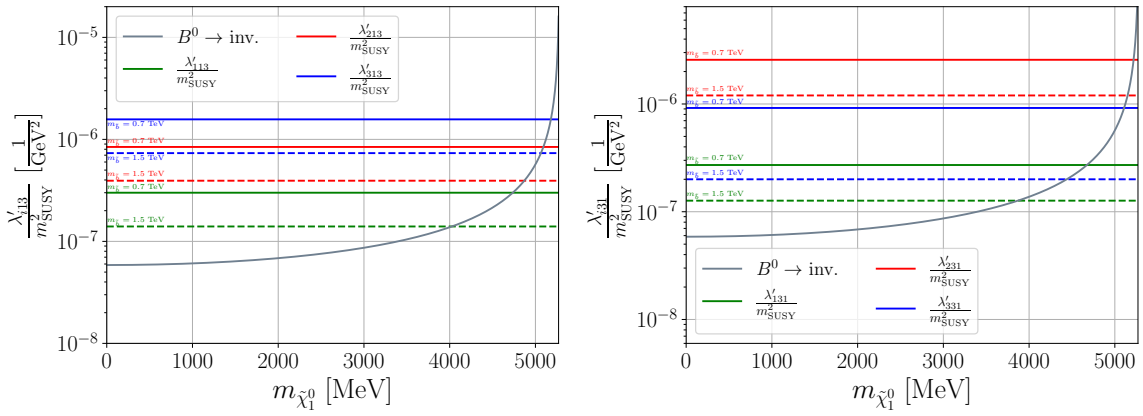

(a) λ'_{i13}. (b) λ'_{i31}.

Figure 5.4: As in Fig. 5.2 but for the $\boldsymbol{\lambda'_{B1}}$ and $\boldsymbol{\lambda'_{B2}}$ benchmarks of Table 5.2. The existing limits on the RPV couplings are shown in red, green, and blue.

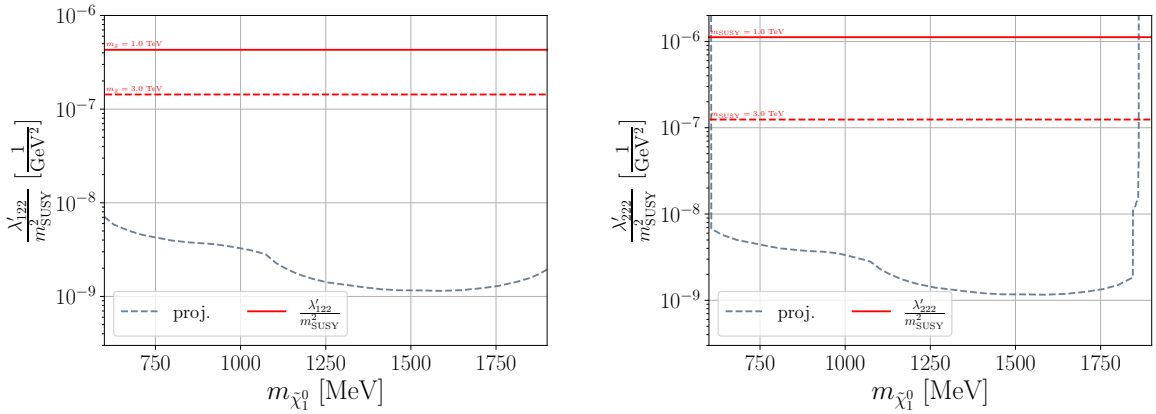

(a) λ'_{122}. (b) λ'_{222}.

Figure 5.5: As in Fig. 5.2 but for the $\boldsymbol{\lambda'_{D_s}}$ benchmarks of Table 5.2.

5.4.2 Two-coupling scenarios

Next, we consider scenarios where two RPV operators are simultaneously switched on; one corresponds to the production of the bino LSP, while the other leads to the decay. We can classify these scenarios based on the parent particle producing the neutralino; this then fixes the production RPV coupling. The relevant possibilities for the parent particles at beam-dump searches and colliders are: pions, kaons, D mesons, D_s mesons, B mesons, B_c mesons, and τ leptons.[9] The corresponding production RPV couplings (and processes) can be read off from Table 5.2, *e.g.*, λ'_{a11} for the pion, etc.

The produced neutralino, owing to its long lifetime, then travels a certain macroscopic distance and decays via the other RPV coupling. Thus, displaced-vertex searches for HNLs

[9] τ leptons are dominantly produced in the decay of the D_s mesons at these experiments.

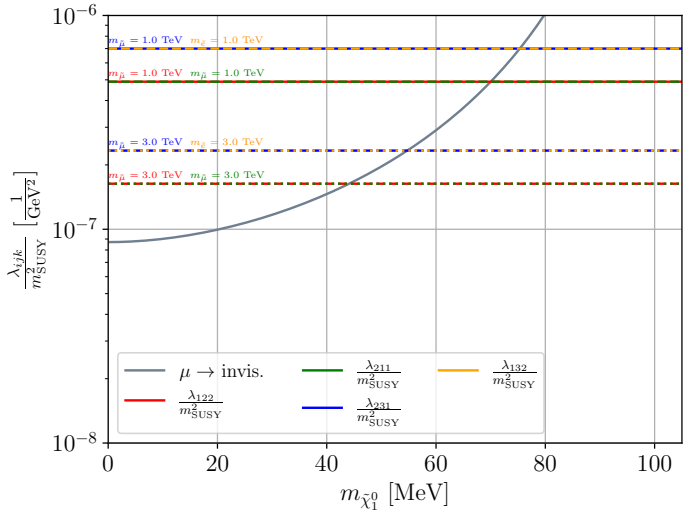

Figure 5.6: As in Fig. 5.2 but for the $\boldsymbol{\lambda'_{\mu}}$ and $\boldsymbol{\lambda'_{\tau/\mu}}$ benchmarks of Table 5.2. The existing limits on the RPV couplings are shown in red, yellow, green, and blue.

are sensitive to such scenarios, if the final states match the decay products of the bino. We list, in Table 5.3, all relevant final states of such searches, along with the relevant kinematic thresholds at which the HNL can decay into them. Consulting the discussion in Sec. 5.2, we see that each of these final states can also arise from bino decays.

Channel	Threshold	Channel	Threshold
$\nu e^+ e^-$	1.02 MeV	$\mu^\mp K^\pm$	599 MeV
$\nu e^\pm \mu^\mp$	105 MeV	$\nu \rho^0$	776 MeV
$\nu \pi^0$	135 MeV	$e^\mp \rho^\pm$	776 MeV
$e^\mp \pi^\pm$	140 MeV	$\nu \omega$	783 MeV
$\nu \mu^+ \mu^-$	210 MeV	$\mu^\mp \rho^\pm$	882 MeV
$\mu^\mp \pi^\pm$	245 MeV	$\nu \eta'$	958 MeV
$e^\mp K^\pm$	494 MeV	$\nu \phi$	1 019 MeV
$\nu \eta$	548 MeV		

Table 5.3: Relevant final states from HNL (and bino) decay sorted by threshold mass. The active neutrino is considered massless.

In Table 5.4, we list, for each production category, the relevant RPV operator(s) leading to the final states of Table 5.3. $\times$ indicates that the given final state can not arise for the considered production mode, owing to kinematics. This table can be used to identify all relevant two-coupling RPV scenarios that can be constrained by existing HNL DV searches. Note that we have not included bino production modes corresponding to the $LL\bar{E}$ decays of the τ leptons in the table since these lead to weak limits, as in the one-coupling scenarios. We now discuss numerical results for a representative subset of the possibilities in the table.

Pion scenarios

For the $\pi^{\pm}$ category, we consider the two benchmark scenarios listed in Table 5.5. The relevant mass range is identified by requiring that the production of the neutralino, and its subsequent decay (*cf.* Table 5.4), should be both kinematically accessible.

We use this opportunity to explain one more subtlety of our recasting procedure for DV searches. In the HNL model, the relevant pion decay process occurs via the neutrino-mixings, *e.g.*, $\pi^{\pm} \to e^{\pm} + N$ via U_e. However, a non-zero U_e also induces the production of the HNL via decays of other particles, *e.g.*, $K^{\pm} \to e^{\pm} + N$ and the three-body decay, $K^{\pm} \to e^{\pm} + \pi^0 + N$. On the other hand, in our RPV benchmarks, this is not the case since λ'_{i11} only couples to the pion. This affects the kinematics of the HNL relative to the bino, and can be an issue for our simple scaling procedure, *cf.* the discussion in Sec. 5.3. For the pion benchmarks of Table 5.5, this is not a problem since the kaon modes are sub-dominant ($\mathcal{O}(1\%)$) for the mass range identified above: $1\,\text{MeV} \lesssim m_N \lesssim 139\,\text{MeV}$; see, for instance, Ref. [435] for a plot with the relevant branching ratios in the HNL scenario. However, in later benchmarks, we deal with this issue – if it arises – by restricting the mass range of the benchmark to ensure that the types of contributing parents are the same in both models (neglecting sub-dominant contributions up to $\mathcal{O}(10\%)$), so that the assumption of the same kinematics taken in the DV quick recasting method still holds.

We show the reinterpreted limits for the benchmarks $\boldsymbol{\pi_1}$ and $\boldsymbol{\pi_2}$ in the RPV coupling vs. mass plane in Fig. 5.7(a) and Fig. 5.7(b), respectively. For two-dimensional visualization, we have set the production and decay couplings to be equal. The exclusion limits come from a corresponding HNL search at `Super-Kamiokande` [417], as well as projections of sensitivity at `DUNE` [408]. The former only constrains the mass range $m_N \gtrsim 50\,\text{MeV}$ and, hence, does not have sensitivity to $\boldsymbol{\pi_2}$. We also show the existing bounds on the RPV couplings, taken from Ref. [67]. There are no existing product bounds on the pairs considered [99, 157]. From Fig. 5.7(a), it appears that the existing bound on λ'_{111} outperforms the reinterpreted bound. However, this is an artefact of the choice to set the production and decay couplings equal. We show the same exclusion limits again in Fig. 5.7(c) – this time in the coupling vs. coupling plane for a fixed neutralino mass, $m_{\tilde{\chi}_1^0} = 120\,\text{MeV}$; one can see that the reinterpreted sensitivity projection can probe a small region of the phase space still allowed by the current limits.

Kaon scenarios

Next, we study benchmarks corresponding to bino production via $K^{\pm}$ decays; the details are summarized in Table 5.6. Note, that for some benchmarks, (*e.g.*, $\boldsymbol{K_3}$), the lower end of the mass range lies significantly above the kinematic threshold requirement of bino decay. This is, as discussed above, to ensure that kaons are the only parents in the HNL model, as they are in the RPV model.

The sensitivity limits for the kaon benchmarks are shown in Fig. 5.8. The single and – wherever relevant – product bounds (taken from Ref. [99, 157]) on RPV couplings are also shown. Current exclusion limits are obtained by combining the results from existing HNL searches at `T2K` [409], `Super-Kamiokande` [417], `NuTeV` [413], and `MicroBooNE` [414, 436], while the projections are all from `DUNE` [408]. In particular, for the benchmark $\boldsymbol{K_1}$, Ref. [325]

Category	$\tilde{\chi}_1^0$ **Decay** / $\tilde{\chi}_1^0$ **Production**	νee	$\nu e\mu$	$\nu\mu\mu$	$e\{\pi/\rho\}$	$\mu\{\pi/\rho\}$	eK	μK	$\nu\{\pi/\rho/\omega\}$	$\nu\{\eta/\eta'/\phi\}$
π	$\lambda'_{111} : \pi^\pm \to e^\pm + \tilde{\chi}_1^0$ ($m_{\tilde{\chi}_1^0} \lesssim 139\,\text{MeV}$)	$\lambda_{121};\lambda_{131}$	$\lambda_{121};\lambda_{122};\lambda_{321};\lambda_{312}$	$\times$	$\times$	$\times$	$\times$	$\times$	$\times$	$\times$
	$\lambda'_{211} : \pi^\pm \to \mu^\pm + \tilde{\chi}_1^0$ ($m_{\tilde{\chi}_1^0} \lesssim 34\,\text{MeV}$)	$\lambda_{121};\lambda_{131}$	$\times$	$\times$	$\times$	$\times$	$\times$	$\times$	$\times$	$\times$
K	$\lambda'_{112} : K^\pm \to e^\pm + \tilde{\chi}_1^0$ ($m_{\tilde{\chi}_1^0} \lesssim 493\,\text{MeV}$)	$\lambda_{121};\lambda_{131}$	$\lambda_{121};\lambda_{122};\lambda_{321};\lambda_{312}$	$\lambda_{122};\lambda_{322}$	λ'_{111}	λ'_{211}	$\times$	$\times$	λ'_{i11}	$\times$
	$\lambda'_{212} : K^\pm \to \mu^\pm + \tilde{\chi}_1^0$ ($m_{\tilde{\chi}_1^0} \lesssim 388\,\text{MeV}$)	$\lambda_{121};\lambda_{131}$	$\lambda_{121};\lambda_{122};\lambda_{321};\lambda_{312}$	$\lambda_{122};\lambda_{322}$	λ'_{111}	λ'_{211}	$\times$	$\times$	λ'_{i11}	$\times$
D	$\lambda'_{a21} : D^\pm \to e_a^\pm + \tilde{\chi}_1^0$ ($m_{\tilde{\chi}_1^0} \leq m_D - m_{e_a}$)	$\lambda_{121};\lambda_{131}$	$\lambda_{121};\lambda_{122};\lambda_{321};\lambda_{312}$	$\lambda_{122};\lambda_{322}$	λ'_{111}	λ'_{211}	λ'_{112}	λ'_{212}	λ'_{i11}	$\lambda'_{i11};\lambda'_{i22}$
D_s	$\lambda'_{a22} : D_s^\pm \to e_a^\pm + \tilde{\chi}_1^0$ ($m_{\tilde{\chi}_1^0} \leq m_{D_s} - m_{e_a}$)	$\lambda_{121};\lambda_{131}$	$\lambda_{121};\lambda_{122};\lambda_{321};\lambda_{312}$	$\lambda_{122};\lambda_{322}$	λ'_{111}	λ'_{211}	λ'_{112}	λ'_{212}	λ'_{i11}	$\lambda'_{i11};\lambda'_{322}$
B	$\lambda'_{i13} : B^\pm(B^0) \to e_i^\pm(\nu_i) + \tilde{\chi}_1^0$ ($m_{\tilde{\chi}_1^0} \leq m_B - m_{e_i}$)	$\lambda_{121};\lambda_{131}$	$\lambda_{121};\lambda_{122};\lambda_{321};\lambda_{312}$	$\lambda_{122};\lambda_{322}$	λ'_{111}	λ'_{211}	λ'_{112}	λ'_{212}	λ'_{i11}	$\lambda'_{i11};\lambda'_{i22}$
B_c	$\lambda'_{i23} : B_c^\pm \to e_i^\pm + \tilde{\chi}_1^0$ ($m_{\tilde{\chi}_1^0} \leq m_{B_c} - m_{e_i}$)	$\lambda_{121};\lambda_{131}$	$\lambda_{121};\lambda_{122};\lambda_{321};\lambda_{312}$	$\lambda_{122};\lambda_{322}$	λ'_{111}	λ'_{211}	λ'_{112}	λ'_{212}	λ'_{i11}	$\lambda'_{i11};\lambda'_{i22}$
τ	$\lambda'_{311} : \tau^\pm \to \{\pi^\pm/\rho^\pm\} + \tilde{\chi}_1^0$ ($m_{\tilde{\chi}_1^0} \lesssim 1\,637\,\text{MeV}$)	$\lambda_{121};\lambda_{131}$	$\lambda_{121};\lambda_{122};\lambda_{321};\lambda_{312}$	$\lambda_{122};\lambda_{322}$	λ'_{111}	λ'_{211}	λ'_{112}	λ'_{212}	λ'_{a11}	$\lambda'_{a11};\lambda'_{i22}$
	$\lambda'_{312} : \tau^\pm \to K^\pm + \tilde{\chi}_1^0$ ($m_{\tilde{\chi}_1^0} \lesssim 1\,283\,\text{MeV}$)	$\lambda_{121};\lambda_{131}$	$\lambda_{121};\lambda_{122};\lambda_{321};\lambda_{312}$	$\lambda_{122};\lambda_{322}$	λ'_{111}	λ'_{211}	λ'_{112}	λ'_{212}	λ'_{i11}	$\lambda'_{i11};\lambda'_{i22}$

Table 5.4: Relevant two-coupling RPV scenarios probed by HNL DV searches. Column one categorizes the parent meson/lepton; column two shows the corresponding RPV coupling, production process, and bino mass range; the remaining columns list the relevant final states of Table 5.3 arising from bino decays and the corresponding decay RPV coupling(s) for each production category. $\times$ indicates that the decay is kinematically disallowed.

Label	Production	Decay	$m_{\tilde{\chi}_1^0}$
$\boldsymbol{\pi_1}$	λ'_{111}	λ_{321}	106 MeV − 139 MeV
$\boldsymbol{\pi_2}$	λ'_{211}	λ_{121}	1 MeV − 34 MeV

Table 5.5: Details of the two-coupling RPV benchmark scenarios we study, corresponding to bino production from pions. The decay coupling in the third column leads to the final state that can be read off from Table 5.4. See the main text for details on how the mass range is determined.

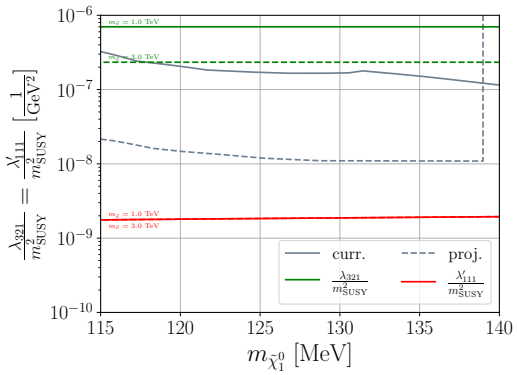

(a) Limits in the RPV coupling vs. bino mass plane for the benchmark $\boldsymbol{\pi_1}$ of Table 5.5.

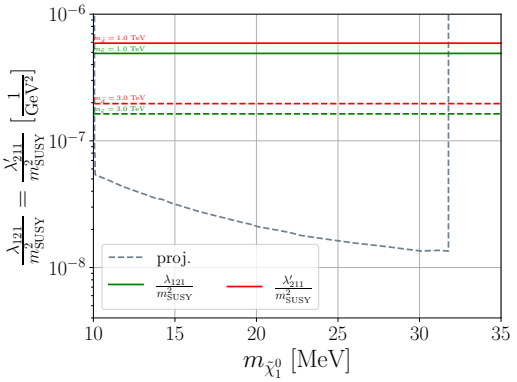

(b) Limits in the RPV coupling vs. bino mass plane for the benchmark $\boldsymbol{\pi_2}$ of Table 5.5.

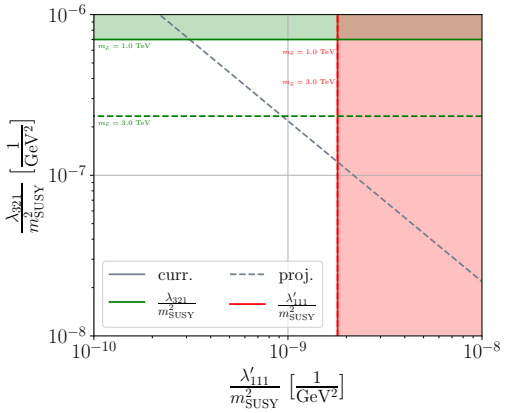

(c) Limits in the production coupling vs. decay coupling plane for the benchmark $\boldsymbol{\pi_1}$ of Table 5.5, with neutralino mass fixed at 120 MeV.

Figure 5.7: Current exclusion (solid lines) and projected sensitivity (dashed lines) limits corresponding to the two-coupling RPV scenarios with binos produced from pions; reinterpreted from HNL searches. The existing limits on the RPV couplings are shown in red, and green.

has studied the sensitivity of `Super-Kamiokande` to the light binos in the RPV-SUSY, using existing data from the experiment. Their results are found to be comparable with ours. Once again, we see that the reinterpreted limits exclude (or are projected to probe) large swathes of parameter space allowed by the current bounds. The sharp reduction in sensitivity in Fig. 5.8(e) below $m_{\tilde{\chi}_1^0} \approx 150\,\text{MeV}$ arises because the most constraining current limit comes

from T2K and only probes regions corresponding to $m_N \gtrsim 150\,\text{MeV}$; below this the low-mass searches from Super-K and MicroBooNE provide exclusion.

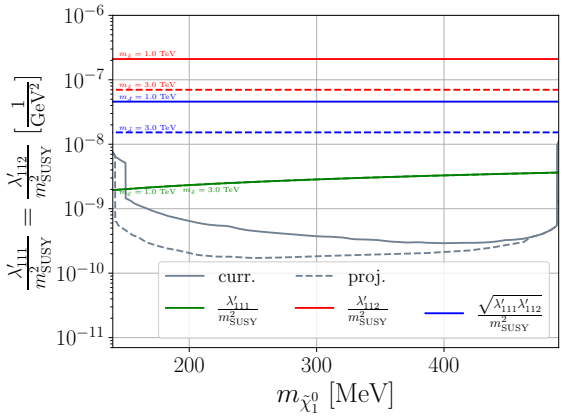

(a) Benchmark $\boldsymbol{K_1}$ from Table 5.6.

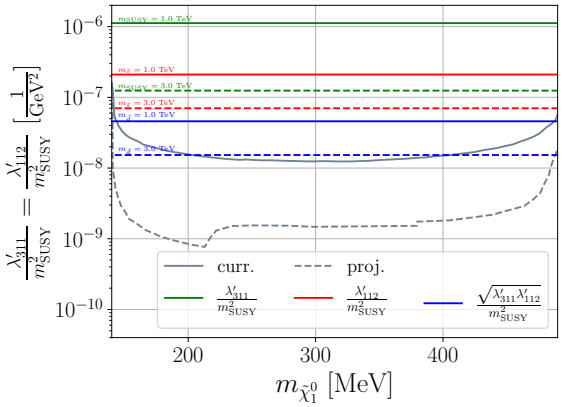

(b) Benchmark $\boldsymbol{K_2}$ from Table 5.6.

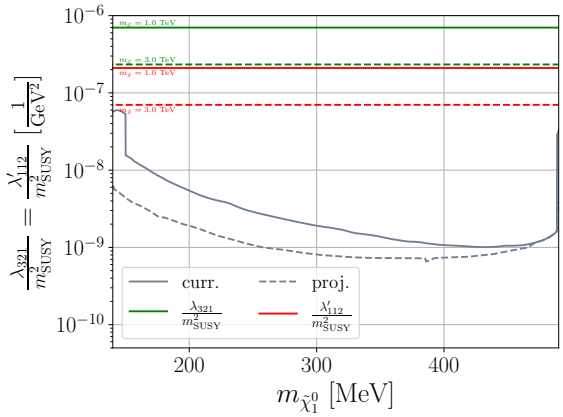

(c) Benchmark $\boldsymbol{K_3}$ from Table 5.6.

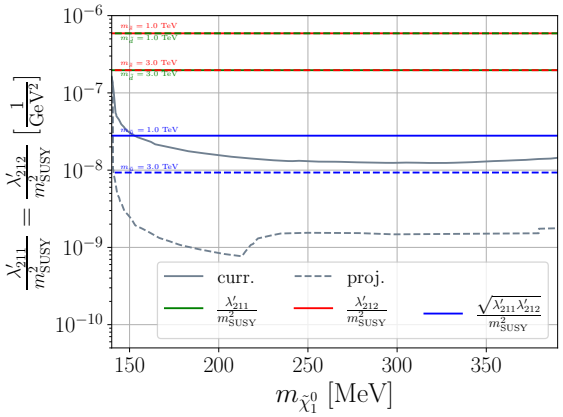

(d) Benchmark $\boldsymbol{K_4}$ from Table 5.6.

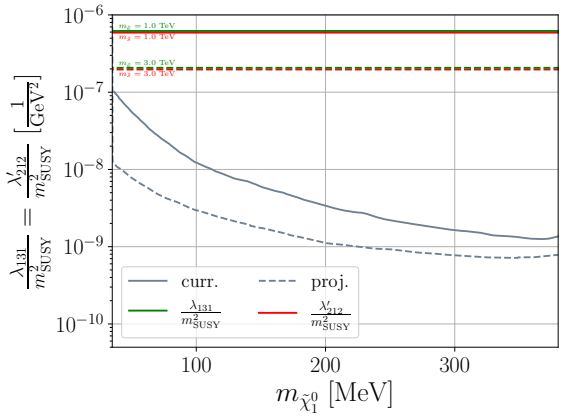

(e) Benchmark $\boldsymbol{K_5}$ from Table 5.6.

Figure 5.8: Current exclusion (solid lines) and projected sensitivity (dashed lines) limits corresponding to the two-coupling RPV scenarios with binos produced from kaons in the RPV coupling vs. bino mass plane; reinterpreted from HNL searches. The existing limits on the RPV couplings are shown in red and green (single bounds), and blue (product bound).

Label	Production	Decay	$m_{\tilde{\chi}_1^0}$
$\boldsymbol{K_1}$	λ'_{112}	λ'_{111}	140 MeV – 493 MeV
$\boldsymbol{K_2}$	λ'_{112}	λ'_{311}	140 MeV – 493 MeV
$\boldsymbol{K_3}$	λ'_{112}	λ_{321}	140 MeV – 493 MeV
$\boldsymbol{K_4}$	λ'_{212}	λ'_{211}	140 MeV – 388 MeV
$\boldsymbol{K_5}$	λ'_{212}	λ_{131}	35 MeV – 388 MeV

Table 5.6: As in Table 5.5 but for bino production from kaons.

D, D_s, and τ scenarios

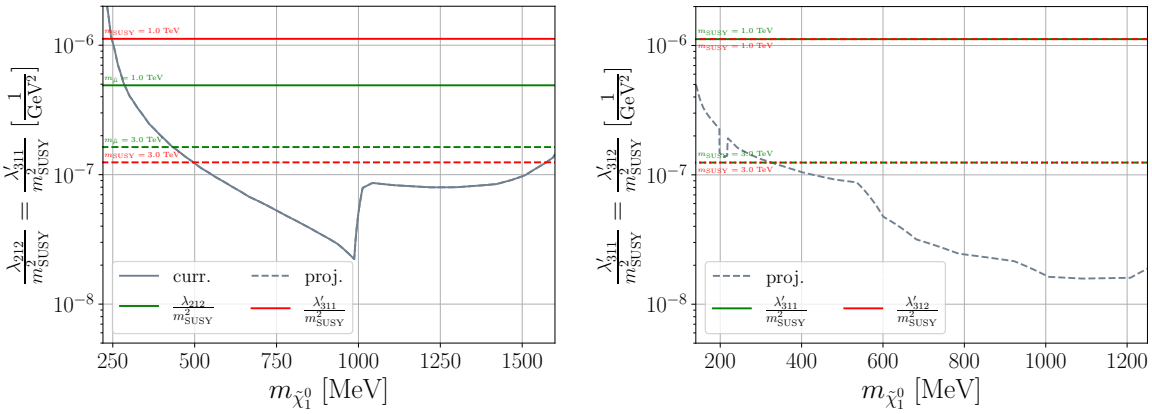

(a) Benchmark $\boldsymbol{\tau_1}$ from Table 5.7.

(b) Benchmark $\boldsymbol{\tau_2}$ from Table 5.7.

Figure 5.9: As in Fig. 5.8 but for binos produced from τ leptons.

We summarize the details for the τ benchmarks we consider, as well as the $D^\pm$ and $D_s^\pm$ meson ones in Table 5.7. We group them together in this section since, at the considered experiments, τ leptons are most copiously produced in the decays of the D_s mesons. The corresponding sensitivity limits are shown in Fig. 5.9 for the τ, and in Fig. 5.10 for the mesons.

For the τ lepton scenarios, the exclusion and projected search sensitivity, shown in Fig. 5.9, come from `BEBC` [415, 416], `CHARM` [410, 437], and `ArgoNeuT` [438]; and `DUNE` [408], `FASER2` [418, 425], and `MoEDAL-MAPP2` [419, 425], respectively. There is no current search targeting the final state of $\boldsymbol{\tau_2}$, while the current limit on $\boldsymbol{\tau_1}$ beats even the projected search sensitivity at `DUNE` and `FASER`. The sharp drop in sensitivity in Fig. 5.9(a) at $m_{\tilde{\chi}_1^0} \approx 1\,000\,\text{MeV}$ occurs because the ρ and bino decay mode of the τ lepton in the RPV model (*cf.* Table 5.2) becomes kinematically inaccessible, leading to the reduction in production.

For the D and D_s mesons, current exclusions are provided by searches at `BEBC` [415, 416], `CHARM` [410], and `NuTeV` [413]. Further, `DUNE` [408], `FASER2` [418], and `MoEDAL-MAPP2` [419, 425] are projected to improve this reach. For all D_s benchmarks except $\boldsymbol{D_7}$, we only consider neutralinos with mass, $m_{\tilde{\chi}_1^0} > 600\,\text{MeV}$. This is because either the above experiments only constrain the corresponding parameter region in the HNL model, or because kaons and

Label	Production	Decay	$m_{\tilde{\chi}_1^0}$
$\boldsymbol{\tau_1}$	λ'_{311}	λ_{212}	211 MeV – 1 637 MeV
$\boldsymbol{\tau_2}$	λ'_{312}	λ'_{311}	140 MeV – 1 283 MeV
$\boldsymbol{D_1}$	λ'_{122}	λ'_{111}	600 MeV – 1 968 MeV
$\boldsymbol{D_2}$	λ'_{122}	λ'_{211}	600 MeV – 1 968 MeV
$\boldsymbol{D_3}$	λ'_{122}	λ'_{112}	600 MeV – 1 968 MeV
$\boldsymbol{D_4}$	λ'_{122}	λ_{121}	600 MeV – 1 968 MeV
$\boldsymbol{D_5}$	λ'_{222}	λ'_{211}	600 MeV – 1 863 MeV
$\boldsymbol{D_6}$	λ'_{222}	λ_{131}	600 MeV – 1 863 MeV
$\boldsymbol{D_7}$	λ'_{221}	λ_{232}	260 MeV – 1 764 MeV

Table 5.7: As in Table 5.5 but for bino production from τ leptons, and D and D_s mesons.

pions dominate the HNL production for lower masses. One exception is BEBC, where nearly all produced pions and kaons are absorbed by a high-density target before they can decay, and HNL production is dominated by D meson decays. Since benchmark $\boldsymbol{D_7}$ involves production from D-mesons, we can probe lower bino masses in our scenario. The kink in the corresponding sensitivity limit in Fig. 5.10(g) at $m_{\tilde{\chi}_1^0} \approx 500\,\text{MeV}$ occurs because CHARM takes over from BEBC. We note that the final states of benchmarks $\boldsymbol{D_1}$ and $\boldsymbol{D_3}$ are not covered by the existing searches but will be covered by the upcoming experiments.

Once again, we see – for all the plots in this section – that reinterpreting existing and projected limits on HNL models in terms of our RPV scenarios gives bounds on the parameter space that improve upon existing limits by orders of magnitude.

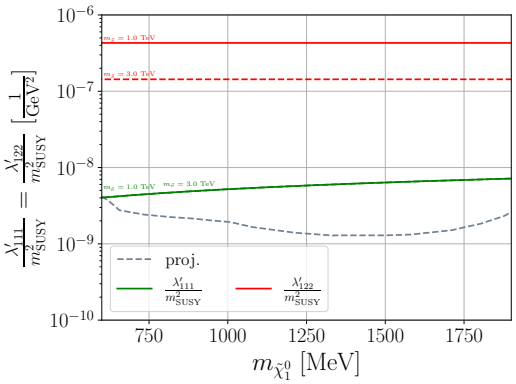

(a) Benchmark $\boldsymbol{D_1}$ from Table 5.7.

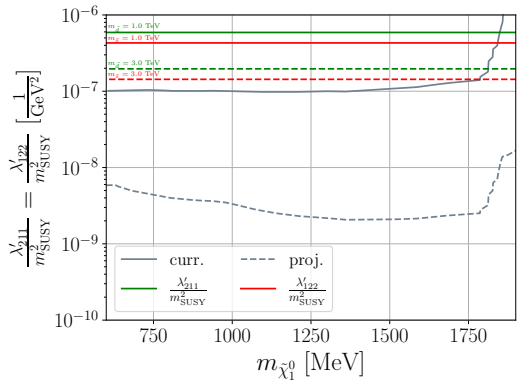

(b) Benchmark $\boldsymbol{D_2}$ from Table 5.7.

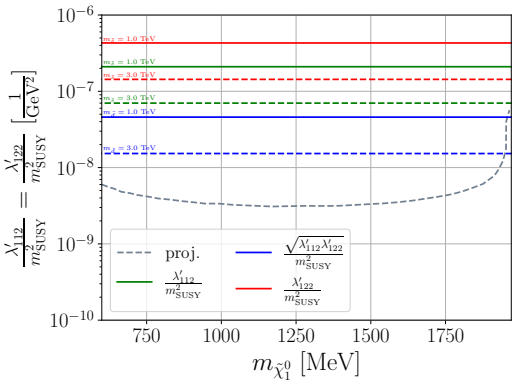

(c) Benchmark $\boldsymbol{D_3}$ from Table 5.7.

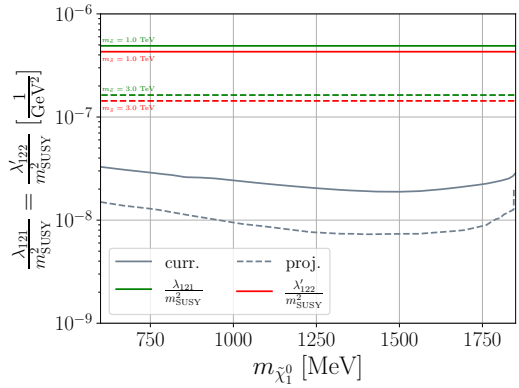

(d) Benchmark $\boldsymbol{D_4}$ from Table 5.7.

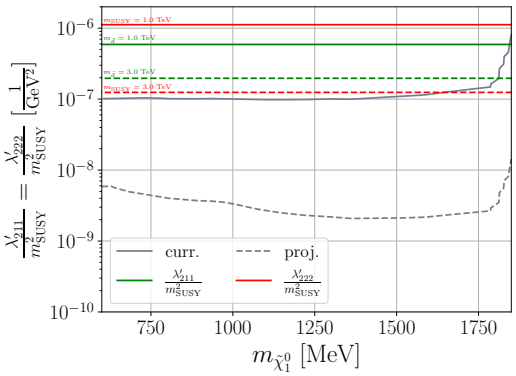

(e) Benchmark $\boldsymbol{D_5}$ from Table 5.7.

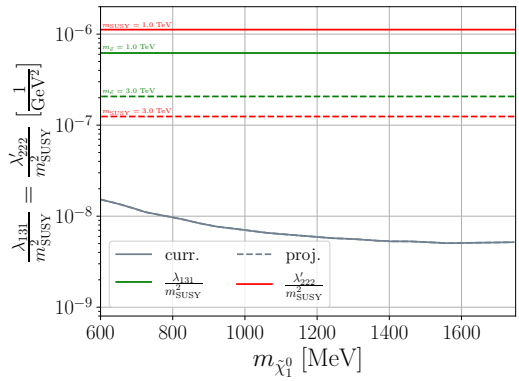

(f) Benchmark $\boldsymbol{D_6}$ from Table 5.7.

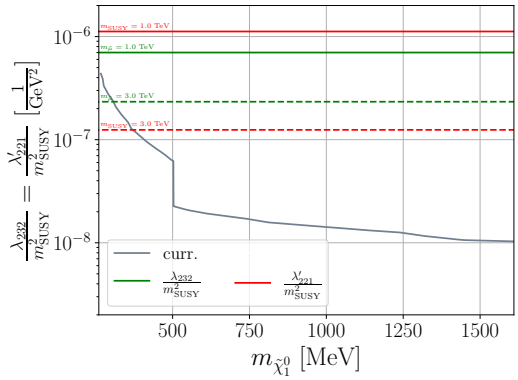

(g) Benchmark $\boldsymbol{D_7}$ from Table 5.7.

Figure 5.10: As in Fig. 5.8 but for binos produced from D and D_s mesons.

B and B_c scenarios

Here, the bino is produced in $B(B^{\pm}/\overset{(-)}{B}{}^{0})$ or $B_c^{\pm}$ decays, *cf.* Table 5.8. While HNL production in these modes only becomes dominant above the D-meson thresholds, the projected search sensitivity for `FASER(2)` provided in Ref. [418] shows the results separately for the HNLs from B-meson decays and from D-meson and kaon decays, enabling us to choose benchmarks with masses lower than the D thresholds. Up to about $m_N \approx 2\,700\,\text{MeV}$, the production is dominated by B decays and we choose the first three benchmarks accordingly. Beyond this, B_c decays also become significant, and for $m_N \gtrsim 3\,500\,\text{MeV}$, they become the dominant modes; the last two benchmarks focus on this.

Label	Production	Decay	$m_{\tilde{\chi}_1^0}$
$\boldsymbol{B_1}$	λ'_{113}	λ'_{122}	$548\,\text{MeV} - 2\,700\,\text{MeV}$
$\boldsymbol{B_2}$	λ'_{113}	λ_{131}	$160\,\text{MeV} - 2\,700\,\text{MeV}$
$\boldsymbol{B_3}$	λ'_{213}	λ'_{211}	$160\,\text{MeV} - 2\,700\,\text{MeV}$
$\boldsymbol{B_4}$	λ'_{123}	λ'_{311}	$3\,500\,\text{MeV} - 6\,275\,\text{MeV}$
$\boldsymbol{B_5}$	λ'_{123}	λ_{131}	$3\,500\,\text{MeV} - 6\,275\,\text{MeV}$

Table 5.8: As in Table 5.5 but for bino production from B and B_c mesons.

The corresponding sensitivity limits are presented in Fig. 5.11. There are no existing constraints; however, projections from `FASER2` [418, 425] and `MoEDAL-MAPP2` [419, 425] show that we should be able to probe the RPV parameter space up to 2-3 orders of magnitude beyond what is ruled out by current limits.

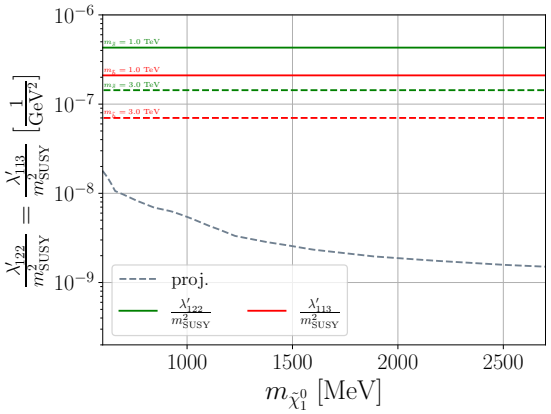

(a) Benchmark $\boldsymbol{B_1}$ from Table 5.8.

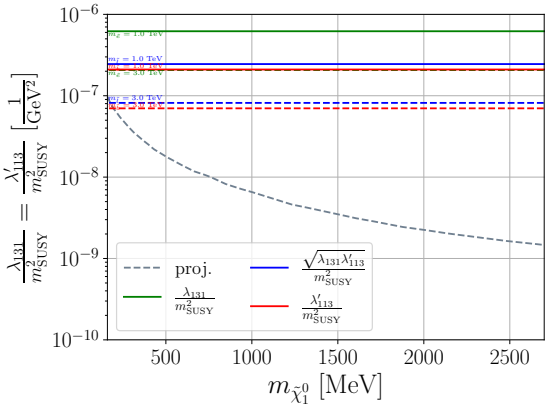

(b) Benchmark $\boldsymbol{B_2}$ from Table 5.8.

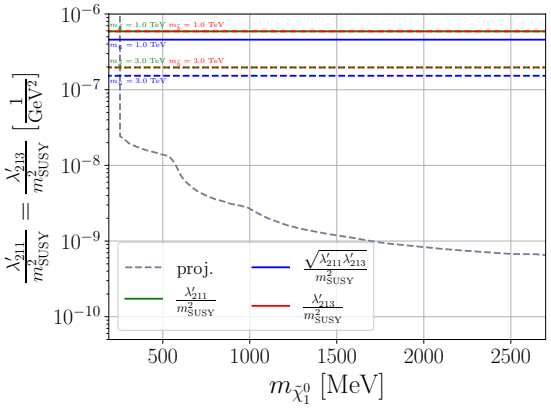

(c) Benchmark $\boldsymbol{B_3}$ from Table 5.8.

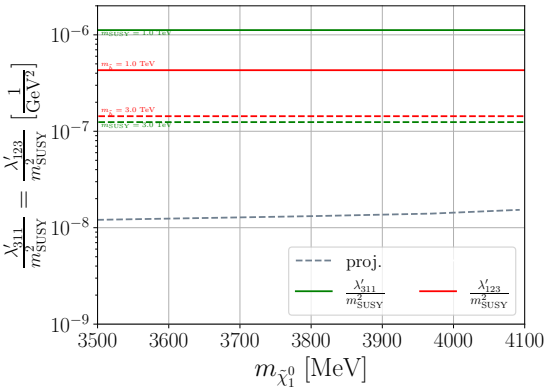

(d) Benchmark $\boldsymbol{B_4}$ from Table 5.8.

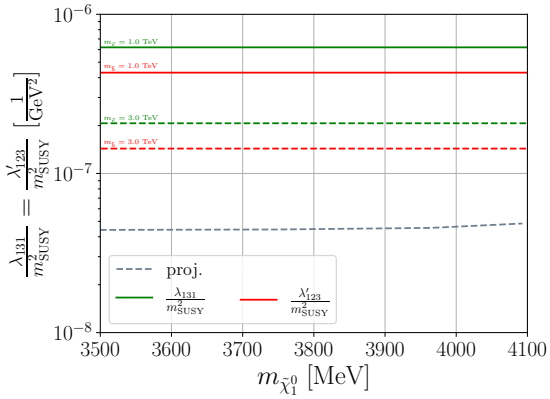

(e) Benchmark $\boldsymbol{B_5}$ from Table 5.8.

Figure 5.11: As in Fig. 5.8 but for binos produced from B and B_c mesons.

5.5 Conclusions

In this work, we have considered a GeV-scale or lighter long-lived lightest neutralino, which is necessarily bino-like, in the minimal R-parity-violating (RPV) supersymmetric model. We have focused on lepton-number-violating operators in the RPV superpotential: LH_u, $LL\bar{E}$, and $LQ\bar{D}$. Such light neutralinos are still allowed by all experimental and observational constraints, as long as they decay, for instance via RPV couplings, so as to avoid overclosing the Universe. Since these RPV couplings are bounded to be small, such light binos, which we assume to be the lightest supersymmetric particle in our theory, are expected to have a relatively long lifetime. Via the considered couplings, the binos can decay leptonically or semi-leptonically. For their production, we have focused on rare decays of mesons and charged leptons which are copiously produced at various facilities such as beam-dump and collider experiments. Once produced, these light binos can lead to exotic signatures such as displaced vertices (DVs) or missing energy. We have used searches for these signatures to constrain the RPV couplings associated with a light bino.

These various strategies are experimentally widely utilized to constrain heavy neutral leptons (HNLs) which may decay to almost the same final-state particles as the lightest neutralino in the RPV models. We have thus used the existing HNL searches to set new strict bounds on the relevant RPV couplings. Furthermore we have translated the prjected sensitivity to the HNL parameters at certain future experiments into the corresponding search sensitivity for the light neutralinos.

We have studied comprehensively the past experiments `PIENU`, `NA62`, `T2K`, and `BaBar`, as well as the approved experiments `FASER`, `MoEDAL-MAPP1`, `PIONEER`, and `DUNE`. We did not consider future experiments that are not yet approved such as `MATHUSLA` and `ANUBIS`, with two exceptions, namely `FASER2` and `MoEDAL-MAPP2` since they would be the follow-up programs of the two currently running experiments `FASER` and `MoEDAL-MAPP1`.

Given the various types and flavor-indices of the RPV operators that can be switched on, we have investigated separately different theoretical benchmark scenarios, which can be bounded by distinct experiments and strategies. For the selected representative benchmark scenarios, we have performed numerical computation and presented the final exclusion bounds. Further, we have compared these recast bounds with the existing limits on the RPV couplings which mainly stem from low-energy processes of meson and lepton decays. In general, we find that in most cases the exclusion limits obtained from recasting past HNL searches surpass the existing bounds on the RPV couplings by orders of magnitude, and the expected limits at the considered ongoing and future experiments can be even stronger.

Simple and analytic reinterpretation methods are becoming an important research tool. This is because most published experimental reports present results only for a limited number of simple models, and a recast with full simulation is often complicated and time-consuming. Some existing works such as Refs. [383, 416, 425] have shown the power of simple and quick reinterpretation of searches for long-lived particles by considering heavy neutral leptons in various models and axion-like particles as examples. Our work exemplifies again the strengths and convenience of such reinterpretation methods, by recasting the bounds on the HNLs in the minimal scenario, into those on the lightest neutralinos in the RPV supersymmetric models, and hence motivates the development of further studies with these reinterpretation methods.

Addendum:
The authors note that Julian Günther et al. are currently working on a dedicated simulation for the same benchmark $\boldsymbol{K_1}$ at `DUNE` in a soon-to-be-released paper.

6

A Novel Proton Decay Signature at DUNE, JUNO and Hyper-K

6.0 Preface

The chapter is based on a collaboration with Herbi K. Dreiner, Saurabh Nangia and Apoorva Shah. The work has not been published yet but will be in the near future.

The author guided Apoorva Shah in her implementation of the Monte Carlo simulation with the RPV-MSSM framework, as described in Section 6.4. Especially, he set up the execution of the code on the cluster. The author provided information about the search strategies of the different proposed experiments and the effect of the nucleus on proton decay, both presented in Section 6.3. Finally, the interpretation of the results was performed by the author together with Saurabh Nangia and Apoorva Shah.

6.1 Introduction

In this chapter our main goal is to consider the decays:

$$p \rightarrow K^+ + X^0, \tag{6.1}$$

$$X^0 \rightarrow \{\pi^\pm \mu^\mp,\, \pi^0 + \nu_\mu,\, \pi^0 + \bar{\nu}_\mu,\, \gamma + \overset{(-)}{\nu}\}\,, \tag{6.2}$$

as novel search modes. Here X^0 is a new electrically neutral BSM particle, which might travel macroscopic distances within the detector before decaying. As we have discussed in the previous chapter, we assume X^0 to be a very light bino-like neutralino and it is likely to be long-lived. Indeed, this scenario represents one of the few remaining ways in which the RPV-MSSM could realistically manifest itself at low energies. Searches for it have received significant attention recently [225–227, 322, 323], along with a general raising interest in LLPs [209, 210, 284, 312, 313, 435], predicted in a wide class of frameworks beyond SUSY.

To our knowledge, this decay mode has not been studied experimentally or theoretically. The above decay channel can be opened by a single RPV operator [101]. In particular, it is interesting to compare it with the canonical mode $p \rightarrow K^+ + \bar{\nu}$, for which `Super-Kamiokande` (`Super-K`) gives the best current limit, $\tau_{p\rightarrow K^+ + \bar{\nu}} > 5.9 \times 10^{33}$ yrs [439]. If the neutralino is long-lived enough, it can escape detection, much like the neutrino. However, the neutralino is usually more massive, which reduces the kaon momentum. On the other hand, the neutralino can also decay inside the detector, leading to a characteristic signature. We analyze both possibilities in detail and describe how the `Super-K` limit can be reinterpreted. We discuss

the search sensitivity of DUNE, JUNO, and Hyper-Kamiokande(Hyper-K) experiments for these decay modes.

The chapter is organized as follows: we discuss the proton decay modes in the RPV-MSSM setup, including the resulting signatures, in Section 6.2. In Section 6.3 we briefly discuss the present and future experimental setups, which might be able to detect proton-decay: Super-K [440], Hyper-K, DUNE and JUNO. In Section 6.4, we describe our simulation procedure for the estimating the sensitivities in the above experiments, and Section 6.5 present the relevant benchmark scenarios. Finally, we present and discuss the numerical results in Section 6.6, and we conclude in Section 6.7.

6.2 Proton Decay in R-Parity Violating MSSM

A brief introduction to our chosen framework of the RPV-MSSM[54] along with a very light neutralino can be found in Section 1.3. We will continue within this framework and now describe the calculation of the proton decay width for the neutralino mode $p \to K^+ + \tilde{\chi}_1^0$, and discuss the relevant signatures from this setup.

6.2.1 Decay Width Calculation

If tree-level proton decay is kinematically allowed via the mode,

$$p \to K^+ + \tilde{\chi}_1^0 \,, \tag{6.3}$$

a light neutralino has to satisfy the mass bound,

$$m_{\tilde{\chi}_1^0} \leq m_p - m_{K^+} \approx 445\,\text{MeV} \,. \tag{6.4}$$

This process requires only a single RPV operator, λ''_{121}, see Eq. (1.10), and lepton number need not be violated. The relevant Feynman diagrams at the parton level level are shown in Fig. 6.1. In addition, higher-order diagrams or effects such as CKM-mixing [149, 441] can induce additional modes, *e.g.*, decay into a pion and a neutralino; however, these effects are subordinate and we do not consider them in this work.[1] An early estimate for the decay rate of Eq. (6.3) was presented in Ref. [109] where, for a photino-like neutralino satisfying $m_{\tilde{\gamma}} \ll m_p - m_{K^+}$, the bound,

$$|\lambda''_{121}| < 10^{-15} \,, \tag{6.5}$$

was obtained using the existing experimental bound on the decay rate for $p \to K^+ + \bar{\nu}$, and assuming the squark mass, $m_{\tilde{q}}$, to be $\mathcal{O}(100\,\text{GeV})$. Using the same technique, Ref. [101] recently updated the bound (for a massless bino-like neutralino),

$$|\lambda''_{121}| < 3.9 \times 10^{-25} \left(\frac{m_{\tilde{q}}}{\text{TeV}}\right)^2 \,. \tag{6.6}$$

However, as pointed out in Ref.[101], it is crucial to take into account the different

[1] For heavier neutralino masses, the kaon mode could be be kinematically forbidden, and decay into a pion would become relevant. We will discuss this elsewhere.

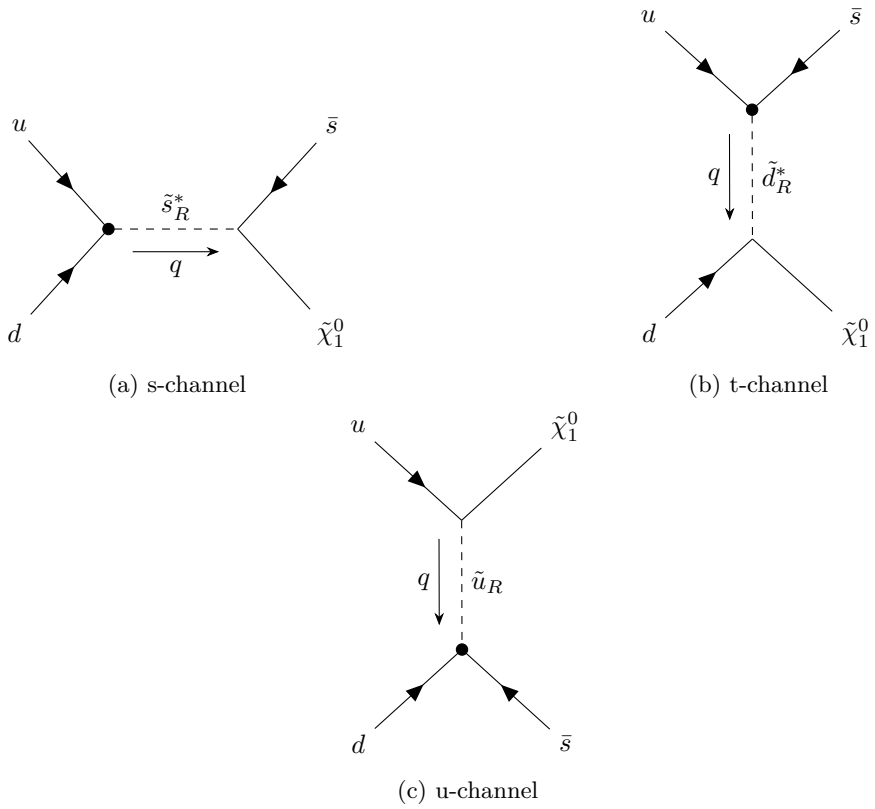

(a) s-channel

(b) t-channel

(c) u-channel

Figure 6.1: Feynman diagrams depicting the decay of a proton into a light neutralino. The black blob shows the RPV vertex. Spectator quarks are omitted.

kinematics of decay into a massive neutralino compared to a (massless) neutrino, which requires an adequate treatment. In addition, the neutralino itself decays in the RPV-MSSM, which will be discussed in more detail later, resulting in the neutralino no longer appearing as missing energy in the detector and making the previous limit inapplicable. Therefore, a comprehensive analysis of the decay mode of Eq. (6.3) is necessary to accurately estimate the sensitivities of the setups at `Hyper-K`, `DUNE` and `JUNO`.

We proceed with the details of our calculation, which closely follows the same methodology described in Ref. [101], where the rate was calculated for the decay mode $p \to K^+ + \bar{\nu}$. First, we study the $p \to K^+ + \tilde{\chi}_1^0$ process at the parton level in the framework of an effective field theory (EFT) governing proton decays up to the sixth dimension on the electroweak (EW) scale, where the chosen UV completion is associated with the RPV-MSSM. The specific dim-6 operators responsible for inducing the decay $p \to K^+ + \bar{\nu}$ are discussed in detail in Ref. [101].

Similarly, we can introduce dim-6 operators that induce $p \to K^+ + \tilde{\chi}_1^0$, using 4-component

spinor notation:

$$\begin{aligned}\hat{\mathcal{Q}}'_1 &= \varepsilon_{\alpha\beta\gamma}[(\overline{d^c})^\alpha P_R u^\beta][(\overline{s^c})^\gamma P_R \tilde{\chi}_1^{0c}]\,,\\ \hat{\mathcal{Q}}_1 &= \varepsilon_{\alpha\beta\gamma}[(\overline{s^c})^\alpha P_R u^\beta][(\overline{d^c})^\gamma P_R \tilde{\chi}_1^{0c}]\,,\\ \hat{\mathcal{Q}}_2 &= \varepsilon_{\alpha\beta\gamma}[(\overline{s^c})^\alpha P_R d^\beta][(\overline{u^c})^\gamma P_R \tilde{\chi}_1^{0c}]\,,\end{aligned} \tag{6.7}$$

where P_R is the right-handed projection operator, $\varepsilon_{\alpha\beta\gamma}$ is the three-dimensional Levi-Civita symbol, and the Greek indices, α, β and $\gamma \in \{1, 2, 3\}$, indicate the $\mathrm{SU}(3)_C$ color. It is important to note that we perform the matching at leading order and consider only the corresponding dim-6 (or effectively dim-6 after EW symmetry-breaking) operators violating B and L. After running the QCD renormalization group equations, all operators undergo a simple scaling factor called η_{QCD}, as discussed in Ref. [442].

From the effective operators of Eq. (6.7), the amplitude for the parton-level process can be written in terms of the operators (Ω) and their corresponding Wilson coefficients (C_Ω) as,

$$\begin{aligned}iM^{EFT}(p \to K^+ + \tilde{\chi}_1^0) = i\varepsilon_{\alpha\beta\gamma}\eta_{\mathrm{QCD}}\{&(C_{\hat{\mathcal{Q}}'_1})[\overline{u^c}^\alpha_d P_R u^\beta_u][\overline{v^c}^\gamma_s P_R v_{\tilde{\chi}_1^0}]\\ &+ (C_{\hat{\mathcal{Q}}_1})[\overline{u^c}^\alpha_d P_R v_{\tilde{\chi}_1^0}][\overline{v^c}^\beta_s P_R u^\gamma_u] - (C_{\hat{\mathcal{Q}}_2})[\overline{v^c}^\alpha_s P_R u^\beta_d][\overline{u^c}^\gamma_u P_R v_{\tilde{\chi}_1^0}]\}\,.\end{aligned} \tag{6.8}$$

In the above, u and v are four-component spinors.

We subsequently perform the matching process by identifying the parton-level scattering amplitudes in the EFT with those in the full RPV MSSM at the releant SUSY scale (the masses of the mediating particles, as shown in Fig. 6.1), which we set to (1 TeV). This allows us to determine the Wilson coefficients,

$$\begin{aligned}(C_{\hat{\mathcal{Q}}'_1}) &= \eta_{\mathrm{QCD}}\frac{(-\lambda''^*_{112})(\sqrt{2}g')}{3m^2_{\tilde{s}_R}}\,,\\ (C_{\hat{\mathcal{Q}}_1}) &= \eta_{\mathrm{QCD}}\frac{(-\lambda''^*_{121})(\sqrt{2}g')}{3m^2_{\tilde{d}_R}}\,,\\ (C_{\hat{\mathcal{Q}}_2}) &= \eta_{\mathrm{QCD}}\frac{(\lambda''^*_{121})(2\sqrt{2}g')}{3m^2_{\tilde{u}_R}}\,.\end{aligned} \tag{6.9}$$

In the above, $\eta_{\mathrm{QCD}} \approx 1.4$, g' is the $\mathrm{U}(1)_Y$ hypercharge gauge coupling and the m's denote the relevant squark masses.

To obtain the full amplitude of the process, we require the hadronic matrix element. To do this, the matrix element for the operators between the proton and kaon states must be evaluated non-perturbatively. In the rest-frame of the proton, the transition associated with the operator Ω can be expressed as follows [443],

$$\begin{aligned}\langle K^+, \tilde{\chi}_1^0(q)|\Omega|p\rangle &= \bar{v}_{\tilde{\chi}_1^0} P_R \left[W_{0,\Omega}^{p\to K^+}(q^2) - \frac{iq_\mu\gamma^\mu}{m_p} W_{1,\Omega}^{p\to K^+}(q^2)\right] u_p\,,\\ &\equiv \bar{v}_{\tilde{\chi}_1^0} P_R \left[W_{\chi,\Omega}^{p\to K^+}(q^2)\right] u_p\,,\end{aligned} \tag{6.10}$$

Operators [Ω]	$W_{0,\Omega}^{p\to K^+}$	$W_{\chi,\Omega}^{p\to K^+}(400\,\text{MeV})$
$\hat{\mathcal{Q}}_1'$	0.139	0.158
$\hat{\mathcal{Q}}_1$	0.041	0.053
$\hat{\mathcal{Q}}_2$	-0.098	-0.092

Table 6.1: Hadronic matrix elements for proton to kaon decays from lattice computations. The values for $W_{0,\Omega}^{p\to K^+}$ are taken from Ref. [444]. The values for $W_{\chi,\Omega}^{p\to K^+}$, which contain corrections for the massive neutralino, are calculated using expressions in Eq. (6.12).

where $W_{0,\Omega}^{p\to K^+}(q^2)$ and $W_{1,\Omega}^{p\to K^+}(q^2)$ are the form factors associated with the operator Ω for the transition $p \to K^+$; these depend on the squared momentum-transfer, q^2. Here, m_p denotes the mass of the proton. We present the numerical values for $W_{0,\Omega}^{p\to K^+}(q^2)$ in Table 6.1.

The process of calculating the relevant form factors using lattice methods is described in detail in Ref. [444]. In situations where the neutralino or neutrino is massless in the final state, as in Ref. [101], the contributions of $W_{1,\Omega}^{p\to K^+}(q^2)$ are negligible. An approximation can be made,

$$W_{\chi,\Omega}^{p\to K^+}(q^2) \approx W_{0,\Omega}^{p\to K^+}(q^2)\,, \quad (m_{\tilde{\chi}_1^0} \approx 0)\,. \tag{6.11}$$

However, for a massive neutralino, there are corrections to $W_{0,\Omega}^{p\to K^+}(q^2)$ that can be significant and cannot be ignored. Methods from chiral perturbation theory are necessary to account for these corrections. A comprehensive expression for the combined form factor $W_{\chi,\Omega}^{p\to K^+}$ can be found in Ref. [443]. We provide an expression for the three form factors in powers of $m_{\tilde{\chi}_1^0}$ up to fourth order (equivalent to second order in q^2) in Eq. (6.12). For our calculations, we use an estimate of $m_{\tilde{\chi}_1^0} = 400\,\text{MeV}$, as given in Table 6.1,

$$\begin{aligned}
W_{\chi,\hat{\mathcal{Q}}_1'}^{p\to K^+} &= W_{0,\hat{\mathcal{Q}}_1'}^{p\to K^+} + 0.109 m_{\tilde{\chi}_1^0}^2 + 0.082 m_{\tilde{\chi}_1^0}^4 + \mathcal{O}(m_{\tilde{\chi}_1^0}^6)\,,\\
W_{\chi,\hat{\mathcal{Q}}_1}^{p\to K^+} &= W_{0,\hat{\mathcal{Q}}_1}^{p\to K^+} + 0.079 m_{\tilde{\chi}_1^0}^2 + 0.060 m_{\tilde{\chi}_1^0}^4 + \mathcal{O}(m_{\tilde{\chi}_1^0}^6)\,,\\
W_{\chi,\hat{\mathcal{Q}}_2}^{p\to K^+} &= W_{0,\hat{\mathcal{Q}}_2}^{p\to K^+} - 0.030 m_{\tilde{\chi}_1^0}^2 - 0.023 m_{\tilde{\chi}_1^0}^4 + \mathcal{O}(m_{\tilde{\chi}_1^0}^6)\,,
\end{aligned} \tag{6.12}$$

Finally, the decay amplitude for the proton can be expressed as,

$$\mathcal{A}\left(p \to K^+ + \tilde{\chi}_1^0\right) = i \sum_{\Omega} C_\Omega \langle K^+, \tilde{\chi}_1^0(q)|\Omega|p\rangle\,, \tag{6.13}$$

which leads to the partial decay width,

$$\Gamma\left(p \to K^+ + \tilde{\chi}_1^0\right) = \frac{|\vec{q}|}{8\pi m_p^2}\left[\frac{1}{2}\sum_{\text{pol.}} |\mathcal{A}\left(p \to K^+ + \tilde{\chi}_1^0\right)|^2\right], \tag{6.14}$$

$$= \frac{|\vec{q}|}{8\pi m_p}\sqrt{m_{\tilde{\chi}_1^0}^2 + \vec{q}^2}\sum_{\Omega} |C_\Omega W_{\chi,\Omega}^{p\to K^+}(q^2)|^2 . \tag{6.15}$$

The Wilson coefficients and form factors are provided in Eq. (6.9) and Eq. (6.12), respectively, and $\eta_{QCD} \approx 3.15$. $|\vec{q}|$ is the absolute value of the momentum of the outgoing kaon, in the proton rest-frame.

$$|\vec{q}| = |\vec{p}_{K^+}| = \frac{m_p}{2}\sqrt{1 - 2\frac{m_K^2 + m_{\tilde{\chi}_1^0}^2}{m_p^2} + \left(\frac{m_K^2 - m_{\tilde{\chi}_1^0}^2}{m_p^2}\right)^2}, \tag{6.16}$$

where m_K denotes the mass of the kaon. We plot this as a function of $m_{\tilde{\chi}_1^0}$ in Fig. 6.2. The momentum of the neutralino is equal and opposite in the proton rest-frame, $\vec{p}_{\tilde{\chi}_1^0} = -\vec{p}_{K^+}$.

In the limit of a massless neutralino, Eq. (6.15) reduces to,

$$\Gamma\left(p \to K^+ + \tilde{\chi}_1^0\right) = \eta_{QCD}^2 \frac{m_p}{32\pi}\left(1 - \frac{m_K^2}{m_p^2}\right)^2 \sum_{\Omega} |C_\Omega W_{0,\Omega}^{p\to K^+}(q^2)|^2 , \quad (m_{\tilde{\chi}_1^0} = 0) . \tag{6.17}$$

The result obtained is also applicable when a neutrino is involved, provided the appropriate Wilson coefficients are used. In this decay process, the momentum of the kaon is approximately $|\vec{p}_{K^+}| \approx 339\,\text{MeV}$.

6.2.2 Signatures

As mentioned above, in the RPV-MSSM, the stability of the LSP is no longer guaranteed. Therefore, the detection signals for the neutralino mode in experiments such as `Super-K`, `Hyper-K`, `JUNO`, and `DUNE` depend on the lifetime of the neutralino and the decay products.

If the neutralino is long-lived at the scale of the detectors or decays primarily invisibly, the observation could be limited to the occurrence of a kaon. This situation is similar to the $p \to K^+ + \bar{\nu}$ mode. However, the momentum of the generated kaon is related to the mass of its partner, *cf.* Fig. 6.2. Consequently, a precise measurement of the kaon momentum provides information about the mass of the neutralino and offers a way to distinguish it from the neutrino mode. A detailed study of the experimental potential in this context can be found in Section 6.3.

Another scenario is the visible decay of the neutralino in the detectors, which has a characteristic signature determined by the RPV operator responsible for the decay process. We will now briefly consider the relevant decay modes that apply to an very light neutralino [328].

At tree-level, neutralinos can decay into a meson and a lepton via an $LQ\bar{D}$ operator. Within the relevant mass range, $m_{\tilde{\chi}_1^0} \lesssim 445\,\text{MeV}$, the only possible decay channel for the neutralino is to decay into a pion. The partial decay width for a pure bino neutralino is given

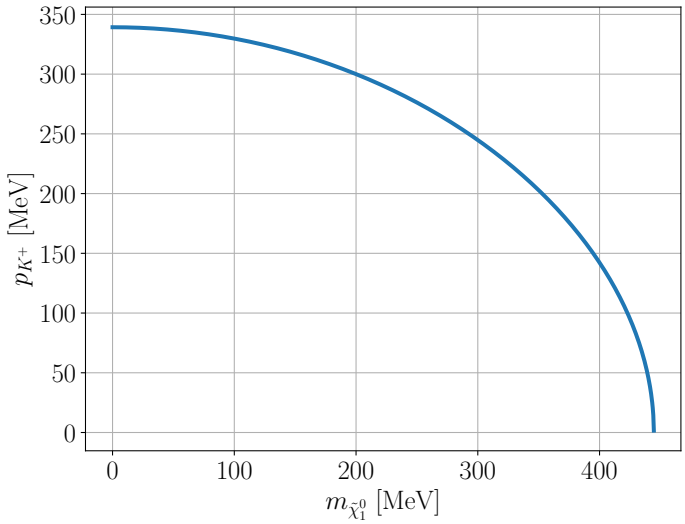

Figure 6.2: Momentum of the final state kaon as a function of the neutralino mass in the process $p \to K^+ + \tilde{\chi}_1^0$.

.

as [225],

$$\Gamma\left(\tilde{\chi}_1^0 \to \pi^{\pm/0} + \ell_i^{\mp}/\nu_i\right) = \eta_{QCD}^2 \frac{\lambda^{1/2}(m_{\tilde{\chi}_1^0}^2, m_\pi^2, m_{l_i}^2)}{128\pi m_{\tilde{\chi}_1^0}^3} |G_i|^2 (f_\pi^S)^2 (m_{\tilde{\chi}_1^0}^2 - m_\pi^2 + m_{l_i}^2)\,, \quad (6.18)$$

where m_π is the mass of the relevant pion, l_i denotes a charged lepton $\ell_i^{\pm}$ or a neutrino ν_i, and $\lambda^{\frac{1}{2}}$ is the Källén function,

$$\lambda^{\frac{1}{2}}(x,y,z) \equiv \sqrt{x^2 + y^2 + z^2 - 2xy - 2xz - 2yz}\,. \quad (6.19)$$

f_π^S is defined as:

$$f_M^S = i\frac{m_M^2}{m_{q_1} + m_{q_2}} f_M\,, \quad (6.20)$$

where f_M denotes the pseudoscalar meson decay constant, and m_M, m_{q_1}, and m_{q_2} represent the masses of the meson M and the quarks q_1 and q_2 that form the meson, respectively [225]. This partial width calculation assumes that the sfermion masses are both degenerate and sufficiently large to allow to integrate out the corresponding fields. The coupling constants are given by,

$$G_i = \frac{3}{2}\frac{\lambda'_{i11} g \tan\theta_w}{\sqrt{2} m_{\tilde{f}}^2}\,, \quad (6.21)$$

where g is the SU(2) gauge coupling constant and $m_{\tilde{f}}$ is the universal sfermion mass.

In scenarios with a $LL\bar{E}$ operator, the neutralino can decay at tree-level leading to a purely leptonic final state. The partial decay width in the case of a pure bino-like neutralino can be

expressed as [401],

$$\Gamma\left(\tilde{\chi}_1^0 \to \bar{\nu}_i + \ell_j^+ + \ell_k^-\right) = \frac{3g'^2\lambda_{ijk}^2}{2^{12}\pi^3}\frac{m_{\tilde{\chi}_1^0}^5}{m_{\tilde{f}}^4}\,, \quad (i \neq j)\,, \tag{6.22}$$

with the same expression holding for the charge-conjugated final state. We note that the above simple formula for the width neglects any mixings in the sfermion sector and uses $m_{\tilde{\chi}_1^0} \ll m_{\tilde{f}}$.

In addition to the tree-level decays, $L_iQ_j\bar{D}_j$ or $L_iL_j\bar{E}_j$ operators can induce the decays,

$$\tilde{\chi}_1^0 \to (\gamma + \nu_i\,, \gamma + \bar{\nu}_i)\,, \tag{6.23}$$

at one-loop level. The decay width is given by [58, 328, 340, 341],

$$\Gamma(\tilde{\chi}_1^0 \to \gamma + \nu_i) = \frac{\lambda^2\alpha^2 m_{\tilde{\chi}_1^0}^3}{512\pi^3\cos^2\theta_W}\left[\sum_f \frac{e_f N_c m_f\,(4e_f+1)}{m_{\tilde{f}}^2}\left(1 + \log\frac{m_f^2}{m_{\tilde{f}}^2}\right)\right]^2\,, \tag{6.24}$$

with the same expression holding for the antineutrino mode. In the above, λ is the relevant coupling $L_iQ_j\bar{D}_j$ or $L_iL_j\bar{E}_j$, α denotes the (QED) fine-structure constant, and the summation includes the (s)fermions involved in the loop: down-type (s)quarks and charged (s)leptons of generation j. Here, e_f, N_c, and $m_f(m_{\tilde{f}})$ represent the electric charge in units of e, the color factor (3 for $LQ\bar{D}$, 1 for $LL\bar{E}$) and the mass of the (s)fermion inside the loop, respectively. It is important to emphasize that we disregard all mixings in the scalar sector. Although this effect could be significant in certain regions of the SUSY parameter space, using the simplified approximation is sufficient at our level of precision. This approach is advantageous because it helps avoid introducing several new undeterminate SUSY parameters into the partial width. We emphasize that in our numerical simulations we fix $m_{\tilde{f}} = 1\,\text{TeV}$ for the logarithmic term in Eq. (6.24). This choice is reasonable because the logarithmic term depends minimally on $m_{\tilde{f}}$ and undergoes only a change by a factor of two if $m_{\tilde{f}}$ is varied between 1 TeV and 100 TeV.

Both tree-level and loop-level decay can be important for light neutralinos. Depending on the mass of the neutralino, tree-level decay may be kinematically forbidden, while loop-level decay has essentially no threshold. Even in scenarios where both modes are possible, the radiative decay becomes particularly significant for very light neutralinos, since the partial width is proportional to $\left(m_{\tilde{\chi}_1^0}^3 m_f^2\right)/m_{\tilde{f}}^4$, shown in Eq. (6.24), as opposed to $m_{\tilde{\chi}_1^0}^5/m_{\tilde{f}}^4$ for the tree-level three-body decay into leptons, shown in Eq. (6.22). We will include benchmark scenarios that effectively demonstrate these principles in Section 6.5. Finally, note that we disregard suppressed higher-order decays, such as the three-body decay $\tilde{\chi}_1^0 \to 3\nu$, which occurs at one loop via off-shell gauge bosons.

6.3 Proton Decay Experiments

In this section, we briefly review the features of prosed proton decay experiments that are central to our study: DUNE, JUNO, and Hyper-K. Essential technical details for each of these detectors have been briefly summarized in Table 6.2.

6.3.1 Detectors

The ongoing construction of the Deep Underground Neutrino Experiment (DUNE) [110–113], includes a far detector (FD) positioned 1.5 km positioned underground at the Sanford Underground Research Facility (SURF), about 1 300 km from the Fermi National Accelerator Laboratory (FNAL). The FD consists of four cuboidal detector volumes, each with dimensions $58.2\,\text{m} \times 14\,\text{m} \times 12\,\text{m}$, containing modular Liquid Argon Time Projection Chambers (LArTPCs) with a combined fiducial mass of 10 kt. At the start of the beam run operations at FNAL, two FDs will be deployed in separate cryostat chambers. The first detector module is expected to be operating in 2026. Our analysis includes results for four volumes that together yield a reference volume of 40 kt. Proton decays within a chamber are assumed to be searched in the same chamber; therefore, we do not consider the possibility of decays being detected in another chamber[2]. Prototype studies estimate a detection efficiency of 30% for $p \to K^+ + \bar{\nu}$ within DUNE [113]. The LArTPC technology has the potential to reduce background to levels below the single-event level for key nucleon decay channels [110]

The Jiangmen Underground Neutrino Observatory (JUNO) [114, 115], is a planned spherical liquid scintillator detector with an inner diameter of 35.4 m and a reference mass of 20 kt, positioned 700 m underground at Kaiping, southern China. The facility is scheduled to be operating in 2023 and uses linear alkylbenzene as the liquid scintillator material. The detector is located in a pool of water to be shielded from radioactivity in the surrounding rock and air. The expected background for $p \to K^+ + \bar{\nu}$ is 0.5 events per 10 years, while the projected detection efficiency is about 36.9% [445].

Hyper-Kamiokande, the planned successor of Super-Kamiokande [440], is a planned large-scale water Cherenkov neutrino detector located underground in Japan. It is scheduled to be operating around 2025 and consists of a cylindrical vertical tank 74 m in diameter and 60 m high. The reference volume, filled with highly transparent purified water, corresponds to a fiducial mass of about 187 kt. Although most of the background is rejected by the surrounding water and veto detectors, neutron and kaon backgrounds remain from cosmic rays. The detection strategy for $p \to K^+ + \bar{\nu}$ involves reconstruction of the pion or muon decay modes of the kaon, the former being more restrictive due to the lower background. The efficiency of the first method is about $10.8 \pm 1.1\%$, with an expected background of 0.7 ± 0.2 per Mt per year.

Although Hyper-K offers a much larger fiducial volume compared to the other detectors, the detection principle has its limitations: both Hyper-K (and Super-K) are unable to measure the momentum of particles that fall below the Cherenkov threshold of water. For kaons, this means that it cannot measure momentum below about 750 MeV [439][3]. This constraint turns

[2] The spacing and placement of the detectors are not explicitly stated in the Technical Design Reports, so a combined analysis is currently not possible.

[3] Hyper-K can nevertheless detect kaons through their decay products since these are produced above the

out to be significant since kaons of $p \to K^+ + \bar{\nu}$ have momenta around 330 MeV, which is even lower for the scenario of $p \to K^+ + \tilde{\chi}_1^0$ with a massive neutralino, *cf.* Fig. 6.2. Consequently, Hyper-K cannot distinguish between the decay of a kaon into a detector-stable (or invisibly decaying) neutralino and that of a decay into a neutrino. This is where the benefits of DUNE and JUNO comes in: as scintillation detectors, they can measure the kinetic energy of a kaon down to a threshold of 50 MeV.

For the scenario with a visibly decaying neutralino, we assume in the simulations zero background and a detection efficiency $\epsilon_{\text{vis.}} = 100\%$ for the neutralino. The characteristic signature containing observable objects from the kaon decay, combined with the subsequent decay of the neutralino (which may have a displaced vertex structure) and timing-coincidence cuts, allows us to implement high-efficiency cuts with a good signal-to-background ratio. Nevertheless, subsequent decay products such as muons and pions within Super-K and Hyper-K could remain invisible due to the Cherenkov radiation threshold. The momentum of these particles is completely determined by the mass and momentum of the parent neutralino. Nevertheless, it is important to recognize that only a fraction produces Cherenkov radiation, depending on the mass and initial momentum of the neutralino[4]. Therefore, we do not focus on this decay strategy but rather focus on signals from the decay products of the secondary particles. These particles come to rest within the detector volume and produce characteristic subsequent decay products. Both the muon and the pion can be identified by a Michel electron so that the event can be identified by characteristic final states. The preceding proton decay can serve as a trigger for reducing background events. However, DUNE and JUNO have the ability to use their tracking chambers to directly identify secondary particles. A precise estimate including the finite size of the fiducial volume, however, would require detailed simulations for each detector.

	Super-K	Hyper-K	JUNO	DUNE
Geometry	Cylindrical 42 m height×39 m diameter	Cylindrical 60 m height×74 m diameter	Spherical 35.4 m diameter	Cuboidal (4 modules) 58.2 m×14 m×12 m
Detector Material	Water	Water	LABs	Liquid Argon
Working Principle	Cherenkov	Cherenkov	Scintillation	Scintillation
Fiducial Mass	22.5 kt	187 kt	20 kt	40 kt
No. of Protons	$\sim 7.5 \times 10^{33}$	$\sim 6.3 \times 10^{34}$	$\sim 6.9 \times 10^{33}$	$\sim 1.1 \times 10^{34}$
$\epsilon_{inv.}$	$\mathcal{O}(10)\,\%$	$\mathcal{O}(10)\,\%$	37%	30%

Table 6.2: Summary of technical details for the upcoming detectors at Hyper-K [116], JUNO [114], and DUNE [110]. We also show the details for Super-K [440] for comparison. $\epsilon_{inv.}$ provides the approximate detection efficiency of the kaon for the neutrino (or invisible neutralino) mode.

Cherenkov threshold.

[4] A detailed simulation of the momentum of the secondary particles is beyond the scope of this work

6.3.2 Proton Decay in Nuclei

In the aforementioned discussion, we have focused primarily on free protons. However, the detectors used in this work do not contain free protons; instead, materials such as water[5] (Super-K and Hyper-K), liquid argon (DUNE), and linear alkylbenzene (JUNO) are considered sources of protons. We will now briefly examine the implications of this consideration.

Effects such as the Fermi motion, nucleon correlations, and nuclear binding energy can cause changes in the kaon moment given in Eq. (6.16) as the kaon leaves the nucleus. These effects can be analyzed by various methods, such as modeling the nucleus as a local Fermi gas or using the so-called approximated spectral function approach. In addition, interactions with surrounding nucleons can lead to scattering of the kaon produced by the decay, which further affects its momentum. This can be modeled within the Bertini cascade model [446–448] implemented via GEANT4 [449, 450].

Due to the above effects, the distribution of kaon momentum becomes more smeared out and deviates from the fixed value given in Eq. (6.16). A significant fraction of the kaons loses energy, although some may gain energy through collisions with high-momentum nucleons. A detailed study for Super-K involving the ^{16}O nucleus can be found in Ref. [439]. A similar simulation on argon can be found in Ref. [451]. A study on liquid scintillators can be found in Ref. [452], from which we expect similar effects for linear alkylbenzene.

For our study, however, these effects are of minor importance, since we are not interested in measuring the momentum of the kaon, but only require the detection of the kaon via its decay. This has only marginal effects on the detection efficiency. For Super-K and Hyper-K, the kaon reconstruction depends on the assumption of kaons decaying at rest. Due to the above effects, some of the kaons acquire so much energy that they do not come to rest in water before decay. Nevertheless, Super-K estimates this fraction to be only 11% [439].

For DUNE, kaon tracks with momentum higher than 180 MeV can be measured with a detection efficiency of 90% [113]. Below this threshold, the track cannot be measured due to the short path length of the kaon before its decay. However, the reconstruction algorithms used in the experiment can still reconstruct the kaon through its dominant decay chain, $K \to \mu \to e$, with an efficiency above 90%[6].

For JUNO, the search strategy is based on the time coincidence and well-defined energies of the kaon decay products [114]. Moreover, the liquid scintillator detects a prompt signal originating from the kaon. We assume that the efficiency in reconstructing the kaon with this approach remains the same across all momenta. A later study [445] suggests that optimal reconstruction can be achieved by a triple coincidence measurement, tracking both the kaon and the decay product and Michel electron from the muon decay. Using the kaon momentum in the reconstruction would also increase detection performance, although this would require extensive detector and proton decay simulation, which was not performed here.

For JUNO the search strategy relies on time coincidence and well-defined energies of the kaon decay products [114]. Additionally, the liquid scintillator detects a prompt signal coming from the kaon. We assume that the efficiency for kaon reconstruction in this way is constant

[5] It is important to emphasize that the following discussion refers exclusively to the oxygen nucleus in water, not the hydrogen nucleus, which can be treated as a free proton.

[6] A study conducted by DUNE evaluated the detection efficiency for a kaon momentum in the range of 150-450 MeV [113]. This efficiency is not used in our study but is claimed to be technically achievable.

for all momenta. A later study [445] indicates that the best reconstruction can be achieved by a triple coincidence, tracking both the kaon and decay product hit as well as the Michel electron from the muon decay. Using the kaon momentum would also increase the detection efficiency, albeit this would require a detailed detector and proton decay simulation, which we have not performed here.

Therefore, we will neglect all nuclear effects in our study. Nevertheless, it is important to emphasize - as mentioned in Section 6.2.2 - that precise momentum measurements of the kaon are essential for determining the mass of the neutralino from kaon decay. In such cases, a precise description of the nuclear effects is crucial.

Before concluding this subsection, we briefly discuss another effect. A proton decaying in a nucleus can leave the nucleus in an excited state that immediately de-excites to its ground state by emitting a gamma ray. The energy of this photon can be estimated and searched for as a coincidence signal. This method provides a way to reduce background events from cosmic ray muons and material radioactivity near the detector wall. Indeed, `Super-K` has searched for such gamma rays [439], and `Hyper-K` is planned to do the same. `JUNO` can use the time coincidence between the prompt signal from kaons hitting the liquid scintillator and a delayed signal from their decay products to reduce background events. Nevertheless, `DUNE` has pointed out the challenges of measuring time differences on the order of the lifetime of kaons [113].

6.4 Simulation Procedure

In the following, we explain the simulation approach used to evaluate the possibilities of different experiments to detect a scenario in which a proton decays into a neutralino, possibly followed by neutralino decay.

The overall number of produced neutralinos (or kaons) in a given experimental setup is determined by,

$$N_{\tilde{\chi}_1^0}^{\text{prod}} = N_p \cdot \Gamma(p \to K^+ + \tilde{\chi}_1^0) \cdot t\,, \tag{6.25}$$

where $\Gamma(p \to K^+ + \tilde{\chi}_1^0)$ is obtained from Eq. (6.15), N_p is the total number of protons present in the detector volume, and t denotes the runtime of the experiment. In the case where the neutralino yields an invisible signature, the total number of observable events can be estimated by directly multiplying the above expression by the kaon detection efficiency as described in the previous section.

In scenarios where the neutralino may decay visibly to a final state X, it is necessary to also calculate the expected number of such decays that can be reconstructed within the limits of the detector volume. The observed events can be estimated as follows,

$$N_{\tilde{\chi}_1^0 \to X}^{\text{obs.}} = N_{\tilde{\chi}_1^0}^{\text{prod}} \cdot \langle P[\tilde{\chi}_1^0 \text{ in d.r.}] \rangle \cdot \epsilon_{\text{vis.}}\,. \tag{6.26}$$

Here, the function $\langle P[\tilde{\chi}_1^0 \text{ in d.r.}] \rangle$ denotes the average probability that the neutralino decays within the fiducial volume of the detector. This probability depends on the lifetime of the neutralino, its kinematics, the point-of-origin within the detector, and the geometric configuration of the detector itself. As for $\epsilon_{\text{vis.}}$ in the above expression, it represents the

detection efficiency for the visible state X, which is assumed to be 100% as discussed in Section 6.3.

To estimate $\langle P[\tilde{\chi}_1^0 \text{ in d.r.}]\rangle$ for each detector, we use a Monte Carlo simulation with $N_{\text{MC}}^{\tilde{\chi}_1^0}$ neutralinos of a given mass originating from random locations within the detector and moving in different directions. The geometric features for each detector are discussed in more detail below. We will then estimate,

$$\langle P[\tilde{\chi}_1^0 \text{ in d.r.}]\rangle = \frac{1}{N_{\tilde{\chi}_1^0}^{\text{MC}}} \sum_{i=1}^{N_{\tilde{\chi}_1^0}^{\text{MC}}} P_i[\tilde{\chi}_1^0 \text{ in d.r.}]\,, \tag{6.27}$$

where the individual probability for the simulated i^{th}-neutralino decay in the detector is given by:

$$P_i[\tilde{\chi}_1^0 \text{ in d.r.}] = 1 - e^{-L_i/\lambda}\,. \tag{6.28}$$

Here L_i denotes the distance between the point where the neutralino originates and the boundary of the detector along its trajectory. The mean decay length λ (independent og i) is given by,

$$\lambda = \gamma\beta/\Gamma_{\text{tot}}\,, \tag{6.29}$$

where Γ_{tot} denotes the overall decay width of the neutralino,

$$\gamma = E/m_{\tilde{\chi}_1^0}\,, \qquad \beta = \sqrt{\gamma^2 - 1}/\gamma\,. \tag{6.30}$$

In the above, $m_{\tilde{\chi}_1^0}$ and E are the mass and energy of the neutralino, respectively.

Thus, L_i is the only factor that depends on the geometry. We will now explain the procedure we use to calculate it for the selected detectors.

`Hyper-K`: `Hyper-K` has a cylindrical shape with a radius of $R = 37\,\text{m}$ and a height of $H = 60\,\text{m}$. For the i^{th} neutralino generated within the `Hyper-K` volume at a location (r, φ, z) using a cylindrical coordinate system centered on the bottom surface ($z = 0$) of the detector. Its three-velocity $\vec{v}$ given at an azimuthal angle φ_v, is given by the components v_z and $v_\perp = \sqrt{\vec{v}^2 - v_z^2}$ along the z-axis and in the polar plane, respectively. In this context, the following relations hold,

$$L_i = |\vec{v}| \times (\min(t_1, t_2))\,, \tag{6.31}$$

where,

$$t_1 \equiv \begin{cases} \frac{(H-z)}{v_z} & \text{if } v_z > 0\,, \\ \frac{-z}{v_z} & \text{if } v_z < 0\,, \end{cases} \tag{6.32}$$

and $t_1 > t_2$ if $v_z = 0$. Here, t_2 is given by,

$$t_2 = \frac{-r\cos(\varphi - \varphi_v) + \sqrt{R^2 - r^2\sin^2(\varphi - \varphi_v)}}{|v_\perp|}\,. \tag{6.33}$$

`Super-K` can be modeled analogously.

`DUNE`: `DUNE` comprises of four rectangular FDs with dimensions $L = 58.2\,\text{m}$, $W = 14.0\,\text{m}$, and $H = 12.0\,\text{m}$. Using a rectangular coordinate system whose origin is at the bottom corner of the detector, we consider the i^{th} neutralino generated in (x, y, z) moving in the direction denoted by the three-vector $\vec{v} = (v_x, v_y, v_z)$. We define,

$$t_x \equiv \begin{cases} \frac{(L-x)}{v_x} & \text{if } v_x > 0\,, \\ \frac{-x}{v_x} & \text{if } v_x < 0\,, \end{cases} \tag{6.34}$$

and $t_x > t_y, t_z$ if $v_x = 0$, and analogous expressions for t_y and t_z, depending on W, H, respectively. L_i is then given by,

$$L_i = |\vec{v}| \times \min(t_x, t_y, t_z)\,. \tag{6.35}$$

`JUNO`: `JUNO` has a spherical configuration with a radius of $R_{\text{max}} = 17.7\,\text{m}$. For a neutralino produced at a random point $\vec{r} = (r_i, \theta_i, \varphi_i)$ within the detector range, with a velocity $\vec{v}$, and moving in a direction given by the angles (θ_j, φ_j), the angle θ between the two can be determined using the relation $\cos\theta = \frac{\vec{r}\cdot\vec{v}}{|\vec{r}||\vec{v}|}$. A coordinate transformation eliminates the dependence of θ on φ_i and φ_j so that $\theta = \theta_i - \theta_j$. The final distance can then be calculated as,

$$L_i = -r_i\cos(\theta) + \sqrt{R_{\text{max}}^2 - r_i^2\sin^2(\theta)}\,, \tag{6.36}$$

such that $\theta \in [0, 2\pi]$.

For illustration, the $\langle P[\tilde{\chi}_1^0 \text{ in d.r.}]\rangle$ is shown in Fig. 6.3, as a function of the neutralino mass for the four detectors. The neutralino momentum $p_{\tilde{\chi}_1^0}$ is related to the neutralino mass $m_{\tilde{\chi}_1^0}$ according to Eq. (6.16). Consequently, as $m_{\tilde{\chi}_1^0}$ increases, $|\vec{v}_{\tilde{\chi}_1^0}|$ decreases, increasing the probability that the neutralino will decay within the detector for a fixed lifetime.

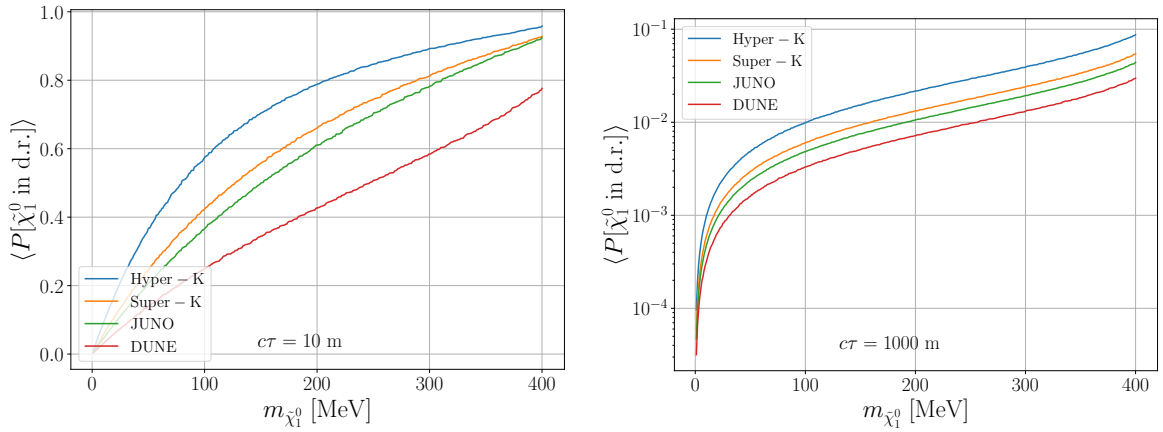

Figure 6.3: Average neutralino decay probabilities as a function of the neutralino mass corresponding to neutralino decay lengths $c\tau = 10\,\text{m}$ (left) and $c\tau = 1\,000\,\text{m}$ (right). These plots have been generated by setting $N_{\text{MC}}^{\tilde{\chi}_1^0} = 10000$.

6.5 Benchmark Scenarios

We now present benchmark scenarios carefully designed to cover, what we believe, all relevant possibilities of proton decay into a neutralino in the `DUNE`, `JUNO`, and `Hyper-K`. In each case, the proton decays via λ''_{121}, as shown in Eq. (6.3). Therefore, we only consider scenarios where the mass of the neutralino is such that $m_{\tilde{\chi}_1^0} \lesssim 445\,\text{MeV}$, *cf.* Eq. (6.4). In these cases, the produced neutralino either escapes the detector as missing energy, or decays into visible modes by an RPV operator λ^D_{ijk}. The benchmark scenarios are summarized in Table 6.3. Corresponding numerical studies are discussed in more detail in Section 6.6. It is important to note that for any given scenario, we assume that the listed couplings represent the only non-zero RPV couplings, with the associated current bounds also shown in the table.

Scenario	$\mathbf{m_{\tilde{\chi}_1^0}}$	Proton Decay	$\tilde{\chi}_1^0$ Decay $\left(\lambda^{\text{D}}_{ijk}\right)$	Product Bound	Min. $\mathbf{c\tau_{\tilde{\chi}_1^0}}$
B1	$0 - 400\,\text{MeV}$	$\lambda''_{121} < 5\times10^{-7}\left(\frac{m_{\tilde{q}}}{\Lambda\text{TeV}}\right)^{5/2}$	–	–	∞
B2	$0 - 400\,\text{MeV}$	$\lambda''_{121} < 5\times10^{-7}\left(\frac{m_{\tilde{q}}}{\Lambda\text{TeV}}\right)^{5/2}$	$\lambda'_{333} < 1.04$	$\lambda'_{333}\lambda''_{121} < 10^{-9}$	$\sim 1\,600\,\text{m}$
B3	$0 - 400\,\text{MeV}$	$\lambda''_{121} < 5\times10^{-7}\left(\frac{m_{\tilde{q}}}{\Lambda\text{TeV}}\right)^{5/2}$	$\lambda_{233} < 0.7\left(\frac{m_{\tilde{t}_R}}{1\,\text{TeV}}\right)$	$\lambda_{233}\lambda''_{121} < 10^{-21}$	$\sim 180\,\text{m}$
B4	$150 - 400\,\text{MeV}$	$\lambda''_{121} < 5\times10^{-7}\left(\frac{m_{\tilde{q}}}{\Lambda\text{TeV}}\right)^{5/2}$	$\lambda'_{211} < 0.59\left(\frac{m_{\tilde{d}_R}}{1\,\text{TeV}}\right)$	$\lambda'_{211}\lambda''_{121} < 6\times10^{-25}$	$\sim 11\,\text{m}$
B5	$150 - 400\,\text{MeV}$	$\lambda''_{121} < 5\times10^{-7}\left(\frac{m_{\tilde{q}}}{\Lambda\text{TeV}}\right)^{5/2}$	$\lambda'_{311} < 1.12$	$\lambda'_{311}\lambda''_{121} < 4\times10^{-24}$	$\sim 30\,\text{m}$

Table 6.3: Details of the benchmark scenarios. The bounds on λ^D_{ijk} are taken from Refs. [67, 157] while the one on λ''_{121} is from Ref. [453]. Product bounds are obtained from Ref. [99] for SUSY masses of 1 TeV, except in the case of $\lambda'_{311}\lambda''_{121}$, where it is the bound on $p \to K^+ + \bar{\nu}$ from [439] reinterpreted for **B5**. `Super-K` imposes constraints on the massless invisible neutralinos, leading to the limit $|\lambda''121| < 3.9\times10^{-25}\left(\frac{m\tilde{q}}{\text{TeV}}\right)^2$. We will present this bound in our results. The mass ranges for each benchmark are according to the discussion in the text, although we have rounded them off.

In the context of the first benchmark, **B1**, we consider a scenario in which the neutralino is

not observed at DUNE, JUNO, and Hyper-K. This is due to the fact that the neutralino is either too long-lived or its decay is invisible. As part of our numerical analyses, we set $\lambda^D_{ijk} = 0$, and, thus, λ''_{121} is the only non-zero RPV coupling. However, the results also apply to scenarios where the neutralino decay is invisible.

For the benchmark **B2**, we choose the decay coupling $\lambda^D_{ijk} = \lambda'_{333}$. In this case, the neutralino decays radiatively via a loop involving a bottom (s)quark with the decay width given by Eq. (6.24). Kinematically, this is the only possible decay mode. The possible decay length of the neutralino in this context is shown in Table 6.3, assuming maximum allowed values for $\lambda^D_{ijk} = \lambda'_{333}$ and the neutralino mass. In **B2**, the neutralino lifetime is already significantly larger compared to the detector dimensions, as listed in Table 6.2. Since the decay width for the loop-induced mode scales approximately with m_f^2, we assume that radiative decays from $LQ\bar{D}$ operators other than λ'_{i33} are negligible in the context of the considered experiments. It is worth noting that comparable sensitivity can be expected if λ'_{333} were replaced by λ'_{233} in the scenario. On the other hand, the λ'_{133} case is less relevant due to its strict current limit [67]:

$$\lambda'_{133} < 0.0044 \times \sqrt{\frac{m_{\tilde{b}}}{1\,\text{TeV}}}\,. \tag{6.37}$$

For benchmark **B3**, we set the decay coupling $\lambda^D_{ijk} = \lambda_{233}$. In this case, the neutralino decays radiatively, but via a τ-$\tilde{\tau}$ loop. Again, the tree-level decay modes are not kinematically allowed, since they require at least one τ-lepton in the final state. As pointed out in Table 6.3, the minimum lifetime, in this case, is much shorter than in **B2**. However, for similar reasons as above, the neutralino decays via $L_iL_1\bar{E}_1$ or $L_iL_2\bar{E}_2$ operators are expected to be too long lifetimes for DUNE, JUNO, or Hyper-K. The $\lambda^D_{ijk} = \lambda_{133}$ scenario is considered irrelevant due to its strict experimental bound.

We then study scenarios in which the neutralino has tree-level decay modes. Within the bounds of the mass given in Eq. (6.4), the decay width for $LL\bar{E}$ operators, Eq. (6.22), is too small for the experiments in question. However, the decay of the neutralino into a pion via $L_iQ_1\bar{D}_1$ operators could be relevant, *cf.* Eq. (6.18). It is noteworthy that the strict bound for λ'_{111} leads to extremely narrow widths. Thus, we consider two final benchmarks corresponding to the other couplings.

For the benchmark **B4**, we decide to use the decay coupling $\lambda^D_{ijk} = \lambda'_{211}$, which leads to the following neutralino decays: $\tilde{\chi}^0_1 \to \pi^\pm + \mu^\mp$, $\tilde{\chi}^0_1 \to \pi^0 + \nu_\mu$, and $\pi^0 + \bar{\nu}_\mu$. he decays are kinematically allowed for

$$135\,\text{MeV} \lesssim m_{\tilde{\chi}^0_1} \lesssim 445\,\text{MeV}\,, \tag{6.38}$$

with the lower limit roughly corresponding to the π^0 mass. For $m_{\pi^0} \leq m_{\tilde{\chi}^0_1} < m_{\pi^\pm} + m_{\mu^\mp}$ only the neutral mode contributes, assuming a massless neutrino. For larger masses, the charged pion mode becomes accessible. In this context, the chosen coupling allows the neutralino to decay radiatively via a d-(s)quark in the loop. However, due to the small mass of the down quark, this mode is suppressed and can be neglected.

Similarly, the benchmark **B5** assumes $\lambda^D_{ijk} = \lambda'_{311}$ as the decay coupling. Consequently, the decay of the neutralino involves $\tilde{\chi}^0_1 \to \pi^0 + \nu_\tau$, where the charged mode is kinematically forbidden, involving a $\tau^\pm$. The mass range is the same as above. Again, the radiative decay

via the d quark can be neglected.

6.6 Numerical Results

In this section, we show the sensitivity projections at a 90% confidence level for the stable/invisible neutralino scenario (benchmark **B1**) corresponding to DUNE [113], JUNO [445], and Hyper-K [116] in Fig. 6.4. The runtime is assumed to be 10 years for all cases. These projections are derived by using the $p \to K^+ + \bar{\nu}$ mode limits stated in their respective technical reports. These limits are then reinterpreted in the context of a massive neutralino. The plot further depicts the (reinterpreted) excluded region from the existing search for $p \to K^+ + \bar{\nu}$ performed at Super-K [439], at a 90% confidence level. For Hyper-K and Super-K, it is not possible to measure the kaon momentum which leads to indistinguishable experimental signatures between the massive and the massless case[7] allowing a direct reinterpretation of the limits. Here, we assume that the signal efficiency and expected backgrounds for the massive mode are the same as for the massless scenario (see *cf.* Section 6.3). However, in the context of the proposed search at DUNE and JUNO, momentum cuts on the kaon are included to reduce the background due to atmospheric neutrinos. This modification implies that the quoted limit would impose less stringent limits on the massive case due to reduced signal efficiency. Nevertheless, we assume that the chosen different momentum cuts, optimized for a massive neutralino, could yield comparable signal efficiency and expected background as in the massless case. Therefore, the numbers given in Section 6.3 are used directly. A more precise estimate would require full simulations of the detector setup and background at DUNE and JUNO, respectively.

We see that the bound derived from Super-K is consistent with Eq. (6.6) and weakens for smaller neutralino masses. The upcoming Hyper-K, DUNE, and JUNO experiments are expected to go beyond the limits of Super-K and probing the parameter space of $\lambda''_{121}/m^2_{\tilde{f}}$ to reach values that are about 2.5, 1.5, and 1.3 times lower, respectively. Although Hyper-K benefits from a larger fiducial mass, DUNE and JUNO are competitive due to their superior efficiency and ability to reject background events. It is noteworthy that momentum measurements of the resulting kaon can only be made in the latter two experiments.

Next, we focus on scenarios in which the decay of the neutralino is visible. Since we assume that there are no background events in these scenarios, the reach corresponding to a confidence level of 95% is shown by 3-event isocurves[8]. Each benchmark is represented in two ways: in the plane of $\lambda^D_{ijk}/m^2_{\tilde{f}}$ versus $\lambda''_{121}/m^2_{\tilde{f}}$, with a fixed value of $m_{\tilde{\chi}^0_1}$ at 400 MeV, and in the plane of $\lambda^D_{ijk}/m^2_{\tilde{f}}$ versus $m_{\tilde{\chi}^0_1}$, where, for illustration, $\lambda''_{121}/m^2_{\tilde{f}}$ is set to its maximum value corresponding to the threshold of the reinterpreted super K limit, as in Fig. 6.4. These results were obtained by simulating with $N^{\tilde{\chi}^0_1}_{\rm MC} = 50{,}000$ for coupling-versus-coupling plots and $N^{\tilde{\chi}^0_1}_{\rm MC} = 10{,}000$ for coupling-versus-mass plots. A runtime of $t = 10\,$yrs is used. Where relevant, the existing constraints from Table 6.3 are shown in gray for single-bounds and in blue for product-bounds.

[7] The majority of kaons ($\sim 80\%$) decay at rest, and muons have no information about the momentum of their parent kaon.

[8] In some cases, contours for 30 and 90 events are also presented where relevant.

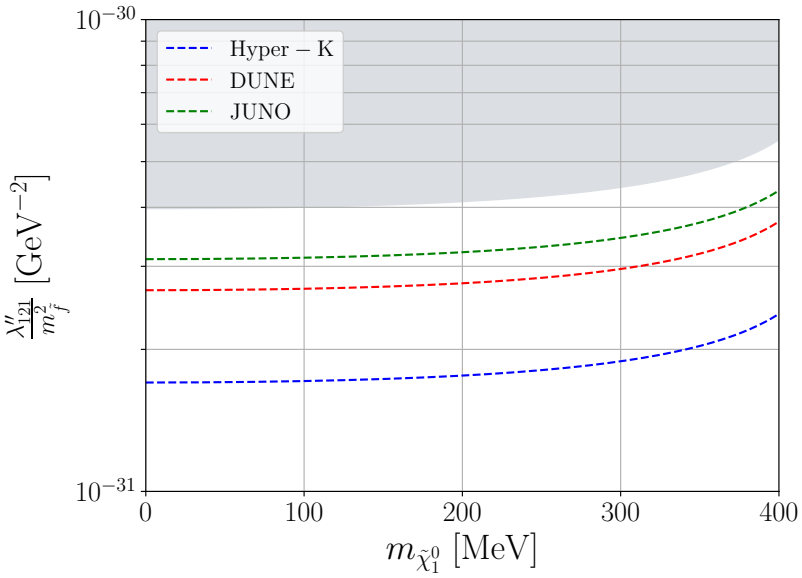

Figure 6.4: Sensitivity reach for the single coupling scenario of benchmark **B1**. The reinterpreted bound from `Super-K` is shown in gray. The bound from Table 6.3 lies above the scale of the plot. The results for `Hyper-K`, `DUNE`, and `JUNO` are for a run-time of 10 years.

The results for the benchmark **B2** are shown in Fig. 6.5. In this figure, two types of sensitivity contours are shown in the plot $\lambda'_{333}/m^2\tilde{f}$ versus $\lambda''_{121}/m^2_{\tilde{f}}$. The downward sloping line illustrates the possibility of detecting 3 neutralino decays within the `Hyper-K` detector, assuming a neutralino mass of $m_{\tilde{\chi}^0_1} = 400\,\text{MeV}$. In the limit that the lifetime becomes very long, the number of decays is directly proportional to $\lambda'_{333}\lambda''_{121}/m^4_{\tilde{f}}$, which explains the shape. The corresponding contours for `DUNE` and `JUNO` are too weak, which is due to the long lifetime of the neutralino in this scenario. Here, the large volume of `Hyper-K` proves to be advantageous. It is noteworthy that there are no constraints from `Super-K` in the visible channel. However, it is important to recognize that the search for stable neutralinos, as seen in the **B1** benchmark, also constrains this scenario. This is due to the fact that some of the neutralinos decay only outside the detector, resulting in a missing-energy signature. Fig. 6.3 indicates that this has to be the case, on average, for over 90% of the neutralinos produced in the **B2** benchmark. The vertical lines in the plot represent the contours resulting from the search for missing energy. These contours are calculated using the same approach as in benchmark **B1**. Consequently, `Hyper-K`, `DUNE`, and `JUNO` all show competitive sensitivity, and the constraint of `Super-K` applies as well. For this particular benchmark, it is important to emphasize that the visible channel does not probe any region beyond what the invisible channel does. Nonetheless, we find that a significant part of the discovery region, where *both* signatures are detectable. This would provide a particular and insightful perspective on the underlying model.

The plot on the right side of the figure shows the achievable sensitivity range of the visible mode within the $\lambda'_{333}/m^2_{\tilde{f}}$ versus $m_{\tilde{\chi}^0_1}$ plane. As the mass of the neutralino increases, the sensitivity is increased for two reasons: first, the lifetime of the neutralino becomes shorter,

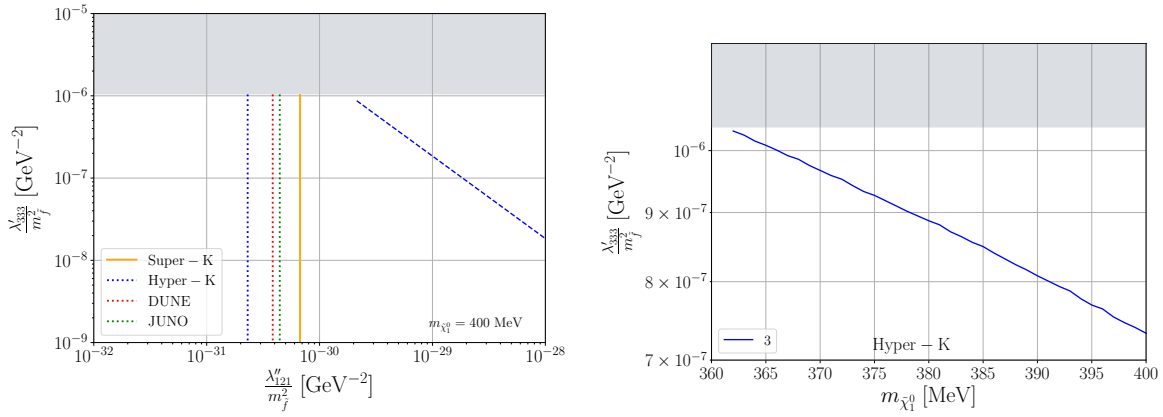

Figure 6.5: Sensitivity reach/`Super-K` limit for benchmark **B2**. The existing single-bound on λ'_{333} from Table 6.3 is shown in gray (with $m_{\tilde{f}} = 1\,\text{TeV}$), while the product-bound lies outside the scale of the plot. *Left:* The limits in the coupling-vs.-coupling plane with $m_{\tilde{\chi}_1^0} = 400\,\text{MeV}$. The contours correspond to the visible mode (blue dashed, downward sloping line) and invisible mode (vertical lines); see discussion in the text. *Right:* The limits in the coupling-vs.-mass plane for the visible mode with $\lambda''_{121}/m_{\tilde{f}}^2$ fixed at the threshold of the `Super-K` bound of Fig. 6.4.

as described in Eq. (6.24), and second, neutralinos with higher mass have lower momentum. Consequently, the decay length $(\beta\gamma c\tau)_{\tilde{\chi}_1^0}$ of the neutralinos is shorter, leading to an increased average decay probability $\langle P[\tilde{\chi}_1^0 \text{ in d.r.}]\rangle$, as shown in Fig. 6.3.

The results for benchmark **B3**, which correspond to a radiative decay, are very similar to benchmark **B2**. In Fig. 6.6, both coupling-versus-coupling (top) and coupling-versus-mass (bottom) are shown. Once again, the experiment of `Hyper-K` remains the only relevant experiment for the detection of the visible mode. In this case, the mode has higher sensitivity due to the shorter lifetime of the neutralino. As can be seen in the top-left plot, there is a significant parameter range where both modes can be detected, providing the opportunity to disentangle the underlying mechanisms of proton decay. In addition, there is a small region within the parameter space where the visible mode is the only detectable signature. In the top-right plot, a zoomed-out version of the same diagram is shown to illustrate the details. Interestingly, large regions of the parameter space beyond the bounds of Table 6.3 are already excluded by the reinterpreted `Super-K` limit, even in scenarios where the neutralino is unstable. Similar to the context in Fig. 6.4, the `Hyper-K`, `DUNE`, and `JUNO` experiments show sensitivity only slightly beyond the `Super-K` limit. The coupling-versus-mass plot (bottom) features similarities to the previously discussed scenarios. This time, we include the 30-event isocurve for reference.

In the **B4** and **B5** benchmark scenarios, the neutralino decays at the tree-level, resulting in maximum coupling values and significantly shorter lifetimes compared to the other benchmarks. The results are shown in Fig. 6.7 and Fig. 6.8, respectively. It is noteworthy that both `DUNE` and `JUNO` show sensitivity to the visible mode in this context. In addition, a significant parameter range is observed with sensitivity well below the `Super-K` limit for λ''_{121}. The other features are as before. The vertical lines show a kink at $\lambda'_{211}/m_{\tilde{f}}^2 \gtrsim 10^{-7}$ and rise linearly in the logarithmic plot as a function of $\lambda'_{i21}/m_{\tilde{f}}^2$ are contours resulting from the missing energy

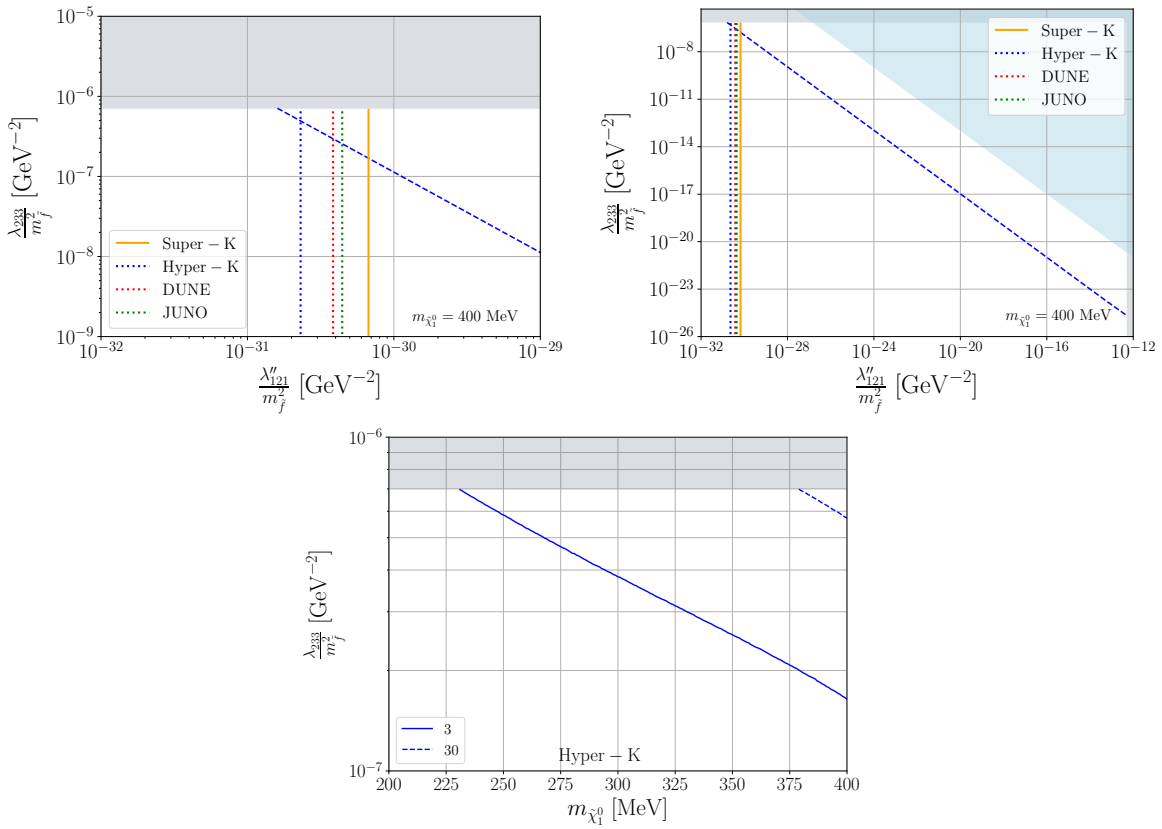

Figure 6.6: Sensitivity reach/`Super-K` limit for benchmark **B3**. The existing single-bounds from Table 6.3 are shown in gray while the product-bound is shown in blue (all with $m_{\tilde{f}} = 1\,\text{TeV}$). *Top Left:* As in left plot of Fig. 6.5 but for benchmark **B3**. *Top Right:* Zoomed-out version of the top-left plot. *Bottom:* As in right plot of Fig. 6.4 but for benchmark **B3**. The solid and dashed lines correspond to 3- and 30-event isocurves, respectively.

search. This shape can be explained as follows: as $\lambda'_{i11}/m^2_{\tilde{f}}$ increases, more neutralinos decay in the detector, reducing the sensitivity of the invisible channel. For $\lambda''_{121}/m^2_{\tilde{f}}$ values falling below the thresholds shown in Fig. 6.4, the production rate of neutralinos is insufficient, so that there is no sensitivity. A notable remark is the sensitivity kink in the right figure around $m_{\tilde{\chi}_1^0} \sim 240\,\text{MeV}$, which is due to the kinematic threshold of modes such as $\tilde{\chi}_1^0 \to \pi^\pm + \mu^\mp$, contributing to an increased total decay width.

In summary, the reinterpreted `Super-K` bound effectively rules out large regions of the RPV-MSSM parameter space and exceeds the bounds of Table 6.3. This happens across all benchmarks, although the `Super-K` bound comes from an invisible search. The `Hyper-K`, `DUNE`, and `JUNO` experiments extend their sensitivity to these decays beyond the invisible limits on $\lambda''_{121}/m^2_{\tilde{f}}$ by about a factor of ~ 2.

Importantly, we now have *two* distinct discovery channels for a wide range of the parameter space. If both channels are observed, this would be a strong indication for the light neutralino proton decay model.

Moreover, considering the visible mode generally offers only a slight extension of the

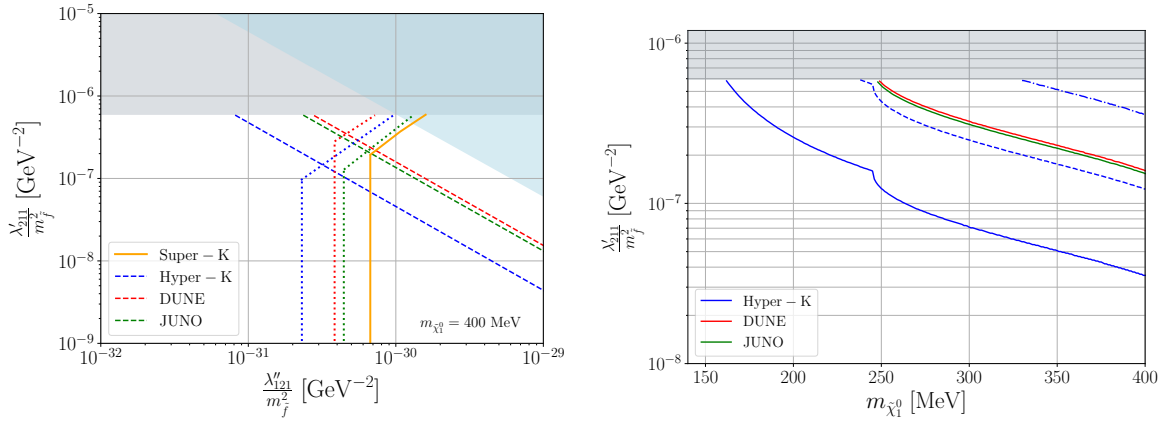

Figure 6.7: Sensitivity reach/`Super-K` limit for benchmark **B4**. The existing single-bound on λ'_{211} from Table 6.3 is shown in gray, the product-bound is in blue (both with $m_{\tilde{f}} = 1\,\text{TeV}$), while the bound on λ''_{121} lies outside the scale of the plot. *Left:* As in left plot of Fig. 6.5 but for benchmark **B4**. *Right:* As in right plot of Fig. 6.4 but for benchmark **B4**. The solid, dashed, and dot-dashed lines correspond to 3-, 30- and 90-event isocurves, respectively.

coverage of the parameter space. However, when neutralino decays occur at tree-level, the visible mode has the potential to explore $\lambda''_{121}/m_{\tilde{f}}^2$ values almost an order of magnitude below the threshold of the invisible mode in certain parameter space regions.

Before concluding this section, two important points need to be emphasized. First, our considerations have focused only on scenarios with a single non-zero RPV operator responsible for the neutralino decay. In cases where multiple couplings contribute simultaneously, the relative importance of the visible (or invisible) mode may either increase (or decrease). Second, there is the possibility of statistically combining the results of the visible and invisible searches, leading to increased sensitivities in all scenarios with a decaying neutralino. However, we have not included this aspect in our presentation of results.

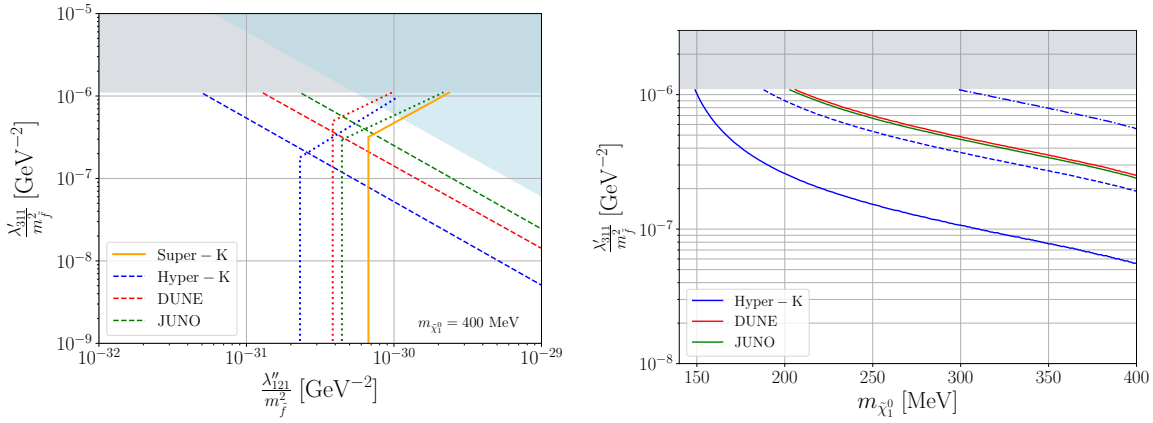

Figure 6.8: Sensitivity reach/`Super-K` limit for benchmark **B5**. The existing single-bound on λ'_{311} from Table 6.3 is shown in gray, the product-bound is in blue (both with $m_{\tilde{f}} = 1\,\text{TeV}$), while the bound on λ''_{121} lies outside the scale of the plot. *Left:* As in left plot of Fig. 6.5 but for benchmark **B5**. *Right:* As in right plot of Fig. 6.4 but for benchmark **B5**. The solid, dashed, and dot-dashed lines correspond to 3-, 30- and 90-event isocurves, respectively.

6.7 Conclusions

Observation of proton decay could shed light on a fundamental puzzle of the Standard Model: the observed matter-antimatter asymmetry. In this work, we investigate proton decay in the context of the RPV-MSSM. The lightest neutralino is allowed to be exceptionally light, possibly even massless. This particular scenario allows proton decay $p \to K^+ + \tilde{\chi}_1^0$ and provides an unconventional avenue to confront SUSY at low energy. Our work includes the calculation of the decay width for this channel and discusses the relevant associated signatures. In particular, if the decay of the neutralino is not visible in the detector, the resulting signature involves missing energy, similar to the process $p \to K^+ + \bar{\nu}$, which is already constrained by `Super-K`. In cases where the neutralino visibly decays, the signature can be more exotic. We use various benchmark scenarios, to cover several possibilities of the RPV landscape. The goal is to reevaluate the constraints imposed by the `Super-K` on the neutralino channel by running numerical simulations. In addition, we evaluate the potential of upcoming experiments such as `Hyper-K`, `DUNE`, and `JUNO` to identify their sensitivity reach. Our results show that the reinterpreted `Super-K` search constraints substantial regions of the RPV-MSSM parameter space, exceeding existing constraints on RPV couplings, even in scenarios in which the neutralino has visible decay modes. These constraints will be further improved with upcoming `Hyper-K`, `DUNE`, and `JUNO` experiments. By combining invisible and visible search channels, the baryon number-violating RPV operator $\lambda''_{121}/m^2_{\tilde{f}}$ can be probed for values about 2 to 10 times smaller than the current `Super-K` limit.

7
Conclusions & Outlook

Since the discovery of the Higgs boson in 2012, which completed the particle spectrum of the SM, particle physics has been faced with the challenge of advancing its development without a clear guiding principle. In response, LHC experiments are now preparing for a new phase which includes a significant upgrade of the LHC, called the high luminosity LHC. This upgrade is scheduled to come online in 2026 and aims to increase the luminosity of the collider, leading to a higher collision rate. This will enable experiments to probe rare phenomena in greater detail. This new era of high-precision physics provides direct access to the high-energy frontier, enabling the search for new physics at previously undiscovered scales. It will make precision measurements of SM parameters, including the flavor sector, and determine the properties of the Higgs boson and its connection to electroweak symmetry breaking. This makes precise theoretical predictions essential to interpret experimental results and distinguish between potential new physics and SM background effects.

The program is continuously developed and broadened in response to the results from the current LHC experiments. Among planned upgrades for the detectors looking for prompt decays, there is extensive interest in forward physics at the LHC, covering interesting physics opportunities in the far-forward region. Due to their unique location, these experiments are very sensitive to various SM and BSM phenomena, filling gaps in searches and serving as a complement to other experimental efforts. These experiments benefit from shielding that allows them to search for extremely rare phenomena, with the goal of reducing the background and potentially finding a signal even in only a few events over the entire high luminosity era. In addition, the search strategy will be complemented by beam-dump experiments. These can probe both various exotic rare decays and potential violation of lepton flavor universality and through these anomalies gain sensitivity to new particles even if their masses are at very high scales.

Although a complete classification of all existing BSM models remains a challenge, the exploration of new horizons is a fundamental driving force for future colliders. The theoretical and experimental challenges encountered by the SM are a clear indication of the existence of new physical phenomena beyond its current scope. As a result, the SM is increasingly conceived as an effective field theory at low energies, integrated into a more comprehensive and fundamental description.

While formulating an exhaustive and complete classification of all existing BSM models is not possible, it is evident that the exploration of the unknown is one of the main drivers of all future colliders. The apparent theoretical and experimental problems that have arisen within the SM strongly suggest the existence of new physics beyond the current framework. Among the various concepts that have been proposed to extend the SM, SUSY stands out as a particularly promising idea. SUSY not only offers a compelling candidate for DM but also

provides a framework for gauge coupling unification, a solution to the hierarchy problem, and mechanisms to generate neutrino masses. As a result, SUSY has attracted multiple studies in the strong and electroweak sectors.

This work addresses the phenomenology of the RPV-MSSM and confronts it with experimental data based on current measurements and future detector estimates. We identify characteristic regions within the RPV-MSSM landscape and explore their characteristic signatures. Depending on the choice and strength of RPV couplings, the model may exhibit different decay patterns for the lightest neutralino, leading to final-state events characterized by high lepton and/or jet multiplicities, with modest or no missing transverse momentum - deviating from typical MSSM signatures. Moreover, in cases where RPV couplings are small, particles can travel macroscopic distances before decaying, making them long-lived.

To investigate these phenomena, we consider various experiments; the large LHC experiments focused on high-p_T physics, which allow for a search for prompt decaying particles. Furthermore, far-forward and beam-dump experiments provide insight into the sensitivity range for detecting long-lived particles. Even neutrino oscillation data have contributed to exploring BSM scenarios. By connecting these distinct areas in the context of RPV-SUSY, we gain both a comprehensive understanding of the SUSY framework and a deeper understanding for these other BSM phenomena.

First, in Chapter 2, we analyzed how the neutrino masses, naturally present in the RPV-MSSM, can be generated in the B_3-conserving RPV-MSSM. Dealing with a large number of undetermined parameters in general RPV models can be challenging and often requires specialization in particular models, which limits its applicability. Instead, we took a different approach and identified four classes of minimal models - the Minimal Oscillation Models - which turned out to be consistent with neutrino oscillation data for two massive neutrinos, but also include the possibility of extending the approach to three massive neutrinos. This allowed us to perform a model-independent investigation, and we were able to show that each MOM class has an infinite space of solutions, consistent with the measured neutrino masses and mixing angles. While MOMs do not solve the most general RPV case their simplicity, predictability, and broad applicability make them valuable for understanding neutrino masses in general RPV scenarios. If one were to extend the framework to the most general RPV-MSSM it would be necessary to drop the assumption of a minimal model. This would increase the number of parameters and lead to an overparameterized fit. The extended model would not be able to show any underlying patterns.

In Chapter 3, our work presented a systematic analysis of the RPV-MSSM and its signatures at the LHC, with the goal of creating a minimal number of experimental searches that provide a comprehensive coverage. For the first time, we provided a fully general and model-independent treatment of phenomenology in the case of small RPV couplings. We relaxed the criteria for a stable LSP in the MSSM and introduced a variety of different possible decay signatures opposing the typical E_T^{miss} signature. However, our framework has certain limitations. We require that all decays within the cascade chain, including the LSP, occur promptly and that the final-state decay products are not too soft to be detected, which constrains scenarios with $m_{\text{LSP}} > \mathcal{O}(200\,\text{GeV})$. In addition, the RPV coupling must balance prompt decay with the preservation of cascade decay patterns. Although our approach may compromise search sensitivity in certain cases, our goal was to check the current coverage of LHC searches.

We identified 17 final-state topologies (six for $LL\bar{E}$, five for $\bar{U}\bar{D}\bar{D}$, and six for $LQ\bar{D}$) that form the "RPV dictionary", comprehensively covering RPV-MSSM at the LHC. By recasting the current experimental coverage, we found that most RPV scenarios, even if not directly searched for, are well covered by the existing ATLAS and CMS searches, providing complete coverage of the possible RPV-MSSM signatures. Numerical simulations focusing on a dominant $LL\bar{E}$ operator show that our approach yields robust exclusion limits comparable to those of the RPC-MSSM, making it a viable and model-independent search strategy. However, some final states, particularly those involving $\bar{U}\bar{D}\bar{D}$ and $LQ\bar{D}$ decays, would benefit from stronger experimental improvements to achieve sensitivity to electroweak production cross-sections. A comprehensive study focusing on these two groups of operators would be valuable to evaluate whether any experimental improvements are needed. In addition, to fully understand the vast landscape of RPV-MSSM, it is critical to establish a classification of collider phenomenology in terms of large RPV couplings.

In Chapter 4, we explore the RPV-MSSM at low energies. As mentioned in Chapter 1, the lightest neutralino, if bino-like, has no experimental constraint on its mass. In our framework, we assumed a sub-GeV mass range for the neutralino with small RPV couplings, resulting in a long lifetime for the bino-like neutralino. Given this scenario, a dedicated study is essential to cover the landscape of the RPV-MSSM since such long-lived particles are escaping past searches at ATLAS and CMS. We considered the production in meson decays - which are produced in a high abundance at the interaction point of ATLAS via $LQ\bar{D}$ operators - and subsequent decay into a photon and a neutrino, being loop-suppressed. We provided an estimation of the sensitivity range of FASER and FASER2 at the LHC for different dominant RPV couplings. Our results show that these experiments exhibit exceptional sensitivity in parameter space, exceeding current limits by up to 2 orders of magnitude. In addition, we showed that the experimental setups of FASER and FASER2 are particularly well suited to detect the resulting single-photon signature in the decay volumes of their detectors.

In Chapter 5, we extended our progress in this framework. We applied several experimental strategies commonly used to constrain HNLs to set new stringent limits on the relevant RPV couplings in the context of RPV models. This is justified due to a similar phenomenology of the light bino and a light HNL in both production and decay mechanisms. By using extensive existing HNL searches, we have translated the expected sensitivity of certain future experiments into a corresponding sensitivity range for light neutralinos. We included previous experiments such as PIENU, NA62, T2K, and BaBar as well as approved experiments such as FASER, MoEDAL-MAPP1, PIONEER, and DUNE and their planned successors. Given the different types and flavor indices of RPV operators, we explored several theoretical benchmark scenarios within the RPV landscape. These representative benchmark scenarios allowed us to present final exclusion limits where we found that exclusion limits surpassed existing bounds on the RPV couplings by orders of magnitude. This allowed us to demonstrate the power of simple reinterpretation methods as a basis for evaluation.

Our two approaches show how future experiments not specifically built to search for SUSY particles can still search for them. With the increased interest in searching for LLPs and the resulting new experiments, there is an opportunity in the future to cover the RPV landscape at this frontier as well.

Another example of this was considered in Chapter 6. Since the considered bino-like neutralino can be very light or even massless, it enables a novel proton decay, $p \to K^+ + \tilde{\chi}_1^0$,

in which SUSY manifests at low energy. We have determined the decay width of this channel and discussed the related signatures. If the neutralino does not decay visibly in the detector, the signature involves missing energy, similar to $p \to K^+ + \bar{\nu}$ constrained by Super-K. For visibly decaying neutralinos, we have analyzed different benchmark scenarios, reinterpreted the limits of Super-Kamiokande for the neutralino channel, and estimated the sensitivities of the upcoming Hyper-K, DUNE, and JUNO experiments. Our results showed that the newly interpreted search constraints for Super-K go beyond the current limits of RPV couplings, even when neutralinos have visible decay modes. The combination of the invisible and visible search channels allowed us to probe the baryon number-violating RPV operator $\lambda''_{121}/m^2_{\tilde{f}}$ down to values about a factor of 2 to 10 smaller than the current Super-K limit.

We showed how all the different searches and model-independent approaches add another puzzle piece to the pursuit of comprehensively covering the vast RPV landscape. The presented improvements to the experiments are intended to further this search, but at the same time offer the possibility of opening the window to even deeper levels of fundamental physics.

Appendix A

A.1 Analytical Expressions for the MOM Solution Spaces

We write the explicit analytical solutions for the first three MOM classes here. As mentioned in the main text, the expressions for Class 4 MOMs are lengthy; we skip presenting them. Throughout, we treat x^1 as our free variable and solve Eq. (2.18) for the other variables. For short, we use the notation $M^{ij} \equiv \mathbf{M}_\nu^{ij}$.

Class 1: $x^i x'^j + x'^i x^j$

$$
\begin{aligned}
x'^1 &= \frac{M^{11}}{2x^1}\,, \quad x'^2 = \frac{M^{22}}{2x^2}\,, \quad x'^3 = \frac{M^{33}}{2x^3}\,, \quad \text{with} \\
x^2 &= \frac{M^{12}}{M^{11}}x^1 \pm \frac{\sqrt{\left(M^{12}\right)^2\left(x^1\right)^2 - M^{11}M^{22}\left(x^1\right)^2}}{M^{11}}\,, \\
x^3 &= \frac{M^{13}}{M^{11}}x^1 \pm \frac{\sqrt{\left(M^{13}\right)^2\left(x^1\right)^2 - M^{11}M^{33}\left(x^1\right)^2}}{M^{11}}\,.
\end{aligned} \tag{A.1}
$$

This represents four distinct solutions corresponding to the various sign choices. The above expressions are general as long as $M^{ii} \neq 0$ for any i, which is true for the experimental neutrino mass matrix.

Class 2: $x^i x^j + \left(x^i x'^j + x'^i x^j\right)$

$$
\begin{aligned}
x'^1 &= \frac{M^{11} - \left(x^1\right)^2}{2x^1}\,, \quad x'^2 = \frac{M^{22} - \left(x^2\right)^2}{2x^2}\,, \\
x'^3 &= \frac{M^{33} - \left(x^3\right)^2}{2x^3}\,,
\end{aligned}
$$

with

$$x^2 = \frac{M^{12}}{M^{11}}x^1 \pm \frac{\sqrt{\left(M^{12}\right)^2\left(x^1\right)^2 - M^{11}M^{22}\left(x^1\right)^2}}{M^{11}}\,,$$
$$x^3 = \frac{M^{13}}{M^{11}}x^1 \pm \frac{\sqrt{\left(M^{13}\right)^2\left(x^1\right)^2 - M^{11}M^{33}\left(x^1\right)^2}}{M^{11}}\,. \tag{A.2}$$

This represents four distinct solutions. Once again, the expressions are valid as long as $M^{ii} \neq 0$ for any i.

Class 3: $x^i x^j + x'^i x'^j$

$$x'^2 = \frac{M^{12} - x^1x^2}{x'^1}\,, \quad x'^3 = \frac{M^{13} - x^1x^3}{x'^1}\,, \quad \text{with}$$
$$x'^1 = \pm\sqrt{M^{11} - \left(x^1\right)^2}\,,$$
$$x^2 = \frac{M^{12}}{M^{11}}x^1 \pm \sqrt{\frac{\left(M^{12}\right)^2}{\left(M^{11}\right)^2}\left(x^1\right)^2 - \frac{M^{22}}{M^{11}}\left(x^1\right)^2 - \frac{\left(M^{12}\right)^2}{M^{11}} + M^{22}}\,,$$

$$x^3 = \frac{M^{13}}{M^{11}}x^1 \pm \sqrt{\frac{\left(M^{13}\right)^2}{\left(M^{11}\right)^2}\left(x^1\right)^2 - \frac{M^{33}}{M^{11}}\left(x^1\right)^2 - \frac{\left(M^{13}\right)^2}{M^{11}} + M^{33}}\,. \tag{A.3}$$

This represents eight distinct solutions. The above expressions are valid for $\left(x^1\right)^2 \neq M^{11}$, and $M^{11} \neq 0$. For the case $\left(x^1\right)^2 = M^{11}$, the solution sets are:

$$x'^1 = 0\,, \quad x'^2 = \pm\frac{\sqrt{M^{11}M^{22} - \left(M^{12}\right)^2}}{\sqrt{M^{11}}}\,,$$
$$x'^2 = \pm\frac{\sqrt{M^{11}M^{33} - \left(M^{13}\right)^2}}{\sqrt{M^{11}}}\,,$$
$$x^2 = \frac{M^{12}}{x^1}\,, \quad x^3 = \frac{M^{13}}{x^1}\,. \tag{A.4}$$

A.2 A Mini-guide to MOMs

In this appendix, we expand upon certain points related to MOMs that were only briefly mentioned in the main text.

RPV parameters and Linearly Independent x^i

Recall from the main text that the variables x^i are directly proportional to the RPV couplings. Nevertheless, there is no simple relation between the number of contributing RPV parameters in a model and the number of linearly independent x^i needed to describe their contributions. We demonstrate this through an explicit example.

Consider a κ-only model with all other RPV parameters zero in some basis. Consulting Table 2.1, our neutrino mass matrix receives contributions at tree level, as well as of types 7, 8 and 13 at one-loop level:

$$\begin{aligned}
\mathbf{M}_\nu^{ij} &\sim m_0 \delta_\kappa^i \delta_\kappa^j + \frac{\delta_\kappa^i \delta_\kappa^j m_{e_i} m_{e_j} h_e^i h_e^j}{16\pi^2 m_{\text{SUSY}}} \\
&+ \frac{\delta_\kappa^i \delta_\kappa^j \left[\left(m_{e_i} h_e^i \right)^2 + \left(m_{e_j} h_e^j \right)^2 \right]}{16\pi^2 m_{\text{SUSY}}} \\
&+ \frac{g\, \delta_\kappa^i \delta_\kappa^j \left(m_{e_i}^2 + m_{e_j}^2 \right)}{16\pi^2 m_{\text{SUSY}}} \\
&\sim x^i x^j + x'^i x'^j \\
&+ \left(x^i x''^j + x''^i x^j \right) \\
&+ \left(x^i x'''^j + x'''^i x^j \right) ,
\end{aligned} \tag{A.5}$$

where, we have defined,

$$\begin{aligned}
x^i &\equiv \sqrt{m_0}\, \delta_\kappa^i , & x'^i &\equiv \frac{m_{e_i} h_e^i \delta_\kappa^i}{4\pi \sqrt{m_{\text{SUSY}}}} , \\
x''^i &\equiv \frac{\left(m_{e_i} h_e^i \right)^2 \delta_\kappa^i}{16\pi^2 m_{\text{SUSY}} \sqrt{m_0}} , & x'''^i &\equiv \frac{2g\, \delta_\kappa^i m_{e_i}^2}{16\pi^2 m_{\text{SUSY}} \sqrt{m_0}} .
\end{aligned} \tag{A.6}$$

It can easily be checked that any three of these four sets are linearly independent. Even though all the contributions come from only one RPV parameter set – κ^i – we need three linearly independent sets to describe the structure.

We can also have situations where the opposite is true, *i.e.*, where several RPV parameter sets lead to fewer linearly independent sets x^i. We already saw an example of this in Section 2.8.4.

Deriving the Class 4 MOM Structure

Recall our observation that the neutrino mass matrix only has contributions of two forms: $x^i x^j$, and $x^i x'^j + x'^i x^j$. Given this fact, and restricting ourselves to the case of two linearly independent sets, it is immediately clear how the first three classes of MOMs arise. Here, we describe how we get the fourth one.

With only the linearly independent sets, x^i and x'^i, contributing, the most general form of the neutrino mass matrix is,

$$\mathbf{M}_\nu^{ij} = x^i x^j + x'^i x'^j + \left(x^i x'^j + x'^i x^j\right) . \tag{A.7}$$

Now, consider an additional contributing set, x''^i. The most general form the matrix can then take is,

$$\begin{aligned}\mathbf{M}_\nu^{ij} = {} & x^i x^j + x'^i x'^j + \left(x^i x'^j + x'^i x^j\right) \\ & + x''^i x''^j + \left(x^i x''^j + x''^i x^j\right) + \left(x'^i x''^j + x''^i x'^j\right) .\end{aligned} \tag{A.8}$$

Since we assume there are only two linearly independent sets, there have to be some a, b (not both zero) such that $x''^i = a x^i + b x'^i$. Substituting this in the above expression, we get, after some algebra,

$$\begin{aligned}\mathbf{M}_\nu^{ij} = {} & \left(1 + a^2 + 2a\right) x^i x^j + \left(1 + b^2 + 2b\right) x'^i x'^j \\ & + (1 + ab + 2a + 2b)\left(x^i x'^j + x'^i x^j\right) .\end{aligned} \tag{A.9}$$

Finally, defining,

$$\begin{aligned}\tilde{x}^i \equiv \sqrt{\left(1 + a^2 + 2a\right)} x^i , \quad \tilde{x}'^i \equiv \sqrt{\left(1 + b^2 + 2b\right)} x'^i , \\ A \equiv \frac{(1 + ab + 2a + 2b)}{\sqrt{\left(1 + a^2 + 2a\right)}\sqrt{\left(1 + b^2 + 2b\right)}} ,\end{aligned} \tag{A.10}$$

we get,

$$\mathbf{M}_\nu^{ij} = \tilde{x}^i \tilde{x}^j + \tilde{x}'^i \tilde{x}'^j + A\left(\tilde{x}^i \tilde{x}'^j + \tilde{x}'^i \tilde{x}^j\right) , \tag{A.11}$$

which is the Class 4 MOM structure. Note that this is not the most general form of A since further couplings could contribute; the arguments remain the same.

Most General Solution and MOMs

We stressed in the main text that the MOM approach does not solve the most general case since there can always be conspiring cancellations. We demonstrate this here with an example.

Consider a scenario where we have three linearly independent sets – x^i, x'^i, x''^i – with the

explicit form,

$$\begin{aligned} x^i &= (1,0,0)\ , \\ x'^i &= (0,1,0)\ , \\ x''^i &= (0,0,1)\ . \end{aligned} \tag{A.12}$$

Now, consider a fourth contribution x'''^i. This can always be written in the form,

$$x'''^i = ax^i + bx'^i + cx''^i\ , \tag{A.13}$$

for some a, b, c. Finally, consider the matrix with the structure,

$$\mathbf{M}_\nu^{ij} = x^i x^j + x'^i x'^j + \left(x''^i x'''^j + x'''^i x''^j\right)\ . \tag{A.14}$$

The above matrix clearly does not have a MOM form since it has three linearly independent sets. However, the matrix is rank two as long as the condition $a^2 + b^2 = 2c$ is satisfied. Thus, a matrix being rank two does not imply that the matrix has a MOM-form. There can always be additional hidden structure – for instance through specific cancellations/relations as in the above case.

A.3 Numerical Plots

CP-Conserving Solutions of MOMs

This appendix contains the numerical fits to the experimental data. Fig. A.1 shows the solution for Class 1 structures, assuming Inverted Ordering. In Fig. A.2 and Fig. A.3, we display the solution for Class 2 and Class 3 structures correspondingly. The fits have been performed using the neutrino data of Table 2.2 (with $\delta_{CP} = 0$) as described in Section 2.7.

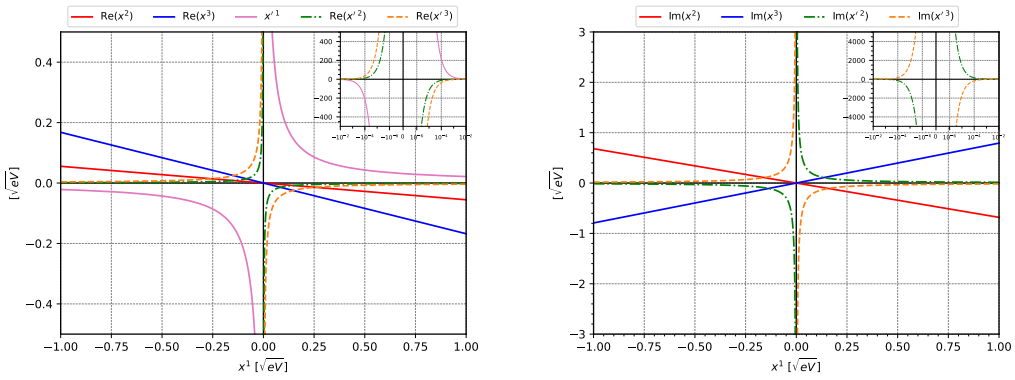

Figure A.1: Real (top) and imaginary (bottom) values of the couplings required to fit the actual neutrino data for the Inverted Ordering limit in models with Class 1 structure.

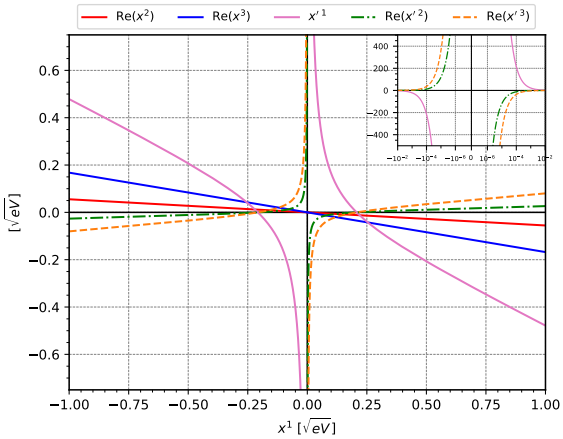

(a) Inverted Ordering

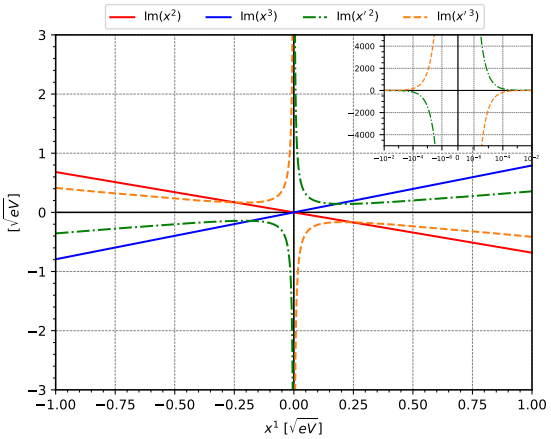

(b) Inverted Ordering

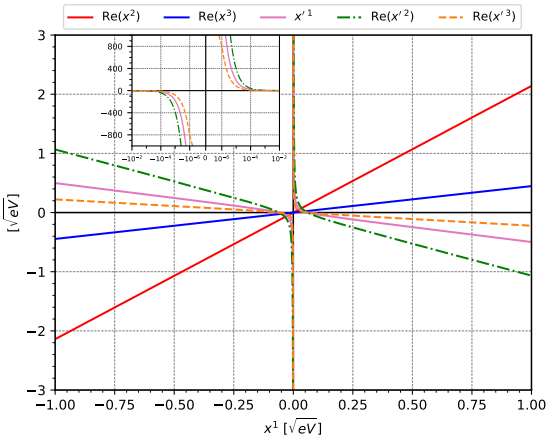

(c) Normal Ordering

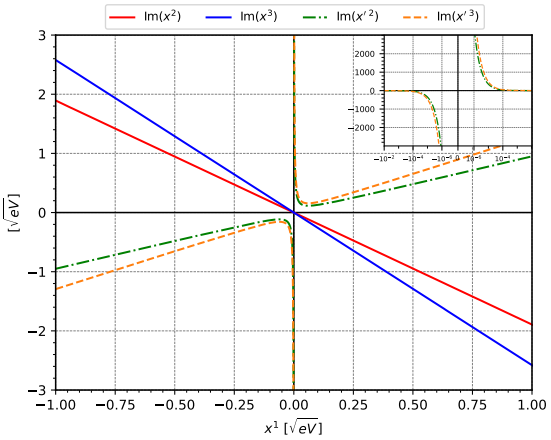

(d) Normal Ordering

Figure A.2: Real (left) and imaginary (right) values of the couplings required in models with Class 2 structure to fit the actual neutrino data for the two mass orderings: IO (top) and NO (bottom).

MOMs and a Non-zero δ_{CP}

We include, here, a fit with non-zero δ_{CP} to show that it is possible to accommodate CP violation in our framework. We show, in Fig. A.4, the fit corresponding to the Normal Ordering data of Table 2.2 for Class 2 MOMs, including the best-fit value for δ_{CP}. The qualitative features are as before. The overall goodness of the fit is also stable, indicating that the minimum of the χ^2 is determined as robustly as before.

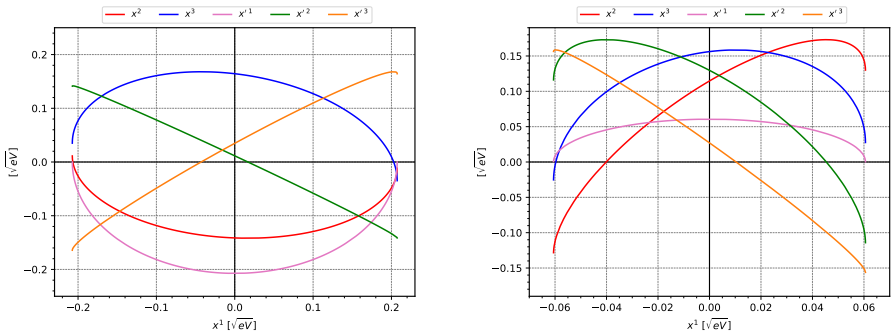

Figure A.3: Values of the couplings required in models with Class 3 structure to fit the actual neutrino data for the two mass orderings: IO (left) and NO (right). For this class, all couplings are real.

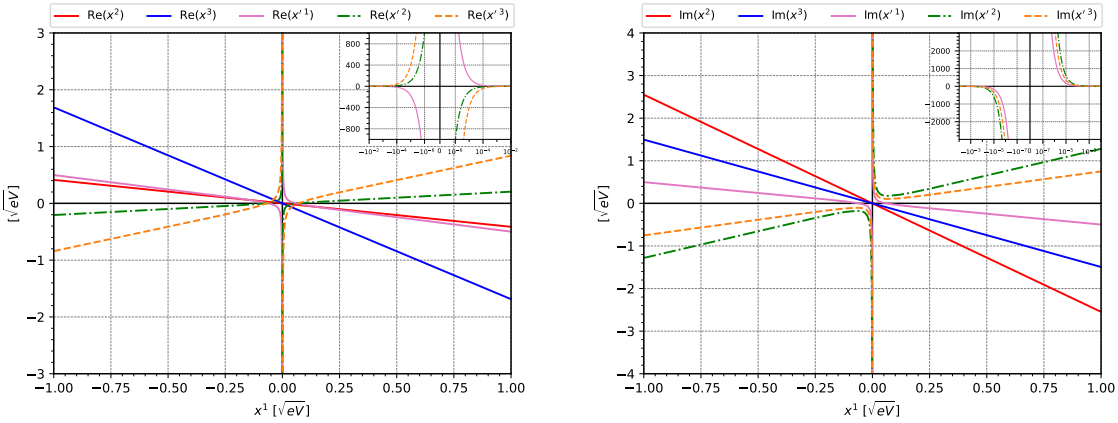

(a) Inverted Ordering

(b) Normal Ordering

Figure A.4: Values of the couplings required to fit the actual neutrino data including δ_{CP} in models with Class 2 structures for normal ordering.

B
Appendix B

B.1 Decay Modes for Numerical Simulations

We discuss the details of the decay modes used in the numerical simulations here. As mentioned in Section 3.4, all two-body decays are computed using `MadGraph5_aMC@NLO`; we only discuss the higher-body decays that we set by hand here.

Gluino LSP Benchmarks: For a given coupling, λ_{iki} with $i, k \in \{1, 2, 3\}$, we assume the chain: $\tilde{g} \to (\tilde{q}/\tilde{q}_3)^* + j \to \tilde{B}^* + 2j \to 2L + E_T^{\rm miss} + 2j$, where $2L = \{L_i^+ + L_i^-\}, \{L_i^+ + L_k^-\}, \{L_k^+ + L_i^-\}$, and we set the corresponding branching ratios (BRs) to be 0.5, 0.25, and 0.25, respectively. In the above, the asterisk denotes off-shell particles, and the nature of the (s)quark is fixed by the scenario considered. We stress that the chosen decay chain and BRs represent a non-trivial choice to facilitate numerical computation; alternate choices are possible – *e.g.*, the bino can be replaced by a wino or one flavor of slepton can be decoupled, thus, affecting the BRs. That is, we take the perspective where the branching ratios are taken to be the free variables, rather than the sparticle masses. Apart from being a simpler approach, this also saves computational time since we no longer need to calculate complicated high-multiplicity decays. Even with alternate BR choices, we expect the general implications of our results to hold.

Squark LSP Benchmarks: This is very similar to the above. For a coupling λ_{iki}, we assume the decay chain for the squarks to be: $(\tilde{q}/\tilde{q}_3)^* \to \tilde{B}^* + j \to 2L + E_T^{\rm miss} + j$, where $2L = \{L_i^+ + L_i^-\}, \{L_i^+ + L_k^-\}, \{L_k^+ + L_i^-\}$, and the BRs are set to 0.5, 0.25, and 0.25, respectively.

Electroweakino LSP Benchmarks:

- $\mathrm{D}_{\tilde{W}}$: The neutral wino decays as: $\tilde{W}^0 \to 2L + E_T^{\rm miss}$, for a coupling λ_{iki}, where $2L = \{L_i^+ + L_i^-\}, \{L_i^+ + L_k^-\}, \{L_k^+ + L_i^-\}$. We set the corresponding BRs to 0.5, 0.25, and 0.25, respectively. For the charged wino, we have the decay modes: $\tilde{W}^+ \to \{L_i^+ + L_i^- + L_k^+\}, \{L_i^+ + L_i^+ + L_k^-\}, \{L_i^+ + E_T^{\rm miss}\}, \{L_k^+ + E_T^{\rm miss}\}$ (analogous for $\tilde{W}^-$). We set the BR to 0.25 for each mode.
- $\mathrm{I}_{\tilde{g}\to\tilde{W}}$: The gluino decays as: $\tilde{g} \to \tilde{q}^* + j_l \to \tilde{W} + 2j_l$.
- $\mathrm{I}_{\tilde{q}\to\tilde{W}}$: The (singlet) squarks decay as: $\tilde{u}/\tilde{d} \to \tilde{g}^* + j_l \to \tilde{q}^* + 2j_l \to \tilde{W} + 3j_l$.

- $D_{\tilde{H}}$: The neutral Higgsinos decay as: $\tilde{H}^0_{1(2)} \to \tilde{B}^* + Z(h) \to 2L + E_T^{\text{miss}} + Z(h)$, for a coupling λ_{iki}, where $2L = \{L_i^+ + L_i^-\}, \{L_i^+ + L_k^-\}, \{L_k^+ + L_i^-\}$, with the BRs fixed to 0.5, 0.25, and 0.25, respectively. The case for $\tilde{H}^\pm$ is analogous, with $Z(h)$ replaced by $W^\pm$.

- $I_{\tilde{g}\to\tilde{H}}$: Here, the gluino is assumed to decay as: $\tilde{g} \to \tilde{q_3}^* + j_3 \to \tilde{H} + 2j_3$.

- In all $\tilde{B}$ LSP scenarios, the bino decays as: $\tilde{B} \to 2L + E_T^{\text{miss}}$, for a coupling λ_{iki}, where $2L = \{L_i^+ + L_i^-\}, \{L_i^+ + L_k^-\}, \{L_k^+ + L_i^-\}$, with the BRs set to 0.5, 0.25, and 0.25, respectively.

- $I_{\tilde{g}\to\tilde{B}}$: The gluino is assumed to decay as: $\tilde{g} \to \tilde{q_3}^* + j_3 \to \tilde{B} + 2j_3$.

Slepton LSP Benchmarks:

- For all $D_{\tilde{L}}$ scenarios, if a particular lepton does not couple directly to the considered operator, the decay is assumed to proceed via an off-shell bino, *e.g.*, $\tilde{\mu}_R \to \tilde{B}^* + \mu \to 2L + \mu + E_T^{\text{miss}}$, where $2L = \{L_i^+ + L_i^-\}, \{L_i^+ + L_k^-\}, \{L_k^+ + L_i^-\}$ (for a coupling λ_{iki}). The corresponding BRs are set to 0.5, 0.25, and 0.25, respectively; and so on.

- $I_{\tilde{g}\to\tilde{L}}$: The gluino is assumed to decay as: $\tilde{g} \to \tilde{q}^* + j_l \to \tilde{B}^* + 2j_l \to \tilde{L} + 2j_l + L$. Here, $\tilde{L}$ refers to all the sleptons.

- $I_{\tilde{W}\to\tilde{L}}$: We assume that the only contributing decays are the two-body decay modes of the wino into the left-handed sleptons; we set the decay widths of the modes into the right-handed sleptons to be zero. This can occur if, for instance, any virtual mediators that can lead to such a decay are completely decoupled.

B.2 Auxiliary Tables

B.2.1 Production Table

While compiling the 'RPV Dictionary' in Section 3.3, we have taken a model-independent approach. In order to completely cover the RPV-MSSM landscape (within our framework assumptions), it is necessary to perform the searches compiled in Tables 3.2-3.11. Often, however, one is not interested in being completely general but may have a bias for certain classes of models. For instance, it is usual in the literature to focus on scenarios where a given LSP is produced at the LHC in cascade decays of the colored sparticles; scenarios where all sparticles other than the LSP are completely decoupled are less common. Given such a bias, one can optimize the 'RPV Dictionary' by adding the objects that would arise from such cascades.

In order to facilitate the inclusion of the above, Table B.1 provides a list of the objects that arise in cascade-decays for each relevant production mode for each LSP. For instance, with a gluino LSP, the only relevant mode is gluino-pair production since every other channel will have a lower cross-section. For squark LSP(s), however, squark-pair, gluino-pair, and associated production are all relevant since the latter two contribute with high cross-sections

when a gluino is not decoupled. Table B.1 shows that the cascade to the LSP from gluino-pair (associated-pair) production leads to 2 extra jets (1 extra jet). These can then be used to optimize searches for models with squark LSPs and non-decoupled gluinos by adding the extra jet(s) to the relevant squark LSP signatures in Tables 3.2-3.11. We note that each value in the table represents the maximal set of objects that is *guaranteed to arise* in the cascade without knowing the details of the spectrum; however, more objects can always be present in specific scenarios. Further, to be economical, we have grouped left-handed and right-handed sparticles into one category but it is straightforward to expand them out.

Table B.1: Objects arising in the cascade decays of various pairs of parent sparticles (columns) down to the LSP(s) (rows). These can be added to the corresponding LSP signatures given in Tables 3.2-3.11 to optimize searches. $+-$ indicates an empty set while $\times$ indicates that the corresponding production channel is not relevant for the given LSP because the cross-section is either lower than or comparable to the cross-section for direct pair production of the LSP.

LSP	$\tilde{g}\tilde{g}$	$\tilde{g}\tilde{q}/\tilde{g}\bar{u}/\tilde{g}\bar{d}$	Squark Pair (1st,2nd gen.)	Squark Pair (3rd gen.)	$\tilde{W}\tilde{W}$	$\tilde{H}\tilde{H}$	Slepton Pair (1st, 2nd gen.)	Slepton Pair (3rd gen.)	$\tilde{B}\tilde{B}$
$\tilde{g}$	$+-$	$\times$	$\times$	$\times$	$\times$	$\times$	$\times$	$\times$	$\times$
$\tilde{q}/\bar{u}/\tilde{d}$	$+2j_1$	$+j_1$	$+-$	$\times$	$\times$	$\times$	$\times$	$\times$	$\times$
$\tilde{q}_3/\tilde{t}/\tilde{b}$	$+2j_3$	$+j_1+2j_3$	$+2j_1+2j_3$	$+-$	$\times$	$\times$	$\times$	$\times$	$\times$
$\tilde{W}$	$+4j$	$+j_1+2j$	$+2j_1$	$+2j_3$	$+-$	$\times$	$\times$	$\times$	$\times$
$\tilde{H}$	$+4j$	$+j_1+2j$	$+2j_1$	$+2j_3$	$\times$	$+-$	$\times$	$\times$	$\times$
$\tilde{\ell}(\tilde{\nu})/\tilde{e}$	$\tilde{\ell}\tilde{\ell}/\tilde{e}\tilde{e}:\ +2\ell+4j$	$+2\ell+j_1+2j$	$+2\ell+2j_1$	$+2\ell+2j_3$	$+\ell+E_T^{\rm miss}$	$+2\ell$	$+-$	$\times$	$\times$
	$\tilde{\ell}\tilde{\nu}:\ +\ell+4j+E_T^{\rm miss}$	$+\ell+j_1+2j+E_T^{\rm miss}$	$+\ell+2j_1+E_T^{\rm miss}$	$+\ell+2j_3+E_T^{\rm miss}$	$+2\ell$	$+\ell+E_T^{\rm miss}$	$+-$	$\times$	$\times$
$\tilde{\tau}_L(\tilde{\nu}_\tau)/\tilde{\tau}_R$	$\tilde{\tau}_L\tilde{\tau}_L/\tilde{\tau}_R\tilde{\tau}_R:\ +2\tau+4j$	$+2\tau+j_1+2j$	$+2\tau+2j_1$	$+2\tau+2j_3$	$+\tau+E_T^{\rm miss}$	$+2\tau$	$+-$	$\times$	$\times$
	$\tilde{\tau}_L\tilde{\nu}_\tau:\ +\tau+4j+E_T^{\rm miss}$	$+\tau+j_1+2j+E_T^{\rm miss}$	$+\tau+2j_1+E_T^{\rm miss}$	$+\tau+2j_3+E_T^{\rm miss}$	$+2\tau$	$+\tau+E_T^{\rm miss}$	$+-$	$\times$	$\times$
$\tilde{B}$	$+4j$	$+j_1+2j$	$+2j_1$	$+2j_3$	$+3\ell+E_T^{\rm miss}/2\ell+E_T^{\rm miss}/4j/2v$	$+4j_3/2v$	$+2\ell/\ell+E_T^{\rm miss}$	$+2\tau/\tau+E_T^{\rm miss}$	$+-$

B.2.2 Flavor, Sign Configurations of Leptons

Here, we compile tables that show the possible flavor and sign combinations of the leptons in the signatures of Tables 3.2-3.11. In all the tables below, the indices $i, j, k \in \{1, 2, 3\}$, while the indices $a, b \in \{1, 2\}$; $\tilde{\ell}_3$ denotes a τ. For each listed configuration, the charge conjugated state (if different) is also possible but we omit listing it explicitly.

LLE Signatures

The flavor and sign combinations of the leptons corresponding to the various $LL\bar{E}$ topologies are shown in Table B.2 ($2L + E_T^{\text{miss}}$); Table B.3 ($3L + E_T^{\text{miss}}$); Table B.4 ($4L$); Table B.5 ($4L + (0-4)j + E_T^{\text{miss}}$); Table B.6 ($5L + E_T^{\text{miss}}$); and Table B.7 ($6L + E_T^{\text{miss}}$). The combinations corresponding to $\tilde{B}$ also apply to the Higgsino and all colored-sector LSPs.

Table B.2: $2L + E_T^{\text{miss}}$.

LSP	Coupling	Signature
$\tilde{e}_a$	λ_{aba} $a \neq b$	$\ell_a^+\ell_a^-/\ell_b^+\ell_b^-/\ell_a^+\ell_b^-$
$\tilde{e}_b$	λ_{a3b}	$\ell_a^+\ell_a^-/\ell_a^+\tau^-$
$\tilde{\tau}_R$	λ_{ab3} $a \neq b$	$\ell_a^+\ell_a^-/\ell_b^+\ell_b^-/\ell_a^+\ell_b^-$
$\tilde{\tau}_R$	λ_{a33}	$\ell_a^+\ell_a^-/\ell_a^+\tau^-$

Table B.3: $3L + E_T^{\text{miss}}$.

LSP	Coupling	Signature
$\tilde{\ell}_a\,(\tilde{\nu}_a)$	λ_{abc} $a \neq b$	$\ell_b^+\ell_c^+\ell_c^-/\ell_b^-\ell_c^+\ell_c^+$
$\tilde{\ell}_a\,(\tilde{\nu}_a)$	λ_{a3b}	$\ell_b^+\ell_b^+\tau^-/\ell_b^+\ell_b^-\tau^+$
$\tilde{\ell}_a\,(\tilde{\nu}_a)$	λ_{ab3} $a \neq b$	$\ell_b^+\tau^+\tau^-/\ell_b^-\tau^+\tau^+$
$\tilde{\ell}_a\,(\tilde{\nu}_a)$	λ_{a33}	$\tau^+\tau^+\tau^-$
$\tilde{\tau}_L\,(\tilde{\nu}_\tau)$	λ_{a3b}	$\ell_a^-\ell_b^+\ell_b^+/\ell_a^+\ell_b^+\ell_b^-$
$\tilde{\tau}_L\,(\tilde{\nu}_\tau)$	λ_{a33}	$\ell_a^+\tau^+\tau^-/\ell_a^-\tau^+\tau^+$

Table B.4: $4L$.

LSP	Coupling	Signature
$\tilde{\ell}_a\,(\tilde{\nu}_a)$	λ_{abc} $a \neq b$	$\ell_b^+\ell_b^+\ell_c^-\ell_c^-/\ell_b^+\ell_b^-\ell_c^+\ell_c^-$
$\tilde{\ell}_a\,(\tilde{\nu}_a)$	λ_{a3b}	$\ell_b^-\ell_b^-\tau^+\tau^+/\ell_b^+\ell_b^-\tau^+\tau^-$
$\tilde{\ell}_a\,(\tilde{\nu}_a)$	λ_{ab3} $a \neq b$	$\ell_b^-\ell_b^-\tau^+\tau^+/\ell_b^+\ell_b^-\tau^+\tau^-$
$\tilde{\ell}_a\,(\tilde{\nu}_a)$	λ_{a33}	$\tau^+\tau^+\tau^-\tau^-$
$\tilde{\tau}_L\,(\tilde{\nu}_\tau)$	λ_{a3b}	$\ell_a^+\ell_a^+\ell_b^-\ell_b^-/\ell_a^+\ell_a^-\ell_b^+\ell_b^-$
$\tilde{\tau}_L\,(\tilde{\nu}_\tau)$	λ_{a33}	$\ell_a^-\ell_a^-\tau^+\tau^+/\ell_a^+\ell_a^-\tau^+\tau^-$

UDD Tables

For the $\bar{U}\bar{D}\bar{D}$ topologies, the possible combinations are shown in Table B.8 ($1L + 2j_l + 4j + E_T^{\text{miss}}$); and Table B.9 ($2L + 2j_l + 4j$).

Table B.5: $4L + (0-4)j + E_T^{\text{miss}}$.

LSP	Coupling	Signature
$\tilde{B}$	λ_{ijk} $i \neq j$	$\ell_i^+\ell_i^+\ell_k^-\ell_k^- / \ell_i^+\ell_i^-\ell_k^+\ell_k^- / \ell_j^+\ell_j^+\ell_k^-\ell_k^- / \ell_j^+\ell_j^-\ell_k^+\ell_k^- / \ell_i^+\ell_j^+\ell_k^-\ell_k^- / \ell_i^+\ell_j^-\ell_k^+\ell_k^-$
$\tilde{W}$	λ_{ijk} $i \neq j$	$\ell_i^+\ell_j^+\ell_k^-\ell_k^- / \ell_i^+\ell_j^-\ell_k^+\ell_k^-$

Table B.6: $5L + E_T^{\text{miss}}$.

LSP	Coupling	Signature
$\tilde{\tau}_L\,(\tilde{\nu})$	λ_{aba} $a \neq b$	$\ell_a^+\ell_a^+\ell_a^-\ell_a^-\tau^+ / \ell_a^+\ell_a^-\ell_b^+\ell_b^-\tau^+ / \ell_a^+\ell_a^+\ell_b^-\ell_b^-\tau^+ / \ell_a^+\ell_a^+\ell_a^-\ell_b^+\tau^+$
$\tilde{\tau}_L\,(\tilde{\nu})$	λ_{ab3} $a \neq b$	$\ell_a^-\ell_a^-\tau^+\tau^+\tau^+ / \ell_b^-\ell_b^-\tau^+\tau^+\tau^+ / \ell_a^+\ell_a^-\tau^+\tau^+\tau^- / \ell_b^+\ell_b^-\tau^+\tau^+\tau^- / \ell_a^-\ell_b^-\tau^+\tau^+\tau^+ / \ell_a^+\ell_b^-\tau^+\tau^+\tau^-$

Table B.7: $6L + E_T^{\text{miss}}$.

LSP	Coupling	Signature
$\tilde{e}_a$	λ_{ab3} $a \neq b$	$\ell_a^+\ell_a^-\ell_a^-\ell_a^-\tau^+\tau^+ / \ell_a^+\ell_a^-\ell_b^-\ell_b^-\tau^+\tau^+ / \ell_a^+\ell_a^+\ell_a^-\ell_a^-\tau^+\tau^- / \ell_a^+\ell_a^-\ell_a^+\ell_b^-\ell_b^-\tau^+\tau^- / \ell_a^+\ell_a^-\ell_a^-\ell_b^-\tau^+\tau^+ / \ell_a^+\ell_a^+\ell_a^-\ell_b^-\tau^+\tau^-$
$\tilde{e}_b$	λ_{a33}	$\ell_a^+\ell_a^-\ell_a^-\tau^+\tau^+\tau^- / \ell_a^+\ell_a^-\ell_a^-\ell_a^-\tau^+\tau^+ / \ell_a^+\ell_a^+\ell_a^-\ell_a^-\tau^+\tau^-$
$\tilde{\tau}_L\,(\tilde{\nu})$	λ_{aba} $a \neq b$	$\ell_a^+\ell_a^+\ell_a^-\ell_a^-\tau^+\tau^- / \ell_a^+\ell_a^-\ell_b^+\ell_b^-\tau^+\tau^- / \ell_a^+\ell_a^+\ell_b^-\ell_b^-\tau^+\tau^- / \ell_a^+\ell_a^+\ell_a^-\ell_b^+\tau^+\tau^-$
$\tilde{\tau}_L\,(\tilde{\nu})$	λ_{ab3} $a \neq b$	$\ell_a^-\ell_a^-\tau^+\tau^+\tau^+\tau^- / \ell_b^-\ell_b^-\tau^+\tau^+\tau^+\tau^- / \ell_a^+\ell_a^-\tau^+\tau^+\tau^-\tau^- / \ell_b^+\ell_b^-\tau^+\tau^+\tau^-\tau^- / \ell_a^-\ell_b^-\tau^+\tau^+\tau^+\tau^- / \ell_a^+\ell_b^-\tau^+\tau^+\tau^-\tau^-$
$\tilde{\tau}_R$	λ_{aba} $a \neq b$	$\ell_a^+\ell_a^+\ell_a^-\ell_a^-\tau^+\tau^- / \ell_a^+\ell_a^-\ell_b^+\ell_b^-\tau^+\tau^- / \ell_a^+\ell_a^+\ell_b^-\ell_b^-\tau^+\tau^- / \ell_a^+\ell_a^-\ell_a^-\ell_b^+\tau^+\tau^-$
$\tilde{\tau}_R$	λ_{a3b}	$\ell_a^+\ell_a^+\ell_b^-\ell_b^-\tau^+\tau^- / \ell_a^+\ell_a^-\ell_b^+\ell_b^-\tau^+\tau^- / \ell_a^+\ell_a^-\ell_b^-\tau^+\tau^+\tau^- / \ell_a^-\ell_b^+\ell_b^-\tau^+\tau^+\tau^-$

LQD Tables

Finally, for the $LQ\bar{D}$ topologies, the possible configurations are shown in Table B.10 ($1L+(2-6)j+E_T^{\text{miss}}$); Table B.11 ($2L+(2-6)j+(E_T^{\text{miss}})$); Table B.12 ($3L+4j+E_T^{\text{miss}}$); and Table B.13 ($4L+4j$). The $\tilde{B}$ configurations apply to the other electroweakinos, and the colored LSPs.

Table B.8: $1L + 2j_l + 4j + E_T^{\text{miss}}$.

LSP	Coupling	Signature
$\tilde{\ell}_a\,(\tilde{\nu}_a)$	λ''_{ijk}	ℓ_a^+
$\tilde{\tau}_L\,(\tilde{\nu})$	λ''_{ijk}	τ^+

Table B.9: $2L + 2j_l + 4j$.

LSP	Coupling	Signature
$\tilde{\ell}_a\,(\tilde{\nu}_a)$	λ''_{ijk}	$\ell_a^+\ell_a^-$
$\tilde{e}_a$	λ''_{ijk}	$\ell_a^+\ell_a^-$
$\tilde{\tau}_L\,(\tilde{\nu})$	λ''_{ijk}	$\tau^+\tau^-$
$\tilde{\tau}_R$	λ''_{ijk}	$\tau^+\tau^-$

Table B.10: $1L + (2-6)j + E_T^{\text{miss}}$.

LSP	Coupling	Signature
$\tilde{B}$	λ'_{ijk}	ℓ_i^+
$\tilde{\ell}_a(\tilde{\nu}_a)$	λ'_{33k}	ℓ_a^+
$\tilde{\tau}_L\,(\tilde{\nu}_\tau)$	λ'_{a3k}	τ^+

Table B.11: $2L + (2-6)j + (E_T^{\text{miss}})$.

LSP	Coupling	Signature
$\tilde{B}$	λ'_{ijk}	$\ell_i^+\ell_i^-/\ell_i^+\ell_i^+$
$\tilde{\ell}_a(\tilde{\nu}_a)$	λ'_{3ak}	$\ell_a^+\tau^+/\ell_a^+\tau^-$
$\tilde{\ell}_a(\tilde{\nu}_a)$	λ'_{33k}	$\ell_a^+\ell_a^-/\ell_a^+\tau^+/\ell_a^+\tau^-$
$\tilde{\tau}_L\,(\tilde{\nu}_\tau)$	λ'_{abk}	$\ell_a^+\tau^+/\ell_a^+\tau^-$
$\tilde{\tau}_L\,(\tilde{\nu}_\tau)$	λ'_{a3k}	$\ell_a^+\tau^+/\ell_a^+\tau^-/\tau^+\tau^-$
$\tilde{e}_a$	λ'_{i3k}	$\ell_a^+\ell_a^-$
$\tilde{\tau}$	λ'_{i3k}	$\tau^+\tau^-$

Table B.12: $3L + 4j + E_T^{\text{miss}}$.

LSP	Coupling	Signature
$\tilde{\ell}_a(\tilde{\nu}_a)$	λ'_{3jk}	$\ell_a^+\ell_a^-\tau^+/\ell_a^+\tau^+\tau^-/\ell_a^+\tau^+\tau^+/\ell_a^+\tau^-\tau^-$
$\tilde{\tau}_L\,(\tilde{\nu}_\tau)$	λ'_{ajk}	$\ell_a^+\ell_a^-\tau^+/\ell_a^+\ell_a^+\tau^+/\ell_a^-\ell_a^-\tau^+/\ell_a^+\tau^+\tau^-$
$\tilde{e}_a$	λ'_{ijk}	$\ell_a^+\ell_a^-\ell_i^+$
$\tilde{\tau}$	λ'_{i3k}	$\ell_i^+\tau^+\tau^-$

Table B.13: $4L + 4j$.

LSP	Coupling	Signature
$\tilde{\ell}_a(\tilde{\nu}_a)$	λ'_{3jk}	$\ell_a^+\ell_a^-\tau^+\tau^-/\ell_a^+\ell_a^-\tau^+\tau^+$
$\tilde{\tau}_L\,(\tilde{\nu}_\tau)$	λ'_{ajk}	$\ell_a^+\ell_a^-\tau^+\tau^-/\ell_a^+\ell_a^+\tau^+\tau^-$
$\tilde{e}_a$	λ'_{ijk}	$\ell_a^+\ell_a^-\ell_i^+\ell_i^-/\ell_a^+\ell_a^-\ell_i^+\ell_i^+$
$\tilde{\tau}$	λ'_{i3k}	$\ell_i^+\ell_i^-\tau^+\tau^-/\ell_i^+\ell_i^+\tau^+\tau^-$

B.3 `abc-rpv`, the RPV Python Library

`abc-rpv`[1] is a Python library that provides a framework for analyzing the collider signatures of the RPV-MSSM. Users are provided with various functionalities to explore the landscape of RPV-MSSM physics within the context of small RPV couplings. In this section, we provide a short introduction to the library. A complete manual will be provided as a separate document/paper in the future.

B.3.1 Introduction

The code starts by generating all possible transitions from one sparticle to another, based on the vertices provided in the input table (`table_notsup.csv`) stored in the input directory. Using this, it can obtain the resulting signature for a decay chain from any LSP to a sparticle directly coupled to an RPV operator; the latter, then, simply decays into purely Standard Model objects. Going through all combinations of LSP type, and RPV couplings (in terms of categories defined in Tables 3.2-3.11), all possible decay chains and signatures are compiled into tables. These tables are the output available to the user that can then be analyzed using the functions described below. By default, all output tables are already generated using the default input table, and are readily available in the data directory. The user does not need to generate the tables unless the input table is modified.

B.3.2 Assumptions and Caveats

In the implementation of our code, there are a few assumptions and caveats worth noting:

- All possible transitions are constructed from vertices provided in `table_notsup.csv` in the input directory. The vertices provided in this table need not be a 3-point vertex.
- The input table (`table_notsup.csv`) contains vertices that allow transitions from one sparticle to another while producing standard model particles. By default, only non-suppressed transitions based on the MSSM interactions are included; we use modified versions of the tables compiled in Ref. [229] for classifying vertices as suppressed or non-suppressed. Note that the input table can be modified by the user, as needed. This allows one to regenerate the output tables with custom vertices.
- While generating the decay chains for the LSPs, only the shortest chain is constructed by default. Users also have the option to generate all possible chains up to 3 transitions.
- The decay chains do not contain repeating sparticles.

B.3.3 Usage

Please refer to `Tutorial.ipynb` available at `https://github.com/kys-sheng/abc-rpv.git` for a complete tutorial of the Python library. We only discuss basic functionality here.

[1] `abc-rpv` Python library is available at: `https://github.com/kys-sheng/abc-rpv.git`

Table B.14: Syntax for sparticles used in the code.

Code Syntax	Sparticles
B	Bino, B
W^+	Charged Wino
W^0	Neutral Wino
G	Gluino
H^+	Charged Higgsino
H^0	Neutral Higgsino
q	$\tilde{u}_L$, $\tilde{d}_L$, $\tilde{c}_L$, $\tilde{s}_L$
d	$\tilde{d}_R$, $\tilde{s}_R$
u	$\tilde{u}_R$, $\tilde{c}_R$
l	$\tilde{e}_L$, $\tilde{\mu}_L$
nu	$\tilde{\nu}_e$, $\tilde{\nu}_\mu$
e	$\tilde{e}_R$, $\tilde{\mu}_R$
t_L	$\tilde{t}_L$
b_L	$\tilde{b}_L$
t	$\tilde{t}_R$
b	$\tilde{b}_R$
tau_L	$\tilde{\tau}_L$
tau	$\tilde{\tau}_R$
nu_tau	$\tilde{\nu}_\tau$

Syntax

Tables B.14 and B.15 show the syntax used in the code. One can also refer to `rpv_definitions.py` for more information.

Dictionaries

In the library, there are a few built-in dictionaries that contain the output tables generated from the code.

- `ONE_LSP_RPV_DECAY_DICT` : Contains details for all possible RPV decays of one LSP. Information regarding RPV coupling category, signature, decay chains, number of vertices is included.
- `TWO_LSP_RPV_DECAY_DICT` : Contains details for all possible RPV decays of a pair[2] of LSPs (decay via same category of RPV coupling). Information regarding RPV coupling category, signature, decay chains, number of vertices is included.
- `TWO_LSP_MIXED_RPV_DECAY_DICT` : Contains details for all possible RPV decays of a pair

[2] We restrict to the case where both LSPs are the same, or belong to the same $SU(2)_L$ doublet.

Table B.15: One-character syntax for final state objects used in the code.

Symbol	Particles (Final State Objects)
`l`	e/μ
`T`	τ
`L`	$e/\mu/\tau$
`j`	$u/d/c/s$ jets
`b`	b jets
`t`	t jets
`3`	t/b jets
`J`	$u/d/c/s/t/b$ jets
`v`	$W/Z/h$
`X`	MET

of LSPs (decay via different categories of RPV couplings). Information regarding RPV coupling categories, signature, decay chains, number of vertices is included.

- `ONE_LSP_SIG_CAT_DICT` : Contains final state signatures arising from decay of one LSP, categorized by RPV coupling; similar to Tables 3.2-3.11.
- `TWO_LSP_SIG_CAT_DICT` : Contains final state signatures arising from decay of pair of LSPs, categorized by RPV coupling; similar to Tables 3.2-3.11.

Note that the above dictionaries are regenerated upon using different input transition tables, as well as different table generation choices (*e.g.*, decay chain length).

Main Functions

Although the dictionaries by themselves contain all relevant information, it is more efficient and powerful to use the functions provided in the library to analyze the data. We describe the basic usage here; refer to `Tutorial.ipynb` for more details.

One LSP Decay:

- `find_one_lsp_from_signature`
  Using the signature as input, this function finds all LSPs with decay chains leading to the given final state. Alongside with the LSP, the relevant RPV couplings and decay chains are also returned.
- `find_one_lsp_from_signature_inclusive`
  Similar to `find_one_lsp_from_signature`, but in the inclusive mode (*e.g.*, one can choose n_{jets} ¿ 3 instead of $n_{jets} = 3$).
- `find_signatures_from_one_lsp`
  Using the LSP as input, this function finds all possible signatures that can arise in

the LSP decay. Alongside with the signatures, the relevant RPV couplings and decay chains are also returned.

LSP Pair Decay; Same Coupling Category:

- `find_two_lsp_from_signature`:
  Similar to `find_one_lsp_from_signature` but returns all pairs of LSPs leading to the input signature.
- `find_two_lsp_from_signature_inclusive`:
  Inclusive mode of `find_two_lsp_from_signature`.
- `find_signatures_from_two_lsp`:
  Similar to `find_signatures_from_one_lsp` but for a pair of input LSPs.

In all of the above, the pair is assumed to decay via the same (category of) RPV coupling.

LSP Pair Decay; Different Coupling Categories:

- `find_two_lsp_from_signature_mixed_couplings`
- `find_two_lsp_from_signature_mixed_couplings_inclusive`
- `find_signatures_from_two_lsp_mixed_couplings`

Analogous to the above but for LSP pair decaying via different (categories of) RPV couplings.

Advanced Usage

By default, all dictionaries and tables are regenerated automatically from the input table if all the csv files in the data directory are deleted. Thus, users can generate all the tables based on their custom input table (`table_notsup.csv`) by deleting the csv files in the data directory and reimporting the library. A step-by-step example demonstrating this will be provided in the complete manual.

C
Appendix C

C.1 Explicit neutralino production/decay widths with $LL\bar{E}$ operators

In this appendix, we will give the explicit general formulae needed for both the neutralino production and decay via $LL\bar{E}$ couplings at tree level. In the framework of the RPV-MSSM, the relevant processes will always involve four external two-component fermions and one intermediate scalar. The external fermions may carry momenta p_i and have masses m_i, where i is a generic label with $i = 0$ (incoming) and $i = 1, 2, 3$ (outgoing). Following Ref. [401], we express the total decay width as

$$\Gamma_{LL\bar{E}}(0;1,2,3)[\alpha,\beta,\gamma] = \frac{m_0}{2^8\pi^3}\int_{z_3^{\min}}^{z_3^{\max}} \mathrm{d}z_3 \int_{z_1^{\min}}^{z_1^{\max}} \mathrm{d}z_1\, \overline{|\mathcal{M}|^2}\,, \tag{C.1}$$

where the spin-averaged matrix element takes the form

$$\begin{aligned}\overline{|\mathcal{M}|^2} = \frac{m_0^4}{2}\Big[&|\alpha|^2\mathcal{Z}_1 + |\beta|^2\mathcal{Z}_2 + |\gamma|^2\mathcal{Z}_3 \\ &- \Re\{\alpha\beta^*\}\Big(+\mathcal{Z}_1 + \mathcal{Z}_2 - \mathcal{Z}_3\Big) \\ &- \Re\{\beta\gamma^*\}\Big(-\mathcal{Z}_1 + \mathcal{Z}_2 + \mathcal{Z}_3\Big) \\ &- \Re\{\alpha\gamma^*\}\Big(+\mathcal{Z}_1 - \mathcal{Z}_2 + \mathcal{Z}_3\Big)\Big]\,,\end{aligned} \tag{C.2}$$

with

$$\mathcal{Z}_i \equiv z_i\left(1 - z_i + 2\xi_i^2 - \sum_{j=1}^{3}\xi_j^2\right). \tag{C.3}$$

The kinematic variables z_i are defined as

$$z_i \equiv 2p_0\cdot p_i/m_0^2 = 2E_i/m_0\,, \tag{C.4}$$

and fulfill the relation $\sum_{i=1}^{3} z_i = 2$. Furthermore we introduce the mass ratios

$$\xi_i \equiv \frac{m_i}{m_0} \quad (i \neq 0)\,. \tag{C.5}$$

The (in general) complex valued coefficients α, β, γ follow from the Feynman rules relevant for the respective process, and can be simplified with the assumption of degenerate sfermion masses, *cf.* Sec. 5.2. Their explicit expressions are given in Eq. (5.2). The integration limits in Eq. (C.1) can be obtained from the minimal and maximal values of the invariant masses of the "$1-2$" and "$2-3$" systems, *cf.* Ref. [65]:

$$(m_{12}^2)_{\max} = (m_0 - m_3)^2\,, \tag{C.6}$$

$$(m_{12}^2)_{\min} = (m_1 + m_2)^2\,, \tag{C.7}$$

$$(m_{23}^2)_{\max} = (E_2^* + E_3^*)^2 - \left(\sqrt{E_2^{*2} - m_2^2} - \sqrt{E_3^{*2} - m_3^2}\right)^2\,, \tag{C.8}$$

$$(m_{23}^2)_{\min} = (E_2^* + E_3^*)^2 - \left(\sqrt{E_2^{*2} - m_2^2} + \sqrt{E_3^{*2} - m_3^2}\right)^2\,, \tag{C.9}$$

where the energies $E_{2,3}^*$ in the "$1-2$" rest frame are given in terms of m_{12} by,

$$E_2^* = (m_{12}^2 - m_1^2 + m_2^2)/2m_{12}\,, \tag{C.10}$$

$$E_3^* = (m_0^2 - m_{12}^2 - m_3^2)/2m_{12}\,. \tag{C.11}$$

From energy-momentum conservation one can deduce that

$$z_3 = \frac{m_0^2 + m_3^2 - m_{12}^2}{m_0^2} \qquad \text{and} \qquad z_1 = \frac{m_0^2 + m_1^2 - m_{23}^2}{m_0^2}\,, \tag{C.12}$$

which then finally yield the integration limits:

$$z_3^{\max} = 1 + \xi_3^2 - \frac{(m_{12}^2)_{\min}}{m_0^2}\,, \tag{C.13}$$

$$z_3^{\min} = 1 + \xi_3^2 - \frac{(m_{12}^2)_{\max}}{m_0^2} = 2\xi_3\,, \tag{C.14}$$

$$z_1^{\max} = 1 + \xi_1^2 - \frac{(m_{23}^2)_{\min}}{m_{\tilde{\chi}_1^0}^2}\,, \tag{C.15}$$

$$z_1^{\min} = 1 + \xi_1^2 - \frac{(m_{23}^2)_{\max}}{m_{\tilde{\chi}_1^0}^2}\,. \tag{C.16}$$

Bibliography

[1] S. L. Glashow, *Partial Symmetries of Weak Interactions*, Nucl. Phys. **22** (1961) 579.

[2] S. Weinberg, *A Model of Leptons*, Phys. Rev. Lett. **19** (1967) 1264.

[3] A. Salam and J. C. Ward, *Weak and electromagnetic interactions*, Nuovo Cim. **11** (1959) 568.

[4] G. Aad et al., *Observation of a new particle in the search for the Standard Model Higgs boson with the ATLAS detector at the LHC*, Phys. Lett. B **716** (2012) 1, arXiv: 1207.7214 [hep-ex].

[5] S. Chatrchyan et al., *Observation of a New Boson at a Mass of 125 GeV with the CMS Experiment at the LHC*, Phys. Lett. B **716** (2012) 30, arXiv: 1207.7235 [hep-ex].

[6] F. Zwicky, *Die Rotverschiebung von extragalaktischen Nebeln*, Helv. Phys. Acta **6** (1933) 110.

[7] H. W. Babcock, *The rotation of the Andromeda Nebula*, Lick Observatory Bulletin **498** (1939) 41.

[8] V. C. Rubin and W. K. Ford Jr., *Rotation of the Andromeda Nebula from a Spectroscopic Survey of Emission Regions*, Astrophys. J. **159** (1970) 379.

[9] E. Komatsu et al., *Seven-Year Wilkinson Microwave Anisotropy Probe (WMAP) Observations: Cosmological Interpretation*, Astrophys. J. Suppl. **192** (2011) 18, arXiv: 1001.4538 [astro-ph.CO].

[10] P. A. R. Ade et al., *Planck 2015 results. XIII. Cosmological parameters*, Astron. Astrophys. **594** (2016) A13, arXiv: 1502.01589 [astro-ph.CO].

[11] N. Aghanim et al., *Planck 2018 results. VI. Cosmological parameters*, Astron. Astrophys. **641** (2020) A6, [Erratum: Astron.Astrophys. 652, C4 (2021)], arXiv: 1807.06209 [astro-ph.CO].

[12] M. C. Gonzalez-Garcia, M. Maltoni and T. Schwetz, *NuFIT: Three-Flavour Global Analyses of Neutrino Oscillation Experiments*, Universe **7** (2021) 459, arXiv: 2111.03086 [hep-ph].

[13] Y. Fukuda et al., *Evidence for oscillation of atmospheric neutrinos*, Phys. Rev. Lett. **81** (1998) 1562, arXiv: hep-ex/9807003.

[14] R. Davis, *A review of the Homestake solar neutrino experiment*, Prog. Part. Nucl. Phys. **32** (1994) 13.

[15] M. Wurm, *Measuring the neutrino mass ordering in JUNO*, International School of Nuclear Physics, Erice, Italy (2017).

[16] G. Steigman, *Observational tests of antimatter cosmologies*, Ann. Rev. Astron. Astrophys. **14** (1976) 339.

[17] L. Canetti, M. Drewes and M. Shaposhnikov, *Matter and Antimatter in the Universe*, New J. Phys. **14** (2012) 095012, arXiv: 1204.4186 [hep-ph].

[18] A. D. Sakharov,
Violation of CP Invariance, C asymmetry, and baryon asymmetry of the universe,
Pisma Zh. Eksp. Teor. Fiz. **5** (1967) 32.

[19] G. 't Hooft,
Computation of the Quantum Effects Due to a Four-Dimensional Pseudoparticle,
Phys. Rev. D **14** (1976) 3432, ed. by M. A. Shifman, [Erratum: Phys.Rev.D 18, 2199 (1978)].

[20] N. S. Manton, *Topology in the Weinberg-Salam Theory*, Phys. Rev. D **28** (1983) 2019.

[21] J. A. Harvey and M. S. Turner, *Cosmological baryon and lepton number in the presence of electroweak fermion number violation*, Phys. Rev. D **42** (1990) 3344.

[22] H. K. Dreiner and G. G. Ross, *Sphaleron erasure of primordial baryogenesis*, Nucl. Phys. B **410** (1993) 188, arXiv: hep-ph/9207221.

[23] V. A. Kuzmin, V. A. Rubakov and M. E. Shaposhnikov, *On the Anomalous Electroweak Baryon Number Nonconservation in the Early Universe*,
Phys. Lett. B **155** (1985) 36.

[24] M. E. Shaposhnikov,
Baryon Asymmetry of the Universe in Standard Electroweak Theory,
Nucl. Phys. B **287** (1987) 757.

[25] M. B. Gavela, P. Hernandez, J. Orloff and O. Pene,
Standard model CP violation and baryon asymmetry,
Mod. Phys. Lett. A **9** (1994) 795, arXiv: hep-ph/9312215.

[26] M. B. Gavela, P. Hernandez, J. Orloff, O. Pene and C. Quimbay,
Standard model CP violation and baryon asymmetry. Part 2: Finite temperature,
Nucl. Phys. B **430** (1994) 382, arXiv: hep-ph/9406289.

[27] C. S. Wu, E. Ambler, R. W. Hayward, D. D. Hoppes and R. P. Hudson,
Experimental Test of Parity Conservation in β Decay, Phys. Rev. **105** (1957) 1413.

[28] J. H. Christenson, J. W. Cronin, V. L. Fitch and R. Turlay,
Evidence for the 2π Decay of the K_2^0 Meson, Phys. Rev. Lett. **13** (1964) 138.

[29] M. Kobayashi and T. Maskawa,
CP Violation in the Renormalizable Theory of Weak Interaction,
Prog. Theor. Phys. **49** (1973) 652.

[30] H. Georgi and S. L. Glashow, *Unity of All Elementary Particle Forces*,
Phys. Rev. Lett. **32** (1974) 438.

[31] E. Hubble,
A relation between distance and radial velocity among extra-galactic nebulae,
Proc. Nat. Acad. Sci. **15** (1929) 168.

[32] A. G. Riess et al., *Observational evidence from supernovae for an accelerating universe and a cosmological constant*, Astron. J. **116** (1998) 1009,
arXiv: astro-ph/9805201.

[33] P. J. E. Peebles and B. Ratra, *The Cosmological Constant and Dark Energy*, Rev. Mod. Phys. **75** (2003) 559, ed. by J.-P. Hsu and D. Fine, arXiv: astro-ph/0207347.

[34] H. P. Nilles, *Supersymmetry, Supergravity and Particle Physics*, Phys. Rept. **110** (1984) 1.

[35] H. E. Haber and G. L. Kane, *The Search for Supersymmetry: Probing Physics Beyond the Standard Model*, Phys. Rept. **117** (1985) 75.

[36] E. Gildener, *Gauge Symmetry Hierarchies*, Phys. Rev. D **14** (1976) 1667.

[37] H. P. Nilles, *Dynamically Broken Supergravity and the Hierarchy Problem*, Phys. Lett. B **115** (1982) 193.

[38] E. Witten, *Dynamical Breaking of Supersymmetry*, Nucl. Phys. B **188** (1981) 513.

[39] R. D. Peccei, *The Strong CP problem and axions*, Lect. Notes Phys. **741** (2008) 3, ed. by M. Kuster, G. Raffelt and B. Beltran, arXiv: hep-ph/0607268.

[40] R. J. Crewther, P. Di Vecchia, G. Veneziano and E. Witten, *Chiral Estimate of the Electric Dipole Moment of the Neutron in Quantum Chromodynamics*, Phys. Lett. B **88** (1979) 123, [Erratum: Phys.Lett.B 91, 487 (1980)].

[41] C. Abel et al., *Measurement of the Permanent Electric Dipole Moment of the Neutron*, Phys. Rev. Lett. **124** (2020) 081803, arXiv: 2001.11966 [hep-ex].

[42] J. E. Kim and G. Carosi, *Axions and the Strong CP Problem*, Rev. Mod. Phys. **82** (2010) 557, [Erratum: Rev.Mod.Phys. 91, 049902 (2019)], arXiv: 0807.3125 [hep-ph].

[43] D. J. E. Marsh, *Axion Cosmology*, Phys. Rept. **643** (2016) 1, arXiv: 1510.07633 [astro-ph.CO].

[44] L. Di Luzio, M. Giannotti, E. Nardi and L. Visinelli, *The landscape of QCD axion models*, Phys. Rept. **870** (2020) 1, arXiv: 2003.01100 [hep-ph].

[45] S. P. Martin, *A Supersymmetry primer*, Adv. Ser. Direct. High Energy Phys. **18** (1998) 1, ed. by G. L. Kane, arXiv: hep-ph/9709356.

[46] H. K. Dreiner, H. E. Haber and S. P. Martin, *From Spinors to Supersymmetry*, Cambridge, UK: Cambridge University Press, 2023.

[47] S. R. Coleman and J. Mandula, *All Possible Symmetries of the S Matrix*, Phys. Rev. **159** (1967) 1251, ed. by A. Zichichi.

[48] R. Haag, J. T. Lopuszanski and M. Sohnius, *All Possible Generators of Supersymmetries of the s Matrix*, Nucl. Phys. B **88** (1975) 257.

[49] H. E. Haber, "Introductory low-energy supersymmetry", *Theoretical Advanced Study Institute (TASI 92): From Black Holes and Strings to Particles*, 1993 589, arXiv: hep-ph/9306207.

[50] S. Weinberg, *Supersymmetry at Ordinary Energies. 1. Masses and Conservation Laws*, Phys. Rev. D **26** (1982) 287.

[51] L. E. Ibanez and G. G. Ross, *Discrete gauge symmetry anomalies*, Phys. Lett. B **260** (1991) 291.

[52] L. E. Ibanez and G. G. Ross, *Discrete gauge symmetries and the origin of baryon and lepton number conservation in supersymmetric versions of the standard model*, Nucl. Phys. B **368** (1992) 3.

[53] H. K. Dreiner, *An Introduction to explicit R-parity violation*, Adv. Ser. Direct. High Energy Phys. **21** (2010) 565, ed. by G. L. Kane, arXiv: hep-ph/9707435.

[54] B. C. Allanach, A. Dedes and H. K. Dreiner, *R parity violating minimal supergravity model*, Phys. Rev. D **69** (2004) 115002, [Erratum: Phys.Rev.D 72, 079902 (2005)], arXiv: hep-ph/0309196.

[55] H. K. Dreiner, C. Luhn and M. Thormeier, *What is the discrete gauge symmetry of the MSSM?*, Phys. Rev. D **73** (2006) 075007, arXiv: hep-ph/0512163.

[56] H. K. Dreiner, C. Luhn, H. Murayama and M. Thormeier, *Proton Hexality from an Anomalous Flavor U(1) and Neutrino Masses: Linking to the String Scale*, Nucl. Phys. B **795** (2008) 172, arXiv: 0708.0989 [hep-ph].

[57] *SUSY Summary Plots March 2023*, (2023).

[58] L. J. Hall and M. Suzuki, *Explicit R-Parity Breaking in Supersymmetric Models*, Nucl. Phys. B **231** (1984) 419.

[59] A. S. Joshipura and M. Nowakowski, *'Just so' oscillations in supersymmetric standard model*, Phys. Rev. D **51** (1995) 2421, arXiv: hep-ph/9408224.

[60] E. Nardi, *Renormalization group induced neutrino masses in supersymmetry without R-parity*, Phys. Rev. D **55** (1997) 5772, arXiv: hep-ph/9610540.

[61] Y. Grossman and H. E. Haber, "Neutrino masses and sneutrino mixing in R-parity violating supersymmetry", 1999, arXiv: hep-ph/9906310.

[62] S. Davidson and M. Losada, *Basis independent neutrino masses in the R(p) violating MSSM*, Phys. Rev. D **65** (2002) 075025, arXiv: hep-ph/0010325.

[63] A. Dedes, S. Rimmer and J. Rosiek,
Neutrino masses in the lepton number violating MSSM, JHEP **08** (2006) 005,
arXiv: hep-ph/0603225.

[64] B. Allanach and C. Kom, *Lepton number violating mSUGRA and neutrino masses*,
JHEP **04** (2008) 081, arXiv: 0712.0852 [hep-ph].

[65] R. L. Workman et al., *Review of Particle Physics*, PTEP **2022** (2022) 083C01.

[66] H. K. Dreiner and S. Grab,
All Possible Lightest Supersymmetric Particles in R-Parity Violating mSUGRA,
Phys. Lett. B **679** (2009) 45, arXiv: 0811.0200 [hep-ph].

[67] D. Dercks, H. Dreiner, M. E. Krauss, T. Opferkuch and A. Reinert,
R-Parity Violation at the LHC, Eur. Phys. J. C **77** (2017) 856,
arXiv: 1706.09418 [hep-ph].

[68] D. Choudhury, H. K. Dreiner, P. Richardson and S. Sarkar,
A Supersymmetric solution to the KARMEN time anomaly,
Phys. Rev. D **61** (2000) 095009, arXiv: hep-ph/9911365.

[69] H. K. Dreiner et al., *Mass Bounds on a Very Light Neutralino*,
Eur. Phys. J. C **62** (2009) 547, arXiv: 0901.3485 [hep-ph].

[70] A. Dedes, H. K. Dreiner and P. Richardson,
Attempts at explaining the NuTeV observation of dimuon events,
Phys. Rev. D **65** (2001) 015001, arXiv: hep-ph/0106199.

[71] H. K. Dreiner et al., *Rare meson decays into very light neutralinos*,
Phys. Rev. D **80** (2009) 035018, arXiv: 0905.2051 [hep-ph].

[72] B. W. Lee and S. Weinberg, *Cosmological Lower Bound on Heavy Neutrino Masses*,
Phys. Rev. Lett. **39** (1977) 165, ed. by M. A. Srednicki.

[73] D. Hooper and T. Plehn, *Supersymmetric dark matter: How light can the LSP be?*,
Phys. Lett. B **562** (2003) 18, arXiv: hep-ph/0212226.

[74] A. Bottino, N. Fornengo and S. Scopel, *Light relic neutralinos*,
Phys. Rev. D **67** (2003) 063519, arXiv: hep-ph/0212379.

[75] A. Bottino, F. Donato, N. Fornengo and S. Scopel,
Light neutralinos and WIMP direct searches, Phys. Rev. D **69** (2004) 037302,
arXiv: hep-ph/0307303.

[76] A. Bottino, F. Donato, N. Fornengo and S. Scopel, *Indirect signals from light neutralinos in supersymmetric models without gaugino mass unification*,
Phys. Rev. D **70** (2004) 015005, arXiv: hep-ph/0401186.

[77] A. Bottino, F. Donato, N. Fornengo and P. Salati,
Antiproton fluxes from light neutralinos, Phys. Rev. D **72** (2005) 083518,
arXiv: hep-ph/0507086.

[78] A. Bottino, F. Donato, N. Fornengo and S. Scopel,
Do current WIMP direct measurements constrain light relic neutralinos?,
Phys. Rev. D **72** (2005) 083521, arXiv: hep-ph/0508270.

[79] A. Bottino, F. Donato, N. Fornengo and S. Scopel, *Zooming in on light relic neutralinos by direct detection and measurements of galactic antimatter*, Phys. Rev. D **77** (2008) 015002, arXiv: 0710.0553 [hep-ph].

[80] A. Bottino, N. Fornengo, G. Polesello and S. Scopel, *Light neutralinos at CERN LHC in cosmologically-inspired scenarios: New benchmarks in the search for supersymmetry*, Phys. Rev. D **77** (2008) 115026, arXiv: 0801.3334 [hep-ph].

[81] G. Belanger, F. Boudjema, A. Cottrant, A. Pukhov and S. Rosier-Lees, *Lower limit on the neutralino mass in the general MSSM*, JHEP **03** (2004) 012, arXiv: hep-ph/0310037.

[82] L. Calibbi, J. M. Lindert, T. Ota and Y. Takanishi, *Cornering light Neutralino Dark Matter at the LHC*, JHEP **10** (2013) 132, arXiv: 1307.4119 [hep-ph].

[83] R. Cowsik and J. McClelland, *An Upper Limit on the Neutrino Rest Mass*, Phys. Rev. Lett. **29** (1972) 669.

[84] G. Aad et al., *Search for charginos and neutralinos in final states with two boosted hadronically decaying bosons and missing transverse momentum in pp collisions at $\sqrt{s}$ = 13 TeV with the ATLAS detector*, Phys. Rev. D **104** (2021) 112010, arXiv: 2108.07586 [hep-ex].

[85] G. Aad et al., *Search for direct production of winos and higgsinos in events with two same-charge leptons or three leptons in pp collision data at $\sqrt{s} = 13$ TeV with the ATLAS detector*, (2023), arXiv: 2305.09322 [hep-ex].

[86] H. K. Dreiner, C. Hanhart, U. Langenfeld and D. R. Phillips, *Supernovae and light neutralinos: SN1987A bounds on supersymmetry revisited*, Phys. Rev. D **68** (2003) 055004, arXiv: hep-ph/0304289.

[87] M. Kachelriess, *The KARMEN anomaly, light neutralinos and supernova SN1987A*, JHEP **02** (2000) 010, arXiv: hep-ph/0001160.

[88] H. K. Dreiner, J.-F. Fortin, J. Isern and L. Ubaldi, *White Dwarfs constrain Dark Forces*, Phys. Rev. D **88** (2013) 043517, arXiv: 1303.7232 [hep-ph].

[89] J. Wess and B. Zumino, *Supergauge Transformations in Four-Dimensions*, Nucl. Phys. B **70** (1974) 39, ed. by A. Salam and E. Sezgin.

[90] J. Wess and B. Zumino, *A Lagrangian Model Invariant Under Supergauge Transformations*, Phys. Lett. B **49** (1974) 52.

[91] M. Fukugita and T. Yanagida, *Baryogenesis Without Grand Unification*, Phys. Lett. B **174** (1986) 45.

[92] S. Davidson and A. Ibarra, *A Lower bound on the right-handed neutrino mass from leptogenesis*, Phys. Lett. B **535** (2002) 25, arXiv: hep-ph/0202239.

[93] W. Buchmuller, P. Di Bari and M. Plumacher, *Leptogenesis for pedestrians*, Annals Phys. **315** (2005) 305, arXiv: hep-ph/0401240.

[94] S. Davidson, E. Nardi and Y. Nir, *Leptogenesis*, Phys. Rept. **466** (2008) 105, arXiv: 0802.2962 [hep-ph].

[95] N. Sakai and T. Yanagida, *Proton Decay in a Class of Supersymmetric Grand Unified Models*, Nucl. Phys. B **197** (1982) 533.

[96] S. W. Hawking, D. N. Page and C. N. Pope, *THE PROPAGATION OF PARTICLES IN SPACE-TIME FOAM*, Phys. Lett. B **86** (1979) 175.

[97] I. Antoniadis, J. R. Ellis, J. S. Hagelin and D. V. Nanopoulos, *The Flipped SU(5) x U(1) String Model Revamped*, Phys. Lett. B **231** (1989) 65.

[98] A. Y. Smirnov and F. Vissani, *Upper bound on all products of R-parity violating couplings lambda-prime and lambda-prime-prime from proton decay*, Phys. Lett. B **380** (1996) 317, arXiv: hep-ph/9601387.

[99] R. Barbier et al., *R-parity violating supersymmetry*, Phys. Rept. **420** (2005) 1, arXiv: hep-ph/0406039.

[100] E. Dudas, T. Gherghetta, K. Kaneta, Y. Mambrini and K. A. Olive, *Limits on R-parity Violation in High Scale Supersymmetry*, Phys. Rev. D **100** (2019) 035004, arXiv: 1905.09243 [hep-ph].

[101] N. Chamoun, F. Domingo and H. K. Dreiner, *Nucleon decay in the R-parity violating MSSM*, Phys. Rev. D **104** (2021) 015020, arXiv: 2012.11623 [hep-ph].

[102] I. Hinchliffe and T. Kaeding, *B+L violating couplings in the minimal supersymmetric Standard Model*, Phys. Rev. D **47** (1993) 279.

[103] F. Vissani, *(B+L) conserving nucleon decays in supersymmetric models*, Phys. Rev. D **52** (1995) 4245, arXiv: hep-ph/9503227.

[104] A. Takenaka et al., *Search for proton decay via $p \to e^+\pi^0$ and $p \to \mu^+\pi^0$ with an enlarged fiducial volume in Super-Kamiokande I-IV*, Phys. Rev. D **102** (2020) 112011, arXiv: 2010.16098 [hep-ex].

[105] C. E. Carlson, P. Roy and M. Sher, *New bounds on R-parity violating couplings*, Phys. Lett. B **357** (1995) 99, arXiv: hep-ph/9506328.

[106] H. N. Long and P. B. Pal, *Nucleon instability in a supersymmetric SU(3) C x SU(3)-L x U(1) model*, Mod. Phys. Lett. A **13** (1998) 2355, arXiv: hep-ph/9711455.

[107] G. Bhattacharyya and P. B. Pal, *Upper bounds on all R-parity violating lambda lambda-prime-prime combinations from proton stability*, Phys. Rev. D **59** (1999) 097701, arXiv: hep-ph/9809493.

[108] G. Bhattacharyya and P. B. Pal,
New constraints on R-parity violation from proton stability,
Phys. Lett. B **439** (1998) 81, arXiv: hep-ph/9806214.

[109] D. Chang and W.-Y. Keung,
New limits on R-parity breakings in supersymmetric standard models,
Phys. Lett. B **389** (1996) 294, arXiv: hep-ph/9608313.

[110] B. Abi et al., *Deep Underground Neutrino Experiment (DUNE), Far Detector Technical Design Report, Volume I Introduction to DUNE*, JINST **15** (2020) T08008, arXiv: 2002.02967 [physics.ins-det].

[111] B. Abi et al., *Deep Underground Neutrino Experiment (DUNE), Far Detector Technical Design Report, Volume III: DUNE Far Detector Technical Coordination*, JINST **15** (2020) T08009, arXiv: 2002.03008 [physics.ins-det].

[112] B. Abi et al., *Deep Underground Neutrino Experiment (DUNE), Far Detector Technical Design Report, Volume IV: Far Detector Single-phase Technology*, JINST **15** (2020) T08010, arXiv: 2002.03010 [physics.ins-det].

[113] B. Abi et al., *Deep Underground Neutrino Experiment (DUNE), Far Detector Technical Design Report, Volume II: DUNE Physics*, (2020), arXiv: 2002.03005 [hep-ex].

[114] Z. Djurcic et al., *JUNO Conceptual Design Report*, (2015), arXiv: 1508.07166 [physics.ins-det].

[115] F. An et al., *Neutrino Physics with JUNO*, J. Phys. G **43** (2016) 030401, arXiv: 1507.05613 [physics.ins-det].

[116] K. Abe et al., *Hyper-Kamiokande Design Report*, (2018), arXiv: 1805.04163 [physics.ins-det].

[117] M. Aker et al., *Direct neutrino-mass measurement with sub-electronvolt sensitivity*, Nature Phys. **18** (2022) 160, arXiv: 2105.08533 [hep-ex].

[118] I. Esteban, M. Gonzalez-Garcia, M. Maltoni, T. Schwetz and A. Zhou,
The fate of hints: updated global analysis of three-flavor neutrino oscillations,
JHEP **09** (2020) 178, arXiv: 2007.14792 [hep-ph].

[119] P. Minkowski, $\mu \to e\gamma$ *at a Rate of One Out of* 10^9 *Muon Decays?*,
Phys. Lett. B **67** (1977) 421.

[120] M. Jezabek and Y. Sumino, *Neutrino mixing and seesaw mechanism*,
Phys. Lett. B **440** (1998) 327, arXiv: hep-ph/9807310.

[121] W. Rodejohann,
The See-saw mechanism: Neutrino mixing, leptogenesis and lepton flavor violation,
Pramana **72** (2009) 217, ed. by R. Basu, arXiv: 0804.3925 [hep-ph].

[122] H. K. Dreiner, C. Luhn, H. Murayama and M. Thormeier,
Baryon triality and neutrino masses from an anomalous flavor U(1),
Nucl. Phys. B **774** (2007) 127, arXiv: hep-ph/0610026.

[123] M. Hirsch, M. A. Diaz, W. Porod, J. C. Romao and J. W. F. Valle,
Neutrino masses and mixings from supersymmetry with bilinear R parity violation: A Theory for solar and atmospheric neutrino oscillations,
Phys. Rev. D **62** (2000) 113008, [Erratum: Phys.Rev.D 65, 119901 (2002)],
arXiv: hep-ph/0004115.

[124] M. Nowakowski and A. Pilaftsis,
W and Z boson interactions in supersymmetric models with explicit R-parity violation,
Nucl. Phys. B **461** (1996) 19, arXiv: hep-ph/9508271.

[125] T. Banks, Y. Grossman, E. Nardi and Y. Nir,
Supersymmetry without R-parity and without lepton number,
Phys. Rev. D **52** (1995) 5319, arXiv: hep-ph/9505248.

[126] R. Hempfling, *Neutrino masses and mixing angles in SUSY GUT theories with explicit R-parity breaking*, Nucl. Phys. B **478** (1996) 3, arXiv: hep-ph/9511288.

[127] E. J. Chun and S. K. Kang, *One loop corrected neutrino masses and mixing in supersymmetric standard model without R-parity*, Phys. Rev. D **61** (2000) 075012,
arXiv: hep-ph/9909429.

[128] D. Kaplan and A. E. Nelson,
Solar and atmospheric neutrino oscillations from bilinear R parity violation,
JHEP **01** (2000) 033, arXiv: hep-ph/9901254.

[129] Y. Grossman and H. E. Haber, *Sneutrino mixing phenomena*,
Phys. Rev. Lett. **78** (1997) 3438, arXiv: hep-ph/9702421.

[130] Y. Grossman and H. E. Haber, *(S)neutrino properties in R-parity violating supersymmetry. 1. CP conserving phenomena*, Phys. Rev. D **59** (1999) 093008,
arXiv: hep-ph/9810536.

[131] Y. Grossman and S. Rakshit,
Neutrino masses in R-parity violating supersymmetric models,
Phys. Rev. D **69** (2004) 093002, arXiv: hep-ph/0311310.

[132] M. Diaz, M. Hirsch, W. Porod, J. Romao and J. Valle,
Solar neutrino masses and mixing from bilinear R parity broken supersymmetry: Analytical versus numerical results,
Phys. Rev. D **68** (2003) 013009, [Erratum: Phys.Rev.D 71, 059904 (2005)],
arXiv: hep-ph/0302021.

[133] S. Davidson and M. Losada, *Neutrino masses in the R(p) violating MSSM*,
JHEP **05** (2000) 021, arXiv: hep-ph/0005080.

[134] A. Abada, S. Davidson and M. Losada,
Neutrino masses and mixings in the MSSM with soft bilinear R(p) violation,
Phys. Rev. D **65** (2002) 075010, arXiv: hep-ph/0111332.

[135] F. Borzumati, Y. Grossman, E. Nardi and Y. Nir,
Neutrino masses and mixing in supersymmetric models without R parity,
Phys. Lett. B **384** (1996) 123, arXiv: hep-ph/9606251.

[136] M. Drees, S. Pakvasa, X. Tata and T. ter Veldhuis,
A Supersymmetric resolution of solar and atmospheric neutrino puzzles,
Phys. Rev. D **57** (1998) 5335, arXiv: hep-ph/9712392.

[137] E. Chun, S. Kang, C. Kim and U. Lee,
Supersymmetric neutrino masses and mixing with R-parity violation,
Nucl. Phys. B **544** (1999) 89, arXiv: hep-ph/9807327.

[138] A. S. Joshipura and S. K. Vempati, *Sneutrino vacuum expectation values and neutrino anomalies through trilinear R-parity violation*,
Phys. Rev. D **60** (1999) 111303, arXiv: hep-ph/9903435.

[139] K. Choi, K. Hwang and E. J. Chun,
Atmospheric and solar neutrino masses from horizontal U(1) symmetry,
Phys. Rev. D **60** (1999) 031301, arXiv: hep-ph/9811363.

[140] O. C. Kong,
Neutrino oscillations and flavor structure of supersymmetry without R-parity,
Mod. Phys. Lett. A **14** (1999) 903, arXiv: hep-ph/9808304.

[141] S. Rakshit, G. Bhattacharyya and A. Raychaudhuri,
R-parity violating trilinear couplings and recent neutrino data,
Phys. Rev. D **59** (1999) 091701, arXiv: hep-ph/9811500.

[142] R. Adhikari and G. Omanovic, *LSND, solar and atmospheric neutrino oscillation experiments, and R-parity violating supersymmetry*, Phys. Rev. D **59** (1999) 073003.

[143] A. Abada and M. Losada, *Constraints on both bilinear and trilinear R-parity violating couplings from neutrino laboratories and astrophysics data*,
Phys. Lett. B **492** (2000) 310, arXiv: hep-ph/0007041.

[144] S. Rakshit, *Neutrino masses and R-parity violation*,
Mod. Phys. Lett. A **19** (2004) 2239, arXiv: hep-ph/0406168.

[145] H. K. Dreiner, M. Hanussek, J.-S. Kim and C. Kom, *Neutrino masses and mixings in the baryon triality constrained minimal supersymmetric standard model*,
Phys. Rev. D **84** (2011) 113005, arXiv: 1106.4338 [hep-ph].

[146] J. Romao, M. Diaz, M. Hirsch, W. Porod and J. Valle,
A Supersymmetric solution to the solar and atmospheric neutrino problems,
Phys. Rev. D **61** (2000) 071703, arXiv: hep-ph/9907499.

[147] K.-m. Cheung and O. C. Kong, *Zee neutrino mass model in SUSY framework*,
Phys. Rev. D **61** (2000) 113012, arXiv: hep-ph/9912238.

[148] G. R. Farrar and P. Fayet, *Phenomenology of the Production, Decay, and Detection of New Hadronic States Associated with Supersymmetry*, Phys. Lett. B **76** (1978) 575.

[149] H. K. Dreiner and G. G. Ross, *R-parity violation at hadron colliders*,
Nucl. Phys. B **365** (1991) 597.

[150] H. K. Dreiner and M. Thormeier,
Supersymmetric Froggatt-Nielsen models with baryon and lepton number violation,
Phys. Rev. D **69** (2004) 053002, arXiv: hep-ph/0305270.

[151] H. K. Dreiner, J. S. Kim, O. Lebedev and M. Thormeier,
Supersymmetric Jarlskog invariants: The Neutrino sector,
Phys. Rev. D **76** (2007) 015006, arXiv: hep-ph/0703074.

[152] H. K. Dreiner, M. Hanussek, J. S. Kim and S. Sarkar,
Gravitino cosmology with a very light neutralino, Phys. Rev. D **85** (2012) 065027,
arXiv: 1111.5715 [hep-ph].

[153] J. Hosaka et al., *Solar neutrino measurements in super-Kamiokande-I*,
Phys. Rev. D **73** (2006) 112001, arXiv: hep-ex/0508053.

[154] Y. Ashie et al.,
Evidence for an oscillatory signature in atmospheric neutrino oscillation,
Phys. Rev. Lett. **93** (2004) 101801, arXiv: hep-ex/0404034.

[155] K. J. Kelly, P. A. N. Machado, S. J. Parke, Y. F. Perez-Gonzalez and R. Z. Funchal,
Neutrino mass ordering in light of recent data, Phys. Rev. D **103** (2021) 013004,
arXiv: 2007.08526 [hep-ph].

[156] P. F. Harrison, D. H. Perkins and W. G. Scott,
Tri-bimaximal mixing and the neutrino oscillation data, Phys. Lett. B **530** (2002) 167,
arXiv: hep-ph/0202074.

[157] B. C. Allanach, A. Dedes and H. K. Dreiner,
Bounds on R-parity violating couplings at the weak scale and at the GUT scale,
Phys. Rev. D **60** (1999) 075014, arXiv: hep-ph/9906209.

[158] F. James and M. Roos, *Minuit: A System for Function Minimization and Analysis of the Parameter Errors and Correlations*, Comput. Phys. Commun. **10** (1975) 343.

[159] P. Bechtle et al.,
What if the LHC does not find supersymmetry in the $\sqrt{s} = 7$ TeV run?,
Phys. Rev. D **84** (2011) 011701, arXiv: 1102.4693 [hep-ph].

[160] J. A. Evans, Y. Kats, D. Shih and M. J. Strassler,
Toward Full LHC Coverage of Natural Supersymmetry, JHEP **07** (2014) 101,
arXiv: 1310.5758 [hep-ph].

[161] M. Lisanti, P. Schuster, M. Strassler and N. Toro,
Study of LHC Searches for a Lepton and Many Jets, JHEP **11** (2012) 081,
arXiv: 1107.5055 [hep-ph].

[162] Y. A. Golfand and E. P. Likhtman,
Extension of the Algebra of Poincare Group Generators and Violation of p Invariance,
JETP Lett. **13** (1971) 323.

[163] D. V. Volkov and V. P. Akulov, *Is the Neutrino a Goldstone Particle?*,
Phys. Lett. B **46** (1973) 109.

[164] M. J. G. Veltman, *The Infrared - Ultraviolet Connection*,
Acta Phys. Polon. B **12** (1981) 437.

[165] M. Drees, R. Godbole and P. Roy, *Theory and phenomenology of sparticles: An account of four-dimensional N=1 supersymmetry in high energy physics*, 2004.

[166] *Search for supersymmetry in final states with missing transverse momentum and three or more b-jets in 139 fb^{-1} of proton−proton collisions at $\sqrt{s} = 13$ TeV with the ATLAS detector*, (2022), arXiv: 2211.08028 [hep-ex].

[167] *Search for new phenomena in final states with photons, jets and missing transverse momentum in pp collisions at $\sqrt{s} = 13$ TeV with the ATLAS detector*, (2022), arXiv: 2206.06012 [hep-ex].

[168] G. Aad et al., *Search for new phenomena in pp collisions in final states with tau leptons, b-jets, and missing transverse momentum with the ATLAS detector*, Phys. Rev. D **104** (2021) 112005, arXiv: 2108.07665 [hep-ex].

[169] G. Aad et al., *Search for new phenomena in events with two opposite-charge leptons, jets and missing transverse momentum in pp collisions at $\sqrt{s}$ = 13 TeV with the ATLAS detector*, JHEP **04** (2021) 165, arXiv: 2102.01444 [hep-ex].

[170] G. Aad et al., *Search for new phenomena in final states with b-jets and missing transverse momentum in $\sqrt{s} = 13$ TeV pp collisions with the ATLAS detector*, JHEP **05** (2021) 093, arXiv: 2101.12527 [hep-ex].

[171] G. Aad et al., *Search for squarks and gluinos in final states with one isolated lepton, jets, and missing transverse momentum at $\sqrt{s} = 13$ with the ATLAS detector*, Eur. Phys. J. C **81** (2021) 600, [Erratum: Eur.Phys.J.C 81, 956 (2021)], arXiv: 2101.01629 [hep-ex].

[172] G. Aad et al., *Search for new phenomena with top quark pairs in final states with one lepton, jets, and missing transverse momentum in pp collisions at $\sqrt{s}$ = 13 TeV with the ATLAS detector*, JHEP **04** (2021) 174, arXiv: 2012.03799 [hep-ex].

[173] G. Aad et al., *Search for squarks and gluinos in final states with jets and missing transverse momentum using 139 fb^{-1} of $\sqrt{s}$ =13 TeV pp collision data with the ATLAS detector*, JHEP **02** (2021) 143, arXiv: 2010.14293 [hep-ex].

[174] G. Aad et al., *Search for new phenomena in final states with large jet multiplicities and missing transverse momentum using $\sqrt{s}$ = 13 TeV proton-proton collisions recorded by ATLAS in Run 2 of the LHC*, JHEP **10** (2020) 062, arXiv: 2008.06032 [hep-ex].

[175] G. Aad et al., *Search for a scalar partner of the top quark in the all-hadronic $t\bar{t}$ plus missing transverse momentum final state at $\sqrt{s} = 13$ TeV with the ATLAS detector*, Eur. Phys. J. C **80** (2020) 737, arXiv: 2004.14060 [hep-ex].

[176] G. Aad et al., *Search for squarks and gluinos in final states with same-sign leptons and jets using 139 fb^{-1} of data collected with the ATLAS detector*, JHEP **06** (2020) 046, arXiv: 1909.08457 [hep-ex].

[177] G. Aad et al., *Search for bottom-squark pair production with the ATLAS detector in final states containing Higgs bosons, b-jets and missing transverse momentum*, JHEP **12** (2019) 060, arXiv: 1908.03122 [hep-ex].

[178] A. Tumasyan et al., *Search for higgsinos decaying to two Higgs bosons and missing transverse momentum in proton-proton collisions at $\sqrt{s}$ = 13 TeV*, JHEP **05** (2022) 014, arXiv: 2201.04206 [hep-ex].

[179] A. Tumasyan et al., *Combined searches for the production of supersymmetric top quark partners in proton–proton collisions at $\sqrt{s} = 13$ TeV*, Eur. Phys. J. C **81** (2021) 970, arXiv: 2107.10892 [hep-ex].

[180] A. Tumasyan et al., *Search for supersymmetry in final states with two or three soft leptons and missing transverse momentum in proton-proton collisions at $\sqrt{s}$ = 13 TeV*, JHEP **04** (2022) 091, arXiv: 2111.06296 [hep-ex].

[181] A. M. Sirunyan et al., *Search for supersymmetry in final states with two oppositely charged same-flavor leptons and missing transverse momentum in proton-proton collisions at $\sqrt{s}$ = 13 TeV*, JHEP **04** (2021) 123, arXiv: 2012.08600 [hep-ex].

[182] A. M. Sirunyan et al., *Search for physics beyond the standard model in events with jets and two same-sign or at least three charged leptons in proton-proton collisions at $\sqrt{s}$ = 13 TeV*, Eur. Phys. J. C **80** (2020) 752, arXiv: 2001.10086 [hep-ex].

[183] A. M. Sirunyan et al., *Search for supersymmetry in proton-proton collisions at $\sqrt{s}$ = 13 TeV in events with high-momentum Z bosons and missing transverse momentum*, JHEP **09** (2020) 149, arXiv: 2008.04422 [hep-ex].

[184] A. M. Sirunyan et al., *Search for supersymmetry in pp collisions at $\sqrt{s}$ = 13 TeV with 137 fb^{-1} in final states with a single lepton using the sum of masses of large-radius jets*, Phys. Rev. D **101** (2020) 052010, arXiv: 1911.07558 [hep-ex].

[185] A. M. Sirunyan et al., *Search for top squark pair production in a final state with two tau leptons in proton-proton collisions at $\sqrt{s}$ = 13 TeV*, JHEP **02** (2020) 015, arXiv: 1910.12932 [hep-ex].

[186] A. M. Sirunyan et al., *Searches for physics beyond the standard model with the M_{T2} variable in hadronic final states with and without disappearing tracks in proton-proton collisions at $\sqrt{s}$ = 13 TeV*, Eur. Phys. J. C **80** (2020) 3, arXiv: 1909.03460 [hep-ex].

[187] A. M. Sirunyan and other, *Search for supersymmetry in proton-proton collisions at 13 TeV in final states with jets and missing transverse momentum*, JHEP **10** (2019) 244, arXiv: 1908.04722 [hep-ex].

[188] *Search for supersymmetry in final states with a single electron or muon using angular correlations and heavy-object identification in proton-proton collisions at $\sqrt{s}$ = 13 TeV*, (2022), Submitted to JHEP, arXiv: 2211.08476 [hep-ex].

[189] *Search for direct pair production of sleptons and charginos decaying to two leptons and neutralinos with mass splittings near the W-boson mass in $\sqrt{s} = 13$ TeV pp collisions with the ATLAS detector*, (2022), arXiv: 2209.13935 [hep-ex].

[190] G. Aad et al.,
Search for chargino–neutralino pair production in final states with three leptons and missing transverse momentum in $\sqrt{s} = 13$ TeV pp collisions with the ATLAS detector,
Eur. Phys. J. C **81** (2021) 1118, arXiv: 2106.01676 [hep-ex].

[191] G. Aad et al.,
Search for chargino-neutralino production with mass splittings near the electroweak scale in three-lepton final states in $\sqrt{s}$=13 TeV pp collisions with the ATLAS detector,
Phys. Rev. D **101** (2020) 072001, arXiv: 1912.08479 [hep-ex].

[192] G. Aad et al., *Searches for electroweak production of supersymmetric particles with compressed mass spectra in $\sqrt{s} = 13$ TeV pp collisions with the ATLAS detector*,
Phys. Rev. D **101** (2020) 052005, arXiv: 1911.12606 [hep-ex].

[193] G. Aad et al., *Search for direct stau production in events with two hadronic τ-leptons in $\sqrt{s} = 13$ TeV pp collisions with the ATLAS detector*,
Phys. Rev. D **101** (2020) 032009, arXiv: 1911.06660 [hep-ex].

[194] G. Aad et al., *Search for direct production of electroweakinos in final states with one lepton, missing transverse momentum and a Higgs boson decaying into two b-jets in pp collisions at $\sqrt{s} = 13$ TeV with the ATLAS detector*,
Eur. Phys. J. C **80** (2020) 691, arXiv: 1909.09226 [hep-ex].

[195] A. Tumasyan et al., *Search for electroweak production of charginos and neutralinos in proton-proton collisions at $\sqrt{s} = 13$ TeV*, JHEP **04** (2022) 147,
arXiv: 2106.14246 [hep-ex].

[196] A. M. Sirunyan et al., *Search for electroweak production of charginos and neutralinos in multilepton final states in proton-proton collisions at $\sqrt{s} = 13$ TeV*,
JHEP **03** (2018) 166, arXiv: 1709.05406 [hep-ex].

[197] A. Tumasyan et al., *Search for chargino-neutralino production in events with Higgs and W bosons using 137 fb^{-1} of proton-proton collisions at $\sqrt{s} = 13$ TeV*,
JHEP **10** (2021) 045, arXiv: 2107.12553 [hep-ex].

[198] A. M. Sirunyan et al., *Search for supersymmetric partners of electrons and muons in proton-proton collisions at $\sqrt{s} = 13$ TeV*, Phys. Lett. B **790** (2019) 140,
arXiv: 1806.05264 [hep-ex].

[199] *Search for direct pair production of supersymmetric partners of τ leptons in the final state with two hadronically decaying τ leptons and missing transverse momentum in proton-proton collisions at $\sqrt{s} = 13$ TeV*,
(2022), Accepted for publication in Phys. Rev. D, arXiv: 2207.02254 [hep-ex].

[200] A. M. Sirunyan et al., *Search for Supersymmetry with a Compressed Mass Spectrum in Events with a Soft τ Lepton, a Highly Energetic Jet, and Large Missing Transverse Momentum in Proton-Proton Collisions at $\sqrt{s} =$ TeV*,
Phys. Rev. Lett. **124** (2020) 041803, arXiv: 1910.01185 [hep-ex].

[201] A. M. Sirunyan et al.,
Search for supersymmetry using Higgs boson to diphoton decays at $\sqrt{s} = 13$ TeV,
JHEP **11** (2019) 109, arXiv: 1908.08500 [hep-ex].

[202] A. Tumasyan et al., *Search for electroweak production of charginos and neutralinos at s=13TeV in final states containing hadronic decays of WW, WZ, or WH and missing transverse momentum*, Phys. Lett. B **842** (2023) 137460, arXiv: 2205.09597 [hep-ex].

[203] A. M. Sirunyan et al., *Search for direct pair production of supersymmetric partners to the τ lepton in proton-proton collisions at $\sqrt{s} = 13$ TeV*, Eur. Phys. J. C **80** (2020) 189, arXiv: 1907.13179 [hep-ex].

[204] G. Aad et al., *Search for R-parity-violating supersymmetry in a final state containing leptons and many jets with the ATLAS experiment using $\sqrt{s} = 13TeV$ proton–proton collision data*, Eur. Phys. J. C **81** (2021) 1023, arXiv: 2106.09609 [hep-ex].

[205] A. M. Sirunyan et al., *Search for top squarks in final states with two top quarks and several light-flavor jets in proton-proton collisions at $\sqrt{s} = 13$ TeV*, Phys. Rev. D **104** (2021) 032006, arXiv: 2102.06976 [hep-ex].

[206] H. K. Dreiner, M. Hanussek and C. Luhn, *What is the discrete gauge symmetry of the R-parity violating MSSM?*, Phys. Rev. D **86** (2012) 055012, arXiv: 1206.6305 [hep-ph].

[207] H. K. Dreiner, M. Kramer and J. Tattersall, *How low can SUSY go? Matching, monojets and compressed spectra*, EPL **99** (2012) 61001, arXiv: 1207.1613 [hep-ph].

[208] F. de Campos et al., *Probing bilinear R-parity violating supergravity at the LHC*, JHEP **05** (2008) 048, arXiv: 0712.2156 [hep-ph].

[209] L. Lee, C. Ohm, A. Soffer and T.-T. Yu, *Collider Searches for Long-Lived Particles Beyond the Standard Model*, Prog. Part. Nucl. Phys. **106** (2019) 210, [Erratum: Prog.Part.Nucl.Phys. 122, 103912 (2022)], arXiv: 1810.12602 [hep-ph].

[210] J. Alimena et al., *Searching for long-lived particles beyond the Standard Model at the Large Hadron Collider*, J. Phys. G **47** (2020) 090501, arXiv: 1903.04497 [hep-ex].

[211] D. Acosta et al., *Review of opportunities for new long-lived particle triggers in Run 3 of the Large Hadron Collider*, (2021), ed. by J. Alimena et al., arXiv: 2110.14675 [hep-ex].

[212] *Search for long-lived, massive particles in events with displaced vertices and multiple jets in pp collisions at $\sqrt{s} = 13$ TeV with the ATLAS detector*, (2023), arXiv: 2301.13866 [hep-ex].

[213] G. Aad et al., *Search for Displaced Leptons in $\sqrt{s} = 13$ TeV pp Collisions with the ATLAS Detector*, Phys. Rev. Lett. **127** (2021) 051802, arXiv: 2011.07812 [hep-ex].

[214] G. Aad et al., *Search for long-lived, massive particles in events with a displaced vertex and a muon with large impact parameter in pp collisions at $\sqrt{s} = 13$ TeV with the ATLAS detector*, Phys. Rev. D **102** (2020) 032006, arXiv: 2003.11956 [hep-ex].

[215] A. M. Sirunyan et al., *Search for long-lived particles using displaced jets in proton-proton collisions at $\sqrt{s} = 13$ TeV*, Phys. Rev. D **104** (2021) 012015, arXiv: 2012.01581 [hep-ex].

[216] A. Tumasyan et al., *Search for long-lived particles decaying to leptons with large impact parameter in proton–proton collisions at $\sqrt{s} = 13$ TeV*, Eur. Phys. J. C **82** (2022) 153, arXiv: 2110.04809 [hep-ex].

[217] A. Tumasyan et al., *Search for long-lived particles decaying into muon pairs in proton-proton collisions at $\sqrt{s} = 13$ TeV collected with a dedicated high-rate data stream*, JHEP **04** (2022) 062, arXiv: 2112.13769 [hep-ex].

[218] A. Tumasyan et al., *Search for long-lived particles decaying to a pair of muons in proton-proton collisions at $\sqrt{s} = 13$ TeV*, JHEP **05** (2023) 228, arXiv: 2205.08582 [hep-ex].

[219] *Search for long-lived particles using out-of-time trackless jets in proton-proton collisions at $\sqrt{s} = 13$ TeV*, (2022), Accepted for publication in JHEP, arXiv: 2212.06695 [hep-ex].

[220] A. M. Sirunyan et al., *Search for long-lived particles decaying to jets with displaced vertices in proton-proton collisions at $\sqrt{s} = 13$ TeV*, Phys. Rev. D **104** (2021) 052011, arXiv: 2104.13474 [hep-ex].

[221] S. Dimopoulos, R. Esmailzadeh, L. J. Hall and G. D. Starkman, *Cross-Sections for Lepton and Baryon Number Violating Processes from Supersymmetry at p anti-p Colliders*, Phys. Rev. D **41** (1990) 2099.

[222] H. K. Dreiner, P. Richardson and M. H. Seymour, *Resonant slepton production in hadron hadron collisions*, Phys. Rev. D **63** (2001) 055008, arXiv: hep-ph/0007228.

[223] H. K. Dreiner and T. Stefaniak, *Bounds on R-parity Violation from Resonant Slepton Production at the LHC*, Phys. Rev. D **86** (2012) 055010, arXiv: 1201.5014 [hep-ph].

[224] A. Monteux, *New signatures and limits on R-parity violation from resonant squark production*, JHEP **03** (2016) 216, arXiv: 1601.03737 [hep-ph].

[225] J. de Vries, H. K. Dreiner and D. Schmeier, *R-Parity Violation and Light Neutralinos at SHiP and the LHC*, Phys. Rev. D **94** (2016) 035006, arXiv: 1511.07436 [hep-ph].

[226] H. K. Dreiner, J. Y. Günther and Z. S. Wang, *R-parity violation and light neutralinos at ANUBIS and MAPP*, Phys. Rev. D **103** (2021) 075013, arXiv: 2008.07539 [hep-ph].

[227] H. K. Dreiner, D. Köhler, S. Nangia and Z. S. Wang, *Searching for a single photon from lightest neutralino decays in R-parity-violating supersymmetry at FASER*, JHEP **02** (2023) 120, arXiv: 2207.05100 [hep-ph].

[228] J. R. Ellis, G. B. Gelmini, J. L. Lopez, D. V. Nanopoulos and S. Sarkar, *Astrophysical constraints on massive unstable neutral relic particles*, Nucl. Phys. B **373** (1992) 399.

[229] H. K. Dreiner, F. Staub, A. Vicente and W. Porod, *General MSSM signatures at the LHC with and without R-parity*, Phys. Rev. D **86** (2012) 035021, arXiv: 1205.0557 [hep-ph].

[230] P. Konar, K. T. Matchev, M. Park and G. K. Sarangi, *How to look for supersymmetry under the lamppost at the LHC*, Phys. Rev. Lett. **105** (2010) 221801, arXiv: 1008.2483 [hep-ph].

[231] A. M. Sirunyan et al., *Search for new physics in events with two soft oppositely charged leptons and missing transverse momentum in proton-proton collisions at $\sqrt{s} = 13$ TeV*, Phys. Lett. B **782** (2018) 440, arXiv: 1801.01846 [hep-ex].

[232] G. Aad et al., *Search for electroweak production of charginos and sleptons decaying into final states with two leptons and missing transverse momentum in $\sqrt{s} = 13$ TeV pp collisions using the ATLAS detector*, Eur. Phys. J. C **80** (2020) 123, arXiv: 1908.08215 [hep-ex].

[233] S. Chatrchyan et al., *Search for Top Squarks in R-Parity-Violating Supersymmetry using Three or More Leptons and B-Tagged Jets*, Phys. Rev. Lett. **111** (2013) 221801, arXiv: 1306.6643 [hep-ex].

[234] A. M. Sirunyan et al., *Search for physics beyond the standard model in multilepton final states in proton-proton collisions at $\sqrt{s} = 13$ TeV*, JHEP **03** (2020) 051, arXiv: 1911.04968 [hep-ex].

[235] G. Aad et al., *Search for new phenomena in three- or four-lepton events in pp collisions at $\sqrt{s}$ =13 TeV with the ATLAS detector*, Phys. Lett. B **824** (2022) 136832, arXiv: 2107.00404 [hep-ex].

[236] M. Aaboud et al., *Search for lepton-flavor violation in different-flavor, high-mass final states in pp collisions at $\sqrt{s} = 13$ TeV with the ATLAS detector*, Phys. Rev. D **98** (2018) 092008, arXiv: 1807.06573 [hep-ex].

[237] G. Aad et al., *Search for type-III seesaw heavy leptons in leptonic final states in pp collisions at $\sqrt{s} = 13$ TeV with the ATLAS detector*, (2022), arXiv: 2202.02039 [hep-ex].

[238] G. Aad et al., *Search for heavy Higgs bosons decaying into two tau leptons with the ATLAS detector using pp collisions at $\sqrt{s} = 13$ TeV*, Phys. Rev. Lett. **125** (2020) 051801, arXiv: 2002.12223 [hep-ex].

[239] V. Khachatryan et al., *Searches for R-parity-violating supersymmetry in ppcollisions at $\sqrt{s} = 8$ TeV in final states with 0-4 leptons*, Phys. Rev. D **94** (2016) 112009, arXiv: 1606.08076 [hep-ex].

[240] G. Aad et al., *Search for supersymmetry in events with four or more charged leptons in 139 fb^{-1} of $\sqrt{s} = 13$ TeV pp collisions with the ATLAS detector*, JHEP **07** (2021) 167, arXiv: 2103.11684 [hep-ex].

[241] A. M. Sirunyan et al., *Search for pair-produced resonances decaying to quark pairs in proton-proton collisions at $\sqrt{s} = 13$ TeV*, Phys. Rev. D **98** (2018) 112014, arXiv: 1808.03124 [hep-ex].

[242] *Search for resonant and nonresonant production of pairs of dijet resonances in proton-proton collisions at $\sqrt{s} = 13$ TeV*, (2022), Accepted for publication in JHEP, arXiv: 2206.09997 [hep-ex].

[243] M. Aaboud et al., *A search for pair-produced resonances in four-jet final states at $\sqrt{s} = 13$ TeV with the ATLAS detector*, Eur. Phys. J. C **78** (2018) 250, arXiv: 1710.07171 [hep-ex].

[244] M. Aaboud et al., *Search for R-parity-violating supersymmetric particles in multi-jet final states produced in p-p collisions at $\sqrt{s} = 13$ TeV using the ATLAS detector at the LHC*, Phys. Lett. B **785** (2018) 136, arXiv: 1804.03568 [hep-ex].

[245] A. M. Sirunyan et al., *Search for pair-produced three-jet resonances in proton-proton collisions at $\sqrt{s}$ =13 TeV*, Phys. Rev. D **99** (2019) 012010, arXiv: 1810.10092 [hep-ex].

[246] G. Aad et al., *Search for phenomena beyond the Standard Model in events with large b-jet multiplicity using the ATLAS detector at the LHC*, Eur. Phys. J. C **81** (2021) 11, [Erratum: Eur.Phys.J.C 81, 249 (2021)], arXiv: 2010.01015 [hep-ex].

[247] A. M. Sirunyan et al., *Search for pair-produced resonances each decaying into at least four quarks in proton-proton collisions at $\sqrt{s} = 13$ TeV*, Phys. Rev. Lett. **121** (2018) 141802, arXiv: 1806.01058 [hep-ex].

[248] V. Khachatryan et al., *Search for new phenomena in events with high jet multiplicity and low missing transverse momentum in proton–proton collisions at $\sqrt{s} = 8$ TeV*, Phys. Lett. B **770** (2017) 257, arXiv: 1608.01224 [hep-ex].

[249] A. M. Sirunyan et al., *Search for R-parity violating supersymmetry in pp collisions at $\sqrt{s} = 13$ TeV using b jets in a final state with a single lepton, many jets, and high sum of large-radius jet masses*, Phys. Lett. B **783** (2018) 114, arXiv: 1712.08920 [hep-ex].

[250] *Search for pair-produced vector-like leptons in final states with third-generation leptons and at least three b quark jets in proton-proton collisions at $\sqrt{s} = 13$ TeV*, (2022), Accepted for publication in Phys. Lett. B, arXiv: 2208.09700 [hep-ex].

[251] V. Khachatryan et al., *Search for R-parity violating decays of a top squark in proton-proton collisions at $\sqrt{s} = 8$ TeV*, Phys. Lett. B **760** (2016) 178, arXiv: 1602.04334 [hep-ex].

[252] *Search for direct production of electroweakinos in final states with one lepton, jets and missing transverse momentum and in p p collisions at $\sqrt{s} = 13$ TeV with the ATLAS detector*, tech. rep., All figures including auxiliary figures are available at https://atlas.web.cern.ch/Atlas/GROUPS/PHYSICS/CONFNOTES/ATLAS-CONF-2022-059: CERN, 2022, URL: https://cds.cern.ch/record/2826702.

[253] A. M. Sirunyan et al., *Search for singly and pair-produced leptoquarks coupling to third-generation fermions in proton-proton collisions at s=13 TeV*, Phys. Lett. B **819** (2021) 136446, arXiv: 2012.04178 [hep-ex].

[254] *Search for direct production of winos and higgsinos in events with two same-sign or three leptons in pp collision data at $\sqrt{s} = 13$ TeV with the ATLAS detector*, tech. rep., All figures including auxiliary figures are available at https://atlas.web.cern.ch/Atlas/GROUPS/PHYSICS/CONFNOTES/ATLAS-CONF-2022-057: CERN, 2022, URL: https://cds.cern.ch/record/2826603.

[255] M. Aaboud et al., *Search for B-L R -parity-violating top squarks in $\sqrt{s}$ =13 TeV pp collisions with the ATLAS experiment*, Phys. Rev. D **97** (2018) 032003, arXiv: 1710.05544 [hep-ex].

[256] *Search for pair-produced scalar and vector leptoquarks decaying into third-generation quarks and first- or second-generation leptons in pp collisions with the ATLAS detector*, (2022), arXiv: 2210.04517 [hep-ex].

[257] G. Aad et al., *Search for pair production of scalar leptoquarks decaying into first- or second-generation leptons and top quarks in proton–proton collisions at $\sqrt{s}$ = 13 TeV with the ATLAS detector*, Eur. Phys. J. C **81** (2021) 313, arXiv: 2010.02098 [hep-ex].

[258] A. M. Sirunyan et al., *Search for an excited lepton that decays via a contact interaction to a lepton and two jets in proton-proton collisions at $\sqrt{s}$ = 13 TeV*, JHEP **05** (2020) 052, arXiv: 2001.04521 [hep-ex].

[259] *Search for pair production of squarks or gluinos decaying via sleptons or weak bosons in final states with two same-sign or three leptons with the ATLAS detector*, tech. rep., All figures including auxiliary figures are available at https://atlas.web.cern.ch/Atlas/GROUPS/PHYSICS/CONFNOTES/ATLAS-CONF-2023-017: CERN, 2023, URL: https://cds.cern.ch/record/2855335.

[260] M. Aaboud et al., *Search for pair production of higgsinos in final states with at least three b-tagged jets in $\sqrt{s} = 13$ TeV pp collisions using the ATLAS detector*, Phys. Rev. D **98** (2018) 092002, arXiv: 1806.04030 [hep-ex].

[261] A. M. Sirunyan et al., *Search for Higgsino pair production in pp collisions at $\sqrt{s}$ = 13 TeV in final states with large missing transverse momentum and two Higgs bosons decaying via $H \to b\bar{b}$*, Phys. Rev. D **97** (2018) 032007, arXiv: 1709.04896 [hep-ex].

[262] J. Alwall et al., *The automated computation of tree-level and next-to-leading order differential cross sections, and their matching to parton shower simulations*, JHEP **07** (2014) 079, arXiv: 1405.0301 [hep-ph].

[263] T. Sjöstrand et al., *An introduction to PYTHIA 8.2*, Comput. Phys. Commun. **191** (2015) 159, arXiv: 1410.3012 [hep-ph].

[264] https://feynrules.irmp.ucl.ac.be/wiki/RPVMSSM, accessed 2021-12-01.

[265] D. Dercks et al., *CheckMATE 2: From the model to the limit*, Comput. Phys. Commun. **221** (2017) 383, arXiv: 1611.09856 [hep-ph].

[266] M. Cacciari, G. P. Salam and G. Soyez, *FastJet User Manual*, Eur. Phys. J. C **72** (2012) 1896, arXiv: 1111.6097 [hep-ph].

[267] M. Cacciari and G. P. Salam, *Dispelling the N^3 myth for the k_t jet-finder*, Phys. Lett. B **641** (2006) 57, arXiv: hep-ph/0512210.

[268] M. Cacciari, G. P. Salam and G. Soyez, *The anti-k_t jet clustering algorithm*, JHEP **04** (2008) 063, arXiv: 0802.1189 [hep-ph].

[269] A. L. Read, *Presentation of search results: The CL(s) technique*, J. Phys. G **28** (2002) 2693, ed. by M. R. Whalley and L. Lyons.

[270] https://checkmate.hepforge.org/, accessed 2022-12-01.

[271] J. de Favereau et al., *DELPHES 3, A modular framework for fast simulation of a generic collider experiment*, JHEP **02** (2014) 057, arXiv: 1307.6346 [hep-ex].

[272] M. Aaboud et al., *Search for supersymmetry in final states with two same-sign or three leptons and jets using 36 fb^{-1} of $\sqrt{s} = 13$ TeV pp collision data with the ATLAS detector*, JHEP **09** (2017) 084, [Erratum: JHEP 08, 121 (2019)], arXiv: 1706.03731 [hep-ex].

[273] C. Borschensky et al., *Squark and gluino production cross sections in pp collisions at $\sqrt{s}$ = 13, 14, 33 and 100 TeV*, Eur. Phys. J. C **74** (2014) 3174, arXiv: 1407.5066 [hep-ph].

[274] S. Bornhauser, M. Drees, H. K. Dreiner and J. S. Kim, *Electroweak contributions to squark pair production at the LHC*, Phys. Rev. D **76** (2007) 095020, arXiv: 0709.2544 [hep-ph].

[275] F. Kling and S. Trojanowski, *Forward experiment sensitivity estimator for the LHC and future hadron colliders*, Phys. Rev. D **104** (2021) 035012, arXiv: 2105.07077 [hep-ph].

[276] P. Ilten, J. Thaler, M. Williams and W. Xue, *Dark photons from charm mesons at LHCb*, Phys. Rev. D **92** (2015) 115017, arXiv: 1509.06765 [hep-ph].

[277] G. Aad et al., *Search for a light Higgs boson decaying to long-lived weakly-interacting particles in proton-proton collisions at $\sqrt{s} = 7$ TeV with the ATLAS detector*, Phys. Rev. Lett. **108** (2012) 251801, arXiv: 1203.1303 [hep-ex].

[278] S. Chatrchyan et al., *Search in Leptonic Channels for Heavy Resonances Decaying to Long-Lived Neutral Particles*, JHEP **02** (2013) 085, arXiv: 1211.2472 [hep-ex].

[279] *The High-Luminosity LHC*, (2015), URL: https://cds.cern.ch/record/2114693.

[280] J. L. Feng, I. Galon, F. Kling and S. Trojanowski, *ForwArd Search ExpeRiment at the LHC*, Phys. Rev. D **97** (2018) 035001, arXiv: 1708.09389 [hep-ph].

[281] A. Ariga et al., *FASER's physics reach for long-lived particles*, Phys. Rev. D **99** (2019) 095011, arXiv: 1811.12522 [hep-ph].

[282] S. Cerci et al., *FACET: A new long-lived particle detector in the very forward region of the CMS experiment*, JHEP **2022** (2022) 110, arXiv: 2201.00019 [hep-ex].

[283] J. P. Chou, D. Curtin and H. J. Lubatti,
New Detectors to Explore the Lifetime Frontier, Phys. Lett. B **767** (2017) 29,
arXiv: 1606.06298 [hep-ph].

[284] D. Curtin et al.,
Long-Lived Particles at the Energy Frontier: The MATHUSLA Physics Case,
Rept. Prog. Phys. **82** (2019) 116201, arXiv: 1806.07396 [hep-ph].

[285] C. Alpigiani et al., *An Update to the Letter of Intent for MATHUSLA: Search for Long-Lived Particles at the HL-LHC*, (2020),
arXiv: 2009.01693 [physics.ins-det].

[286] V. V. Gligorov, S. Knapen, M. Papucci and D. J. Robinson,
Searching for Long-lived Particles: A Compact Detector for Exotics at LHCb,
Phys. Rev. D **97** (2018) 015023, arXiv: 1708.09395 [hep-ph].

[287] M. Bauer, O. Brandt, L. Lee and C. Ohm,
ANUBIS: Proposal to search for long-lived neutral particles in CERN service shafts,
(2019), arXiv: 1909.13022 [physics.ins-det].

[288] V. Mitsou, *MoEDAL, MAPP and future endeavours*,
PoS **DISCRETE2020-2021** (2022) 017.

[289] P. F. de Salas et al., *2020 global reassessment of the neutrino oscillation picture*,
JHEP **02** (2021) 071, arXiv: 2006.11237 [hep-ph].

[290] F. Capozzi et al., *Global constraints on absolute neutrino masses and their ordering*,
Phys. Rev. D **95** (2017) 096014, [Addendum: Phys.Rev.D 101, 116013 (2020)],
arXiv: 2003.08511 [hep-ph].

[291] G. Aad et al., *The ATLAS Experiment at the CERN Large Hadron Collider*,
JINST **3** (2008) S08003.

[292] S. Chatrchyan et al., *The CMS Experiment at the CERN LHC*,
JINST **3** (2008) S08004.

[293] G. F. Giudice and R. Rattazzi, *Theories with gauge mediated supersymmetry breaking*,
Phys. Rept. **322** (1999) 419, arXiv: hep-ph/9801271.

[294] J. L. Feng, M. Kamionkowski and S. K. Lee,
Light Gravitinos at Colliders and Implications for Cosmology,
Phys. Rev. D **82** (2010) 015012, arXiv: 1004.4213 [hep-ph].

[295] S. Knapen and D. Redigolo, *Gauge mediation at the LHC: status and prospects*,
JHEP **01** (2017) 135, arXiv: 1606.07501 [hep-ph].

[296] J. S. Kim, M. E. Krauss and V. Martin-Lozano,
Probing the Electroweakino Sector of General Gauge Mediation at the LHC,
Phys. Lett. B **783** (2018) 150, arXiv: 1705.06497 [hep-ph].

[297] J. S. Kim, S. Pokorski, K. Rolbiecki and K. Sakurai,
Gravitino vs Neutralino LSP at the LHC, JHEP **09** (2019) 082,
arXiv: 1905.05648 [hep-ph].

[298] V. M. Abazov et al.,
Search for supersymmetry with gauge-mediated breaking in diphoton events at D0,
Phys. Rev. Lett. **94** (2005) 041801, arXiv: hep-ex/0408146.

[299] T. Aaltonen et al., *Signature-Based Search for Delayed Photons in Exclusive Photon Plus Missing Transverse Energy Events from $p\bar{p}$ Collisions with $\sqrt{s}$=1.96 TeV*,
Phys. Rev. D **88** (2013) 031103, arXiv: 1307.0474 [hep-ex].

[300] M. Aaboud et al., *Search for photonic signatures of gauge-mediated supersymmetry in 13 TeV pp collisions with the ATLAS detector*, Phys. Rev. D **97** (2018) 092006,
arXiv: 1802.03158 [hep-ex].

[301] A. M. Sirunyan et al., *Search for long-lived particles using delayed photons in proton-proton collisions at $\sqrt{s}$ = 13 TeV*, Phys. Rev. D **100** (2019) 112003,
arXiv: 1909.06166 [hep-ex].

[302] T. Appelquist, H.-C. Cheng and B. A. Dobrescu,
Bounds on universal extra dimensions, Phys. Rev. D **64** (2001) 035002,
arXiv: hep-ph/0012100.

[303] R. N. Mohapatra, *Supersymmetry and R-parity: an Overview*,
Phys. Scripta **90** (2015) 088004, arXiv: 1503.06478 [hep-ph].

[304] S. Trifinopoulos, *B -physics anomalies: The bridge between R -parity violating supersymmetry and flavored dark matter*, Phys. Rev. D **100** (2019) 115022,
arXiv: 1904.12940 [hep-ph].

[305] Q.-Y. Hu, Y.-D. Yang and M.-D. Zheng,
Revisiting the B-physics anomalies in R-parity violating MSSM,
Eur. Phys. J. C **80** (2020) 365, arXiv: 2002.09875 [hep-ph].

[306] Q.-Y. Hu and L.-L. Huang,
Explaining $b \to s\ell^+\ell^-$ data by sneutrinos in the R -parity violating MSSM,
Phys. Rev. D **101** (2020) 035030, arXiv: 1912.03676 [hep-ph].

[307] M.-D. Zheng and H.-H. Zhang, *Studying the $b \to s\ell^+\ell^-$ Anomalies and $(g-2)_\mu$ in RPV-MSSM Framework with Inverse Seesaw*, (2021), arXiv: 2105.06954 [hep-ph].

[308] W. Altmannshofer, P. S. B. Dev, A. Soni and Y. Sui,
Addressing $R_{D^{(*)}}$, $R_{K^{(*)}}$, muon $g-2$ and ANITA anomalies in a minimal R-parity violating supersymmetric framework, Phys. Rev. D **102** (2020) 015031,
arXiv: 2002.12910 [hep-ph].

[309] P. S. Bhupal Dev, A. Soni and F. Xu,
Hints of Natural Supersymmetry in Flavor Anomalies?, (2021),
arXiv: 2106.15647 [hep-ph].

[310] J. H. Collins, P. S. Bhupal Dev and Y. Sui,
R-parity Violating Supersymmetric Explanation of the Anomalous Events at ANITA,
Phys. Rev. D **99** (2019) 043009, arXiv: 1810.08479 [hep-ph].

[311] P. D. Bolton, F. F. Deppisch and P. S. B. Dev, *Neutrinoless double beta decay via light neutralinos in R-parity violating supersymmetry*, JHEP **03** (2022) 152,
arXiv: 2112.12658 [hep-ph].

[312] A. Filimonova, R. Schäfer and S. Westhoff,
Probing dark sectors with long-lived particles at BELLE II,
Phys. Rev. D **101** (2020) 095006, arXiv: 1911.03490 [hep-ph].

[313] J. L. Feng et al., *The Forward Physics Facility at the High-Luminosity LHC*, (2022),
arXiv: 2203.05090 [hep-ex].

[314] R. Schäfer, F. Tillinger and S. Westhoff, *Near or Far Detectors? Optimizing Long-Lived Particle Searches at Electron-Positron Colliders*, (2022),
arXiv: 2202.11714 [hep-ph].

[315] J. L. Feng, I. Galon, F. Kling and S. Trojanowski,
Axionlike particles at FASER: The LHC as a photon beam dump,
Phys. Rev. D **98** (2018) 055021, arXiv: 1806.02348 [hep-ph].

[316] A. Berlin and F. Kling, *Inelastic Dark Matter at the LHC Lifetime Frontier: ATLAS, CMS, LHCb, CODEX-b, FASER, and MATHUSLA*, Phys. Rev. D **99** (2019) 015021,
arXiv: 1810.01879 [hep-ph].

[317] L. A. Anchordoqui et al.,
The Forward Physics Facility: Sites, Experiments, and Physics Potential, (2021),
arXiv: 2109.10905 [hep-ph].

[318] S. Foroughi-Abari, F. Kling and Y.-D. Tsai,
Looking forward to millicharged dark sectors at the LHC,
Phys. Rev. D **104** (2021) 035014, arXiv: 2010.07941 [hep-ph].

[319] B. Batell, J. L. Feng and S. Trojanowski, *Detecting Dark Matter with Far-Forward Emulsion and Liquid Argon Detectors at the LHC*, Phys. Rev. D **103** (2021) 075023,
arXiv: 2101.10338 [hep-ph].

[320] D. Gorbunov and I. Timiryasov, *Decaying light particles in the SHiP experiment. II. Signal rate estimates for light neutralinos*, Phys. Rev. D **92** (2015) 075015,
arXiv: 1508.01780 [hep-ph].

[321] J. C. Helo, M. Hirsch and Z. S. Wang,
Heavy neutral fermions at the high-luminosity LHC, JHEP **07** (2018) 056,
arXiv: 1803.02212 [hep-ph].

[322] D. Dercks, J. De Vries, H. K. Dreiner and Z. S. Wang,
R-parity Violation and Light Neutralinos at CODEX-b, FASER, and MATHUSLA,
Phys. Rev. D **99** (2019) 055039, arXiv: 1810.03617 [hep-ph].

[323] D. Dercks, H. K. Dreiner, M. Hirsch and Z. S. Wang, *Long-Lived Fermions at AL3X*,
Phys. Rev. D **99** (2019) 055020, arXiv: 1811.01995 [hep-ph].

[324] S. Dey et al., *Long-lived light neutralinos at Belle II*, JHEP **02** (2021) 211,
arXiv: 2012.00438 [hep-ph].

[325] P. Candia, G. Cottin, A. Méndez and V. Muñoz,
Searching for light long-lived neutralinos at Super-Kamiokande,
Phys. Rev. D **104** (2021) 055024, arXiv: 2107.02804 [hep-ph].

[326] Z. S. Wang and K. Wang, *Long-lived light neutralinos at future $Z-$factories*,
Phys. Rev. D **101** (2020) 115018, arXiv: 1904.10661 [hep-ph].

[327] Z. S. Wang and K. Wang, *Physics with far detectors at future lepton colliders*, Phys. Rev. D **101** (2020) 075046, arXiv: 1911.06576 [hep-ph].

[328] F. Domingo and H. K. Dreiner, *Decays of a bino-like particle in the low-mass regime*, (2022), arXiv: 2205.08141 [hep-ph].

[329] O. Fischer, Á. Hernández-Cabezudo and T. Schwetz, *Explaining the MiniBooNE excess by a decaying sterile neutrino with mass in the 250 MeV range*, Phys. Rev. D **101** (2020) 075045, arXiv: 1909.09561 [hep-ph].

[330] V. Brdar, O. Fischer and A. Y. Smirnov, *Model-independent bounds on the nonoscillatory explanations of the MiniBooNE excess*, Phys. Rev. D **103** (2021) 075008, arXiv: 2007.14411 [hep-ph].

[331] P. Abratenko et al., *Search for an Excess of Electron Neutrino Interactions in MicroBooNE Using Multiple Final State Topologies*, (2021), arXiv: 2110.14054 [hep-ex].

[332] C. Giunti, A. Ioannisian and G. Ranucci, *A new analysis of the MiniBooNE low-energy excess*, JHEP **11** (2020) 146, [Erratum: JHEP 02, 078 (2021)], arXiv: 1912.01524 [hep-ph].

[333] A. Ioannisian, *A Standard Model explanation for the excess of electron-like events in MiniBooNE*, (2019), arXiv: 1909.08571 [hep-ph].

[334] P. A. Zyla et al., *Review of Particle Physics*, PTEP **2020** (2020) 083C01.

[335] K. Desch, S. Fleischmann, P. Wienemann, H. K. Dreiner and S. Grab, *Stau as the Lightest Supersymmetric Particle in R-Parity Violating SUSY Models: Discovery Potential with Early LHC Data*, Phys. Rev. D **83** (2011) 015013, arXiv: 1008.1580 [hep-ph].

[336] G. Belanger, F. Boudjema, A. Cottrant, R. M. Godbole and A. Semenov, *The MSSM invisible Higgs in the light of dark matter and g-2*, Phys. Lett. B **519** (2001) 93, arXiv: hep-ph/0106275.

[337] D. Albornoz Vasquez, G. Belanger, C. Boehm, A. Pukhov and J. Silk, *Can neutralinos in the MSSM and NMSSM scenarios still be light?*, Phys. Rev. D **82** (2010) 115027, arXiv: 1009.4380 [hep-ph].

[338] R. Kumar Barman, G. Belanger and R. M. Godbole, *Status of low mass LSP in SUSY*, Eur. Phys. J. ST **229** (2020) 3159, arXiv: 2010.11674 [hep-ph].

[339] G. Aad et al., *Search for trilepton resonances from chargino and neutralino pair production in $\sqrt{s}$ = 13 TeV pp collisions with the ATLAS detector*, Phys. Rev. D **103** (2021) 112003, arXiv: 2011.10543 [hep-ex].

[340] S. Dawson, *R-Parity Breaking in Supersymmetric Theories*, Nucl. Phys. B **261** (1985) 297.

[341] H. E. Haber and D. Wyler, *RADIATIVE NEUTRALINO DECAY*, Nucl. Phys. B **323** (1989) 267.

[342] H. Abreu et al.,
Detecting and Studying High-Energy Collider Neutrinos with FASER at the LHC,
Eur. Phys. J. C **80** (2020) 61, arXiv: 1908.02310 [hep-ex].

[343] H. Abreu et al., *Technical Proposal: FASERnu*, (2020),
arXiv: 2001.03073 [physics.ins-det].

[344] K. Jodłowski and S. Trojanowski,
Neutrino beam-dump experiment with FASER at the LHC, JHEP **05** (2021) 191,
arXiv: 2011.04751 [hep-ph].

[345] H. Abreu et al., *The trigger and data acquisition system of the FASER experiment*,
(2021), arXiv: 2110.15186 [physics.ins-det].

[346] J. Boyd, *The FASER W-Si High Precision Preshower Technical Proposal*, tech. rep.,
CERN, 2022, URL: https://cds.cern.ch/record/2803084.

[347] C. Athanassopoulos et al.,
The Liquid scintillator neutrino detector and LAMPF neutrino source,
Nucl. Instrum. Meth. A **388** (1997) 149, arXiv: nucl-ex/9605002.

[348] R. Ball et al., *The neutrino beam dump experiment at Fermilab (E613)*,
eConf **C801002** (1980) 172, ed. by V. Barger and D. Cline.

[349] A. A. Aguilar-Arevalo et al., *The Neutrino Flux prediction at MiniBooNE*,
Phys. Rev. D **79** (2009) 072002, arXiv: 0806.1449 [hep-ex].

[350] J. D. Bjorken et al., *Search for Neutral Metastable Penetrating Particles Produced in the SLAC Beam Dump*, Phys. Rev. D **38** (1988) 3375.

[351] S. N. Gninenko, N. V. Krasnikov, M. M. Kirsanov and D. V. Kirpichnikov,
Missing energy signature from invisible decays of dark photons at the CERN SPS,
Phys. Rev. D **94** (2016) 095025, arXiv: 1604.08432 [hep-ph].

[352] S. N. Gninenko,
Search for MeV dark photons in a light-shining-through-walls experiment at CERN,
Phys. Rev. D **89** (2014) 075008, arXiv: 1308.6521 [hep-ph].

[353] D. Banerjee et al.,
Search for vector mediator of Dark Matter production in invisible decay mode,
Phys. Rev. D **97** (2018) 072002, arXiv: 1710.00971 [hep-ex].

[354] B. Aubert et al., *The BaBar detector*, Nucl. Instrum. Meth. A **479** (2002) 1,
arXiv: hep-ex/0105044.

[355] T. Abe et al., *Belle II Technical Design Report*, (2010),
arXiv: 1011.0352 [physics.ins-det].

[356] W. Altmannshofer et al., *The Belle II Physics Book*, PTEP **2019** (2019) 123C01,
ed. by E. Kou and P. Urquijo, [Erratum: PTEP 2020, 029201 (2020)],
arXiv: 1808.10567 [hep-ex].

[357] M. Daum et al.,
Search for Admixtures of Massive Neutrinos in the Decay $\pi^+ \to \mu^+$ Neutrino,
Phys. Rev. D **36** (1987) 2624.

[358] A. Aguilar-Arevalo et al., *Search for heavy neutrinos in $\pi \to \mu\nu$ decay*, Phys. Lett. B **798** (2019) 134980, arXiv: 1904.03269 [hep-ex].

[359] D. Gorbunov, I. Krasnov, Y. Kudenko and S. Suvorov, *Heavy Neutral Leptons from kaon decays in the SHiP experiment*, Phys. Lett. B **810** (2020) 135817, arXiv: 2004.07974 [hep-ph].

[360] T. Yamazaki et al., *Search for Heavy Neutrinos in Kaon Decay*, Conf. Proc. C **840719** (1984) 262, ed. by A. Meyer and E. Wieczorek.

[361] E. Cortina Gil et al., *Search for K^+ decays to a muon and invisible particles*, Phys. Lett. B **816** (2021) 136259, arXiv: 2101.12304 [hep-ex].

[362] J. L. Feng et al., "Planning the Future of U.S. Particle Physics (Snowmass 2013): Chapter 4: Cosmic Frontier", *Snowmass 2013: Snowmass on the Mississippi*, 2014, arXiv: 1401.6085 [hep-ex].

[363] J. L. Hewett et al., "Planning the Future of U.S. Particle Physics (Snowmass 2013): Chapter 2: Intensity Frontier", *Snowmass 2013: Snowmass on the Mississippi*, 2014, arXiv: 1401.6077 [hep-ex].

[364] J. Alexander et al., "Dark Sectors 2016 Workshop: Community Report", 2016, arXiv: 1608.08632 [hep-ph].

[365] M. Battaglieri et al., "US Cosmic Visions: New Ideas in Dark Matter 2017: Community Report", *U.S. Cosmic Visions: New Ideas in Dark Matter*, 2017, arXiv: 1707.04591 [hep-ph].

[366] J. Beacham et al., *Physics Beyond Colliders at CERN: Beyond the Standard Model Working Group Report*, J. Phys. G **47** (2020) 010501, arXiv: 1901.09966 [hep-ex].

[367] C. A. Argüelles et al., *New opportunities at the next-generation neutrino experiments I: BSM neutrino physics and dark matter*, Rept. Prog. Phys. **83** (2020) 124201, arXiv: 1907.08311 [hep-ph].

[368] R. K. Ellis et al., *Physics Briefing Book: Input for the European Strategy for Particle Physics Update 2020*, (2019), arXiv: 1910.11775 [hep-ex].

[369] P. Agrawal et al., *Feebly-interacting particles: FIPs 2020 workshop report*, Eur. Phys. J. C **81** (2021) 1015, arXiv: 2102.12143 [hep-ph].

[370] S. Knapen and S. Lowette, *A guide to hunting long-lived particles at the LHC*, (2022), arXiv: 2212.03883 [hep-ph].

[371] T. Asaka and M. Shaposhnikov, *The νMSM, dark matter and baryon asymmetry of the universe*, Phys. Lett. B **620** (2005) 17, arXiv: hep-ph/0505013.

[372] F. Capozzi et al., *Unfinished fabric of the three neutrino paradigm*, Phys. Rev. D **104** (2021) 083031, arXiv: 2107.00532 [hep-ph].

[373] T. Yanagida, *Horizontal gauge symmetry and masses of neutrinos*, Conf. Proc. C **7902131** (1979) 95, ed. by O. Sawada and A. Sugamoto.

[374] M. Gell-Mann, P. Ramond and R. Slansky, *Complex Spinors and Unified Theories*, Conf. Proc. C **790927** (1979) 315, arXiv: 1306.4669 [hep-th].

[375] R. N. Mohapatra and G. Senjanovic,
Neutrino Mass and Spontaneous Parity Nonconservation,
Phys. Rev. Lett. **44** (1980) 912.

[376] J. Schechter and J. W. F. Valle, *Neutrino Masses in SU(2) x U(1) Theories*,
Phys. Rev. D **22** (1980) 2227.

[377] E. K. Akhmedov, M. Lindner, E. Schnapka and J. W. F. Valle,
Left-right symmetry breaking in NJL approach, Phys. Lett. B **368** (1996) 270,
arXiv: hep-ph/9507275.

[378] E. K. Akhmedov, M. Lindner, E. Schnapka and J. W. F. Valle,
Dynamical left-right symmetry breaking, Phys. Rev. D **53** (1996) 2752,
arXiv: hep-ph/9509255.

[379] M. Malinsky, J. C. Romao and J. W. F. Valle,
Novel supersymmetric SO(10) seesaw mechanism, Phys. Rev. Lett. **95** (2005) 161801,
arXiv: hep-ph/0506296.

[380] R. N. Mohapatra and J. W. F. Valle,
Neutrino Mass and Baryon Number Nonconservation in Superstring Models,
Phys. Rev. D **34** (1986) 1642.

[381] M. C. Gonzalez-Garcia and J. W. F. Valle, *Fast Decaying Neutrinos and Observable Flavor Violation in a New Class of Majoron Models*, Phys. Lett. B **216** (1989) 360.

[382] HNL, "Heavy Neutrino Limits:
https://github.com/mhostert/Heavy-Neutrino-Limits".

[383] E. Fernández-Martínez, M. González-López, J. Hernández-García, M. Hostert and J. López-Pavón, *Effective portals to heavy neutral leptons*, (2023),
arXiv: 2304.06772 [hep-ph].

[384] G. Aad et al., *Search for long-lived charginos based on a disappearing-track signature using 136 fb^{-1} of pp collisions at $\sqrt{s}$ = 13 TeV with the ATLAS detector*,
Eur. Phys. J. C **82** (2022) 606, arXiv: 2201.02472 [hep-ex].

[385] A. M. Sirunyan et al.,
Search for disappearing tracks in proton-proton collisions at $\sqrt{s}$ = 13 TeV,
Phys. Lett. B **806** (2020) 135502, arXiv: 2004.05153 [hep-ex].

[386] I. Gogoladze, J. D. Lykken, C. Macesanu and S. Nandi,
Implications of a Massless Neutralino for Neutrino Physics,
Phys. Rev. D **68** (2003) 073004, arXiv: hep-ph/0211391.

[387] J. A. Grifols, E. Masso and S. Peris, *Photinos From Gravitational Collapse*,
Phys. Lett. B **220** (1989) 591.

[388] J. R. Ellis, K. A. Olive, S. Sarkar and D. W. Sciama,
Low Mass Photinos and Supernova SN1987A, Phys. Lett. B **215** (1988) 404.

[389] K. Lau, *Constraints on supersymmetry from SN1987A*, Phys. Rev. D **47** (1993) 1087.

[390] H. K. Dreiner, M. Kramer and B. O'Leary, *Bounds on R-parity violating supersymmetric couplings from leptonic and semi-leptonic meson decays*,
Phys. Rev. D **75** (2007) 114016, arXiv: hep-ph/0612278.

[391] S. Profumo, *Hunting the lightest lightest neutralinos*, Phys. Rev. D **78** (2008) 023507, arXiv: 0806.2150 [hep-ph].

[392] P. Bechtle et al., *Killing the cMSSM softly*, Eur. Phys. J. C **76** (2016) 96, arXiv: 1508.05951 [hep-ph].

[393] H. K. Dreiner et al., *The ABC of RPV: classification of R-parity violating signatures at the LHC for small couplings*, JHEP **07** (2023) 215, arXiv: 2306.07317 [hep-ph].

[394] H.-S. Lee, *Minimal gauge origin of baryon triality and flavorful signatures at the LHC*, Phys. Lett. B **704** (2011) 316, arXiv: 1007.1040 [hep-ph].

[395] S. Bansal, A. Delgado, C. Kolda and M. Quiros, *Limits on R-parity-violating couplings from Drell-Yan processes at the LHC*, Phys. Rev. D **99** (2019) 093008, arXiv: 1812.04232 [hep-ph].

[396] S. Bansal, A. Delgado, C. Kolda and M. Quiros, *Constraining R-parity-violating couplings in τ-processes at the LHC and in electroweak precision measurements*, Phys. Rev. D **100** (2019) 093005, arXiv: 1906.01063 [hep-ph].

[397] J. L. Pinfold, *The MoEDAL Experiment at the LHC–A Progress Report*, Universe **5** (2019) 47.

[398] J. L. Pinfold, *The MoEDAL experiment: a new light on the high-energy frontier*, Phil. Trans. Roy. Soc. Lond. A **377** (2019) 20190382, ed. by J. Dainton.

[399] K. Abe et al., *Letter of Intent: The Hyper-Kamiokande Experiment — Detector Design and Physics Potential —*, (2011), arXiv: 1109.3262 [hep-ex].

[400] E. Kearns et al., "Hyper-Kamiokande Physics Opportunities", *Snowmass 2013: Snowmass on the Mississippi*, 2013, arXiv: 1309.0184 [hep-ex].

[401] H. K. Dreiner, H. E. Haber and S. P. Martin, *Two-component spinor techniques and Feynman rules for quantum field theory and supersymmetry*, Phys. Rept. **494** (2010) 1, arXiv: 0812.1594 [hep-ph].

[402] M. A. Diaz, "Bilinear R-parity violation", *International Workshop on Physics Beyond the Standard Model: From Theory to Experiment (Valencia 97)*, 1998 188, arXiv: hep-ph/9802407.

[403] A. Aguilar-Arevalo et al., *Improved search for heavy neutrinos in the decay $\pi \to e\nu$*, Phys. Rev. D **97** (2018) 072012, arXiv: 1712.03275 [hep-ex].

[404] W. Altmannshofer et al., "Testing Lepton Flavor Universality and CKM Unitarity with Rare Pion Decays in the PIONEER experiment", *Snowmass 2021*, 2022, arXiv: 2203.05505 [hep-ex].

[405] E. Cortina Gil et al., *Search for heavy neutral lepton production in K^+ decays to positrons*, Phys. Lett. B **807** (2020) 135599, arXiv: 2005.09575 [hep-ex].

[406] Y. Asano et al., *Search for a Heavy Neutrino Emitted in $K^+ \to \mu^+$ Neutrino Decay*, Phys. Lett. B **104** (1981) 84.

[407] R. S. Hayano et al., *HEAVY NEUTRINO SEARCH USING K(mu2) DECAY*, Phys. Rev. Lett. **49** (1982) 1305.

[408] P. Ballett, T. Boschi and S. Pascoli, *Heavy Neutral Leptons from low-scale seesaws at the DUNE Near Detector*, JHEP **03** (2020) 111, arXiv: 1905.00284 [hep-ph].

[409] K. Abe et al., *Search for heavy neutrinos with the T2K near detector ND280*, Phys. Rev. D **100** (2019) 052006, arXiv: 1902.07598 [hep-ex].

[410] F. Bergsma et al., *A Search for Decays of Heavy Neutrinos in the Mass Range 0.5-GeV to 2.8-GeV*, Phys. Lett. B **166** (1986) 473.

[411] P. Vilain et al., *Search for heavy isosinglet neutrinos*, Phys. Lett. B **343** (1995) 453.

[412] J. Orloff, A. N. Rozanov and C. Santoni, *Limits on the mixing of tau neutrino to heavy neutrinos*, Phys. Lett. B **550** (2002) 8, arXiv: hep-ph/0208075.

[413] A. Vaitaitis et al., *Search for neutral heavy leptons in a high-energy neutrino beam*, Phys. Rev. Lett. **83** (1999) 4943, arXiv: hep-ex/9908011.

[414] K. J. Kelly and P. A. N. Machado, *MicroBooNE experiment, NuMI absorber, and heavy neutral leptons*, Phys. Rev. D **104** (2021) 055015, arXiv: 2106.06548 [hep-ph].

[415] A. M. Cooper-Sarkar et al., *Search for Heavy Neutrino Decays in the BEBC Beam Dump Experiment*, Phys. Lett. B **160** (1985) 207.

[416] R. Barouki, G. Marocco and S. Sarkar, *Blast from the past II: Constraints on heavy neutral leptons from the BEBC WA66 beam dump experiment*, SciPost Phys. **13** (2022) 118, arXiv: 2208.00416 [hep-ph].

[417] P. Coloma, P. Hernández, V. Muñoz and I. M. Shoemaker, *New constraints on Heavy Neutral Leptons from Super-Kamiokande data*, Eur. Phys. J. C **80** (2020) 235, arXiv: 1911.09129 [hep-ph].

[418] F. Kling and S. Trojanowski, *Heavy Neutral Leptons at FASER*, Phys. Rev. D **97** (2018) 095016, arXiv: 1801.08947 [hep-ph].

[419] J. De Vries, H. K. Dreiner, J. Y. Günther, Z. S. Wang and G. Zhou, *Long-lived Sterile Neutrinos at the LHC in Effective Field Theory*, JHEP **03** (2021) 148, arXiv: 2010.07305 [hep-ph].

[420] J. P. Lees et al., *Search for heavy neutral leptons using tau lepton decays at BaBaR*, Phys. Rev. D **107** (2023) 052009, arXiv: 2207.09575 [hep-ex].

[421] E. Cortina Gil et al., *Search for π^0 decays to invisible particles*, JHEP **02** (2021) 201, arXiv: 2010.07644 [hep-ex].

[422] J. P. Lees et al., *Improved Limits on B^0 Decays to Invisible Final States and to $\nu\bar{\nu}\gamma$*, Phys. Rev. D **86** (2012) 051105, arXiv: 1206.2543 [hep-ex].

[423] A. Aguilar-Arevalo et al., *Improved Measurement of the $\pi \to e\nu$ Branching Ratio*, Phys. Rev. Lett. **115** (2015) 071801, arXiv: 1506.05845 [hep-ex].

[424] G. Marocco and S. Sarkar, *Blast from the past: Constraints on the dark sector from the BEBC WA66 beam dump experiment*, SciPost Phys. **10** (2021) 043, arXiv: 2011.08153 [hep-ph].

[425] R. Beltrán, G. Cottin, M. Hirsch, A. Titov and Z. S. Wang, *Reinterpretation of searches for long-lived particles from meson decays*, JHEP **05** (2023) 031, arXiv: 2302.03216 [hep-ph].

[426] A. M. Baldini et al., *Search for the lepton flavour violating decay $\mu^+ \to e^+\gamma$ with the full dataset of the MEG experiment*, Eur. Phys. J. C **76** (2016) 434, arXiv: 1605.05081 [hep-ex].

[427] D. I. Britton et al., *Improved search for massive neutrinos in pi+ —> e+ neutrino decay*, Phys. Rev. D **46** (1992) R885.

[428] G. Bellini et al., *New limits on heavy sterile neutrino mixing in B8 decay obtained with the Borexino detector*, Phys. Rev. D **88** (2013) 072010, arXiv: 1311.5347 [hep-ex].

[429] R. Plestid, *Luminous solar neutrinos II: Mass-mixing portals*, Phys. Rev. D **104** (2021) 075028, [Erratum: Phys.Rev.D 105, 099901 (2022), Erratum: Phys.Rev.D 105, 099901 (2022)], arXiv: 2010.09523 [hep-ph].

[430] M. Dentler et al., *Updated Global Analysis of Neutrino Oscillations in the Presence of eV-Scale Sterile Neutrinos*, JHEP **08** (2018) 010, arXiv: 1803.10661 [hep-ph].

[431] D. Gorbunov and M. Shaposhnikov, *How to find neutral leptons of the νMSM?*, JHEP **10** (2007) 015, [Erratum: JHEP 11, 101 (2013)], arXiv: 0705.1729 [hep-ph].

[432] K. Bondarenko, A. Boyarsky, D. Gorbunov and O. Ruchayskiy, *Phenomenology of GeV-scale Heavy Neutral Leptons*, JHEP **11** (2018) 032, arXiv: 1805.08567 [hep-ph].

[433] C. A. Argüelles, N. Foppiani and M. Hostert, *Heavy neutral leptons below the kaon mass at hodoscopic neutrino detectors*, Phys. Rev. D **105** (2022) 095006, arXiv: 2109.03831 [hep-ph].

[434] M. Hirsch and J. W. F. Valle, *Neutrinoless double beta decay in supersymmetry with bilinear R parity breaking*, Nucl. Phys. B **557** (1999) 60, arXiv: hep-ph/9812463.

[435] J. M. Berryman et al., *Searches for Decays of New Particles in the DUNE Multi-Purpose Near Detector*, JHEP **02** (2020) 174, arXiv: 1912.07622 [hep-ph].

[436] P. Abratenko et al., *Search for long-lived heavy neutral leptons and Higgs portal scalars decaying in the MicroBooNE detector*, Phys. Rev. D **106** (2022) 092006, arXiv: 2207.03840 [hep-ex].

[437] I. Boiarska, A. Boyarsky, O. Mikulenko and M. Ovchynnikov, *Constraints from the CHARM experiment on heavy neutral leptons with tau mixing*, Phys. Rev. D **104** (2021) 095019, arXiv: 2107.14685 [hep-ph].

[438] R. Acciarri et al., *New Constraints on Tau-Coupled Heavy Neutral Leptons with Masses mN=280–970 MeV*, Phys. Rev. Lett. **127** (2021) 121801, arXiv: 2106.13684 [hep-ex].

[439] K. Abe et al., *Search for proton decay via $p \to \nu K^+$ using 260 kiloton · year data of Super-Kamiokande*, Phys. Rev. D **90** (2014) 072005, arXiv: 1408.1195 [hep-ex].

[440] Y. Fukuda et al., *The Super-Kamiokande detector*, Nucl. Instrum. Meth. A **501** (2003) 418, ed. by V. A. Ilyin, V. V. Korenkov and D. Perret-Gallix.

[441] K. Agashe and M. Graesser, *R-parity violation in flavor changing neutral current processes and top quark decays*, Phys. Rev. D **54** (1996) 4445, arXiv: hep-ph/9510439.

[442] L. F. Abbott and M. B. Wise, *The Effective Hamiltonian for Nucleon Decay*, Phys. Rev. D **22** (1980) 2208.

[443] S. Aoki et al., *Nucleon decay matrix elements from lattice QCD*, Phys. Rev. D **62** (2000) 014506, arXiv: hep-lat/9911026.

[444] Y. Aoki, T. Izubuchi, E. Shintani and A. Soni, *Improved lattice computation of proton decay matrix elements*, Phys. Rev. D **96** (2017) 014506, arXiv: 1705.01338 [hep-lat].

[445] A. Abusleme et al., *JUNO Sensitivity on Proton Decay $p \to \bar{\nu} K^+$ Searches*, (2022), arXiv: 2212.08502 [hep-ex].

[446] H. W. Bertini, *Low-Energy Intranuclear Cascade Calculation*, Phys. Rev. **131** (1963) 1801.

[447] H. W. Bertini, *Intranuclear-cascade calculation of the secondary nucleon spectra from nucleon-nucleus interactions in the energy range 340 to 2900 mev and comparisons with experiment*, Phys. Rev. **188** (1969) 1711.

[448] H. W. Bertini and M. P. Guthrie, *News item results from medium-energy intranuclear-cascade calculation*, Nucl. Phys. A **169** (1971) 670.

[449] S. Agostinelli et al., *GEANT4–a simulation toolkit*, Nucl. Instrum. Meth. A **506** (2003) 250.

[450] A. Heikkinen, N. Stepanov and J. P. Wellisch, *Bertini intranuclear cascade implementation in GEANT4*, eConf **C0303241** (2003) MOMT008, arXiv: nucl-th/0306008.

[451] D. Stefan and A. M. Ankowski, *Nuclear effects in proton decay*, Acta Phys. Polon. B **40** (2009) 671, ed. by W. Krolas, B. Fornal and M. Kmiecik, arXiv: 0811.1892 [nucl-th].

[452] T. M. Undagoitia et al., *Search for the proton decay p —> K+ anti-nu in the large liquid scintillator low energy neutrino astronomy detector LENA*, Phys. Rev. D **72** (2005) 075014, arXiv: hep-ph/0511230.

[453] M. Litos et al., *Search for Dinucleon Decay into Kaons in Super-Kamiokande*, Phys. Rev. Lett. **112** (2014) 131803.

List of Figures

1.1 Neutrino mass eigenstate flavor composition and mass pattern in the two cases of normal (left) and inverted (right) ordering. Figure taken from [15]. 4

2.1 Absolute values of the couplings required to fit the IO limit of the TBM scenario in models with Class 1 structure. 32
2.2 A measure of the amount of RPV required by each point in the solution space for Class 1 models. The plot corresponds to the IO limit of the TBM case. . . 34
2.3 Absolute values of the couplings required to fit the IO limit of the TBM scenario in models with Class 2 structure. 35
2.4 A measure of the amount of RPV required by each point in the solution space for Class 2 models. The plot corresponds to the IO limit of the TBM case. . . 35
2.5 Absolute values of the couplings required to fit the TBM scenario in models with Class 3 structure. The notation f_{neg} means $f\left(-x^1\right)$ has been plotted instead of $f\left(x^1\right)$. 36
2.6 A measure of the amount of RPV required by each point in the solution space for Class 3 models. The plots correspond to the TBM scenario. 37
2.7 Real (left) and imaginary (right) values of the couplings required to fit the actual neutrino data for the NO limit in models with Class 1 structure. . . . 38
2.8 Variation of χ^2 as a function of the fitted parameter x_1' for the Class 3 NO scenario around the best-fit point as determined by MINUIT2. The other couplings are held fixed. 39
2.9 The IO (left) and NO (right) solution spaces for the non-diagonal trilinear model of Abschnitt 2.8.5 including δ_{CP}. The grey regions are the ones ruled out by the bounds of Gleichung (2.67). The bounds of Gleichung (2.66) are beyond the scale of the plots. 44
2.10 The NO limit solution space for the bilinear-trilinear mixed model of Abschnitt 2.8.6 including δ_{CP}. 45

3.1 Some possible paths a $\tilde{q}$ LSP can take while decaying through λ''_{312}. Since $\tilde{q}$ is the LSP here, all the intermediate sparticles are virtual. See Tabelle 3.1 for the notation employed. 55
3.2 95% confidence-level mass-exclusion limits for various LSPs corresponding to direct pair production. In each scenario, all sparticles other than the LSP(s) ($\tilde{p}$) are assumed to be decoupled, while the LSP decays are still prompt. . . . 71
3.3 Exclusion regions (in green) corresponding to 95% confidence level for the $I_{\tilde{g}\to\tilde{q}}$ (left) and $I_{\tilde{g}\to\tilde{q}_3}$ (right) scenarios. The bounds of Abb. 3.2 from direct squark production also apply to the scenario and are shown in red. The gray region is kinematically disallowed in the scenario. The dotted (dashed) contours correspond to coupling λ_{121} (λ_{313}). 73
3.4 As in Abb. 3.3 but for the $I_{\tilde{g}\to\tilde{W}}$ (left) and $I_{\tilde{q}\to\tilde{W}}$ (right) scenarios. 74
3.5 As in Abb. 3.3 but for the $I_{\tilde{g}\to\tilde{H}}$ (left) and $I_{\tilde{q}_3\to\tilde{H}}$ (right) scenarios. 74

3.6 As in Abb. 3.3 but for the $I_{\tilde{x}\to\tilde{B}}$ scenarios. 75
3.7 As in Abb. 3.3 but for the $I_{\tilde{x}\to\tilde{\ell}/\tilde{\tau}}$ scenarios. 77
3.8 Summary of minimum mass bounds on sparticle $\tilde{p}$ across the various $I_{\tilde{p}\to\tilde{x}}$ benchmarks considered, where $\tilde{x}$ corresponds to the LSPs. The vertical red line represents the direct production mass bound when $\tilde{p}$ is the LSP, *i.e.*, the limit corresponding to $D_{\tilde{p}}$. 78

4.1 Feynman diagrams for the radiative neutralino decay. 88
4.2 Branching ratios of the lightest neutralino into the single-photon signature, with varying neutralino mass. 90
4.3 Sensitivity reach for FASER (solid lines) and FASER2 (dashed lines) for the benchmark scenario **B1**, *cf.* Tabelle 4.1. The left plot shows the sensitivity reach in the production coupling ($\frac{\lambda'_{211}}{m^2_{\rm SUSY}}$) vs. decay coupling ($\frac{\lambda'_{333}}{m^2_{\rm SUSY}}$) plane, for a neutralino mass of 30 MeV. The gray areas are excluded by the low-energy bounds, also given in Tabelle 4.1. The right plot shows the sensitivity reach in $\mathrm{BR}(\pi^\pm \to \tilde{\chi}^0_1 + \mu^\pm)\times\mathrm{BR}(\tilde{\chi}^0_1 \to \text{signature})$ as a function of the neutralino decay length, $c\tau$, for $m_{\tilde{\chi}^0_1} = 10$ and 30 MeV. The shaded regions correspond to existing constraints from HNL searches. 94
4.4 Sensitivity reach in the neutralino mass-coupling plane for FASER2 for the same physics scenario as in **B1** but with variable neutralino mass. The production ($\frac{\lambda'_{211}}{m^2_{\rm SUSY}}$) and decay ($\frac{\lambda'_{333}}{m^2_{\rm SUSY}}$) couplings have been set equal. The gray areas are excluded by the low-energy bounds. 94
4.5 As in Abb. 4.3 but for the benchmark scenario **B2** with $m_{\tilde{\chi}^0_1} = 75$ MeV, *cf.* Tabelle 4.1. The right plot shows the sensitivity reach in $\mathrm{BR}(K^\pm \to \tilde{\chi}^0_1 + \mu^\pm)\times\mathrm{BR}(\tilde{\chi}^0_1 \to \text{signature})$ as a function of the neutralino decay length, $c\tau$, for $m_{\tilde{\chi}^0_1} = 75$ and 300 MeV. 95
4.6 As in Abb. 4.4 but for the benchmark scenarios **B2** (left) and **B3** (right). The sensitivity reach corresponds to FASER (solid line) and FASER2 (dashed line). . 96
4.7 As in Abb. 4.3 but for the benchmark scenario **B4** with $m_{\tilde{\chi}^0_1} = 300$ MeV, *cf.* Tabelle 4.1. The right plot shows the sensitivity reach in $\mathrm{BR}(D^\pm \to \tilde{\chi}^0_1 + \mu^\pm)\times\mathrm{BR}(\tilde{\chi}^0_1 \to \text{signature})$ as a function of the neutralino decay length, $c\tau$, for $m_{\tilde{\chi}^0_1} = 490$ and 1 200 MeV. 97
4.8 As in Abb. 4.4 but for the benchmark scenario in **B4** while varying the neutralino mass. The sensitivity reach corresponds to FASER (solid line) and FASER2 (dashed line). 97
4.9 The left plot is as in Abb. 4.4 but for the single coupling benchmark scenario in **B5** while varying the neutralino mass. The right plot shows the sensitivity reach in $\mathrm{BR}(D_S^\pm \to \tilde{\chi}^0_1 + \mu^\pm)\times\mathrm{BR}(\tilde{\chi}^0_1 \to \text{signature})$ as a function of the neutralino decay length, $c\tau$, for $m_{\tilde{\chi}^0_1} = 500$ MeV. The sensitivity reaches correspond to FASER (solid line) and FASER2 (dashed line). 98

4.10 As in Abb. 4.3 but for the benchmark scenario **B6** with $m_{\tilde{\chi}_1^0} = 1\,\text{GeV}$, *cf.* Tabelle 4.1. The right plot shows the sensitivity reach in $\text{BR}(B^\pm \to \tilde{\chi}_1^0 + \tau^\pm) \times \text{BR}(\tilde{\chi}_1^0 \to \text{signature})$ as a function of the neutralino decay length, $c\tau$, for $m_{\tilde{\chi}_1^0} = 200$ and $1\,000\,\text{MeV}$. 99
4.11 As in Abb. 4.4 but for the benchmark scenario in **B6** while varying the neutralino mass. The sensitivity reach corresponds to `FASER` (solid line) and `FASER2` (dashed line). 100

5.1 Exclusion limits on bilinear RPV couplings as a function of the light bino mass, reinterpreted from existing HNL searches. The current limit on the bilinear couplings is shown as a horizontal gray line. 118
5.2 Sensitivity limits on the $\boldsymbol{\lambda'_\pi}$ one-coupling scenarios of Tabelle 5.2 as a function of the light bino mass, reinterpreted from existing HNL searches. Current (projected) limits obtained from the reinterpretation are shown as solid (dashed) gray lines. The existing limits on the RPV couplings are also shown in red, with the solid and dashed lines corresponding to varying assumptions of unknown SUSY mass scales. 119
5.3 As in Abb. 5.2 but for the $\boldsymbol{\lambda'_K}$ and $\boldsymbol{\lambda'_{D/K}}$ benchmarks of Tabelle 5.2. The existing limits on the RPV couplings are shown in red, yellow, green, and blue. 120
5.4 As in Abb. 5.2 but for the $\boldsymbol{\lambda'_{B1}}$ and $\boldsymbol{\lambda'_{B2}}$ benchmarks of Tabelle 5.2. The existing limits on the RPV couplings are shown in red, green, and blue. . . . 121
5.5 As in Abb. 5.2 but for the $\boldsymbol{\lambda'_{D_s}}$ benchmarks of Tabelle 5.2. 121
5.6 As in Abb. 5.2 but for the $\boldsymbol{\lambda'_\mu}$ and $\boldsymbol{\lambda'_{\tau/\mu}}$ benchmarks of Tabelle 5.2. The existing limits on the RPV couplings are shown in red, yellow, green, and blue. 122
5.7 Current exclusion (solid lines) and projected sensitivity (dashed lines) limits corresponding to the two-coupling RPV scenarios with binos produced from pions; reinterpreted from HNL searches. The existing limits on the RPV couplings are shown in red, and green. 125
5.8 Current exclusion (solid lines) and projected sensitivity (dashed lines) limits corresponding to the two-coupling RPV scenarios with binos produced from kaons in the RPV coupling vs. bino mass plane; reinterpreted from HNL searches. The existing limits on the RPV couplings are shown in red and green (single bounds), and blue (product bound). 127
5.9 As in Abb. 5.8 but for binos produced from τ leptons. 128
5.10 As in Abb. 5.8 but for binos produced from D and D_s mesons. 130
5.11 As in Abb. 5.8 but for binos produced from B and B_c mesons. 132

6.1 Feynman diagrams depicting the decay of a proton into a light neutralino. The black blob shows the RPV vertex. Spectator quarks are omitted. 137
6.2 Momentum of the final state kaon as a function of the neutralino mass in the process $p \to K^+ + \tilde{\chi}_1^0$. 141
6.3 Average neutralino decay probabilities as a function of the neutralino mass corresponding to neutralino decay lengths $c\tau = 10\,\text{m}$ (left) and $c\tau = 1\,000\,\text{m}$ (right). These plots have been generated by setting $N_{\text{MC}}^{\tilde{\chi}_1^0} = 10000$. 149

6.4 Sensitivity reach for the single coupling scenario of benchmark **B1**. The reinterpreted bound from Super-K is shown in gray. The bound from Tabelle 6.3 lies above the scale of the plot. The results for Hyper-K, DUNE, and JUNO are for a run-time of 10 years. 152
6.5 Sensitivity reach/Super-K limit for benchmark **B2**. The existing single-bound on λ'_{333} from Tabelle 6.3 is shown in gray (with $m_{\tilde{f}} = 1\,\text{TeV}$), while the product-bound lies outside the scale of the plot. *Left:* The limits in the coupling-vs.-coupling plane with $m_{\tilde{\chi}_1^0} = 400\,\text{MeV}$. The contours correspond to the visible mode (blue dashed, downward sloping line) and invisible mode (vertical lines); see discussion in the text. *Right:* The limits in the coupling-vs.-mass plane for the visible mode with $\lambda''_{121}/m^2_{\tilde{f}}$ fixed at the threshold of the Super-K bound of Abb. 6.4. 153
6.6 Sensitivity reach/Super-K limit for benchmark **B3**. The existing single-bounds from Tabelle 6.3 are shown in gray while the product-bound is shown in blue (all with $m_{\tilde{f}} = 1\,\text{TeV}$). *Top Left:* As in left plot of Abb. 6.5 but for benchmark **B3**. *Top Right:* Zoomed-out version of the top-left plot. *Bottom:* As in right plot of Abb. 6.4 but for benchmark **B3**. The solid and dashed lines correspond to 3- and 30-event isocurves, respectively. 154
6.7 Sensitivity reach/Super-K limit for benchmark **B4**. The existing single-bound on λ'_{211} from Tabelle 6.3 is shown in gray, the product-bound is in blue (both with $m_{\tilde{f}} = 1\,\text{TeV}$), while the bound on λ''_{121} lies outside the scale of the plot. *Left:* As in left plot of Abb. 6.5 but for benchmark **B4**. *Right:* As in right plot of Abb. 6.4 but for benchmark **B4**. The solid, dashed, and dot-dashed lines correspond to 3-, 30- and 90-event isocurves, respectively. 155
6.8 Sensitivity reach/Super-K limit for benchmark **B5**. The existing single-bound on λ'_{311} from Tabelle 6.3 is shown in gray, the product-bound is in blue (both with $m_{\tilde{f}} = 1\,\text{TeV}$), while the bound on λ''_{121} lies outside the scale of the plot. *Left:* As in left plot of Abb. 6.5 but for benchmark **B5**. *Right:* As in right plot of Abb. 6.4 but for benchmark **B5**. The solid, dashed, and dot-dashed lines correspond to 3-, 30- and 90-event isocurves, respectively. 156

A.1 Real (top) and imaginary (bottom) values of the couplings required to fit the actual neutrino data for the Inverted Ordering limit in models with Class 1 structure. 165
A.2 Real (left) and imaginary (right) values of the couplings required in models with Class 2 structure to fit the actual neutrino data for the two mass orderings: IO (top) and NO (bottom). 166
A.3 Values of the couplings required in models with Class 3 structure to fit the actual neutrino data for the two mass orderings: IO (left) and NO (right). For this class, all couplings are real. 167
A.4 Values of the couplings required to fit the actual neutrino data including δ_{CP} in models with Class 2 structures for normal ordering. 167

List of Tables

1.1 Chiral supermultiplets in the MSSM 8
1.2 Gauge supermultiplets in the MSSM 8

2.1 $\mathbf{M}_\nu$ contributions as calculated in Ref. [62]. The numbered entries are due to one-loop diagrams. Summation is implied over all repeated indices other than i, j. The δ's are the RPV basis invariants. m_0 is the tree-level mass scale of Gleichung (2.14), the remaining m's are the SM fermion masses, and the h's are the Yukawas. 24
2.2 Neutrino oscillation parameters from a global fit to data. The first (second) column depicts the best fit assuming NO (IO). Note that $\Delta^2_{3l} \equiv \Delta^2_{31} > 0$ for NO and $\Delta^2_{3l} \equiv \Delta^2_{32} < 0$ for IO. 29

3.1 Summary of notation for labeling the RPV-MSSM particle content used in this work. For the particles not mentioned in the table, we use standard notation. 52
3.2 Characteristic signatures arising from LSP decays for $L_iL_j\bar{E}_k$ operators. The first column depicts the LSPs. The second and third columns represent the signatures from *pair-production* of LSPs for the cases where the indices $i, j, k \in \{1, 2\}$, and where the indices $i, k \in \{1, 2\}$ and $j = 3$, respectively. For cases involving degenerate LSPs, *e.g.*, $\tilde{\ell}\,(\tilde{\nu})$, all pair combinations are considered. Further, only the relevant signatures are retained and we have introduced color-coding to improve the readability of the table; the details are in the main text. 56
3.3 Same as Tabelle 3.2 but for $L_iL_j\bar{E}_k$ operators with $i, j \in \{1, 2\}$ and $k = 3$ (second column), and $j, k = 3$ and $i \in \{1, 2\}$ (third column). 57
3.4 Characteristic signatures arising from LSP decays for $\bar{U}_i\bar{D}_j\bar{D}_k$ operators. The first column depicts the LSPs. The second and third columns represent the signatures from *pair-production* of LSPs for the cases where the indices $i, j, k \in \{1, 2\}$, and where the indices $i, k \in \{1, 2\}$ and $j = 3$, respectively. For cases involving degenerate LSPs, *e.g.*, $\tilde{\ell}\,(\tilde{\nu})$, all pair combinations are considered. Further, only the relevant signatures are retained and we have introduced color-coding to improve the readability of the table; the details are in the main text. 59
3.5 Same as Tabelle 3.4 but for $\bar{U}_i\bar{D}_j\bar{D}_k$ operators with $j, k \in \{1, 2\}$ and $i = 3$ (second column), and $i, j = 3$ and $k \in \{1, 2\}$ (third column). 60
3.6 Characteristic signatures arising from LSP decays for $L_iQ_j\bar{D}_k$ operators. The first column depicts the LSPs. The second and third columns represent the signatures from *pair-production* of LSPs for the cases where the indices $i, j, k \in \{1, 2\}$, and where the indices $i, j \in \{1, 2\}$ and $k = 3$, respectively. For cases involving degenerate LSPs, *e.g.*, $\tilde{\ell}\,(\tilde{\nu})$, all pair combinations are considered. Further, only the relevant signatures are retained and we have introduced color-coding to improve the readability of the table; the details are in the main text. 61

3.7 Same as Tabelle 3.6 but for $L_iQ_j\bar{D}_k$ operators with $i,k \in \{1,2\}$ and $j=3$. . . 62

3.8 Same as Tabelle 3.6 but for $L_iQ_j\bar{D}_k$ operators with $j,k=3$ and $i \in \{1,2\}$. . . 62

3.9 Same as Tabelle 3.6 but for $L_iQ_j\bar{D}_k$ operators with $j,k \in \{1,2\}$ and $i=3$ (second column), and $i,k=3$ and $j \in \{1,2\}$ (third column). 63

3.10 Same as Tabelle 3.6 but for $L_iQ_j\bar{D}_k$ operators with $i,j=3$ and $k \in \{1,2\}$. . . 63

3.11 Same as Tabelle 3.6 but for $L_iQ_j\bar{D}_k$ operators with $i,j,k=3$. 64

3.12 Details of our benchmarks: the first two columns depict the LSP and the production mode considered, respectively; the RPV coupling assumed to be non-zero is shown in the third column; the fourth column represents the possible decays of the LSP (these are split into two columns for better readability); the last column shows the notation we use for labeling the scenario. 65

3.13 As in Tabelle 3.12 but for the squark LSP benchmarks. 66

3.14 As in Tabelle 3.12 but for the electroweakino LSP benchmarks. 68

3.15 As in Tabelle 3.12 but for the slepton LSP benchmarks. For brevity, we skip showing decay modes explicitly (indicated by $*$) for some sleptons that do not couple directly to the relevant RPV operator (*e.g.*, $\tilde{\mu}_R$ LSP with λ_{121}). However, the details of how we include these modes in our simulations can be found in Anhang B.1. 69

3.16 Summary of the most sensitive searches in our numerical simulations. The first column lists existing ATLAS and CMS searches providing sensitivity and our shorthand notation for each; the second column summarizes the relevant cuts; and the last column refers to the scenario labels presented in Tables 3.12-3.15. We have color-coded the labels according to the final state topologies of Abschnitt 3.3: $3L + E_T^{\text{miss}}$, $4L + (0-4)j + E_T^{\text{miss}}$, and $5L + E_T^{\text{miss}}$. The same searches also constrain the $\text{I}_{\tilde{x}\to\tilde{p}}$ scenarios (not shown here). 70

4.1 Benchmark scenarios considered in this paper. The neutralino is produced through the rare decay of the meson M via the coupling λ^{P}_{ijk}: $M \to \tilde{\chi}^0_1 + \ell\,(\nu)$. The neutralino decay is as in Gleichung (4.5) via the coupling λ^{D}_{ijj}. The photon energy in the neutralino rest frame is $E_\gamma = m_{\tilde{\chi}^0_1}/2$, but can range from $\mathcal{O}\,(0.1)$ to $\mathcal{O}\,(1)$ TeV at FASER. In the furthest-to-the-right column, we list the current best bounds on the couplings, see for example, Ref. [157]. 89

4.2 Integrated luminosities and geometries of the detectors used in the simulations. Here, $\mathcal{L}$, $\sqrt{\mathbf{s}}$, $\mathbf{L}$, $\mathbf{\Delta}$, and $\mathbf{R}$ label, respectively, the integrated luminosity, the collider center-of-mass energy, the distance from the IP, the detector length, and the detector radius. 93

5.1 Summary of experiments reviewed in Sec. 5.3, sorted by search strategy. We list the relevant references, the status of derived bounds (current or projected), the relevant HNL mixing, and the experimentally accessible HNL mass range. 109

5.2 Details of the searches providing constraints when only one non-zero RPV operator contributes at a time. We list all the bilinear, $LQ\bar{D}$, and $LL\bar{E}$ operators in the first column (by coupling). The second to fourth columns contain the physical processes that provide constraints and the references to the relevant existing HNL searches targeting them. The fifth column indicates our labeling scheme for the scenarios. × denotes the absence of a constraining process, while (×) labels that, in principle, the listed process may provide constraints but we could not find a relevant existing HNL search. In the table, $a \in \{1, 2\}$ and $i \in \{1, 2, 3\}$. 117

5.3 Relevant final states from HNL (and bino) decay sorted by threshold mass. The active neutrino is considered massless. 122

5.4 Relevant two-coupling RPV scenarios probed by HNL DV searches. Column one categorizes the parent meson/lepton; column two shows the corresponding RPV coupling, production process, and bino mass range; the remaining columns list the relevant final states of Tabelle 5.3 arising from bino decays and the corresponding decay RPV coupling(s) for each production category. × indicates that the decay is kinematically disallowed. 124

5.5 Details of the two-coupling RPV benchmark scenarios we study, corresponding to bino production from pions. The decay coupling in the third column leads to the final state that can be read off from Tabelle 5.4. See the main text for details on how the mass range is determined. 125

5.6 As in Tabelle 5.5 but for bino production from kaons. 128

5.7 As in Tabelle 5.5 but for bino production from τ leptons, and D and D_s mesons. 129

5.8 As in Tabelle 5.5 but for bino production from B and B_c mesons. 131

6.1 Hadronic matrix elements for proton to kaon decays from lattice computations. The values for $W_{0,\Omega}^{p\to K^+}$ are taken from Ref. [444]. The values for $W_{\chi,\Omega}^{p\to K^+}$, which contain corrections for the massive neutralino, are calculated using expressions in Gleichung (6.12). 139

6.2 Summary of technical details for the upcoming detectors at `Hyper-K` [116], `JUNO` [114], and `DUNE` [110]. We also show the details for `Super-K` [440] for comparison. $\epsilon_{inv.}$ provides the approximate detection efficiency of the kaon for the neutrino (or invisible neutralino) mode. 144

6.3 Details of the benchmark scenarios. The bounds on λ_{ijk}^D are taken from Refs. [67, 157] while the one on λ''_{121} is from Ref. [453]. Product bounds are obtained from Ref. [99] for SUSY masses of 1 TeV, except in the case of $\lambda'_{311}\lambda''_{121}$, where it is the bound on $p \to K^+ + \bar{\nu}$ from [439] reinterpreted for **B5**. `Super-K` imposes constraints on the massless invisible neutralinos, leading to the limit $|\lambda''121| < 3.9 \times 10^{-25} \left(\frac{m\tilde{q}}{\text{TeV}}\right)^2$. We will present this bound in our results. The mass ranges for each benchmark are according to the discussion in the text, although we have rounded them off. 149

B.1 Objects arising in the cascade decays of various pairs of parent sparticles (columns) down to the LSP(s) (rows). These can be added to the corresponding LSP signatures given in Tables 3.2-3.11 to optimize searches. $+-$ indicates an empty set while $\times$ indicates that the corresponding production channel is not relevant for the given LSP because the cross-section is either lower than or comparable to the cross-section for direct pair production of the LSP. 172
B.2 $2L + E_T^{\text{miss}}$. 173
B.3 $3L + E_T^{\text{miss}}$. 173
B.4 $4L$. 173
B.5 $4L + (0-4)j + E_T^{\text{miss}}$. 174
B.6 $5L + E_T^{\text{miss}}$. 174
B.7 $6L + E_T^{\text{miss}}$. 174
B.8 $1L + 2j_l + 4j + E_T^{\text{miss}}$. 175
B.9 $2L + 2j_l + 4j$. 175
B.10 $1L + (2-6)j + E_T^{\text{miss}}$. 175
B.11 $2L + (2-6)j + (E_T^{\text{miss}})$. 175
B.12 $3L + 4j + E_T^{\text{miss}}$. 175
B.13 $4L + 4j$. 175
B.14 Syntax for sparticles used in the code. 177
B.15 One-character syntax for final state objects used in the code. 178